

**High Strain Rate Elastic and Fracture Characterization of Isotropic and Orthotropic  
Materials with and without Nano Fillers**

by

Robert W. Bedsole

A dissertation submitted to the Graduate Faculty of  
Auburn University  
in partial fulfillment of the  
requirements for the Degree of  
Doctor of Philosophy

Auburn, Alabama  
August 1, 2015

Keywords: dynamic fracture, digital image correlation, high-speed photography, cortical bone,  
carbon nanotubes, carbon fiber reinforced polymers

Copyright 2015 by Robert W. Bedsole

Approved by

Hareesh V. Tippur, Chair, McWane Professor of Mechanical Engineering  
Jeffrey C. Suhling, Quina Distinguished Professor of Mechanical Engineering  
James S. Davidson, Professor of Civil Engineering  
Ruel A. Overfelt, Professor of Materials Engineering  
Philip B. Bogert, Senior Aerospace Engineer, NASA Langley Research Center

## Abstract

A long-bar apparatus for subjecting relatively small samples to mode-I stress-wave loading has been devised for failure characterization. A methodology based on digital image correlation (DIC) used in conjunction with ultrahigh-speed photography and a long-bar impactor has been developed for determining dynamic crack initiation stress intensity factors (SIFs), as well as SIFs for rapidly growing cracks during high-strain rate events in isotropic and orthotropic materials. By altering the material of the pulse shaper to cushion the impact, a range of strain rates has been attained.

Commercial grade acrylic was first used to calibrate the device, and then dynamic fracture characterization was carried out for the first time on acrylic bone cement. Despite several key compositional differences, the two materials performed similarly during quasi-static fracture tests; however, under dynamic loading conditions, bone cement exhibited significantly lower crack initiation SIFs ( $K_{I-init}^d$ ), lower dynamic SIFs ( $K_I^d$ ), and higher crack tip velocities for three different dynamic loading rates in the range  $\dot{K} = 6.5 - 24 \times 10^4 \text{ MPa}\sqrt{\text{m}} \text{ s}^{-1}$ .

In the second phase, orthotropic cortical bone fracture was characterized under dynamic impact loading conditions. This is the first reported study of dynamic axial fracture of cortical bone, which is considered a naturally occurring nanomaterial. In order to measure SIFs using in-plane displacements for an orthotropic material, all nine independent elastic constants were

determined ultrasonically. The measured  $K_{I-ini}^d$  values were  $2.7 \text{ MPa}\sqrt{m}$  for a crack growing in the axial direction.

In the third phase of this research, synthetic carbon nanotubes (CNTs) were dispersed into epoxy with the goal of improving the quasi-static tensile, quasi-static fracture, and dynamic fracture properties of epoxy. Subsequently, the optimally-dispersed CNT-modified epoxy was to be used as the matrix material for 3-phase CNT/epoxy/carbon fiber composites. Despite using many different dispersion techniques to achieve different levels of dispersion using different types of CNTs, epoxy systems, and curing cycles, no tangible mechanical improvements significant enough to warrant elaborate and high-cost material processing were found. Dynamic mechanical analysis pointed towards the possible influence of CNTs on crosslink density, which can significantly affect the mechanical properties.

In the last phase, thick carbon fiber reinforced polymers (CFRPs) were built in order to study quasi-static and dynamic interlaminar fracture using DIC and ultrahigh-speed photography. Thick CFRPs were unidirectional, such that interlaminar and intralaminar fracture behaviors could be compared between specimens with identical geometry and cut from the same CFRP plate. Two additional CFRPs containing CNTs or milled carbon fibers (MCFs) were also fabricated in order to examine the size-effects of fillers on the interlaminar properties of reinforced CFRPs. CNTs had little effect on critical SIFs, but critical energy release rate showed +34% and +16% enhancements under static ( $G_{IC}$ ) and dynamic ( $G_{I-ini}^d$ ) conditions, respectively. These were, however, considered insignificant relative to the experimental scatter in these stiff/brittle materials. In the case of MCFs as fillers in the matrix, a +17% improvement in  $K_{IC}$  but a -23% decline in  $K_{I-ini}^d$ , respectively, were observed under static and dynamic loading conditions. The corresponding critical energy release rates for CFRPs with MCFs had a +106%

improvement in quasi-static  $G_{IC}$  and a -15% reduction in dynamic  $G_{I-ini}^d$ . The decline in the dynamic case was attributed to MCFs acting as microscopic spacers between laminae, thereby contributing to the resin-rich interlaminar region.

## Acknowledgments

I would like to thank Dr. Hareesh V. Tippur for his active support and guidance throughout my study at Auburn University. The sponsorship of the research by the NASA Office of the Chief Technologist's Space Technology Research Fellowship (NSTRF #NNX11AM80H) is gratefully acknowledged.

This research project could not have been possible without the support of Drs. Cheol Park, Philip Bogert, Sang-Hyon Chu, Jeffrey Hinkley, Catharine Fay, Luke Gibbons, Tan-Hung Hou, Sharon Lowther, Joseph Smith, Mr. John Hocker, Mr. Sean Britton, Mr. Richard Chattin, Mr. Richard Martin of NASA Langley Research Center; Drs. Lewis Payton, Maria Auad, Mr. Ivey Marcell, Mr. Chase Wortman, Mr. Drew Sherer, Mr. Steven Moore, Ms. MariAnne Sullivan, Mr. Bernal Sibaja of Auburn University; and Drs. Mahesh Hosur, Alfred Tcherbi-Narteh, Eldon Triggs, Mr. Morgan Davis of Tuskegee University.

Special thanks to DePuy Orthopaedics, Inc. (Blane Cagle), Bayer Ag, V2 Composites, Inc. and Momentive Specialty Chemicals, Inc. for providing bone cement, carbon nanotubes, unidirectional carbon fiber, and epoxy, respectively, for this investigation.

I would like to thank my parents, grandparents, sister, and wife, Samantha, for all the love and support throughout my graduate research. I dedicate this dissertation to them.

## Table of Contents

Abstract.....	ii
Acknowledgments.....	v
List of Tables.....	x
List of Illustrations.....	xii
List of Abbreviations.....	xxiii
Chapter 1. Introduction.....	1
1.1 Fracture Mechanics Essentials.....	1
1.2 High-Strain Rate Loading.....	3
1.3 Motivation and Literature Review.....	4
1.3.1 Dynamic Fracture Methodologies.....	6
1.3.2 Acrylic Bone Cement Fracture.....	8
1.3.3 Cortical Bone Fracture.....	10
1.3.4 CNT-modified Epoxy Fracture.....	13
1.3.5 Carbon Fiber Composites.....	24
1.4 Objectives.....	27
1.5 Organization of Dissertation.....	29
Chapter 2. Experimental Methods.....	31
2.1 Development of a Modified Kolsky Bar Apparatus.....	31
2.2 High-Speed Photography.....	37
2.3 Digital Image Correlation (DIC).....	38
Chapter 3. Fracture of Acrylic and Acrylic Bone Cement: Calibration of Experimental Method.....	42

3.1	Specimen Preparation.....	42
3.1.1	Industrial Grade Acrylic vs. Acrylic Bone Cement .....	42
3.1.2	Specimen Preparation .....	43
3.2	Experimental Details .....	45
3.2.1	Quasi-Static Fracture Tests .....	45
3.2.2	Dynamic Fracture Tests .....	46
3.2.3	Ultrasonic Determination of Elastic Constants: Isotropic Materials .....	52
3.2.4	Finite Element Analysis .....	53
3.3	Results .....	57
3.3.1	Quasi-Static Results .....	57
3.3.2	Dynamic Results .....	57
3.4	Discussion .....	70
Chapter 4.	Dynamic Fracture of Orthotropic Cortical Bone.....	73
4.1	Specimen Preparation.....	73
4.2	Experimental Details .....	75
4.2.1	Dynamic Fracture Tests .....	75
4.2.2	Ultrasonic Determination of Orthotropic Elastic Constants .....	78
4.2.3	Finite Element Analysis .....	84
4.3	Results .....	85
4.4	Discussion .....	87
Chapter 5.	Quasi-static and Dynamic Characterization of CNT/Epoxy Nanocomposites .....	89
5.1	Experimental Details .....	89
5.1.1	Quasi-Static Fracture and Tensile Tests .....	89
5.1.2	Dynamic Fracture Tests .....	90
5.1.3	Ultrasonic Determination of Isotropic Elastic Constants.....	91
5.1.4	Finite Element Analysis .....	92
5.2	Carbon Nanotube Dispersion Techniques.....	94
5.2.1	Bath Sonication with Mechanical Stirring .....	94
5.2.1.1	Methods .....	94

5.2.1.2	Results .....	96
5.2.1.3	Microscopy of Fracture Surfaces.....	99
5.2.2	Optimization of Dispersion.....	100
5.2.2.1	Methods .....	100
5.2.2.2	Results .....	103
5.2.3	Other Methods of Dispersing CNTs into the Hardener First.....	104
5.2.3.1	Methods .....	104
5.2.3.2	Results .....	106
5.2.3.3	Microscopy .....	110
5.2.4	Dispersing CNTs into the Resin First.....	114
5.2.4.1	Methods .....	114
5.2.4.2	Results .....	117
5.2.4.3	Microscopy .....	121
5.2.5	Altering Resin Stoichiometry .....	125
5.2.5.1	Methods .....	125
5.2.5.2	Results .....	126
5.3	Discussion and Conclusions.....	131
Chapter 6.	Quasi-static and Dynamic Fracture of CFRPs .....	136
6.1	Specimen Preparation.....	136
6.1.1	Dispersion of Fillers.....	137
6.1.2	Fabrication of Carbon Fiber Reinforced Polymers (CFRPs).....	138
6.2	Experimental Details .....	141
6.2.1	Quasi-Static Fracture Tests .....	141
6.2.2	Dynamic Fracture Tests .....	142
6.2.3	Ultrasonic Determination of Orthotropic Elastic Constants .....	145
6.2.4	Finite Element Analysis .....	149
6.3	Results .....	150
6.3.1	Quasi-Static Results .....	150
6.3.2	Dynamic Results .....	154
6.4	Discussion and Conclusions.....	164



Chapter 7. Conclusions .....	167
7.1 Future Directions.....	169
References.....	171
Appendix A. Comparison of Critical K vs. Critical G.....	179

## List of Tables

<b>Table 1.1:</b>	The quasi-static crack initiation SIF ( $K_{IC}$ ) of various clinical bone cements, including Cemex® with and without a radiopacifier.....	9
<b>Table 1.2:</b>	The quasi-static crack initiation SIF values ( $K_{IC}$ ) for PMMA determined by several research teams, along with the dynamic crack initiation SIF ( $K_{I-init}^d$ ) and corresponding dynamic loading rates ( $\dot{K}$ ).....	10
<b>Table 1.3:</b>	The quasi-static crack initiation SIF $K_{IC}$ of bone.....	11
<b>Table 1.4:</b>	The dynamic transverse crack initiation SIF $K_{I-init}^d$ of bone.....	11
<b>Table 1.5:</b>	$K_{IC}$ of Epoxy Toughened with CNTs.....	14
<b>Table 1.6:</b>	Fracture toughness of epoxy resins and their composites. Reproduced from [50].....	23
<b>Table 1.7:</b>	Tensile properties of epoxy resins and their composites. Reproduced from [50].....	24
<b>Table 1.8:</b>	Reported critical energy release rate ( $G_{IC}$ ) of carbon fiber nanocomposites with CNTs dispersed into the resin first.....	26
<b>Table 1.9:</b>	Reported critical energy release rate ( $G_{IC}$ ) of carbon fiber nanocomposites with CNTs added last to epoxy/carbon fiber prepreg. ....	27
<b>Table 3.1:</b>	Material properties used in the computational and experimental analyses.....	53
<b>Table 3.2:</b>	Compilation of crack initiation SIFs for PMMA and BC for each of the four loading rates. ....	66
<b>Table 3.3:</b>	Average distance ( $r$ ) from the original crack front to fracture regions for each loading rate. $r$ increases with decreasing loading rate.....	68
<b>Table 4.1:</b>	Ultrasonically-determined elastic constants of dried bovine cortical bone. ....	83
<b>Table 5.1:</b>	Material properties used in the computational and experimental analyses.....	92
<b>Table 5.2:</b>	Summary of important $K_{IC}$ results when dispersing CNTs into the hardener first .....	109

<b>Table 5.3:</b>	Summary of important $K_{IC}$ results when dispersing CNTs into the hardener first .....	120
<b>Table 5.4:</b>	Details of multi-walled CNTs used and largest improvement in $K_{IC}$ .....	132
<b>Table 5.5:</b>	Different epoxy systems used and largest improvement in $K_{IC}$ of neat epoxy. ....	133
<b>Table 6.1:</b>	Dimensions of Fillers: NH <sub>2</sub> -CNTs vs. MCFs .....	137
<b>Table 6.2:</b>	Material properties of thick CFRPs ('Neat' refers to epoxy/carbon fiber composites. 'CNT' refers to CNT/epoxy/carbon fiber nanocomposites. 'MCF' refers to MCF/epoxy/carbon fiber composites.) .....	148
<b>Table 6.3:</b>	Average quasi-static (QS) and dynamic (D) critical SIF values for interlaminar and intralaminar specimens. ....	160
<b>Table 6.4:</b>	Average critical energy release rate $G_{IC} / G_{I-ini}^d$ calculated from $K_{IC} / K_{I-ini}^d$ values (QS = Quasi-Static and D = Dynamic).....	160
<b>Table 6.5:</b>	Neat critical SIF assigned to the image before vs. after crack initiation, reported in terms of $K_{IC} / K_{I-ini}^d$ and $G_{IC} / G_{I-ini}^d$ (QS = Quasi-Static and D = Dynamic). ....	162
<b>Table A.1:</b>	Compilation of critical SIFs and energy release rates for PMMA and BC for each of the four loading rates. ....	179

## List of Illustrations

<b>Fig. 1.1:</b>	Three modes of fracture: a) mode-I opening/symmetric fracture, b) mode-II in-plane shearing fracture, and c) mode-III out-of-plane tearing fracture. ....	3
<b>Fig. 1.2:</b>	Kolsky bar for the measurement of the dynamic stress-strain response of a material. Reproduced from [8]. ....	4
<b>Fig. 1.3:</b>	Dynamic fracture apparatus used by [37, 41] to study dynamic fracture of cortical bone. Reproduced from [37]. ....	12
<b>Fig. 1.4:</b>	Dynamic fracture samples and modification of the Kolsky bar (Fig. 1.3) to achieve: a) dynamic 3-point bending used by [37] (reproduced from [37]) and b) dynamic 4-point bending used by [41] (reproduced from [41]). ....	12
<b>Fig. 1.5:</b>	Variations of fracture toughness ( $K_{Ic}$ ) of nanocomposites with different CNT contents. Reproduced from [62]. ....	16
<b>Fig. 1.6:</b>	Variations of a) flexural modulus and b) flexural strength of nanocomposites with different CNT contents. Reproduced from [62]. ....	16
<b>Fig. 1.7:</b>	Quasi-static fracture toughness of nanocomposites as a function of CNT content. (For interpretation of the references to color in these figure legends, the reader is referred to the web version of this article.) Reproduced from [60]. ....	17
<b>Fig. 1.8:</b>	Young's modulus of nanocomposites as a function of CNT content. The predictions are based on the Halpin-Tsai model. (For interpretation of the references to color in these figure legends, the reader is referred to the web version of this article.) Reproduced from [60]. ....	18
<b>Fig. 1.9:</b>	Fracture toughness of the MWCNT-reinforced composites. The dashed line represents the neat epoxy without modification. Note that "aligned" refers to the way the CNTs were grown, not to their orientation within the nanocomposite; all CNTs are randomly aligned in these specimens. Reproduced from [69]. ....	18
<b>Fig. 1.10:</b>	Dispersion quality evolution during the cure for different hardeners: a) IPD at 25°C; b) IPD at 75°C; c) IPD/N3 at 25°C; d) IPD/N3 at 75°C; e) TETA at 25°C; f) TETA after 2 h at 150°C; g) IPD/TETA at 25°C; h) IPD/TETA after 24 h at 25°C. Reproduced from [63]. ....	20

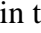
<b>Fig. 1.11:</b>	Fracture toughness test results: a) bisphenol-A with 0.3 wt% MWNT and different types of hardener; b) bisphenol-A with 0.3 wt% MWNT with different IPD:TETA ratio. Reproduced from [63].	21
<b>Fig. 1.12:</b>	Effect of processing methods on dispersion of pristine MWCNT in epoxy resin a) US; b) PSM; c) US + PSM; d) MF; and e) MF + PSM. (US = ultrasound, PSM = planetary shear mixing, MF = microfluidizer). Reproduced from [51].	21
<b>Fig. 1.13:</b>	Tensile strength data (MPa) for MWCNTs/epoxy nanocomposites processed by different methods. Reproduced from [51].	22
<b>Fig. 2.1:</b>	Photographs of long-bar impactor setup for studying crack initiation and propagation of relatively small size specimens: a) full setup, b) close-up of specimen and camera, and c) off-axis view of specimen, camera, and data acquisition system.	32
<b>Fig. 2.2:</b>	Photograph of the high-speed camera system.	33
<b>Fig. 2.3:</b>	Schematic of long-bar impactor setup for studying crack initiation and propagation of relatively small size specimens.	34
<b>Fig. 2.4:</b>	Close-up of the impact loading setup. Specimen with pre-notch is placed in contact with the semi-circular impactor head of the long-bar prior to testing. Putty is used to ensure symmetry of reflected waves from the top and bottom specimen edges.	34
<b>Fig. 2.5:</b>	Photograph of the Ectron 563H amplifier used to amplify the strain gage signal on the long-bar.	35
<b>Fig. 2.6:</b>	Photograph of the Lecroy Waverunner 104Xi oscilloscope used to digitize and record the strain gage signal from the long-bar.	35
<b>Fig. 2.7:</b>	a) Strain histories recorded on the long-bar corresponding to three different pulse shapers. X marks the portion of the strain history coinciding with crack initiation. b) The first 80 $\mu$ s of Fig. 2.7a are shown.	36
<b>Fig. 2.8:</b>	Velocity of the aluminum 7075-T6 striker bar as a function of gas chamber pressure.	37
<b>Fig. 2.9:</b>	a) A pair of images (magnification = 32 $\mu$ m/pixel) recorded from the same CCD sensor of the high-speed camera. A sample sub-image is shown in the undeformed and deformed images. b) Point <i>O</i> in the undeformed sub-image displaces to a location <i>O'</i> in the deformed sub-image. The difference in these coordinates gives the sliding ( <i>u</i> ) and opening ( <i>v</i> ) displacements for the sub-image.	40
<b>Fig. 2.10:</b>	Opening ( <i>v</i> ) displacement contours on a PMMA sample. Data is extracted and interpolated in the region indicated behind the crack tip. A polar coordinate system is assigned with origin at the crack tip.	41
<b>Fig. 3.1:</b>	Bone cement sheet cures between two plates using spacers for desired thickness.	44

<b>Fig. 3.2:</b>	Static a) and dynamic b) specimen geometry. ....	45
<b>Fig. 3.3:</b>	Contours of displacement from 10 x 10 pixel sub-images (a, b) indicate noisy data, while 20 x 20 pixel sub-images (c, d) indicate over-smoothing of raw data. The former shows the crack tip location more precisely compared to the latter.....	47
<b>Fig. 3.4:</b>	Contours of displacement from pixel sub-images 30 x 30 (a, b) and 40 x 40 pixel sub-images (c, d) give very smooth contours but greatly reduce displacement matrices compared to those used in Fig. 3.3, where the crack tip location can be determined much more accurately.....	48
<b>Fig. 3.5:</b>	Displacement contours for 15x15 pixel sub-images with no overlap (a, b), 5 pixel overlap (c, d), and 10 pixel overlap (e, f).....	49
<b>Fig. 3.6:</b>	a) Finite element model with corresponding crack opening displacement contours shown on the specimen, along with the far left end of the long-bar. b) A fine mesh is used near the impact site to ensure that contact and crack tip deformation responses are captured accurately. The field corresponds to a time instant 35 $\mu$ s after impact. ....	54
<b>Fig. 3.7:</b>	Particle velocity input for FEA for each of three different loading rates at 15 psi. Particle velocity is independent of sample material properties. ....	55
<b>Fig. 3.8:</b>	Stress intensity factors are determined for each time increment of the FEA simulation by first finding the crack opening displacements for a series of nodes along the upper crack lip in Fig. 3.6. $K_I^*$ values are calculated using Eq. 3.7, where $r$ is the distance from the crack tip and $u_y$ is the crack opening displacement associated with each node. The y-intercept of the best fit curve of the asymptote (away from the singularity caused by the crack tip) indicates the actual mode-I stress intensity factor ( $K_I$ ) for that time step. ....	55
<b>Fig. 3.9:</b>	SIF histories for three different FEA mesh densities: Coarse (4 mm node spacing), Fine (2 mm node spacing) and Finer (1 mm node spacing). FEA models are in good agreement a) when they are aligned according to crack initiation, whereas convergence is demonstrated when b) they are aligned according to time of impact. ....	56
<b>Fig. 3.10:</b>	Quasi-static load vs. displacement curves for PMMA and bone cement. Loads have been normalized by specimen thickness. Peak loads are similar, but BC fracture is relatively less catastrophic than PMMA. ....	57
<b>Fig. 3.11:</b>	SIFs corresponding to the displacement fields given in Fig. 3.3 – 3.5. a) and b) give the $K_I^d$ and $K_{II}^d$ values when sub-image size is varied. c) and d) give the $K_I^d$ and $K_{II}^d$ values when sub-images of size 15 x 15 pixels are overlapped by 0, 5, and 10 pixels. ....	59
<b>Fig. 3.12:</b>	Images recorded of a crack growing in bone cement using an Al pulse shaper at 2.5, 5, and 7.5 $\mu$ s after initiation. Corresponding crack opening	

	b) and sliding c) displacement fields are shown. Contour interval is 10 $\mu\text{m}$ . Magnification is 30 $\mu\text{m}/\text{pixel}$ . Symmetry of sliding displacements indicates mode-I dominant fracture. Arrows indicate crack tip location.....	60
<b>Fig. 3.13:</b>	SIF histories for a) PMMA with no pulse shaper, b) PMMA with Al pulse shaper, c) PMMA with Al/PC sandwich pulse shaper, d) BC with no pulse shaper, e) BC with Al pulse shaper, f) BC with Al/PC sandwich pulse shaper. Curves have been aligned according to time of crack initiation ( $t_i$ ). (Note: The scale used is consistent for a material type but different for PMMA and BC.).....	61
<b>Fig. 3.14:</b>	Representative SIF histories from each of 6 testing groups from Fig. 3.13. Curves have been aligned according to time of impact rather than time of crack initiation as in Fig. 3.13.....	63
<b>Fig. 3.15:</b>	The effect of material type on crack velocity is shown for a) no pulse shaper (high loading rate: 42.0 $\text{second}^{-1}$ ), b) Al pulse shaper (medium loading rate: 10.7 $\text{second}^{-1}$ ), and c) Al/PC pulse shaper (low loading rate: 3.7 $\text{second}^{-1}$ ). $t = 0$ corresponds to crack initiation. Error bars indicate one standard deviation relative to the average value. ....	64
<b>Fig. 3.16:</b>	The effect of material type on dynamic SIF is shown for a) no pulse shaper (high loading rate: 42.0 $\text{second}^{-1}$ ), b) Al pulse shaper (medium loading rate: 10.7 $\text{second}^{-1}$ ), and c) Al/PC pulse shaper (low loading rate: 3.7 $\text{second}^{-1}$ ). $t = 0$ corresponds to crack initiation. Error bars indicate one standard deviation relative to the average value. ....	65
<b>Fig. 3.17:</b>	Micrographs of PMMA fracture surfaces: a) no pulse shaper and b) Al/PC pulse shaper. Arrows indicate the beginning of common fracture surface regions. Increasing distance $r$ is related to decreased resistance to crack growth. ....	67
<b>Fig. 3.18:</b>	SEM micrographs of fractured BC samples: a) no pulse shaper (100x and 500x) and b) Al/PC pulse shaper (100x and 500x). Higher roughness is shown for the higher loading rate in a), and both images exhibit more roughness than PMMA (Fig. 3.17). Images were captured at a distance of $\sim 5\text{mm}$ from crack front. ....	69
<b>Fig. 3.19:</b>	JEOL JSM-7000F used to generate SEM images.....	70
<b>Fig. 4.1:</b>	Specimen geometry for dynamic fracture of bovine cortical bone.....	73
<b>Fig. 4.2:</b>	a) Orientation of dynamic fracture specimens within bovine metacarpal for ultrasonic determination of orthotropic elastic constants. b) Photograph of a dried bovine cortical bone sample machined for axial dynamic fracture. Arrows indicate the axial direction, while “new” indicates that the sample was recently removed from the freezer for dynamic fracture testing. ....	74
<b>Fig. 4.3:</b>	Posterior portion of bovine cortical bone after axial slicing. Dynamic fracture specimens (Fig. 4.4) were milled from the central region.....	75
<b>Fig. 4.4:</b>	Specimen geometry for the ultrasonic determination of orthotropic elastic constants of bovine cortical bone.....	79

<b>Fig. 4.5:</b>	Photographs of measuring $V_{22}$ with the Epoch 600 Ultrasonic Flaw Detector. Specimen is held between longitudinal transducer and receiver with the 1- and 3-faces showing. Note that all orthotropic measurements were made in through-transmission mode (requiring 2 identical transducers, one of which acts like a receiver). Also pictured are the three additional specimens required to measure off-diagonal C-matrix coefficients.....	80
<b>Fig. 4.6:</b>	In order to measure $V_{66}$ , a) an original cube like the one in Fig. 4.5 is machined. b) Opposite corners are milled off between the 2- and 3-faces, such that ultrasonic transducer and receiver can be placed on the newly milled faces. Note that all ultrasonic measurements were made in through-transmission mode. ....	81
<b>Fig. 4.7:</b>	Photograph of measuring $V_{44}$ with the Epoch 600 Ultrasonic Flaw Detector. Opposite corners that have been milled off between the 1- and 2-faces, such that longitudinal transducer and receiver can be placed on the newly milled faces. ....	82
<b>Fig. 4.8:</b>	Finite element model with corresponding crack opening displacement contours are shown on the bovine cortical bone specimen, along with the far left end of the long-bar. A fine mesh is used near the impact site to ensure that contact and crack tip deformation responses are captured accurately. The field corresponds to a time instant $8 \mu\text{s}$ after impact and $1 \mu\text{s}$ before crack initiation. ....	85
<b>Fig. 4.9:</b>	Images recorded of a crack growing in bovine cortical bone using no AI pulse shaper at crack initiation and $10 \mu\text{s}$ later. Corresponding b) crack opening and c) sliding displacement fields are shown. Contour interval is $2 \mu\text{m}$ . Magnification is $33 \mu\text{m}/\text{pixel}$ . Arrows indicate crack tip location.....	86
<b>Fig. 4.10:</b>	Dynamic SIF histories for dried bovine cortical bone specimens with cracks growing in the axial direction. FEA is indicated by the solid line. Open symbols denote crack initiation at time $t=0$ . ....	87
<b>Fig. 5.1:</b>	Specimen geometries used for quasi-static a) tension and b) fracture.....	90
<b>Fig. 5.2:</b>	Specimen geometry used for dynamic fracture studies. ....	91
<b>Fig. 5.3:</b>	Finite element model with corresponding crack opening displacement contours shown on the specimen, along with the far left end of the long-bar. A fine mesh is used near the impact site to ensure that contact and crack tip deformation responses are captured accurately. The field corresponds to a time instant $48 \mu\text{s}$ after impact and $5 \mu\text{s}$ before crack initiation. ....	93
<b>Fig. 5.4:</b>	Eurostar 20 overhead stirrer from IKA used for simultaneous bath sonication and mechanical stirring. (Also used independently of bath sonication for mechanical stirring of some samples.).....	95
<b>Fig. 5.5:</b>	Transsonic Ti-H-6 ultrasonic cleaner from Elma Ultrasonics used for simultaneous bath sonication and mechanical stirring.....	96



<b>Fig. 5.6:</b>	Results from quasi-static tension tests using hand-stirring (HS) or bath sonication with mechanical stirring (BS/MS) for 0-1.5 wt% CNTs: a) representative stress-strain curves ('x' indicates failure point), b) average Young's modulus, and c) average ultimate stress. Error bars here and throughout indicate one standard deviation from the mean. ....	97
<b>Fig. 5.7:</b>	Results from quasi-static fracture tests using hand-stirring (HS) or bath sonication with mechanical stirring (BS/MS) for 0-1.5 wt% CNTs: a) representative load-displacement curves normalized by specimen thickness, where 'x' indicates crack initiation, and b) average crack initiation SIF ( $K_{Ic}$ ). $K_{Ic}$ of neat epoxy increases from $1.26 \text{ MPa}\sqrt{m}$ to $1.43 \text{ MPa}\sqrt{m}$ when the control sample is mechanically stirred and bath sonicated instead of only hand-stirred. ....	98
<b>Fig. 5.8:</b>	Optical microscopy of fracture surfaces: a) 1 wt% CNTs and b) 1.5 wt% CNTs. Large agglomerates (nearly 1 mm in diameter) settled to the bottom (left side in the images) during curing. (The higher concentration of agglomerates to the left of the cross-section is due to settling during curing.) .....	99
<b>Fig. 5.9:</b>	Labgen 7 homogenizer from Cole-Parmer used to break up large agglomerates. ....	102
<b>Fig. 5.10:</b>	Optical microscopy of optimization process of 0.1 wt% Baytubes dispersed into Epikure W: a) hand-stirring (HS); b) hand-stirring and homogenization (HS+H); c) hand-stirring, homogenization, and cup horn sonication (HS+H+CS); d) hand-stirring, homogenization, and 45 kHz bath sonication (HS+H+BS); e) hand-stirring, homogenization, and 25 kHz bath sonication; and f) hand-stirring, homogenization, 25 kHz bath sonication, and 45 kHz bath sonication.  indicates a final step in the optimization process. ....	102
<b>Fig. 5.11:</b>	Optical microscope image from the optimized methodology of uncured Epon 862, Epikure W, and 0.2 wt% Baytubes. ....	103
<b>Fig. 5.12:</b>	Crack initiation SIF for samples from the optimized methodology samples. No improvements in $K_{Ic}$ for 0.05-0.25 wt% CNTs are evident. ....	104
<b>Fig. 5.13:</b>	Vibracell VCX 750 probe tip sonicator provides high cavitation intensity for the dispersion of CNT agglomerates. ....	105
<b>Fig. 5.14:</b>	Results of quasi-static tension and fracture tests of methods involving homogenization and less bath sonication time than the optimized methods with two different types of unfunctionalized 0.2 wt% CNTs (Baytubes and NAMs). No change is observed in a) Young's modulus, and decreases in b) ultimate stress and c) ultimate strain are not significant. Improvements in d) crack initiation SIF are not significant with respect to the error bars. ....	107
<b>Fig. 5.15:</b>	Results of quasi-static tension and fracture tests of methods involving higher cavitation intensity (CS = cup horn sonication, PS = probe tip	

	sonication) using 0.2 wt% Baytubes. No significant changes are observed in a) Young's modulus or c) ultimate strain. Improvements in b) ultimate stress and d) crack initiation SIF are significant with respect to the error bars using the CS methodology. ....	108
<b>Fig. 5.16:</b>	SIF history for 0.5 wt% CNTs, added by HBS (homogenization and bath sonication), and 1.5 wt% CNTs, added by BS (bath sonication), compared to neat epoxy, prepared by HBS. ....	109
<b>Fig. 5.17:</b>	Dynamic crack initiation SIF for 0.2 wt% samples from several different methodologies. HBS = homogenization and bath sonication, BS = bath sonication, and PS = probe tip sonication. No improvements in $K_{I-ini}^d$ are evident due to CNTs. ....	110
<b>Fig. 5.18:</b>	Optical microscopy of uncured 0.2 wt% unfunctionalized CNTs dispersed into both hardener and resin: a) Baytubes with homogenization and less bath sonication than the optimized methods, b) CNTs from NAMs with homogenization and less bath sonication than the optimized methods, c) cup horn sonication (CS), and d) probe tip sonication (PS). All images contain Baytubes except in b). ....	111
<b>Fig. 5.19:</b>	Optical micrographs of fracture surfaces of 0.2 wt% unfunctionalized CNTs. Baytubes show the highest surface roughness, while the neat epoxy has the lowest. ....	112
<b>Fig. 5.20:</b>	Optical micrographs of fracture surfaces of (a) neat epoxy, (b) 0.2 wt% NAMs, and (c) 0.2 wt% Baytubes. Baytubes show the highest surface roughness, while the neat epoxy has the lowest. ....	113
<b>Fig. 5.21:</b>	Exakt 80E calender used to disperse relatively large quantities of nanomaterials. ....	115
<b>Fig. 5.22:</b>	FlakTek DAC 150 FVZ-K SpeedMixer. ....	116
<b>Fig. 5.23:</b>	Elmasonic E60H ultrasonic cleaner from Elma Ultrasonics used for simultaneous bath sonication and mechanical stirring. ....	117
<b>Fig. 5.24:</b>	Crack initiation SIF of different wt.% NH <sub>2</sub> -CNTs dispersed first into resin using homogenization and calendaring with a masterbatch (CM). ....	118
<b>Fig. 5.25:</b>	Crack initiation SIF of NH <sub>2</sub> -CNTs dispersed first into resin using a) several different methodologies all at 0.3 wt% (HBS = homogenization and bath sonication, C = calendaring, CM = calendaring with a materbatch, and PTC = probe tip sonication and calendaring), and b) using calendaring with a masterbatch (no homogenization) at three different weight percentages. All methodologies gave small improvements in $K_{Ic}$ ....	119
<b>Fig. 5.26:</b>	Crack initiation SIF of 0.3 wt% NH <sub>2</sub> -CNTs and 1 wt% Baytubes dispersed by calendaring and speedmixing (CMS). Baytubes gave a small but significant improvement in $K_{Ic}$ ....	120

<b>Fig. 5.27:</b>	Optical micrographs of uncured CNT dispersions: a) 0.25 wt% Baytubes dispersed in hardener using homogenization and bath sonication, b) resin added to a), and c) 0.5 wt% NH <sub>2</sub> -CNTs dispersed into resin first using calendaring with a masterbatch (CM) after the addition of hardener. The final dispersion state in c) is far superior to the final dispersion state in b). .....	122
<b>Fig. 5.28:</b>	Optical micrographs of uncured CNTs, resin and hardener: a) 0.3 wt% NH <sub>2</sub> -CNTs and b) 1 wt% Baytubes. Both samples were dispersed using calendaring and speedmixing (CMS). The dispersion state in b) is superior to the dispersion state in a).....	123
<b>Fig. 5.29:</b>	SEM of 0.3 wt% NH <sub>2</sub> -CNTs dispersed first into the resin using different calendaring methodologies: a) calendaring without a masterbatch (C), b) calendaring with a masterbatch (CM), and c) probe tip sonication and calendaring (PTC). .....	124
<b>Fig. 5.30:</b>	Optical micrographs of fracture surfaces of (a) neat epoxy, (b) 0.3 wt% NH <sub>2</sub> -CNTs calendaring with a masterbatch, (c) 0.3 wt% % NH <sub>2</sub> -CNTs calendaring with a masterbatch and speedmixing, and (d) 1 wt% Baytubes calendaring with a masterbatch and speedmixing. ....	125
<b>Fig. 5.31:</b>	Effect of additional hardener (+5%, +10%, +25%) beyond the manufacturer-recommended (1:1 molar) ratio, with and without 0.2 wt% NH <sub>2</sub> -CNTs on storage modulus of a) neat epoxy samples and b) CNT-modified epoxy samples. ....	127
<b>Fig. 5.32:</b>	Effect of additional hardener (+5%, +10%, +25%) beyond the manufacturer-recommended (1:1 molar) ratio, with and without 0.2 wt% NH <sub>2</sub> -CNTs on tan delta of a) neat epoxy samples and b) CNT-modified epoxy samples. ....	128
<b>Fig. 5.33:</b>	Effect of altering the stoichiometry with additional hardener (+5%, +10%, +25%) (beyond the manufacturer-recommended resin:hardener 1:1 molar ratio), with and without 0.2 wt% NH <sub>2</sub> -CNTs, on a) glass transition temperature ( $T_g$ ), b) crosslink density, c) Young's modulus, d) ultimate stress, e) ultimate strain, and f) crack initiation SIF ( $K_{Ic}$ ). .....	130
<b>Fig. 5.34:</b>	a) Molecucular structure of Epon 862 and Epikure W and b) primary reaction between Epon 862 and Epikure W. Note that up to four epoxide groups can react with a single molecule of Epikure W, but the primary reaction is the most reactive. Thus additional hardener beyond the stoichiometric ratio results in reduced crosslink density. ....	131
<b>Fig. 6.1:</b>	CFRP plate preparation details: a) Wet layup procedure for 60-layer CFRPs. b) Orientation of interlaminar and intralaminar slices machined from the same thick composite plate. ....	139
<b>Fig. 6.2:</b>	Interlaminar specimen preparation details: a) Dimensions of a single interlaminar slice machined from the CFRP manufactured in Fig. 6.1 for dynamic fracture experiments. b) Preparation of dynamic interlaminar	

	fracture specimens by stacking and gluing three blocks with the dimensions shown in a).....	140
<b>Fig. 6.3:</b>	Dimensions of fracture specimens subjected to a) quasi-static loading and b) dynamic impact loading. White dash lines indicate epoxy glue lines for interlaminar specimens. Both specimens were given a speckle coating for performing DIC.....	141
<b>Fig. 6.4:</b>	Specimen and experimental setup details: a) Quasi-static 3-point bending of edge-cracked specimen and b) Dynamic 1-point impact of edge-cracked specimen. ....	142
<b>Fig. 6.5:</b>	Orientation of cube specimens for ultrasonic determination of orthotropic elastic constants. ....	146
<b>Fig. 6.6:</b>	CNT/epoxy/carbon fiber ultrasonic specimens used to evaluate the orthotropic elastic constants listed in Table 6.2.....	146
<b>Fig. 6.7:</b>	Finite element model with corresponding crack opening displacement contours are shown on the neat intralaminar specimen, along with the far left end of the long-bar. A fine mesh is used near the impact site to ensure that contact and crack tip deformation responses are captured accurately. The field corresponds to a time instant 23 $\mu$ s after impact and 1 $\mu$ s before crack initiation. ....	149
<b>Fig. 6.8:</b>	Representative intralaminar and interlaminar load-displacement curves for Neat fracture specimens tested under quasi-static loading conditions.....	151
<b>Fig. 6.9:</b>	Thermo-plastic coated fiberglass scrim material (white) on the front and back surfaces of unidirectional carbon fiber fabric. Carbon fibers are running vertically. Intralaminar cracks propagated through this material, whereas interlaminar cracks propagated between layers of carbon fiber and scrim.....	151
<b>Fig. 6.10:</b>	Dynamic fracture specimens from Fig. 6.3b with the thermoplastic-coated fiberglass scrim drawn in green. Note that there are actually about 300 layers of scrim across the sample from left to right in the interlaminar specimen a), and about 40 layers of scrim through the thickness in the intralaminar specimen b). Note also that the scrim orientation will be similar for quasi-static specimens. ....	152
<b>Fig. 6.11:</b>	Quasi-static SIF histories (cross-head speed = 0.01 mm/sec) for edge-cracked CFRP 3-point bend specimens with cracks growing in the interlaminar or intralaminar directions. The presence of a fiberglass scrim caused an increase in $K_{IC}$ and post-initiation SIFs of intralaminar specimens, whereas the presence of CNTs and MCFs did not significantly improve critical SIFs. Three experimental results for each case are presented to show repeatability, and the open symbols denote crack initiation (designated by time $t = 0$ ).....	153

<b>Fig. 6.12:</b>	Average of measured quasi-static $K_{IC}$ values. Intralaminar specimens had significantly higher $K_{IC}$ than interlaminar specimens, whereas the addition of CNTs and MCFs did not have a significant effect on $K_{IC}$ . .....	154
<b>Fig. 6.13:</b>	Full-field measurement of deformations using DIC: a) Three of 32 images collected during an interlaminar dynamic fracture test of neat epoxy/carbon fiber, with arrows indicating the approximate location of the crack tip, b) $v$ -opening contours of displacement, and c) $u$ -sliding contours of displacement. The crack initiates at time $t=0$ . Contour interval is 10 $\mu\text{m}$ . Magnification is 54 $\mu\text{m}/\text{pixel}$ . .....	155
<b>Fig. 6.14:</b>	Dynamic SIF histories for CFRP specimens with cracks growing in the interlaminar and intralaminar directions. The presence of scrim caused an increase in ( $K_{I-ini}^d$ ) and post-initiation SIFs of intralaminar specimens, whereas the presence of CNTs and MCFs did not significantly improve SIFs at or after crack initiation. Results from FEA are indicated by the solid line in a) and b). Open symbols denote values at crack initiation, at time $t = 0$ . .....	156
<b>Fig. 6.15:</b>	Crack tip velocities of CFRPs. Following crack initiation, intralaminar cracks (blue) decelerated quickly and arrested, whereas interlaminar cracks (red) accelerated to $\sim 800$ m/s. ....	157
<b>Fig. 6.16:</b>	CNT dynamic fracture specimens. a) Interlaminar cracks propagated through the sample every time. b) Intralaminar samples always initiated, propagated a few millimeters, and then arrested. ....	158
<b>Fig. 6.17:</b>	Average of measured dynamic $K_{I-ini}^d$ values. Intralaminar specimens had significantly higher $K_{I-ini}^d$ than interlaminar specimens, whereas the addition of CNTs and MCFs caused reductions in $K_{I-ini}^d$ . ....	159
<b>Fig. 6.18:</b>	Average critical energy release rate values from critical SIFs using Eqs. 6.9 and 6.10 a) quasi-static $G_{IC}$ and b) dynamic $G_{I-ini}^d$ values. CNTs led to statistically insignificant improvements in both quasi-static (+34%) and dynamic (+16%) critical energy release rate for interlaminar specimens, whereas interlaminar MCFs led to a large improvement (+106%) in the quasi-static case and a reduction (-15%) in the dynamic case. In all cases, intralaminar fracture, affected by fiberglass scrim, had similar critical energy release rate compared to Neat samples. ....	161
<b>Fig. 6.19:</b>	a) Scanning electron micrograph of a fracture surface of an $\text{NH}_2$ -CNT/epoxy nanocomposite. CNTs are well-dispersed. b) Optical microscope image of a fracture surface of an MCF/epoxy/composite. ....	162
<b>Fig. 6.20:</b>	Scanning electron microscopy of a) Neat CFRP at 1,000x, b) CNT CFRP at 4,000x, and c) CNT CFRP at 15,000x. Crack growth is in the vertical direction. CNTs appear to be reasonably well-dispersed throughout the	

resin layers but have little effect on resin layer fracture features or  
measured critical SIF. ....163

## List of Abbreviations

CFRP	Carbon Fiber Reinforced Plastic (carbon fiber composite material)
CNT	Carbon Nanotube
DIC	Digital Image Correlation
FEA	Finite Element Analysis
$G_{IC}$	Mode-I critical energy release rate under quasi-static loading conditions
$G_{I-ini}^d$	Mode-I critical energy release rate under dynamic loading conditions
$K_{IC}$	Critical mode-I SIF under quasi-static loading conditions
$K_I^d$	Dynamic mode-I SIF
$K_{I-ini}^d$	Critical mode-I SIF under dynamic loading conditions
$\dot{K}$	Rate of change in SIF
MCF	Milled Carbon Fiber
SEM	Scanning Electron Microscopy
SIF	Stress Intensity Factor

## **Chapter 1. Introduction**

This dissertation broadly deals with the fracture mechanics of isotropic and orthotropic materials, with and without nano-filler modification. Thus it includes aspects of material processing, optical metrology, fracture mechanics, material characterization, and high strain-rate mechanical testing of engineered and biological materials. In light of this, the opening chapter provides a review of various aspects covered in this work before stating the objectives, hypotheses, and layout of the dissertation.

### **1.1 Fracture Mechanics Essentials**

The field of fracture mechanics is considered to be about seventy years old, but its origins date back much further. Leonard da Vinci studied the relationship between the strength of a wire and its length. Longer wires were more likely to have defects, and were thus more susceptible to failure. However this “size effect” was not fully appreciated for another 500 years [1].

Early failure theories included an experimentally-measured uniaxial failure stress that should not exceed either the maximum normal strain (St. Venant theory) or maximum principal stress (Rankine theory). Other early failure theories commonly used today are Tresca theory (maximum shear stress) and von-Mises theory (critical value of distortional energy). Mohr and Coulomb theory accounted for the observation that compressive failure stress is typically higher than the tensile failure stress (due to the presence of material defects) in their failure theories. However, none of these theories could account for the failure of many Liberty ships (manufactured 1940-1944) and Comet commercial aircrafts (1952) [1].



In 1913, Inglis attempted to compute the intensities of stresses around a crack by solving the problem of an elliptical hole in a uniformly loaded plate and then allowing the ratio of the minor and major axes to approach zero [2]. In 1921, Griffith developed an energy balance theory of brittle fracture after finding a difference of several orders of magnitude between the theoretical and measured tensile strength of glass, which he attributed to microscopic cracks that he believed to be inherent to all materials [3]. In 1939, Westergaard used complex variables to relate stresses and strains in a body surrounding a symmetrically loaded crack tip that showed a stress singularity to exist at the crack tip in elastic solids [4]. In 1958, Irwin was credited with developing fracture mechanics from the works of Inglis, Griffith, and Westergaard [5]. Irwin introduced  $K_I$ , the stress intensity factor (SIF), as:

$$K_I = \lim_{r \rightarrow 0} (\sqrt{2\pi r} \sigma_{yy}), \quad (1.1)$$

where a polar coordinate system  $(r, \theta)$  and a Cartesian coordinate system  $(x, y)$  each originate at the crack tip, with the crack to grow in the  $\theta = 0$  and positive  $x$ -directions (Fig. 1.1a). By taking the limit of the tensile stress  $(\sigma_{yy})$  ahead of the crack tip,  $K_I$  becomes a finite value that is linearly related to the far-field stresses applied to the body while describing the stress state near the singularity caused by the crack tip [6].

Three modes of fracture are identified in fracture mechanics (Fig. 1.1). In this work, all cracks will be loaded symmetrically in mode-I, such that experimentally-measured mode-II SIFs ( $K_{II}$ ) are negligible. The critical mode-I SIF ( $K_{IC}$ ), also known as the “crack-initiation SIF” or simply “critical SIF,” is considered a material property, and will be measured under quasi-static loading conditions and under plane stress assumptions. Under dynamic (impact) loading conditions, the mode-I critical dynamic SIF will be designated by  $K_{I-ini}^d$ , while all other

measured dynamic mode-I SIFs before and after crack initiation will be referred to as  $K_I^d$ . Also, in this work, in-plane displacement fields will be used to simultaneously measure mode-I and mode-II SIFs under plane stress conditions.

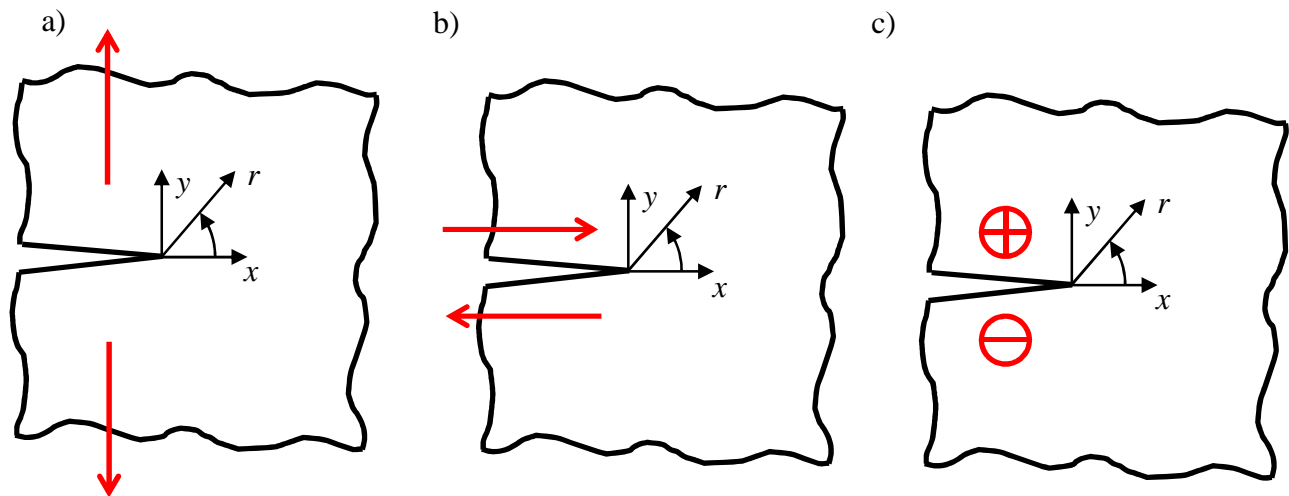


**Fig. 1.1:** Three modes of fracture: a) mode-I opening/symmetric fracture, b) mode-II in-plane shearing fracture, and c) mode-III out-of-plane tearing fracture.

## 1.2 High-Strain Rate Loading

In 1913, Hopkinson used a metal bar to investigate stress wave propagation [7]. In 1949, Kolsky modified the Hopkinson bar for characterizing the dynamic compression behavior of a material [8]. Fig. 1.2 shows Kolsky's apparatus, which includes an anvil and a specimen placed between two long bars. With this device, Kolsky demonstrated the strain-rate dependence of stress-strain responses of polythene, Perspex, and copper.

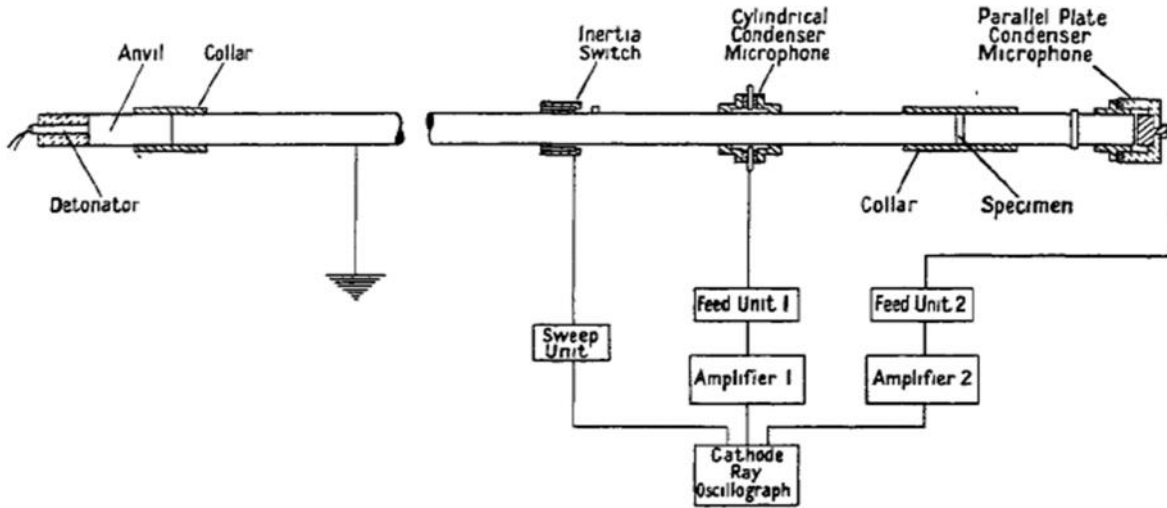


**Fig. 1.2:**<sup>1</sup> Kolsky bar for the measurement of the dynamic stress-strain response of a material. Reproduced from [8].

### 1.3 Motivation and Literature Review

It is now well known that most materials behave in a brittle fashion under impact (stress wave dominant) loading conditions, similar to their behavior in extremely cold and/or high-constraint conditions. Section 1.3.1 will review current methodologies used to study dynamic fracture. The remaining sections will review the quasi-static and (in some cases) the dynamic fracture properties of materials to be further investigated with the methodology proposed in this dissertation (Chapter 2).

Cemented hip and knee implants must typically be replaced after about 15 years *in vivo*, and sometimes they fail sooner. These failures initiate both at the interface between bone cement and bone, as well as from voids entirely within the bone cement layer. A better understanding of the quasi-static and dynamic fracture properties of bone cement will therefore enhance the understanding of how joint implant systems fail *in vivo*. To author's knowledge, the dynamic

<sup>1</sup> Reprinted from Proceedings of the Physical Society- Section B, 62, H. Kolsky, An investigation of the mechanical properties of materials at very high rates of loading, 676-700, (1949), © IOP Publishing. Reproduced by permission of IOP Publishing. All rights reserved.

fracture of bone cement has not been reported in the literature. This gap needs to be bridged because failure of the implant could initiate in the cement mantle under impact or shock loading during day-to-day events such as jumping, falling, and tackling. More active patients, considered most likely to experience these types of loading events, are typically given uncemented prostheses, where bone mechanically interlocks with the roughened surface of the implant. This tendency will likely be supported in this work after quantifying the dynamic fracture response of bone cement. Additionally, whether unstable crack growth within the cement mantle is caused by a dynamic loading event or fatigue crack growth that gives way to sudden rapid crack growth, the resulting outcome is very similar; in both cases, it is important to assess the material's ability to arrest a rapidly growing crack. A review of quasi-static fracture of acrylic bone cement, as well as the quasi-static and dynamic fracture of acrylic is provided in Section 1.3.2.

Despite the fact that clinical bone fractures are almost always the result of a dynamic loading event, this material has been studied much more thoroughly under quasi-static conditions than dynamic conditions. Therefore, a better understanding of the dynamic fracture of cortical bone is necessary. Because of the nature of this orthotropic material, it is extremely difficult to quasi-statically evaluate all of the elastic properties necessary to determine fracture parameters. Therefore a review of the ultrasonic determination of orthotropic elastic constants is included, along with a review of quasi-static and dynamic fracture of cortical bone, in Section 1.3.3.

Carbon nanotubes (CNTs) have been shown previously to improve the tensile and fracture properties of epoxy under quasi-static conditions, although no one has studied the dynamic fracture of these nanocomposite materials rigorously. A review of quasi-static fracture of CNT-infused epoxy is provided in Section 1.3.4.

Of particular interest today is the high strain-rate behavior of carbon fiber reinforced polymers (CFRPs), which are currently being used extensively in commercial aircraft structures. As such, CFRPs will experience both dynamic loading and cold temperatures, under which conditions these materials are likely to elicit a more brittle response than under traditional quasi-static loading conditions. These materials are highly anisotropic, and it is difficult to obtain sufficiently thick CFRPs to quasi-statically assess out-of-plane elastic properties. Therefore, several researchers have measured the elastic properties of orthotropic CFRPs with ultrasound using similar techniques to those described in Section 1.3.3. CFRPs are particularly susceptible to interlaminar fracture and damage; however, it is experimentally tedious to measure interlaminar critical energy release rate ( $G_{ic}$ ) using current ASTM standards, and it is difficult to extend this methodology to dynamic fracture. Several research teams have therefore prepared unidirectional CFRPs in order to compare interlaminar critical energy release rate to a more traditional fracture test setup with an intralaminar crack. Others have attempted to improve the interlaminar critical energy release rate of CFRPs by adding CNTs to the relatively compliant and brittle epoxy matrix. A review of quasi-static interlaminar vs. intralaminar fracture of CFRPs, quasi-static interlaminar fracture of CNT-infused CFRPs, and dynamic interlaminar fracture of CFRPs is provided in Section 1.3.5.

### ***1.3.1 Dynamic Fracture Methodologies***

Many researchers offer techniques for finding the dynamic crack initiation stress intensity factor (SIF), but few have developed methods for characterizing the material's ability to resist crack growth once it has begun. Both types of fracture data are crucial for evaluating the suitability of a material under dynamic loading. Nam et al. [9] impacted metal-matrix composites

(100 x 15 x 3mm) at 1-7 m/s using a falling dart fitted with a load cell in order to determine the peak load assumed to be at crack initiation and calculate the corresponding SIF. Martins et al. [10] used strain gages on a modified Kolsky bar with rigid supports for 3-point bending in order to determine critical energy release rate of linear medium density polyethylene (50 x 10 x 10mm). Weisbrod and Rittel [11] measured crack initiation SIF with a modified Kolsky bar that delivered 1-point impact loading to small tungsten alloy specimens (23 x 10 x 8mm) with strain gages placed both on the long-bar and on the specimen. None of the above methods addressed the resistance of the material to subsequent crack growth once initiation had occurred.

Several teams have modified the Kolsky bar to measure fracture parameters on Brazilian disc specimens [12-15]. These researchers have used strain gages on the incident and transmission bars to determine the peak load, fracture gages on the specimen to monitor fracture, and laser gap gages to measure crack opening displacement. These techniques either do not offer full-field information about crack initiation or growth characteristics, or they may interfere with stress wave propagation in the sample. For any method that does not monitor the position of the crack tip, SIFs measured after initiation could be unreliable, as these depend on the instantaneous crack tip velocity.

Shukla et al. [16] used a Kolsky bar modified for 3-point bending tests, along with high-speed photography and photoelasticity, to find dynamic crack initiation SIF as a function of velocity in nanocomposites; however, the samples tested were relatively large in size (280 x 150 mm and 254 x 240 mm). Lee et al. [17] used a low velocity falling dart, along with high-speed photography and Digital Image Correlation (DIC), to find dynamic crack initiation SIF as a function of time for unidirectional composites (200 x 50 x 6.2mm). The methodology presented here involves higher velocity fracture tests with smaller specimens than Lee et al. [17] by

utilizing a 1-point impactor, high-speed photography (~300,000 frames per second), and DIC during crack initiation and propagation. SIFs are extracted from two-dimensional data fields with hundreds of data points on the specimen surface using DIC. The high-speed images also help locate the instantaneous crack tip, such that crack tip velocities can be estimated.

### ***1.3.2 Acrylic Bone Cement Fracture***

In 1960, Charnley began anchoring femoral head prostheses with acrylic cement in order to improve the load distribution between implant and femur. Instead of high adhesion or mechanical strength, this solution offered a “tailored” fit to the bone that previous metal-only implants could not achieve [18]. Charnley’s method is still widely used [19], although uncemented techniques have also been developed in which the surrounding bone grows directly into the roughened surface of the implant in order to anchor the prosthesis via mechanical interlock. These newer uncemented prostheses are designed primarily for younger patients and have not been as consistently successful as cemented implants [20].

Due to the poor adhesive properties of acrylic (PMMA) bone cement, corresponding implant designs include holes, grooves, and other geometric features for mechanical interlocking between implant and cement. The roughened bone surface (due to reaming) then ensures mechanical interlock between cement and bone. Over time, these interfaces can deteriorate, eventually leading to revision surgeries [21]. Additional problems associated with cemented prosthesis interfaces include necrosis of surrounding bone tissue due to exothermic polymerization [19, 21, 22], stress concentrations due to nonuniform temperature distribution during cooling [21], shrinkage of the cement mantle during hardening [19, 21, 22], and potential release of toxic monomer. Any untreated MMA monomer is a toxic fat solvent [19] and may

result in allergic reaction and an unsafe drop in blood pressure [22], as well as interfere with postoperative healing [19].

In addition to the cement-implant and cement-bone interfaces, the cement mantle itself has been implicated as the implant failure initiation site [23, 24]. Pore formation in the cement mantle is unavoidable [25] and has been the origin of fracture *in vivo* [23, 24]. While Jasty et al. [25] showed some improvement in the bulk porosity of certain bone cements through the usage of centrifugation, voids could not be eliminated completely.

The quasi-static crack initiation stress intensity factor (SIF) of acrylic bone cement is well documented in the literature [26-29] (Table 1.1). This value characterizes the ability of a material to resist crack growth. However to date, the authors are unaware of reports on dynamic fracture properties of bone cement, either at crack initiation or during crack propagation. On the other hand, commercial grade acrylic has been well documented in both quasi-static and dynamic fracture [30-34] (Table 1.2), and has therefore been used to calibrate the dynamic loading device (see Chapter 3).

Author	Type	$K_I$ ( $MPa\sqrt{m}$ )	Radiopacifier
Buckley et al. 2003	CMW <sup>3</sup>	2.19	BaSO <sub>4</sub>
Ishihara & Goshima 2002	CMW <sup>3</sup>	2.22	BaSO <sub>4</sub>
Vallo et al. 1997	Súbiton Gun	1.60	BaSO <sub>4</sub>
Vallo et al. 1997	Súbiton 6'	1.33	BaSO <sub>4</sub>
Vallo et al. 1997	Palacos R	1.78	ZrO <sub>2</sub>
Baleani & Viceconti 2010	Cemex	1.36	BaSO <sub>4</sub>
Baleani & Viceconti 2010	Cemex	1.56	none

**Table 1.1:** The quasi-static crack initiation SIF ( $K_{IC}$ ) of various clinical bone cements, including Cemex® with and without a radiopacifier.



Author	Quasi-static $K_{IC}$ (MPa $\sqrt{m}$ )	Dynamic Loading Rate $\dot{K}$ (MPa $\sqrt{m}$ s $^{-1}$ )	Dynamic $K_{I-ini}^d$ (MPa $\sqrt{m}$ )
Johnson & Jones 1994	1.2	--	--
Rittel & Maigre 1996	2.2	4.52 x 10 $^4$ - 2.10 x 10 $^5$	2.17 - 6.15
Weerasooriya et al. 2006	1.42 - 1.68	5 x 10 $^3$ - 5 x 10 $^4$	2.47 - 4.06
Wada 1992	1.45 - 1.66	5.2 x 10 $^3$ - 8.3 x 10 $^4$	1.00 - 1.34
Wada and Seika 1993	--	0.7 x 10 $^4$ - 9.0 x 10 $^4$	0.28 - 3.68

**Table 1.2:** The quasi-static crack initiation SIF values ( $K_{IC}$ ) for PMMA determined by several research teams, along with the dynamic crack initiation SIF ( $K_{I-ini}^d$ ) and corresponding dynamic loading rates ( $\dot{K}$ ).

### 1.3.3 Cortical Bone Fracture

Cortical bone is a naturally occurring orthotropic nanomaterial [35]. While it is present along with cancellous (spongy) bone throughout most of the skeletal system, it occurs independently of cancellous bone in the central, hollow portions of the long bones, where the osteons grow along the long axis of the bone to impart additional stiffness in this direction. Due to natural geometric limitations, its elastic properties are difficult to assess quasi-statically, particularly in the radial direction. For the determination of dynamic SIFs, it is ideal to use dynamic elastic properties, which can be measured using ultrasound. Van Buskirk et al. [36] measured the elastic constants of cortical bone in a method to be further described in Chapter 4.

Table 1.3 gives a wide range of quasi-static  $K_{IC}$  found in the literature for axial and transverse fracture of cortical bone [37-48]. Possible variables affecting measured  $K_{IC}$  values include age, geometry, species, preservation technique, and the specific bone from which the fracture sample was machined.

Author	Bone Type	Axial $K_{IC}$ ( $MPa\sqrt{m}$ )	Transverse $K_{IC}$ ( $MPa\sqrt{m}$ )
Adharapurapu et al. 2006	Bovine	--	3 - 6
Ager et al. 2006	Human	1.2 vs. 2.0	--
Behiri & Bonfield 1989	Bovine	3.2	6.5
Feng et al. 2000	Bovine	3.0	6.0
Kulin et al. 2011	Equine	--	5.6 vs. 8.4
Kuninori et al. 2009	Bovine	--	6.8 - 7.1
Lucksanasombool et al. 2001	Bovine	2.1 - 2.9	3.4 - 6.6
Malik et al. 2003	Equine	--	4.4 - 4.7
McCormack et al. 2012	Equine	--	3.3
Norman et al. 1995	--	4.2 vs. 6.5	--
Wang & Agrawal 1996	Bovine	2.1 - 4.0	--
Yan et al. 2007	Bovine	2.6	5.1

**Table 1.3:** The quasi-static crack initiation SIF  $K_{IC}$  of bone.

Author	Bone Type	Dry $K_{I-ini}^d$ ( $MPa\sqrt{m}$ )	Wet $K_{I-ini}^d$ ( $MPa\sqrt{m}$ )
Adharapurapu et al. 2006	Bovine	1.0	2.5
Kulin et al. 2011	Equine	-	5.7

**Table 1.4:** The dynamic transverse crack initiation SIF  $K_{I-ini}^d$  of bone.

Dynamic fracture of cortical bone has been much more limited (Table 1.4), and to date has only included transverse fracture. Adharapurapu et al. [37] measured transverse dynamic fracture of bovine cortical bone using a modified Kolsky bar for 3-point bending and used strain gages to measure  $K_{I-ini}^d$  (Fig. 1.3, Fig. 1.4a). Assessment of crack initiation time was based on peak load measurements from the strain gage on the transmission bar and was perhaps a source of error in determining critical SIFs. They measured significantly higher  $K_{I-ini}^d$  for wet bovine bone

compared to dried bovine bone under dynamic loading conditions. Kulin et al. [41] used a similar apparatus and methodology to study dynamic 4-point bending of equine cortical bone (Fig. 1.4b). Despite the similarity of the experimental setup, Kulin et al. measured  $K_{I-ini}^d$  more than twice the magnitude of [37] using similar wet transverse samples.

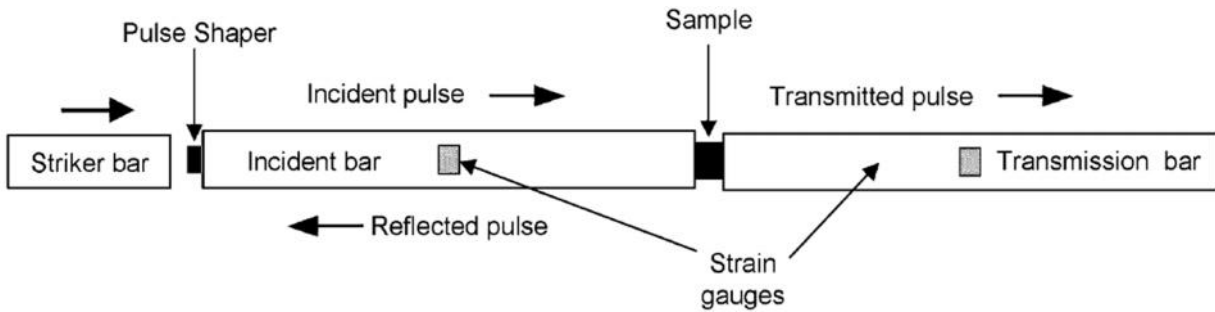


**Fig. 1.3:**<sup>2</sup> Dynamic fracture apparatus used by [37, 41] to study dynamic fracture of cortical bone. Reproduced from [37].

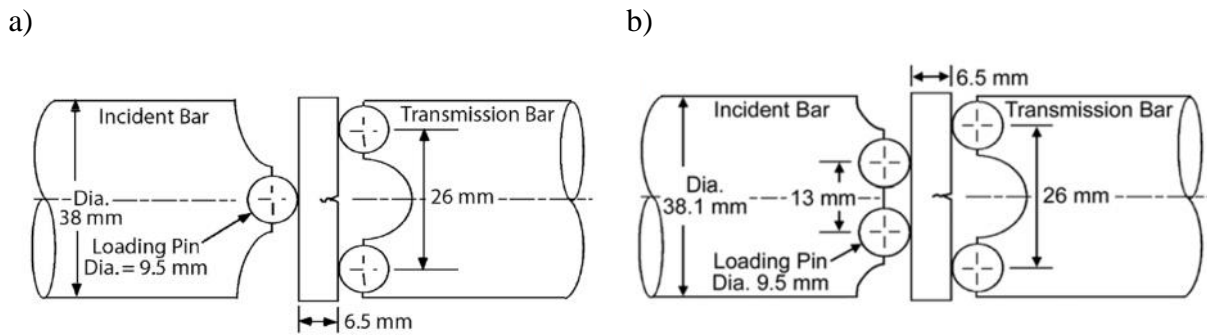


**Fig. 1.4:** Dynamic fracture samples and modification of the Kolsky bar (Fig. 1.3) to achieve: a) dynamic 3-point bending used by [37] (reproduced from<sup>3</sup> [37]) and b) dynamic 4-point bending used by [41] (reproduced from<sup>4</sup> [41]).

<sup>2</sup> Reprinted from Materials Science & Engineering C-Biomimetic and Supramolecular Systems, 26, R. R. Adharapurapu, F. Jiang, K. S. Vecchio, Dynamic fracture of bovine bone, 1325-1332, (2006), with permission from Elsevier.

<sup>3</sup> Reprinted from Materials Science & Engineering C-Biomimetic and Supramolecular Systems, 26, R. R. Adharapurapu, F. Jiang, K. S. Vecchio, Dynamic fracture of bovine bone, 1325-1332, (2006), with permission from Elsevier.

<sup>4</sup> Reprinted from Journal of the Mechanical Behavior of Biomedical Materials, 4, R. M. Kulin, F. Jiang, K. S. Vecchio, Effects of age and loading rate on equine cortical bone failure, 57-75, (2011), with permission from Elsevier.

### 1.3.4 CNT-modified Epoxy Fracture

Synthetic carbon nanotubes (CNTs) have exceptional thermal, electrical, and mechanical properties. CNTs are thermally stable up to 2800°C (in vacuum or 400°C in air) and possess twice the thermal conductivity of diamond. They have 1,000 times higher electric-current-carrying capacity than copper wire. They have elastic modulus greater than 1,000 GPa, at least 10 times the strength of steel, and high ductility (because of adiabatic deformation through the  $sp^2$  network), as large nonlinear deformations have been observed before CNT fracture. Carbon nanotubes therefore have high potential in future multifunctional materials and should theoretically provide great enhancement in composite materials [49].

Epoxies have been used widely (as adhesives and as the matrix material in composites) for their mechanical properties (high stiffness, strength, and hardness), durability (strong chemical and wear resistance), and good adhesion to fillers. However, they are relatively brittle and have poor resistance to crack growth [50, 51]. Therefore many authors have attempted to improve the fracture toughness<sup>5</sup> ( $K_{Ic}$ ) of epoxy by adding carbon nanotubes [50, 52-73] (Table 1.5)<sup>6</sup>. Their improvements in fracture toughness ( $K_{Ic}$ ) have been widely attributed to the extraordinary mechanical properties of CNTs [53-62, 64-68, 60-73], the quality of dispersion within the epoxy matrix [50, 52-66, 68, 70-72], and the strength of the bond between CNTs and epoxy [50, 52, 53, 55-58, 60-62, 65, 66, 71]. Many different types of CNTs have been used to achieve these improvements in  $K_{Ic}$ , including functionalized (FN) and unfunctionalized (UFN) CNTs, single-walled (SWCNT) and multi-walled (MWCNT), and a wide array of weight percentages (0.1-3

---

<sup>5</sup> Note that CNT community typically reports the value of crack initiation SIF as fracture toughness.

<sup>6</sup> The average % improvement in Table 1.5 is much higher than the improvement of average neat epoxy vs. average CNT-modified epoxy. This is due to the large improvements of a few outliers such as Gkikas et al. [55] and Shtein et al. [66].

Author	Neat $K_{IC}$ ( $MPa\sqrt{m}$ )	CNT-Modified $K_{IC}$ ( $MPa\sqrt{m}$ )	CNT Type	Dispersion Technique
Alishahi et al. 2013	2.1	2.6 (+24%)	0.5 wt% UFN MWCNT	probe tip sonication
Ashrafi et al. 2013	1.09	1.51 (+39%)	0.2 wt% FN SWCNT	bath & probe tip sonication
Ayatollahi et al. 2011	1.62	2.05 (+27%)	0.5 wt% UFN MWCNT	probe tip sonication
Chatterjee et al. 2012	0.5	0.9 (+80%)	0.5 wt% COOH MWCNT	bath sonication, homogenizer, & calender
Gkikas et al. 2012	0.7	2.2 (+214%)	0.5 wt% UFN MWCNT	probe tip sonication
Gojny et al. 2005	0.65	0.93 (+43%)	0.5 wt% NH <sub>2</sub> DWCNT	calender
Hsieh et al. 2011	0.69	0.98 (+42%)	0.5 wt% UFN MWCNT	probe tip sonication
Hu et al. 2012	0.6	1.2 (+100%)	2 wt% UFN MWCNT	planetary mixer
Jyotishkumar et al. 2012	0.35	0.48 (+37%)	0.22 wt% UFN MWCNT	sonication
Khan et al. 2013	1.0	1.2 (+20%)	0.3 wt% FN MWCNT	sonication & calender
Lachman & Wagner 2010	0.67	1.23 (+84%)	0.34 wt% NH <sub>2</sub> MWCNT	probe tip sonication
Ma et al. 2007	1.2	1.3 (+8%)	0.5 wt% Silane MWCNT	sonication
Mirjalili et al. 2012	1.13	1.32 (+17%)	0.3 wt% FN MWCNT	high shear mixer
Miyagawa et al. 2005	0.55	0.75 (+36%)	0.2 wt% F SWCNT	sonication
Rahman et al. 2012 <sup>a</sup>	1.9	2.7 (+42%)	0.3 wt% NH <sub>2</sub> MWCNT	probe tip & calender
Shtein et al. 2013	0.9	2 (+122%)	0.1 vol% UFN MWCNT	probe tip sonication
Solodilov et al. 2012	0.4	0.4 (+0%)	0.3-1.0 wt% UFN MWCNT	probe tip sonication
Srikanth et al. 2012	0.96	1.28 (+33%)	0.5 wt% NH <sub>2</sub> MWCNT	probe tip & ball mill
Sumfleth et al. 2010	0.58	0.67 (+16%)	0.5 wt% UFN MWCNT	calender w/ masterbatch
Tang et al. 2013	0.548	0.698 (+27%)	1 wt% UFN MWCNT	ball mill w/ masterbatch
Thostenson & Chou 2006 <sup>a b</sup>	0.7	1.2 (+71%)	0.25 wt% UFN MWCNT	calender
Yu et al. 2008	0.45	0.72 (+60%)	3 wt% UFN MWCNT	sonication
Zhou et al. 2008 <sup>a b c</sup>	3.6	4.7 (+31%)	0.3 wt% UFN MWCNT	probe tip sonication
<b>Average</b>	<b>1.00</b>	<b>1.29 (+51%)</b>		

**Table 1.5:**  $K_{IC}$  of Epoxy Toughened with CNTs

<sup>a</sup> Recreated similar methodology during this research

<sup>b</sup> Used Epon 862/Epikure W

<sup>c</sup> Converted from  $MPa\sqrt{mm}$  to  $MPa\sqrt{m}$ .

wt%). Additionally, many different dispersion techniques have been used to improve  $K_{IC}$ , including various types of sonication and high shear techniques, often used in some combination with each other. Many of these techniques will be explained further in Chapter 5, including several different types of sonication and “calendering with a masterbatch.” *These numerous variants have left a high-degree of uncertainty in terms of the benefits of using CNTs as an epoxy filler for enhancing mechanical performance – strength, stiffness and fracture toughness – for quasi-static real-world applications. Furthermore, there are very few reported studies on the benefits of CNTs in case high strain-rate loading.* Interestingly, the reported improvements in  $K_{IC}$  range from 0 to 214%, compared to neat epoxies with an initial untoughened (neat)  $K_{IC}$  ranging from 0.35 to 3.7  $MPa\sqrt{m}$ , with an average of 1.0  $MPa\sqrt{m}$  and a median of 0.7  $MPa\sqrt{m}$ . Nine of the 23 CNT-modified  $K_{IC}$  values in Table 1.5 are actually lower than the average initial toughness of neat epoxy in Table 1.5, indicating both the wide range of epoxies available commercially and the wide range of reported outcomes in the literature. In a practical sense, the improvement of 214% from 0.7  $MPa\sqrt{m}$  to 2.2  $MPa\sqrt{m}$  of Gkikas et al. [55] by adding 0.5 wt% unfunctionalized MWCNTs using probe tip sonication is much more significant than the nine reported CNT-modified epoxy  $K_{IC}$  values less than 1  $MPa\sqrt{m}$ .

For the sake of this review, *significant improvement* is defined as improvement beyond the reported error bars, typically one standard deviation outside the mean value for  $K_{IC}$ . With this as the measure, many authors were unable to significantly improve the fracture toughness of neat epoxy with CNTs [62, 63, 67]. Several of the authors who showed improvements in  $K_{IC}$  with functionalized CNTs also reported no significant improvement with unfunctionalized CNTs [50,

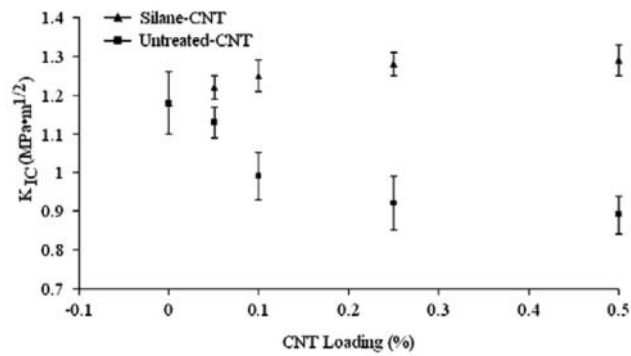


**Fig. 1.5:**<sup>7</sup> Variations of fracture toughness ( $K_{IC}$ ) of nanocomposites with different CNT contents. Reproduced from [62].

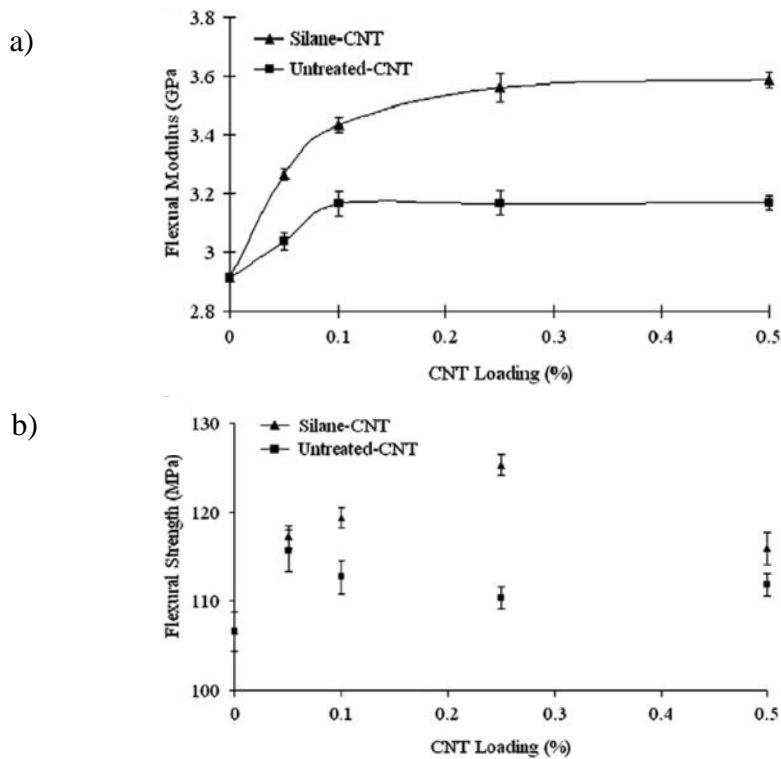


**Fig. 1.6:**<sup>8</sup> Variations of a) flexural modulus and b) flexural strength of nanocomposites with different CNT contents. Reproduced from [62].

<sup>7</sup> Reprinted from Composites Science and Technology, 67, P. C. Ma, J. K. Kim, B. Z. Tang, Effects of silane functionalization on the properties of carbon nanotube/epoxy nanocomposites, 2965-2972, (2007), with permission from Elsevier.

<sup>8</sup> Reprinted from Composites Science and Technology, 67, P. C. Ma, J. K. Kim, B. Z. Tang, Effects of silane functionalization on the properties of carbon nanotube/epoxy nanocomposites, 2965-2972, (2007), with permission from Elsevier.

61], and Ma et al. [62] even reported a significant decrease in  $K_{IC}$  when using unfunctionalized CNTs (Fig. 1.5). Ma et al. [62] did, however, report significant improvements in flexural modulus for both functionalized and unfunctionalized CNTs, a significant improvement in flexural strength with functionalized CNTs, and a significant decrease in flexural strength with unfunctionalized CNTs (Fig. 1.6).

Khan et al. [60] found a modest but significant (~20%) improvement in  $K_{IC}$  using randomly oriented CNTs; however, after electrically aligning the CNTs perpendicular to the crack tip, a +51% improvement in  $K_{IC}$  was observed (Fig. 1.7). Significant improvements in Young's modulus were found both for randomly-oriented and aligned CNTs (Fig. 1.8), although the aligned CNTs gave much greater improvements in Young's modulus.

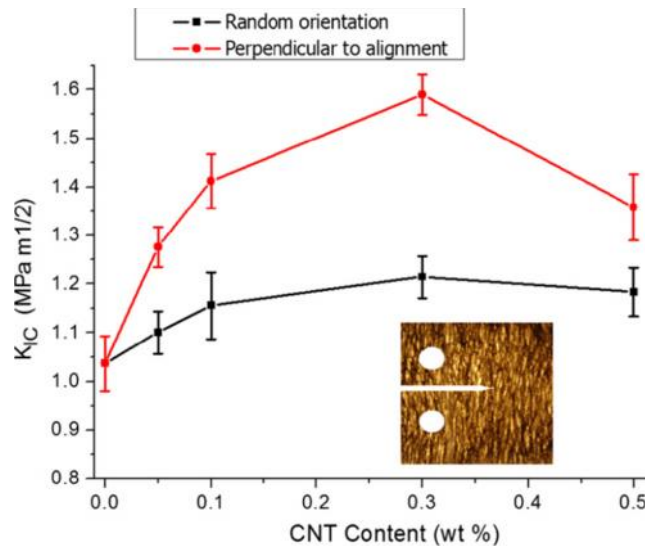


**Fig. 1.7:**<sup>9</sup> Quasi-static fracture toughness of nanocomposites as a function of CNT content. (For interpretation of the references to color in this figure legend, the reader is referred to the web version of this article.) Reproduced from [60].

<sup>9</sup> Reprinted from Composites Part A-Applied Science and Manufacturing, 49, S. U. Khan, J. R. Pothnis, J. K. Kim, Effects of carbon nanotube alignment on electrical and mechanical properties of epoxy nanocomposites, 26-34, (2013), with permission from Elsevier.



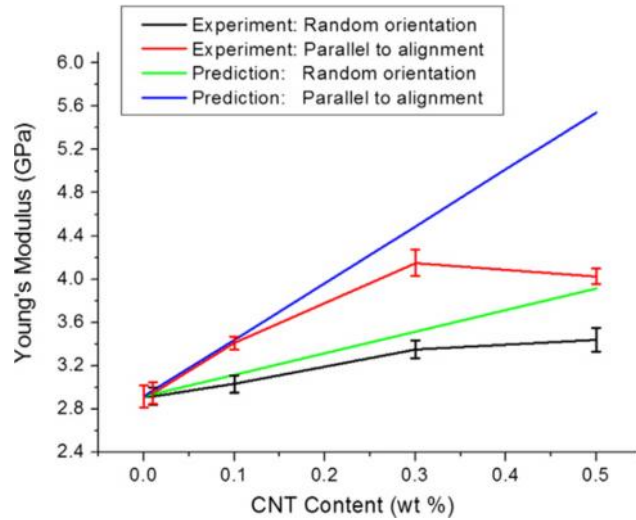


**Fig. 1.8:**<sup>10</sup> Young's modulus of nanocomposites as a function of CNT content. The predictions are based on the Halpin-Tsai model. (For interpretation of the references to color in these figure legends, the reader is referred to the web version of this article.) Reproduced from [60].

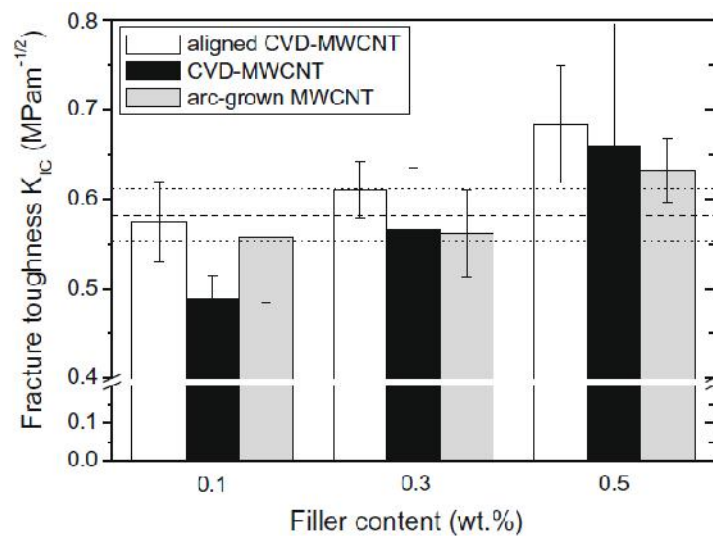


**Fig. 1.9:**<sup>11</sup> Fracture toughness of the MWCNT-reinforced composites. The dashed line represents the neat epoxy without modification. Note that “aligned” refers to the way the CNTs were grown, not to their orientation within the nanocomposite; all CNTs are randomly aligned in these specimens. Reproduced from [69].

<sup>10</sup> Reprinted from Composites Part A-Applied Science and Manufacturing, 49, S. U. Khan, J. R. Pothnis, J. K. Kim, Effects of carbon nanotube alignment on electrical and mechanical properties of epoxy nanocomposites, 26-34, (2013), with permission from Elsevier.

<sup>11</sup> Reprinted from Composites Science and Technology, 70, J. Sumfleth, K. Prehn, M. H. G. Wichmann, S. Wedekind, K. Schulte, A comparative study of the electrical and mechanical properties of epoxy nanocomposites reinforced by CVD- and arc-grown multi-wall carbon nanotubes, 173-180, (2010), with permission from Elsevier.

Sumfleth et al. [69] dispersed three different types of unfunctionalized CNTs at three different weight percentages. The CNTs caused decreases in  $K_{IC}$  in five of the nine nanocomposites (one of which was a significant decrease), while only one nanocomposite led to a significant improvement in  $K_{IC}$  compared to neat epoxy (Fig. 1.9). Note that “aligned” refers to the way the CNTs were grown, not to their orientation within the nanocomposite; all CNTs are randomly aligned in these specimens.

Mirjalili et al. [63] used a hot stage with optical microscope to observe changes in the degree of dispersion during curing. *They observed significant re-agglomeration of the CNTs when curing at high temperatures* (IPD = high temperature hardener) (Fig. 1.10a and 1.10b), which led to a reduction in  $K_{IC}$  (Fig. 1.11a). When adding a catalyst (N3), less re-agglomeration was observed during curing (Fig. 1.10c and 1.10d), and this led to the best improvements in  $K_{IC}$  (Fig. 1.11a), although the significance with respect to the error bars is difficult to assess. When using a room temperature cure (TETA = triethylenetriamine hardener), minimal re-agglomeration was observed (Fig. 1.10e and 1.10f), yet there was almost no corresponding improvement in  $K_{IC}$  (Fig. 1.11a). When using a combination of IPD and TETA, again minimal re-agglomeration occurred (Fig. 1.10g and 1.10h), and yet almost no improvement in  $K_{IC}$  occurred (Fig. 1.11b). Mirjalili et al. [63] quantified the dispersion based on the equation:

$$A_r = \frac{\text{Area of CNT agglomerates (dark area)}}{\text{Total area}}, \quad (1.2)$$

where  $A_f$  values are the area fraction in which carbon nanotubes are present (Fig. 1.11). If improvement in dispersion ( $A_f$  values) corresponds with increasing fracture toughness, it does so only up to a point in this case.

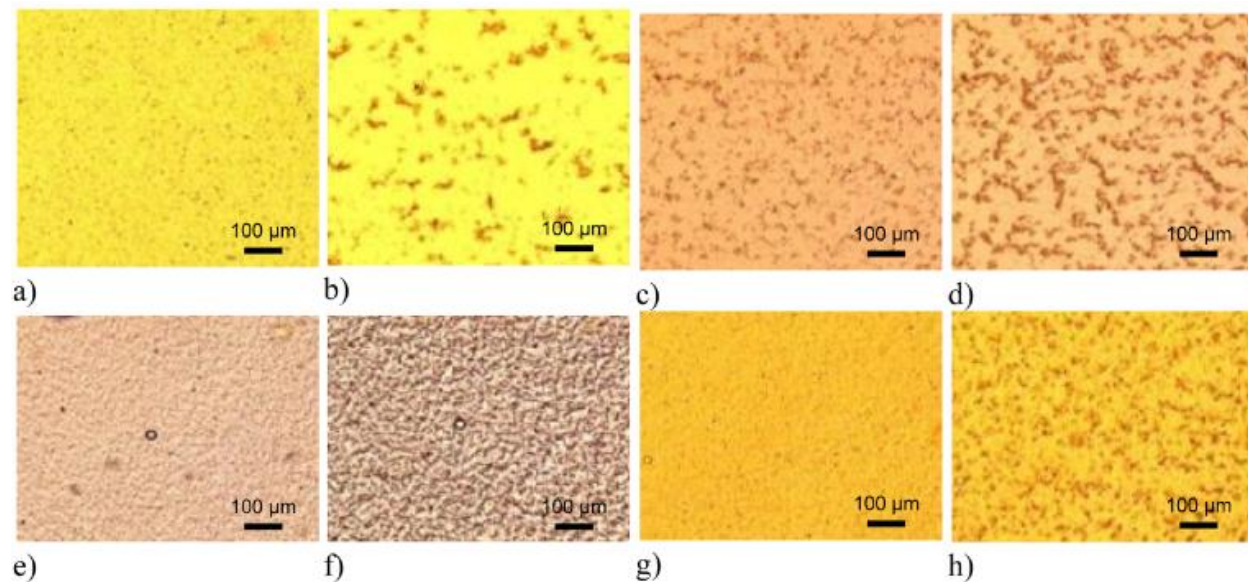


**Fig. 1.10:**<sup>12</sup> Dispersion quality evolution during the cure for different hardeners: a) IPD at 25°C; b) IPD at 75°C; c) IPD/N3 at 25°C; d) IPD/N3 at 75°C; e) TETA at 25°C; f) TETA after 2 h at 150°C; g) IPD/TETA at 25°C; h) IPD/TETA after 24 h at 25°C. Reproduced from [63].

Gupta et al. (2013) [51] also reported qualitative changes in dispersion via optical microscopy (Fig. 1.12), along with the resulting effect on tensile strength (Fig. 1.13). They dispersed 0.5 wt% unfunctionalized MWCNTs into Epon 862 and Epikure W, the same resin system used in the current work, by several different dispersion techniques. The only reported (insignificant) improvement in tensile strength (Fig. 1.13) corresponds to Fig. 1.12e.

<sup>12</sup> Reprinted from Nanotechnology, 23, V. Mirjalili, M. Yourdkhani, P. Hubert, Dispersion stability in carbon nanotube modified polymers and its effect on the fracture toughness, 1-8, (2012), © IOP Publishing. Reproduced by permission of IOP Publishing. All rights reserved.

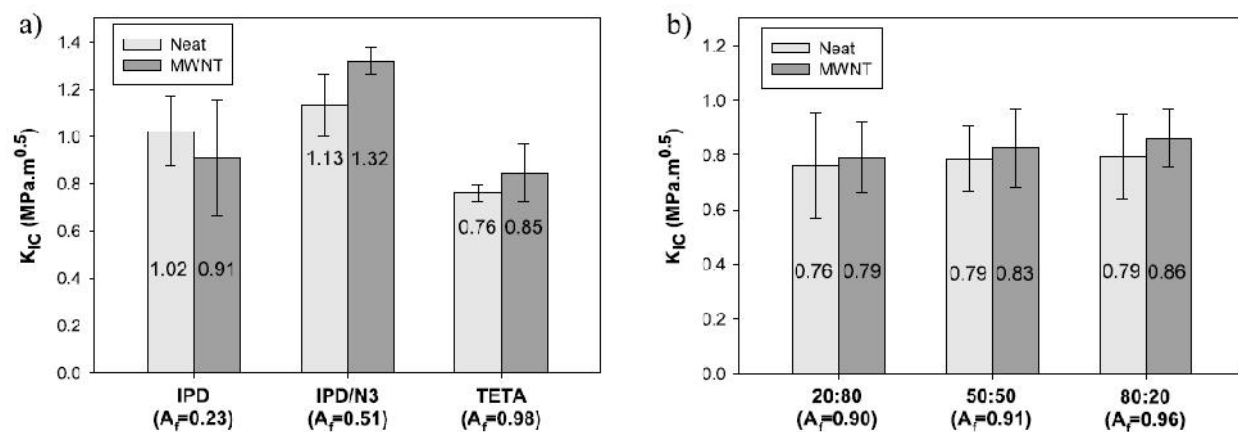


**Fig. 1.11:**<sup>13</sup> Fracture toughness test results: a) bisphenol-A with 0.3 wt% MWNT and different types of hardener; b) bisphenol-A with 0.3 wt% MWNT with different IPD:TETA ratio. Reproduced from [63].

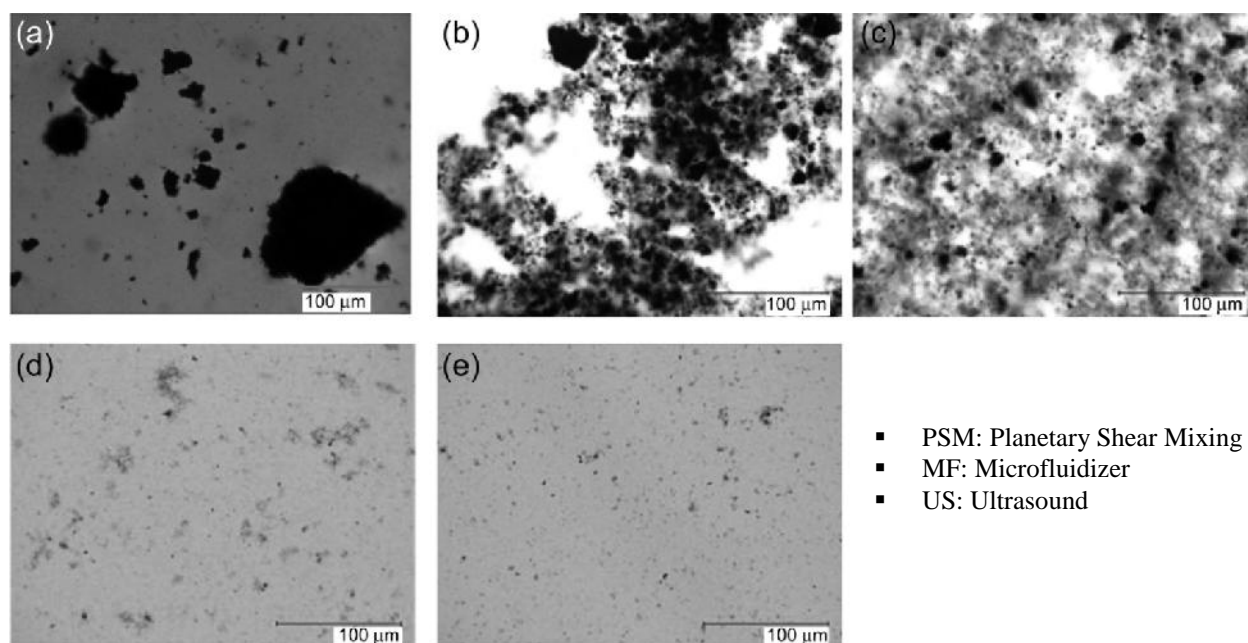


**Fig. 1.12:**<sup>14</sup> Effect of processing methods on dispersion of pristine MWCNT in epoxy resin a) US; b) PSM; c) US + PSM; d) MF; and e) MF + PSM. (US = ultrasound, PSM = planetary shear mixing, MF = microfluidizer). Reproduced from [51].

<sup>13</sup> Reprinted from Nanotechnology, 23, V. Mirjalili, M. Yourdkhani, P. Hubert, Dispersion stability in carbon nanotube modified polymers and its effect on the fracture toughness, 1-8, (2012), © IOP Publishing. Reproduced by permission of IOP Publishing. All rights reserved.

<sup>14</sup> Reprinted from Journal of Polymer Science Part B-Polymer Physics, 51, M. L. Gupta et al., The effect of mixing methods on the dispersion of carbon nanotubes during the solvent-free processing of multiwalled carbon nanotube/epoxy composites, 410-420, (2013), with permission from Wiley.

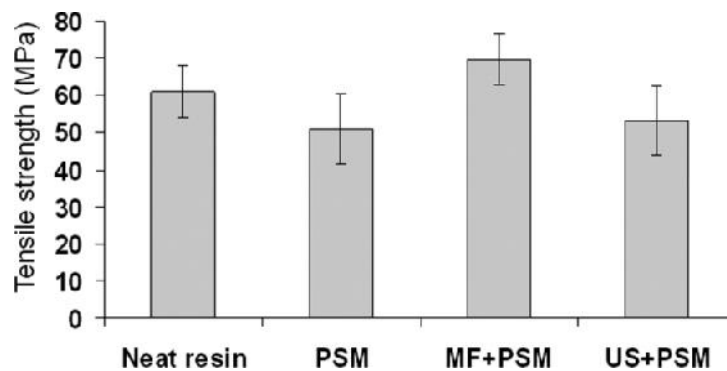


**Fig. 1.13:**<sup>15</sup> Tensile strength data (MPa) for MWCNTs/epoxy nanocomposites processed by different methods. Reproduced from [51].

Ashrafi et al. [50] synthesized SWCNTs and then functionalized them (r-SWCNT). When 0.2 wt% CNTs were added at the manufacturer recommended stoichiometry of 1:0.8 molar ratio of resin:hardener,  $K_{IC}$  increased insignificantly from  $1.10 \text{ MPa}\sqrt{m}$  to  $1.33 \text{ MPa}\sqrt{m}$  (Table 1.6). Then they considered a case where 25% more hardener was added to reach a molar ratio of 1:1. While  $K_{IC}$  of neat epoxy did not change, a statistically significant increase in  $K_{IC}$  of 0.2 wt% r-SWCNT was found ( $1.51 \text{ MPa}\sqrt{m}$ ). This composition containing 0.2 wt% r-SWCNT and 1:1 molar ratio of resin:hardener gave them significant increases in ultimate tensile strength, ultimate tensile strain, and tensile toughness, as well as an insignificant increase in elastic modulus, when compared to the manufacturer-recommended neat epoxy (Table 1.7). This material also gave significant increases in ultimate tensile strength, ultimate tensile strain, and tensile toughness, as well as an insignificant decrease in elastic modulus, when compared to the 1:1 molar ratio neat epoxy. When the molar ratio of *neat* epoxy was increased to 1:1.1,  $K_{IC}$  increased to the same value ( $1.51 \text{ MPa}\sqrt{m}$ ) as 1:1 molar ratio 0.2 wt% r-SWCNT, but with much more scatter. In addition, the ultimate tensile strength and ultimate tensile strain decreased significantly, and the

<sup>15</sup> Reprinted from Journal of Polymer Science Part B-Polymer Physics, 51, M. L. Gupta et al., The effect of mixing methods on the dispersion of carbon nanotubes during the solvent-free processing of multiwalled carbon nanotube/epoxy composites, 410-420, (2013), with permission from Wiley.

elastic modulus increased insignificantly compared to the manufacturer-recommended molar ratio (1:0.8) of neat epoxy. When unfunctionalized nanotubes (u-SWCNT) were added to epoxies at different stoichiometries, improvements were found in elastic modulus, while improvements were not found in  $K_{IC}$ , ultimate tensile stress, ultimate tensile strain, or tensile toughness.

	Sample names	Fracture toughness, $K_{IC}$ (MPa m <sup>0.5</sup> )	$K_{IC}$ increase/decrease (%)	Reduction in variation of $K_{IC}$ (%)
1:0.8 molar ratio	Epoxy	1.10 ± 0.34		
	0.06 wt% r-SWCNT	1.19 ± 0.24	+8 [0.65] <sup>a</sup>	29
	0.2 wt% r-SWCNT	1.33 ± 0.10	+20 [0.19]	70
	0.2 wt% u-SWCNT	0.80 ± 0.18	<u>-28</u> <sup>b</sup> [0.10]	47
1:1 molar ratio	Epoxy	1.09 ± 0.30		
	0.06 wt% r-SWCNT	1.31 ± 0.28	+20 [0.28]	5
	0.2 wt% r-SWCNT	1.51 ± 0.06	+38 [0.017]	80
	0.2 wt% u-SWCNT	1.15 ± 0.20	+5 [0.74]	33
1:1.1 molar ratio	Epoxy	1.51 ± 0.44		
	0.06 wt% r-SWCNT	1.42 ± 0.19	-5 [0.72]	56
	0.2 wt% r-SWCNT	1.17 ± 0.13	-23 [0.14]	71
	0.2 wt% u-SWCNT	1.09 ± 0.10	<u>-28</u> [0.075]	78

<sup>a</sup> The numbers in brackets giving the results of Student's  $T$ -test ( $p$  value) for probability of null hypothesis.

<sup>b</sup> The underscored number suggesting a statistically significant difference based on a 10% probability of null hypothesis or less ( $p \leq 0.1$ ).

**Table 1.6:**<sup>16</sup> Fracture toughness of epoxy resins and their composites. Reproduced from [50].

<sup>16</sup> Reprinted from Nanotechnology, 24, B. Ashrafi et al., Influence of the reaction stoichiometry on the mechanical and thermal properties of SWCNT-modified epoxy composites, 1-9, (2013), © IOP Publishing. Reproduced by permission of IOP Publishing. All rights reserved.



Samples	Tensile modulus, $E$ (GPa)	Ultimate tensile strength, $UTS$ (MPa)	Ultimate tensile strain, $\varepsilon_{max}$ (%)	Tensile toughness, $G$ (MPa)
Epoxy (1:0.8) <sup>a</sup>	4.02 ± 0.16	92.2 ± 8.9	3.21 ± 0.54	1.73 ± 0.49
Epoxy (1:1)	4.32 ± 0.30	87.7 ± 14.2	2.76 ± 0.67	1.34 ± 0.55
Epoxy (1:1.1)	4.27 ± 0.26	48.1 ± 20.9	1.31 ± 0.68	0.41 ± 0.25
0.2 wt% r-SWCNT (1:0.8)	4.08 ± 0.45	81.0 ± 7.7	2.72 ± 0.38	1.28 ± 0.35
Changes	+1.5% [0.79] <sup>b</sup>	-12% <sup>c</sup> [0.08]	-16% [0.17]	-26% [0.17]
0.2 wt% r-SWCNT (1:1)	4.13 ± 0.07	117.8 ± 2.4	4.15 ± 0.20	2.83 ± 0.18
Changes	-4.4% [0.34]	34% [0.013]	+56% [0.01]	+111% [0.004]
0.06 wt% r-SWCNT (1:1)	4.31 ± 0.31	110.6 ± 15.0	3.81 ± 0.70	2.49 ± 0.77
Changes	-0.2% [0.96]	+26% [0.039]	+43 [0.029]	+85% [0.027]
0.2 wt% u-SWCNT (1:0.8)	4.4 ± 0.5	71.2 ± 2.5	2.28 ± 0.15	0.94 ± 0.10
Changes	+7% [0.02]	-23% [0.003]	-29 [0.013]	-46% [0.016]
0.2 wt% u-SWCNT (1:1)	4.28 ± 0.13	86.3 ± 4.5	2.59 ± 0.10	1.25 ± 0.13
Changes	-4.4% [0.34]	-1.7% [0.87]	-2.7% [0.86]	-6.8% [0.79]

<sup>a</sup> The numbers in parenthesis are the resin-to-hardener molar ratios.

<sup>b</sup> The numbers in brackets giving the results of Student's  $T$ -test ( $p$  value) for probability of null hypothesis.

<sup>c</sup> The underscored number suggesting a statistically significant difference based on a 10% probability of null hypothesis or less ( $p \leq 0.1$ ).

**Table 1.7:**<sup>17</sup> Tensile properties of epoxy resins and their composites. Reproduced from [50].

This literature review indicates that adding CNTs to epoxy *does not always improve the fracture toughness*, even when the dispersion is deemed good. Researchers have found that when straightforward techniques do not lead to significant improvements in  $K_{IC}$  of CNT-modified epoxy, these may be achieved by electrically aligning CNTs, using different types of CNTs, or adding additional hardener beyond the manufacturer-recommended stoichiometry.

### 1.3.5 Carbon Fiber Composites

In recent years carbon fiber reinforced polymers (CFRPs) have become a mainstay of aerospace structures. These layered systems are susceptible to fracture/damage in the interlaminar regions, particularly as a result of fatigue and/or impact loading. Several authors [74-77] have fabricated unidirectional CFRPs in order to compare interlaminar fracture

<sup>17</sup> Reprinted from Nanotechnology, 24, B. Ashrafi et al., Influence of the reaction stoichiometry on the mechanical and thermal properties of SWCNT-modified epoxy composites, 1-9, (2013), © IOP Publishing. Reproduced by permission of IOP Publishing. All rights reserved.

specimens to intralaminar fracture specimens under quasi-static loading conditions. These intralaminar specimens are far less tedious to manufacture and characterize. However, to the authors' knowledge, none have used the same specimen geometry when comparing intralaminar and interlaminar specimens. This gap is significant because measured SIFs have been shown to be dependent on specimen geometry [78-80]. Most [74, 75, 77] used double cantilever beam (DCB) specimens to examine interlaminar fracture and compact tension specimens to examine intralaminar fracture, whereas de Moura et al. [76] used DCB specimens of different geometries to examine interlaminar and intralaminar fracture.

A few previous works on this topic [81-84] have employed strain gages to evaluate dynamic fracture parameters. Strain gages, when applied to the specimen surface, interfere with stress wave propagation. Strain gages also provide a spatially-limited number of data points. Without a camera to find the current crack tip location, these methods are less accurate at predicting crack initiation time and are unable to properly account for crack tip velocity, which is necessary for accurate determination of post-initiation SIFs. This is particularly important because different CFRP systems could have different post-initiation resistance behaviors [85], an important factor in material selection. Most of these researchers [82-85] extrapolated statically measured properties to estimate dynamic fracture parameters and/or relied on other material characteristics of similar materials reported by others to accomplish the task. These authors [82-85] also used in-plane characteristics to estimate out-of-plane properties by assuming transverse isotropy.

Without investigating fracture parameters, several authors have used ultrasound to measure the elastic constants of orthotropic composite materials [86, 87]. These techniques were similar to that of Van Buskirk et al. [36], used to characterize cortical bone.



Several investigators [58, 88-95] have attempted to reinforce the interlaminar regions of CFRPs using carbon nanotubes (CNTs). All used a DCB specimen to measure critical energy release rate ( $G_{ic}$ , also known as fracture toughness) under quasi-static loading conditions (typically following the ASTM Standard D5528 [88-95]). Some of the authors [89, 90, 92, 94, 95] formed their three-phase nanocomposites by dispersing CNTs into the resin first (Table 1.8), while others [58, 88, 91, 93] began with carbon fiber sheets pre-impregnated with resin and then added CNTs by a sifting or spraying technique (Table 1.9). Note that SWCNTs, DWCNTs, and MWCNTs refer to single-walled, double-walled, and multi-walled CNTs, while “UFN” refers to unfunctionalized CNTs. Most [58, 88, 91] of the latter group added CNTs only to the interlayer where the pre-crack would be introduced.

Author	+% $G_{ic}$	Fiber Layout (manufacturing technique)	Fiber $V_f$ %	CNT Type (dispersion technique)
Ashrafi et al. 2011	3 <sup>a</sup>	[0°] <sub>n</sub> fabric (prepreg with CNTs) <sup>b</sup>	-	0.1 wt% SWCNTs (bath sonication + solvent)
Godara et al. 2009	40	[0°] <sub>n</sub> fabric (prepreg with CNTs) <sup>b</sup>	50-60	0.5 wt% NH <sub>2</sub> DWCNTs (calendering)
Karapappas et al. 2009	60	[0°] <sub>n</sub> fabric (hand layup)	56	1 wt% UFN MWCNTs (high shear mill)
Romhany & Szebenyi 2009	13 <sup>a</sup>	[0°] <sub>n</sub> fabric (hand layup)	52	0.3 wt% UFN MWCNTs (calendering)
Sager et al. <sup>c</sup> 2011	18 <sup>a</sup>	Woven fabric (VARTM + interleaf film)	55	0.5 wt% NH <sub>2</sub> CNTs (bath sonication + solvent)

**Table 1.8:** Reported critical energy release rate ( $G_{ic}$ ) of carbon fiber nanocomposites with CNTs dispersed into the resin first.

<sup>a</sup> Indicates % improvement that was not significant relative to the reported error bars.

<sup>b</sup> Prepreg in this table indicates that CNTs were dispersed into the resin before the impregnation of dry fibers.

<sup>c</sup> Used the same epoxy system as the current work.

Author	+% $G_{ic}$	Fiber Layout (manufacturing technique)	Fiber $V_f$ %	CNT Type (dispersion technique)
Almuhammadi et al. 2014	17	$[0^\circ]_n$ prepreg <sup>b</sup> (CNTs sprayed on)	57	0.5 wt% COOH MWCNTs (sonication + solvent)
Hu et al. 2012	58	$[0^\circ]_n$ prepreg <sup>b</sup> (CNTs sifted onto interlayer)	-	10 g/m <sup>2</sup> UFN MWCNTs
Joshi & Dikshit 2012	40	Woven prepreg <sup>b</sup> (CNTs sprayed on)	67	1.32 g/m <sup>2</sup> UFN MWCNTs (bath sonication + solvent)
Kim & Hahn 2011	6	$[0^\circ]_n$ prepreg <sup>b</sup> (CNTs sprayed on)	65	0.5 wt% COOH SWCNTs (bath sonication + solvent)

**Table 1.9:** Reported critical energy release rate ( $G_{ic}$ ) of carbon fiber nanocomposites with CNTs added last to epoxy/carbon fiber prepreg.

<sup>a</sup> All % improvements in this table were significant relative to the error bars.

<sup>b</sup> Prepreg in this table indicates that CNTs were added to carbon fibers that had been previously impregnated with resin.

#### 1.4 Objectives

The literature review indicates several gaps in the dynamic fracture of bio- and nano-materials, many of which can be approached with an improved dynamic fracture methodology. Therefore, the first objective of this dissertation is to introduce a methodology involving digital image correlation (DIC) and high-speed photography for determining the dynamic fracture properties of relatively small size specimens. Some materials, such as cortical bone, are only available naturally in limited size. Many synthetic materials, such as carbon fiber composites, can be expensive and time-consuming to fabricate, particularly when nanomaterials such as CNTs are introduced as a third phase in order to improve interlaminar properties. Because post-crack-initiation response is also of interest for the determination of a particular material's ability to resist continued crack growth after initiation, samples must still be sufficiently sized to assess these parameters of crack tips growing as fast as 1 km/s using current technology. Therefore a methodology will be introduced for the dynamic fracture characterization of samples much

smaller than what is typically used [16, 17] to analyze SIFs both at crack initiation and after crack initiation.

The second objective is to calibrate the dynamic fracture methodology using acrylic, as it has been well documented in the literature under both quasi-static and dynamic fracture conditions (Table 1.2).

The third objective is to characterize the dynamic fracture behavior of acrylic bone cement, which has not been investigated previously. These results will be compared to quasi-static fracture results, which have been studied thoroughly by previous research teams (Table 1.1).

The fourth objective to extend this methodology to the orthotropic nanomaterial, cortical bone, which has not been studied extensively under dynamic fracture conditions (Table 1.4). This will be the first reported measurement of dynamic fracture crack initiation SIF ( $K_{I-ini}^d$ ) of cortical bone in the axial direction. In order to measure SIFs using DIC, the orthotropic elastic properties of this material must be known. Therefore, this objective also includes the ultrasonic characterization of the elastic properties of cortical bone.

With the eventual goal of improving the interlaminar fracture properties of engineered orthotropic materials such as CFRPs using synthetic nanoparticles in mind, the fifth objective is to achieve a good dispersion of CNTs in epoxy, with the hypothesis that this will lead to improvements in fracture properties over neat epoxy [50, 52-66, 68, 70-72]. In order to confirm that these properties are indeed improving, CNT/epoxy nanocomposites will be evaluated under quasi-static tensile, quasi-static fracture, and dynamic fracture conditions.

As stated previously, the ultimate objective of this work is to significantly enhance the interlaminar fracture properties of CFRPs under quasi-static and dynamic fracture conditions by the addition of CNTs to the interlayer. In order to study this with the proposed methodology,

sufficiently thick CFRPs must be fabricated. Additionally, these interlaminar fracture results will be compared to intralaminar fracture specimens for the first time under dynamic conditions. These specimens will be machined to the same geometry and from the same original unidirectional composite plate (because measured stress intensity factors (SIFs) are dependent on specimen geometry [78-80]) with the expectation that interlaminar and intralaminar fracture properties will be similar. In order to measure these SIFs, the elastic constants of this orthotropic material will be determined using the same ultrasonic procedure originally applied to cortical bone, which has a lower degree of anisotropy. This will also be the first work to use digital image correlation (DIC) to map full-field deformations before and after crack initiation in order to determine interlaminar SIF histories in fiber-reinforced composite specimens subjected to dynamic impact loading.

## **1.5 Organization of Dissertation**

This dissertation is organized into 7 chapters including the current chapter.

In Chapter 2, the experimental methodology involving dynamic 1-point impact of fracture specimens evaluated using digital image correlation (DIC) and high-speed photography is introduced.

In Chapter 3, the experimental approach and the apparatus are calibrated using isotropic commercial grade acrylic and then extended to the dynamic fracture of acrylic bone cement used in joint replacement surgeries.

In Chapter 4, the experimental methodology is applied to orthotropic cortical bone, which fails almost exclusively under dynamic loading conditions in a clinical sense. In order to

determine fracture parameters for this material, its elastic properties are first determined ultrasonically.

In Chapter 5, carbon nanotubes (CNTs) are dispersed using many different techniques with the goal of ultimately improving the interlaminar fracture properties of 3-phase carbon fiber reinforced polymers (CFRPs). The suitability of 2-phase CNT/epoxy nanocomposites for this application is mechanically characterized under quasi-static tensile, quasi-static fracture, and dynamic fracture conditions. The quality of dispersion is examined using optical microscopy and scanning electron microscopy (SEM).

In Chapter 6, the experimental methodology is applied to thick, unidirectional CFRPs. The orthotropic elastic constants are determined for this material using the ultrasonic technique first applied to cortical bone in Chapter 4. Interlaminar fracture results are compared with intralaminar fracture specimens machined to the same geometry from the same original composite plate. CNTs are added to the epoxy matrix in order to form 3-phase CFRPs, and their effect on interlaminar and intralaminar fracture properties is examined.

In Chapter 7, final conclusions are presented related to the methodology proposed in Chapter 2 and demonstrated in all subsequent chapters. Future applications of the methodology are discussed.

## **Chapter 2. Experimental Methods**

In this chapter, details about the modified Kolsky bar impactor apparatus, high-speed photography, and digital image correlation (DIC) are provided. The modified Kolsky bar apparatus has been designed to deliver 1-point impact loading to plate-shaped, pre-notched, dynamic fracture specimens. The entire dynamic fracture events are recorded with the high-speed camera. Using DIC, displacements on fracture specimen surfaces are measured in order to determine stress intensity factors (SIFs) corresponding to each image from the high-speed camera as detailed in subsequent chapters.

### **2.1 Development of a Modified Kolsky Bar Apparatus**

In order to study dynamic fracture of relatively small specimens, a methodology (Figs. 2.1-2.3) that employs DIC and high-speed photography to monitor in-plane deformations on a plate-shaped specimen during a 1-point impact loading event has been developed. It consists of a gas-gun, a striker, and a long-bar aligned co-axially as shown in the Fig. 2.3. The striker is a 0.30 m long, 25.4 mm diameter aluminum cylindrical rod, initially housed in the barrel of the gas-gun. The striker end of the long-bar, a 1.83 m long, 25.4 mm diameter aluminum rod, is machined flat whereas its other end is machined with a bull-nose head (diameter 6.35 mm half-cylinder). The cylindrical head of the long-bar is registered against the specimen to deliver a transient impact force as a line-load. The sample is placed on an adjustable platform and aligned using blocks of pliable putty (Fig. 2.4) to create approximately ‘free-free’ boundary conditions, as the specimen is loaded utilizing its inertia.

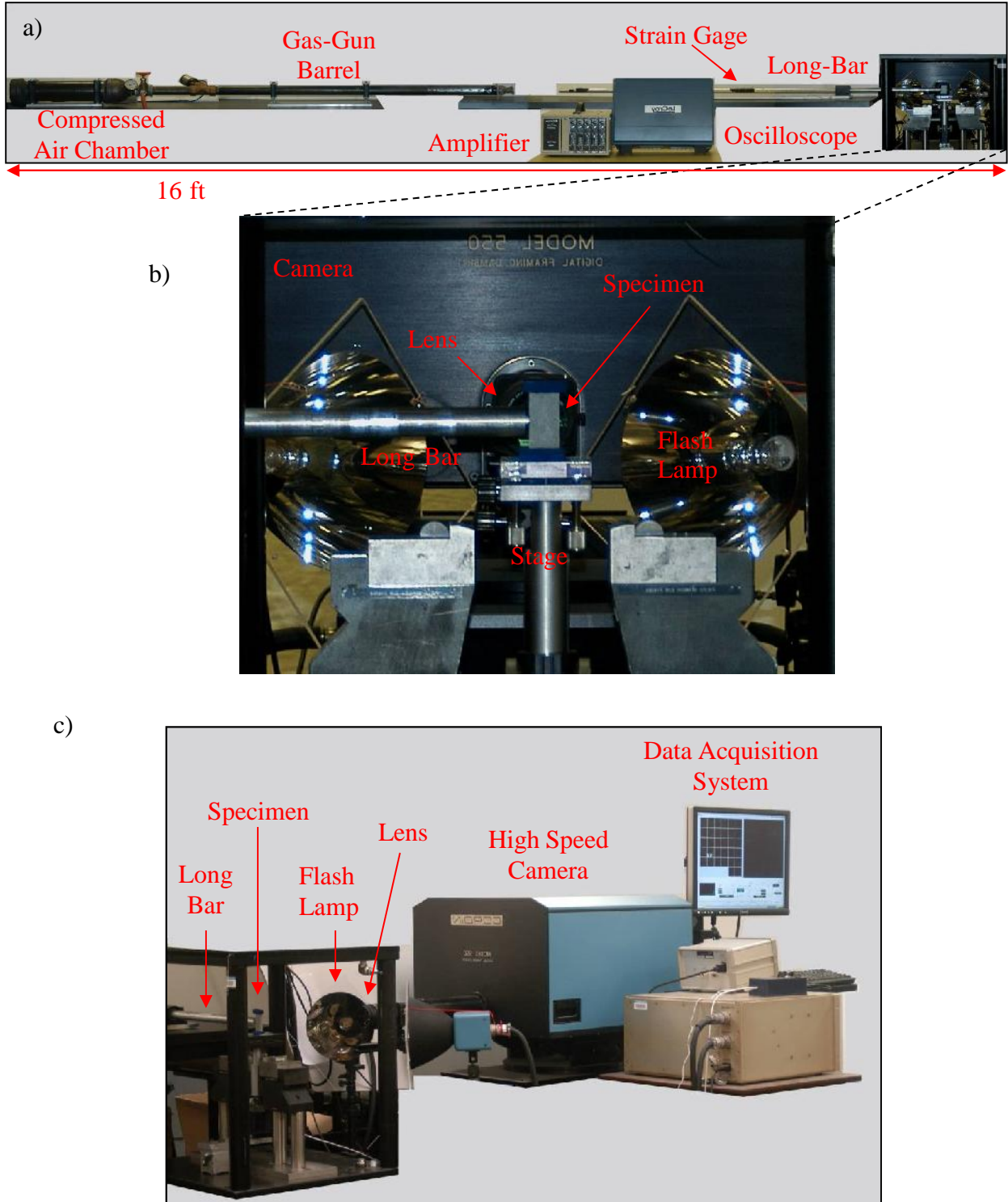


**Fig. 2.1:** Photographs of long-bar impactor setup for studying crack initiation and propagation of relatively small size specimens: a) full setup, b) close-up of specimen and camera, and c) off-axis view of specimen, camera, and data acquisition system.

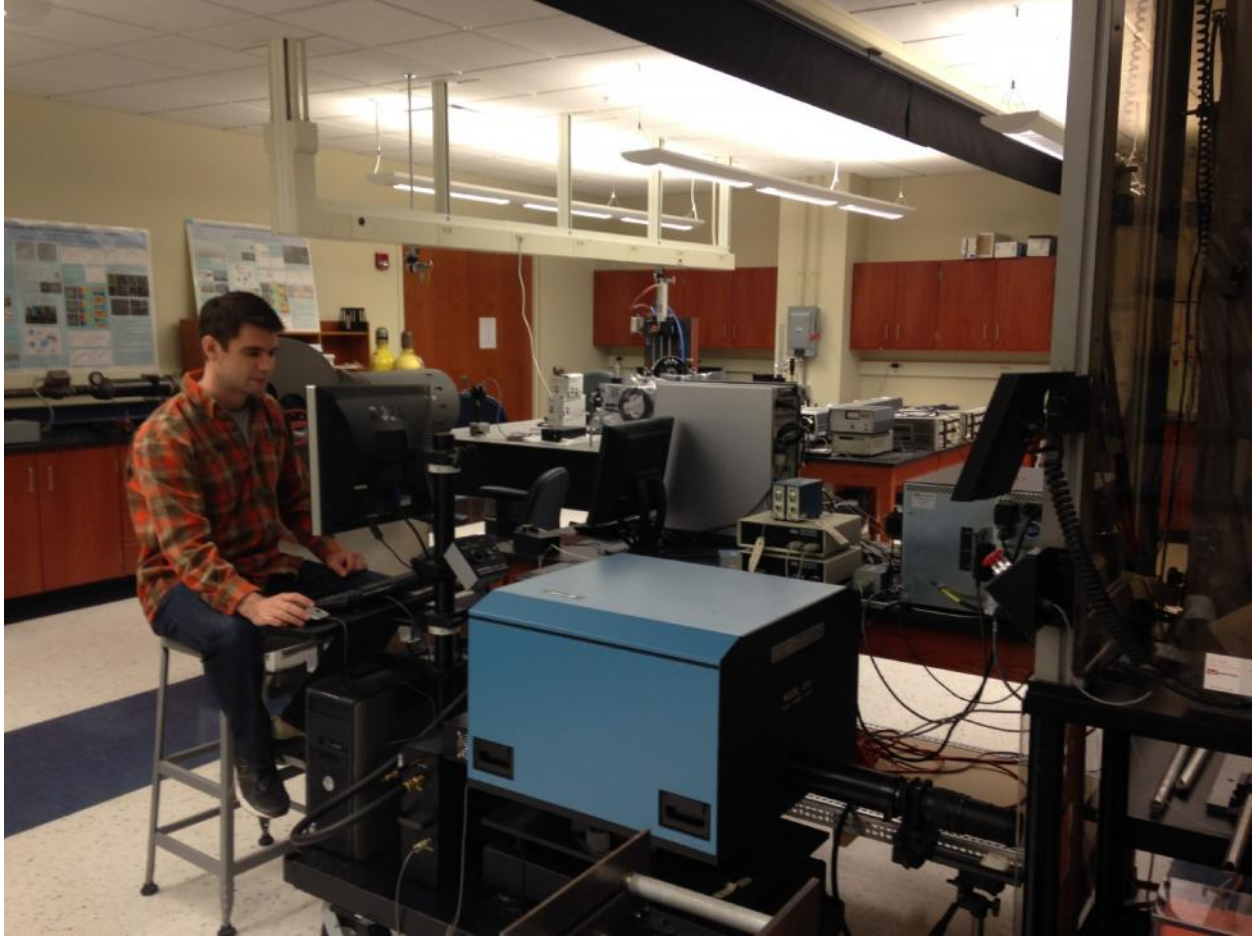


**Fig. 2.2:** Photograph of the high-speed camera system.

The striker is launched at approximately 16 m/s from the compressed air chamber (15 psi) into the long-bar (incident bar), both made of strain-rate independent Al 7075-T6. A pulse shaper is used between the striker and long-bar as needed in order to affect the loading rate. The stress waves then enter the specimen via a semi-circular head machined onto the end of the long-bar. The sample loading is symmetric with respect to the pre-notch in order to achieve mode-I fracture. The stress waves enter the specimen as compressive waves and reflect back as tensile waves from the free edges including the pre-notched edge. Due to inertia, the reflected tensile waves subject the crack to mode-I opening deformations and propagation long before the specimen leaves the field of view of the high-speed camera.



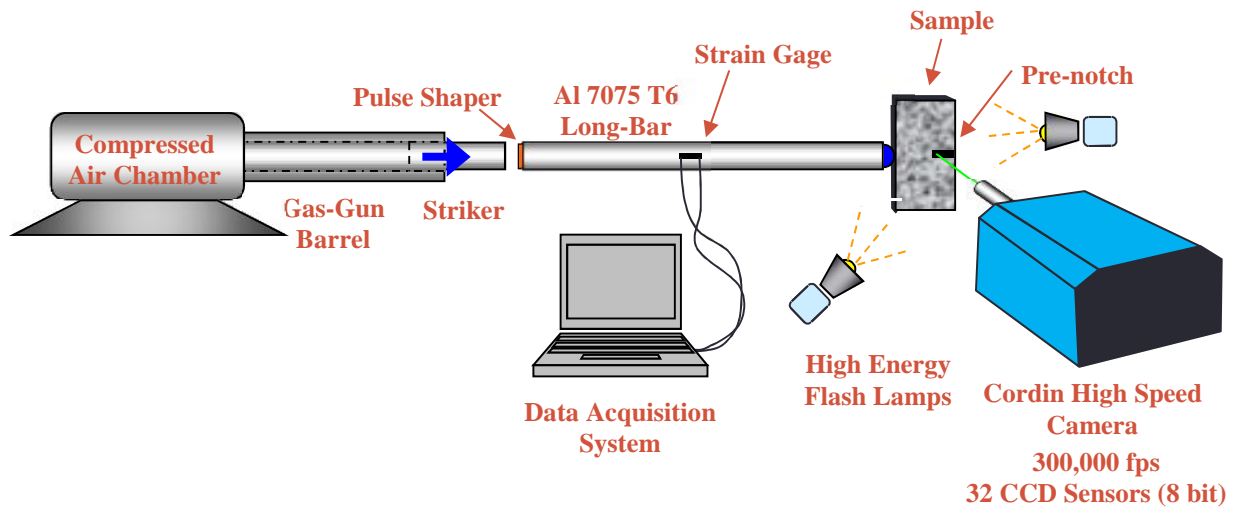


**Fig. 2.3:** Schematic of long-bar impactor setup for studying crack initiation and propagation of relatively small size specimens.

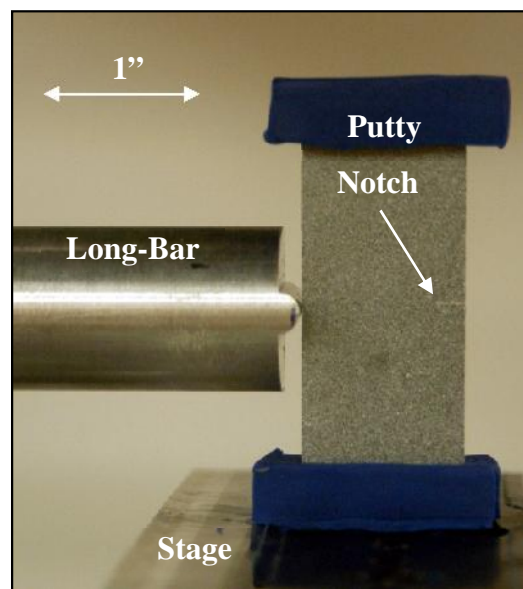


**Fig. 2.4:** Close-up of the impact loading setup. Specimen with pre-notch is placed in contact with the semi-circular impactor head of the long-bar prior to testing. Putty is used to ensure symmetry of reflected waves from the top and bottom specimen edges.

A strain gage (CAE-13-125UN-120 from Vishay Micro-Measurements, gage factor = 2.110, quarter bridge configuration) on the long-bar records the incident stress wave, whose strain signal is later used as input in a computational model to complement optical

measurements. This analog signal is amplified using an Ectron 563H amplifier (Fig. 2.5) before being converted to a digital signal and collected using a Lecroy Waverunner 104Xi oscilloscope (Fig. 2.6).



**Fig. 2.5:** Photograph of the Ectron 563H amplifier used to amplify the strain gage signal on the long-bar.

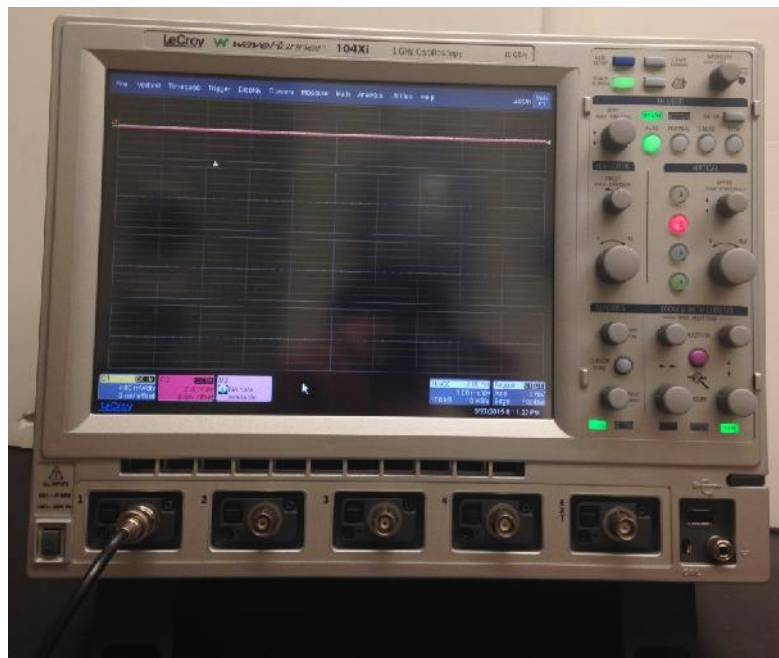


**Fig. 2.6:** Photograph of the Lecroy Waverunner 104Xi oscilloscope used to digitize and record the strain gage signal from the long-bar.

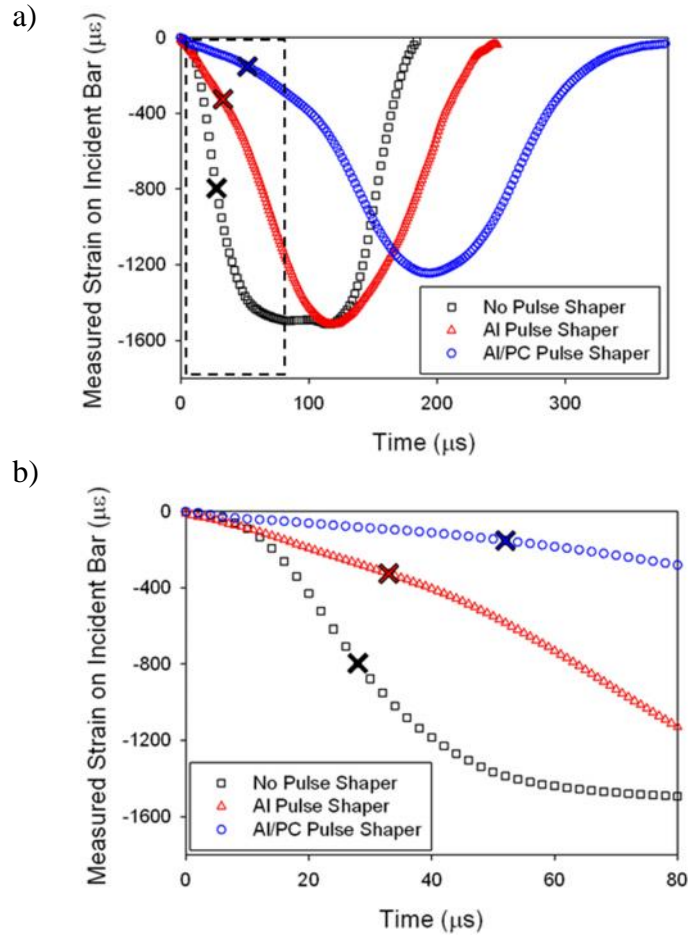


**Fig. 2.7:** a) Strain histories recorded on the long-bar corresponding to three different pulse shapers. X marks the portion of the strain history coinciding with crack initiation. b) The first 80  $\mu\text{s}$  of Fig. 2.7a are shown.

To study the strain-rate effects on the fracture behavior, three different shapes of incident waves were achieved using different pulse shapers (Fig. 2.7) placed between the striker and the long-bar. A soft Aluminum 1100 disc (Al) of diameter 8 mm and thickness 0.9 mm produced a strain-rate of  $10.7 \text{ second}^{-1}$ , measured on the long-bar. A combined polycarbonate washer (outer diameter 6.3 mm, inner diameter 2.2 mm and thickness 0.7 mm) and Al 1100 sandwich pulse shaper (Al/PC) produced a slightly lower strain rate of  $3.7 \text{ second}^{-1}$ . The highest strain rate was  $42.0 \text{ second}^{-1}$  when no pulse shaper (designated as “none”) was used.

A linear relationship was found between pressure of the gas chamber and velocity of the striker (Fig. 2.8), although the velocity was found to only affect the peak amplitude and to not have any significant effect on the strain-rate.

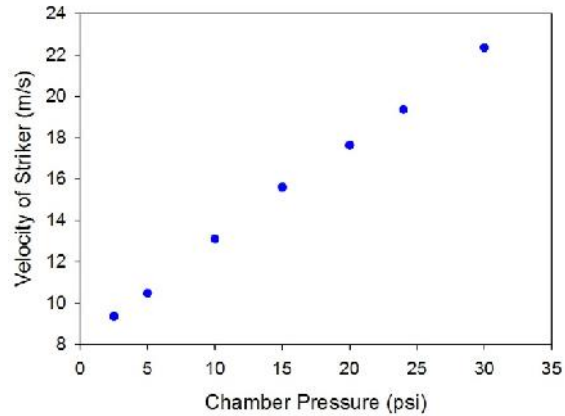


**Fig. 2.8:** Velocity of the aluminum 7075-T6 striker bar as a function of gas chamber pressure.

## 2.2 High-Speed Photography

A Cordin model 550 high-speed digital camera was used for recording images of dynamic fracture events at 200,000-400,000 frames per second. The camera has a maximum recording speed of 2 million frames per second and produces 32 individual 1000 x 1000 pixel images. This means the total time of the recorded footage was 80-160  $\mu$ s, depending on the framing rate utilized. The camera has 32 CCD sensors and uses a five-facet rotating mirror to sweep the image over the sensors during the fracture event. The camera was triggered when the striker made contact with the long-bar. Approximately 340  $\mu$ s later, the stress wave would reach the sample at the other end of the long-bar. A delay generator was used to account for this time, as well as the time for the wave to propagate across the pulse shaper. Trigger delays of approximately 360  $\mu$ s without a pulse shaper, 400  $\mu$ s with a soft aluminum pulse shaper, and 420  $\mu$ s with a soft aluminum and polycarbonate pulse shaper were typically used. Prior to each event,

32 undeformed images were recorded at the same framing rate as the deformed images for comparison with the deformed images using DIC.

### 2.3 Digital Image Correlation (DIC)

The Cordin camera has 32 individual CCD sensors, and each sensor with its optics has variations relative to the others. This precludes correlation of speckle images captured by different sensors. Therefore, undeformed and deformed images from the same sensor were paired (Fig. 2.9a), and 2D Digital Image Correlation (DIC) was carried out on each of the 32 image pairs using ARAMIS® software. In order to determine in-plane displacement fields, all DIC specimens were given a speckle coating, such that the speckle size typically encompassed 4-6 pixels. Individual 1000 x 1000 pixel images were segmented into sub-images. For a sub-image identified in an undeformed image, the corresponding speckle pattern is searched in the deformed image. The distance between the center points of the matched undeformed sub-image ( $O$ ) and deformed sub-image ( $O'$ ) are the in-plane displacements,  $u$  and  $v$  (Fig. 2.9b). By repeating this process for all sub-images, matrices (~60 x 60 data points) of in-plane displacements were created for each image.

Although ARAMIS does not release the exact searching function used for correlation, one common method is to minimize the normalized cross-correlation function [96],

$$R\left(u, v, \frac{\partial u}{\partial x}, \frac{\partial u}{\partial y}, \frac{\partial v}{\partial x}, \frac{\partial v}{\partial y}\right) = 1 - \frac{\sum_{i,j} [F(x_i, y_j) - \bar{F}] [H(x_i^*, y_j^*) - \bar{H}]}{\sqrt{\sum_{i,j} [(F(x_i, y_j) - \bar{F})^2] \sum_{i,j} [(H(x_i^*, y_j^*) - \bar{H})^2]}}. \quad (2.1)$$

Here,  $F(x_i, y_j)$  is the pixel intensity (grayscale value which must be an integer 0-255 when using the 8-bit Cordin camera) at the discrete location  $(x_i, y_j)$  in the undeformed sub-image,

whereas  $H(x_i^*, y_j^*)$  is the grayscale value for the pixel located at  $(x_i^*, y_j^*)$  in the deformed sub-image.  $\bar{F}$  and  $\bar{H}$  are the mean grayscale values for the  $F$  and  $H$  intensity matrices of the undeformed and deformed sub-images, respectively.

In Fig. 2.9b, the coordinates of a generic point  $P'(x^*, y^*)$  in the deformed sub-image relative to point  $P(x, y)$  in the undeformed sub-image are approximated by the Affine transformation:

$$\begin{aligned} x^* &= x + u + \frac{\partial u}{\partial x} \Delta x + \frac{\partial u}{\partial y} \Delta y, \\ y^* &= y + v + \frac{\partial v}{\partial x} \Delta x + \frac{\partial v}{\partial y} \Delta y, \end{aligned} \tag{2.2}$$

assuming that the deformation occurs in the plane perpendicular to the optical axis. Here,  $u$  and  $v$  are the in-plane displacements of the center points ( $O$  and  $O'$ ) of the sub-images. The coordinates of  $P'(x^*, y^*)$  are a function of the in-plane displacements and the gradients of the in-plane displacements of the entire sub-image as follows:

$$P'(x + u + \frac{\partial u}{\partial x} \Delta x + \frac{\partial u}{\partial y} \Delta y, y + v + \frac{\partial v}{\partial x} \Delta x + \frac{\partial v}{\partial y} \Delta y). \tag{2.3}$$

Thus, undeformed and deformed sub-images can be located relative to each other by minimizing  $R$  in Eq. 2.1, often using a Newton-Raphson method.

The crack tip is located manually for each deformed image and set to zero displacement. A polar coordinate system is assigned with origin at the crack tip in order to comply with linear elastic fracture mechanics (LEFM) convention as shown in Fig. 2.10. The  $u$  and  $v$  displacements from DIC for the region of interest are then interpolated from the original matrices in the highlighted (green) region indicated in Fig. 2.10. This region [ $0.5 < r/B < 1.5$  and  $-150^\circ < <$

-90° and 90° < < 150°] was chosen to avoid noisy data ahead of the crack tip with relatively small  $v$  displacements (and hence large relative error), as well as 3-D effects near the crack tip and far field effects on this relatively small specimen. Hundreds of data points from this region are then used to calculate a single pair of SIFs ( $K_I^d$  and  $K_{II}^d$ ) corresponding to each deformed image using a least squares method. These equations will be detailed in the following chapters.

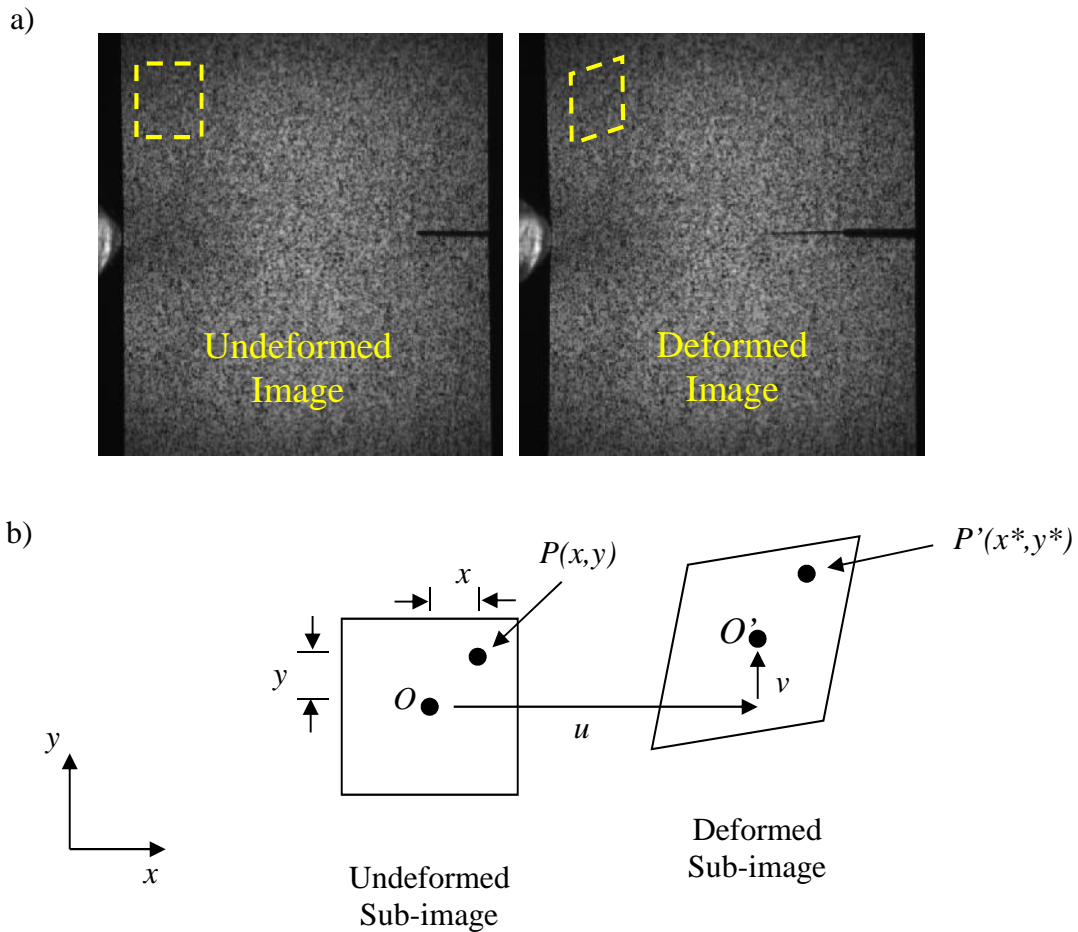


**Fig. 2.9:** a) A pair of images (magnification = 32  $\mu\text{m}/\text{pixel}$ ) recorded from the same CCD sensor of the high-speed camera. A sample sub-image is shown in the undeformed and deformed images. b) Point  $O$  in the undeformed sub-image displaces to a location  $O'$  in the deformed sub-image. The difference in these coordinates gives the sliding ( $u$ ) and opening ( $v$ ) displacements for the sub-image.

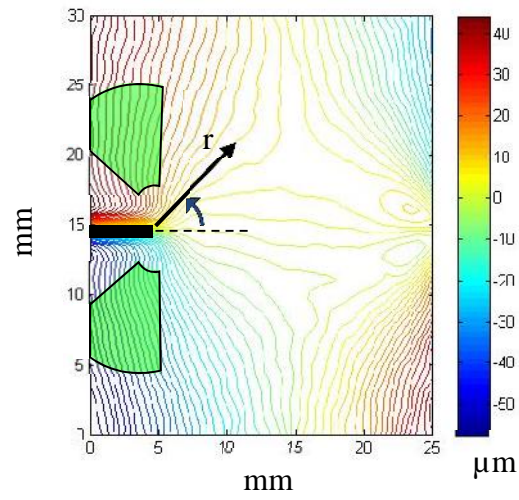


**Fig. 2.10:** Opening ( $v$ ) displacement contours on a PMMA sample. Data is extracted and interpolated in the region indicated behind the crack tip. A polar coordinate system is assigned with origin at the crack tip.



## **Chapter 3. Fracture of Acrylic and Acrylic Bone Cement: Calibration of Experimental Method**

In this chapter, details are provided on the quasi-static and dynamic fracture of two isotropic materials: industrial grade acrylic and acrylic bone cement. Displacement field equations for the determination of stress intensity factors (SIFs) using in-plane deformations determined using DIC (Chapter 2) are presented. The determination of isotropic elastic properties, necessary to solve the field equations, is described. The modified Kolsky bar apparatus is calibrated using industrial grade acrylic, which has been thoroughly studied in the literature under quasi-static and dynamic fracture conditions (Table 1.2). The device is then used to investigate the dynamic fracture properties of bone cement for the first time.

### **3.1 Specimen Preparation**

#### ***3.1.1 Industrial Grade Acrylic vs. Acrylic Bone Cement***

Because of the dangers of MMA monomer (detailed in Section 1.3.3) that occur when the filler material PMMA polymerizes inside of a patient during a surgical procedure, there are several major differences between commercial grade acrylic sheets and the DePuy<sup>®</sup> CMW MV bone cement used in this study. Both polymerization reactions include pre-polymerized PMMA beads, MMA monomer, and an initiator. However, commercial grade acrylic sheets are cured slowly (in about twelve hours) under high pressure and high temperature, while the DePuy<sup>®</sup> bone cement is cured in less than 20 minutes at relatively low pressure and temperature and is partially cured before it is packed into the hollow medullary cavity of the patient's long bone (femur or

tibia). Thus the porosity of bone cement will generally be higher than that of industrial acrylic. As explained in Section 1.3.3, these bone cement pores are present both in the surgical theatre as well as in the laboratory experiments described below. Relatively large pores (~1 mm) are believed to be caused by air entrapment during mixing of the liquid phase with the powder phase, while smaller voids (~100  $\mu\text{m}$ ) are created by gaseous byproducts of the polymerization reaction [25]. In addition, the conditions of the industrial grade acrylic reaction lead to a homogeneous dispersion of fully entangled PMMA chains, while the bone cement reaction creates a two-phase material: pre-polymerized beads within an interbead matrix. The interbead matrix shrinks during polymerization, potentially causing shrinkage stresses between the two phases. The interbead matrix also contains a radiopacifier (barium sulfate) so that the bone cement mantle can be visualized on X-ray after surgery. Previous studies have shown that the addition of  $\text{BaSO}_4$  to pure PMMA leads to a significant reduction in fatigue strength [97] and quasi-static crack initiation SIF [29] (Table 1.1). This is likely due to the poor bonding between  $\text{BaSO}_4$  particles and the interbead matrix. Finally, a cross-linking agent has been added to this particular commercial grade acrylic, increasing its  $T_g$  from the typical value of  $105^\circ\text{C}$  for PMMA to  $122^\circ\text{C}$ . The  $T_g$  for bone cement was  $101^\circ\text{C}$  (as measured by Differential Scanning Calorimetry).

### ***3.1.2 Specimen Preparation***

Two specimen material types were used: commercial grade cast acrylic (hereon referred to as PMMA) purchased from McMaster Carr and DePuy<sup>®</sup> CMW SmartSet Endurance Medium Viscosity Bone Cement (BC), prepared according to manufacturer instructions. The powder phase (10% by weight  $\text{BaSO}_4$ ) of BC was combined with the liquid phase using a DePuy<sup>®</sup>

vacuum mixer. After 90 seconds, the BC was poured onto a plate and allowed to cure for 20 minutes (Fig. 3.1). Due to fast curing, low temperature, and low pressure of medical grade bone cement, some degree of pore formation was unavoidable [25]. These voids typically rose to the surface and most were skimmed during processing or removed with a mill during sizing. However, some pores remained in the final BC specimens (estimated to be ~1% porosity by area measured on fracture surfaces), while PMMA specimens did not have these defects.

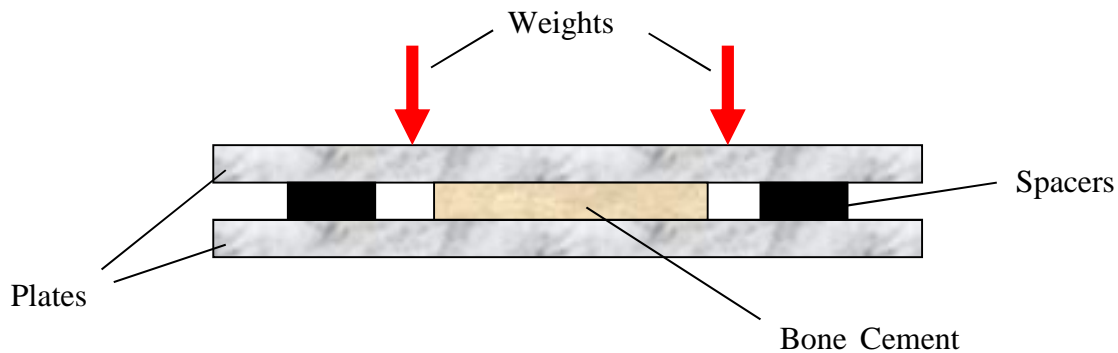


**Fig. 3.1:** Bone cement sheet cures between two plates using spacers for desired thickness.

For the static 3-point bending tests, PMMA and BC specimens were machined into beams of 60 x 15 x 4-6 mm (Fig. 3.2a). For the dynamic 1-point impact tests, plate-like specimens of 50 x 25 x 5 mm were used (Fig. 3.2b). The larger width of the dynamic specimens allowed for additional investigation of fracture parameters for the growing crack. All specimens were pre-notched using a diamond tipped saw. A speckle pattern was spray-painted onto dynamic fracture specimens in order to monitor in-plane displacements using DIC (explained in Section 2.3).

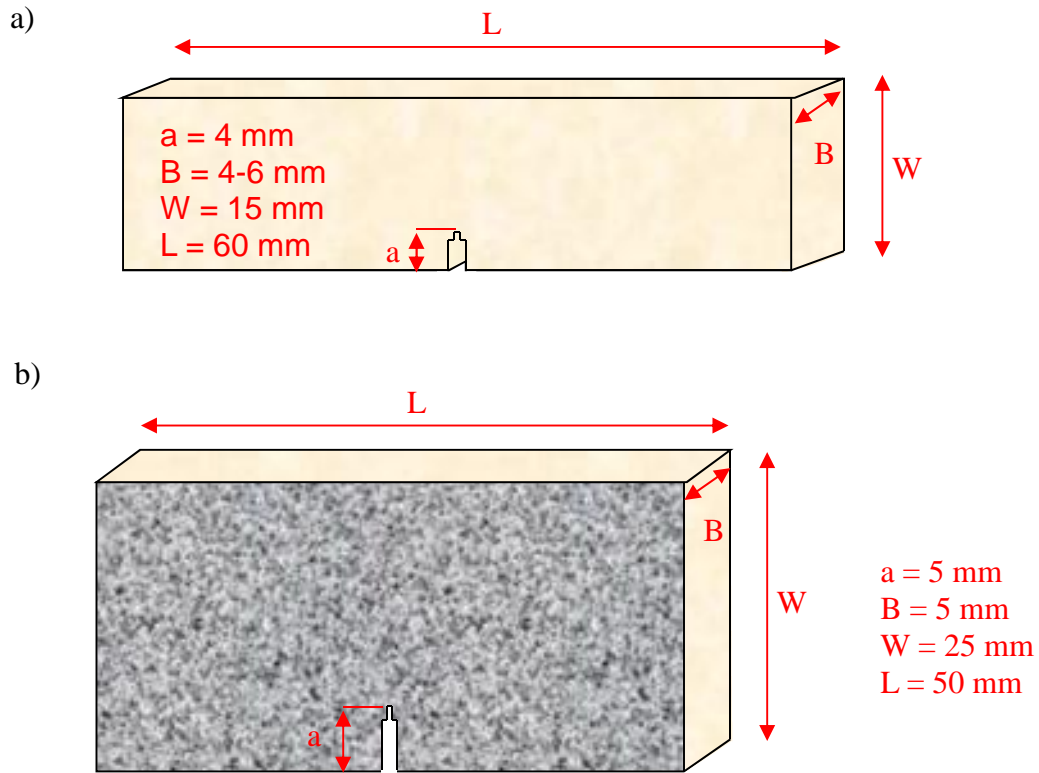


**Fig. 3.2:** Static a) and dynamic b) specimen geometry.

## 3.2 Experimental Details

### 3.2.1 Quasi-Static Fracture Tests

PMMA and BC specimens were tested in symmetric 3-Point bending configuration using an Instron 4465 testing machine in displacement control mode (cross-head speed = 0.01 mm/second). The samples were loaded monotonically up to fracture. The load-displacement responses were essentially linear up to crack initiation and fracture occurred abruptly during the tests. The quasi-static initiation SIFs ( $K_{IC}$ ) were calculated based on the maximum recorded load using,

$$K_{IC} = \frac{\left(\frac{P_{\max}}{B\sqrt{W}}\right)\left(3\frac{S}{W}\sqrt{\frac{a}{W}}\right)}{2\left(1+2\frac{a}{W}\right)\left(1-\frac{a}{W}\right)^{3/2}} \left[ 1.99 - \frac{a}{W}\left(1-\frac{a}{W}\right) \left\{ 2.15 - 3.93\left(\frac{a}{W}\right) + 2.7\left(\frac{a}{W}\right)^2 \right\} \right], \quad (3.1)$$

where  $P_{\max}$  is the peak load prior to fracture,  $B$  is thickness,  $W$  is width,  $S$  is span (50.9 mm), and  $a$  is crack length.

### 3.2.2 Dynamic Fracture Tests

The methodology involving digital image correlation (DIC) and high-speed photography for determining the dynamic fracture properties of relatively small size specimens (detailed in Chapter 2) was used to examine dynamic SIFs of PMMA and BC using all three dynamic loading rates (no pulse shaper- “none”, soft aluminum pulse shaper- “Al”, and soft aluminum + polycarbonate pulse shaper- “Al/PC”) (see Fig. 2.7).

In order to determine an appropriate sub-image size for DIC, a pair of images (Fig. 2.9) from a dynamic fracture test of PMMA was correlated over a range of possible sizes. For this study, 28.5 micrometers on the specimen corresponds to 1 pixel of the camera sensor. Fig. 3.3 shows the contours of displacement when non-overlapping 10 x 10 pixel sub-images (Fig. 3.3a and 3.3b) and 20 x 20 pixel sub-images (Fig 3.3c and 3.3d) were used. Due to limitations of correlation around the edges of pictures and the black bars on the left and right sides of images (Fig. 2.9), 1000 x 1000 pixel images with 10 x 10 pixel sub-images resulted in 89 x 81 matrices of opening displacements (Fig. 3.3a) and sliding displacements (Fig. 3.3b). Meanwhile, the 20 x 20 pixel sub-images resulted in 48 x 46 matrices of opening displacements (Fig. 3.3c) and sliding displacements (Fig. 3.3d). The 10 x 10 pixel sub-images show relatively noisy displacement

contours, whereas the 20 x 20 pixel sub-images result in much smoother contours due to averaging effects.

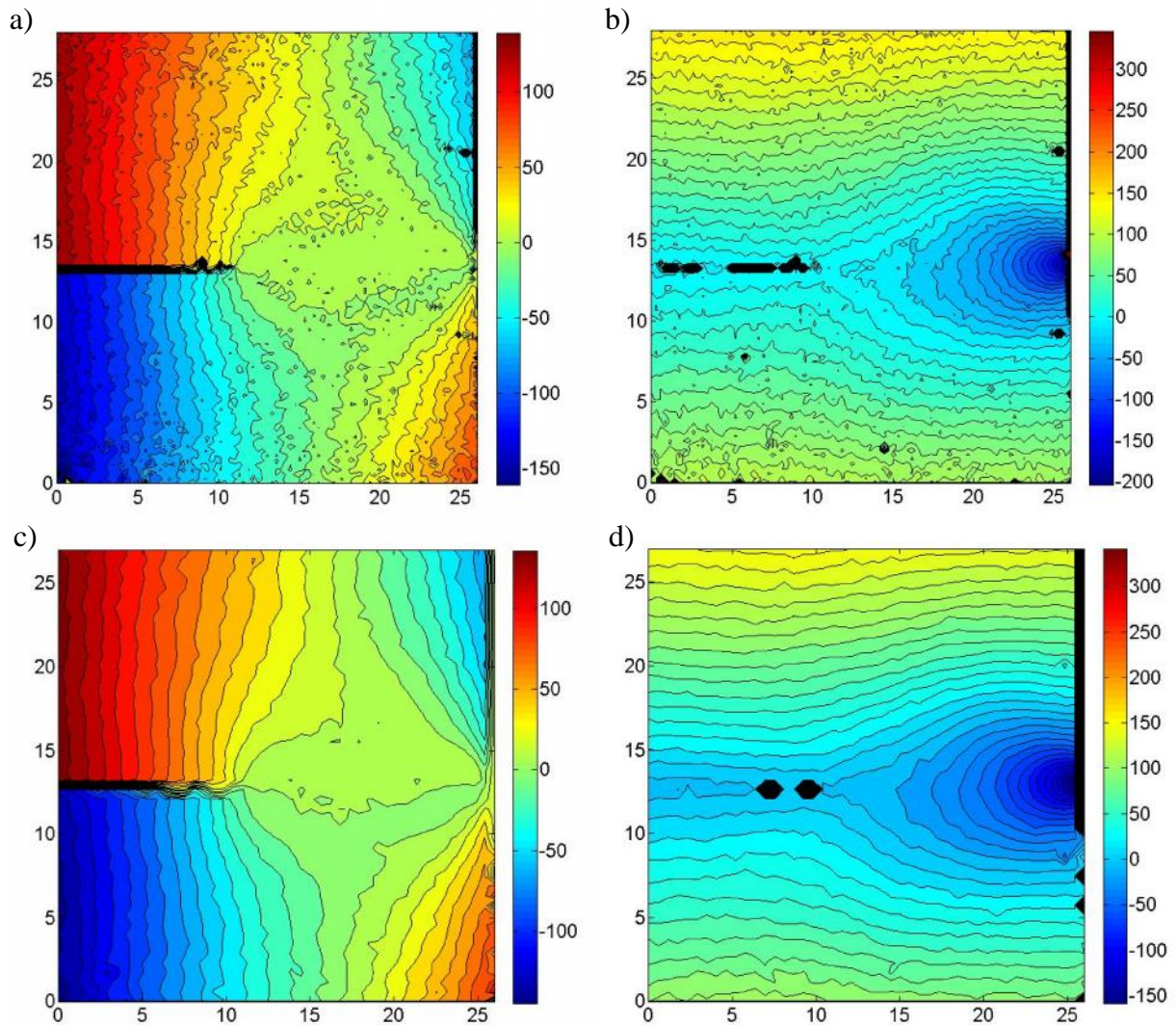


**Fig. 3.3:** Contours of displacement from 10 x 10 pixel sub-images (a, b) indicate noisy data, while 20 x 20 pixel sub-images (c, d) indicate over-smoothing of raw data. The former shows the crack tip location more precisely compared to the latter.

Fig. 3.4 shows the contours of displacement when non-overlapping 30 x 30 pixel sub-images (Fig. 3.4a and 3.4b) and 40 x 40 pixel sub-images (Fig. 3.4c and 3.4d) were used. The 30 x 30 pixel sub-images resulted in 32 x 30 matrices of opening displacements (Fig. 3.4a) and



sliding displacements (Fig. 3.4b), whereas the 40 x 40 pixel sub-images resulted in 23 x 22 matrices of opening displacements (Fig. 3.4c) and sliding displacements (Fig. 3.4d). Both the 30 x 30 pixel sub-images and the 40 x 40 pixel sub-images gave relatively smooth displacement contours; however, this smoothed data was accompanied by increased data loss and greater averaging of displacement data.

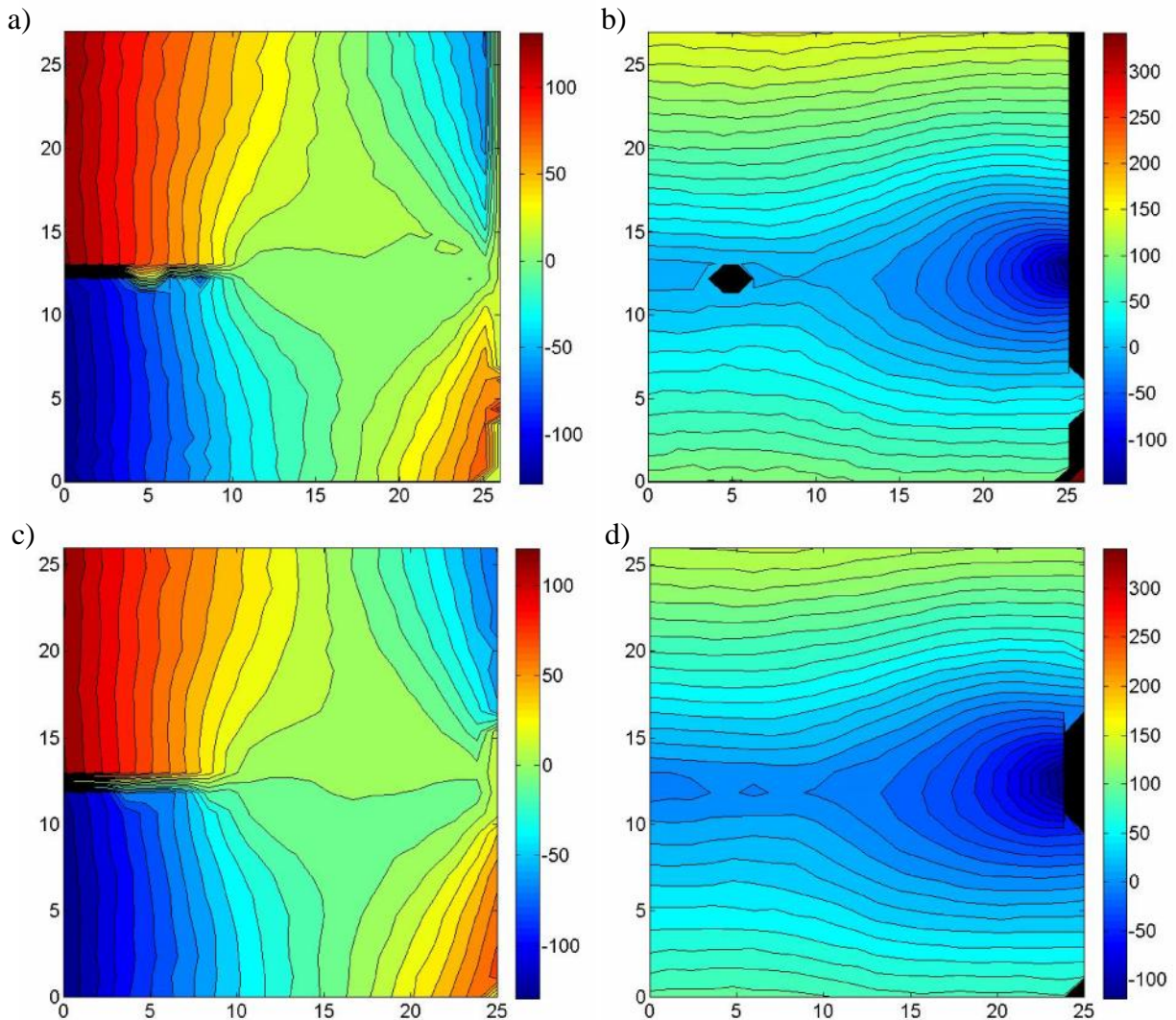


**Fig. 3.4:** Contours of displacement from pixel sub-images 30 x 30 (a, b) and 40 x 40 pixel sub-images (c, d) give very smooth contours but greatly reduce displacement matrices compared to those used in Fig. 3.3, where the crack tip location can be determined much more accurately.



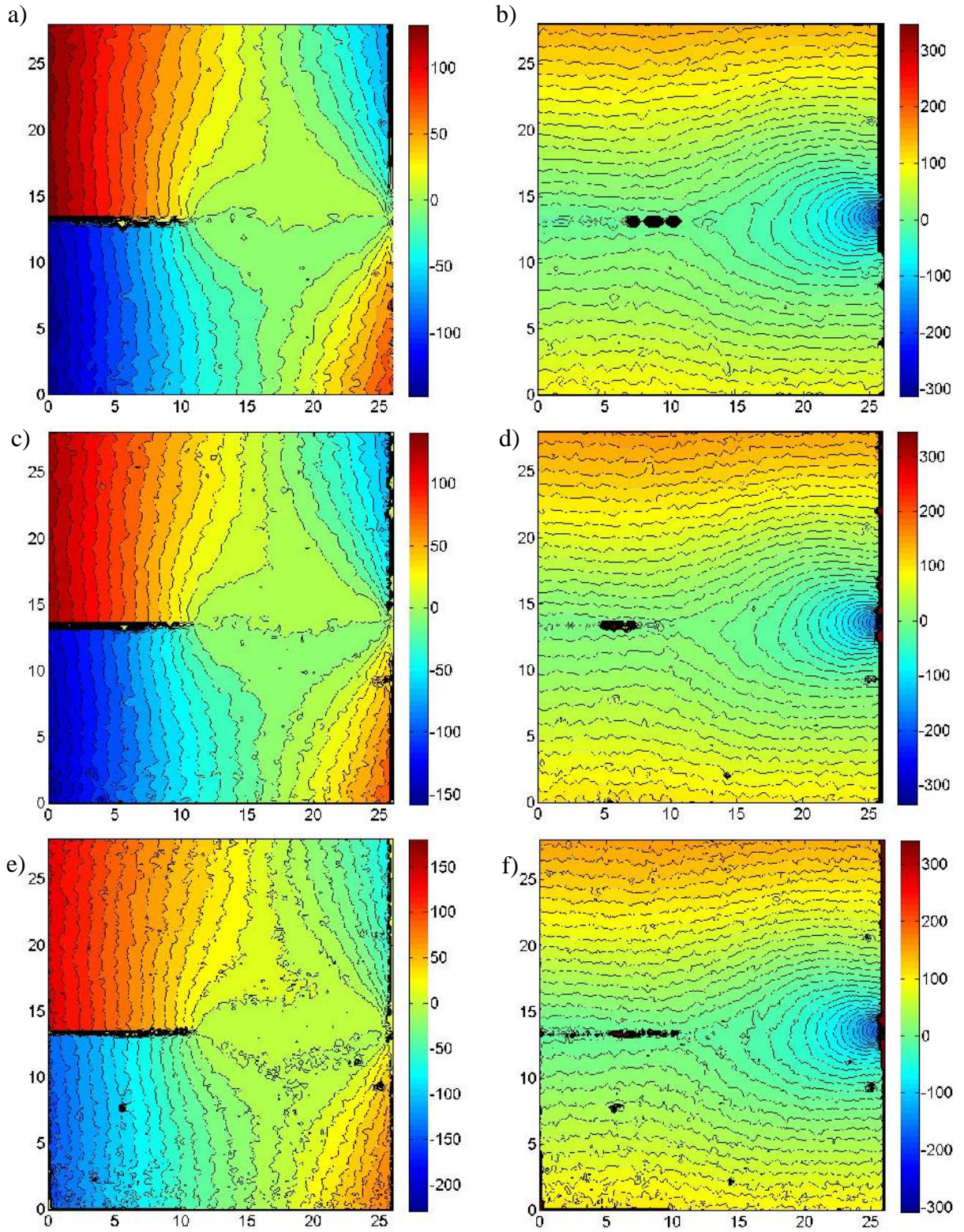


**Fig. 3.5:** Displacement contours for 15x15 pixel sub-images with no overlap (a, b), 5 pixel overlap (c, d), and 10 pixel overlap (e, f).



Because displacement data for determining SIFs is only considered from a relatively small region of interest behind the crack tip (Fig. 2.10), the selected sub-image size was 15 x 15 pixels due to the inherent tradeoff between data loss, averaging effect, and noise. Note also that the least squares method used to determine a single pair of SIFs ( $K_I^d$  and  $K_{II}^d$ ) from each pair of images involves hundreds of data points interpolated from within this region of interest behind the crack tip, which results in further averaging.

Pixel overlap during DIC was also investigated. Fig. 3.5 shows crack tip displacement contours when non-overlapping 15 x 15 pixel sub-images were used for DIC (Fig. 3.5a and 3.5b: 65 x 61 matrices of displacements), when 15 x 15 pixel sub-images were overlapped by 5 pixels (Fig. 3.4c and 3.4d: 97 x 92 matrices of displacements), and when 15 x 15 pixel sub-images were overlapped by 10 pixels (Fig. 3.4e and 3.4f: 195 x 185 matrices of displacements). Increased image overlapping led to increased noise, such that the final sub-image size chosen for this study was 15 x 15 pixel non-overlapping sub-images.

The isotropic stress intensity factors (SIFs) were determined for each image prior to crack initiation using a least squares method and the asymptotic expressions for displacements (determined by DIC as detailed in Section 2.3):

$$\begin{aligned}
u(r, \theta) &= \sum_{n=1}^{\infty} \frac{(K_I)_n}{2\sqrt{2f}} \frac{r^{n/2}}{\sqrt{2f}} \left\{ \left| \cos \frac{n}{2} \theta - \frac{n}{2} \cos \left( \frac{n}{2} - 2 \right) \theta + \left\{ \frac{n}{2} + (-1)^n \right\} \cos \frac{n}{2} \theta \right\} \right. \\
&\quad \left. + \sum_{n=1}^{\infty} \frac{(K_{II})_n}{2\sqrt{2f}} \frac{r^{n/2}}{\sqrt{2f}} \left\{ \left| \sin \frac{n}{2} \theta - \frac{n}{2} \sin \left( \frac{n}{2} - 2 \right) \theta + \left\{ \frac{n}{2} - (-1)^n \right\} \sin \frac{n}{2} \theta \right\} \right\}, \\
v(r, \theta) &= \sum_{n=1}^{\infty} \frac{(K_I)_n}{2\sqrt{2f}} \frac{r^{n/2}}{\sqrt{2f}} \left\{ \left| \sin \frac{n}{2} \theta + \frac{n}{2} \sin \left( \frac{n}{2} - 2 \right) \theta - \left\{ \frac{n}{2} + (-1)^n \right\} \sin \frac{n}{2} \theta \right\} \right. \\
&\quad \left. + \sum_{n=1}^{\infty} \frac{(K_{II})_n}{2\sqrt{2f}} \frac{r^{n/2}}{\sqrt{2f}} \left\{ - \left| \cos \frac{n}{2} \theta - \frac{n}{2} \cos \left( \frac{n}{2} - 2 \right) \theta + \left\{ \frac{n}{2} - (-1)^n \right\} \cos \frac{n}{2} \theta \right\} \right\},
\end{aligned} \tag{3.2}$$

in the region of interest (Fig. 2.10). Here  $r$  and  $\theta$  are the polar coordinates with origin at the crack tip,  $(K_I)_1$  is the SIF associated with mode-I fracture,  $(K_{II})_1$  is the SIF associated with mode-II fracture,  $\mu$  is the shear modulus,  $\nu$  is the Poisson's ratio, and  $\lambda = (3 - 2\nu)/(1 + \nu)$  for plane stress. Because  $K_I$  is most closely associated with opening displacements and  $K_{II}$  with sliding displacements, least squares solutions for  $K_I$  were recorded from the  $v$  field, and  $K_{II}$  values were determined from the  $u$  field. Similarly, the crack tip deformations described by Nishioka and Atluri's [98] equations were employed for finding SIFs for the growing crack:

$$\begin{aligned}
u(r, \theta) = & \sum_{n=1}^{\infty} \frac{(K_I)_n B_I(c)}{2\mu} \sqrt{\frac{2}{f}} (n+1) \left\{ r_1^{n/2} \cos \frac{n}{2} \theta_1 - h(n) r_2^{n/2} \cos \frac{n}{2} \theta_2 \right\} \\
& + \sum_{n=1}^{\infty} \frac{(K_{II})_n B_{II}(c)}{2\mu} \sqrt{\frac{2}{f}} (n+1) \left\{ r_1^{n/2} \sin \frac{n}{2} \theta_1 - h(\bar{n}) r_2^{n/2} \sin \frac{n}{2} \theta_2 \right\}, \\
v(r, \theta) = & \sum_{n=1}^{\infty} \frac{(K_I)_n B_I(c)}{2\mu} \sqrt{\frac{2}{f}} (n+1) \left\{ -S_1 r_1^{n/2} \sin \frac{n}{2} \theta_1 - \frac{h(n)}{S_2} r_2^{n/2} \sin \frac{n}{2} \theta_2 \right\} \\
& + \sum_{n=1}^{\infty} \frac{(K_{II})_n B_{II}(c)}{2\mu} \sqrt{\frac{2}{f}} (n+1) \left\{ S_1 r_1^{n/2} \cos \frac{n}{2} \theta_1 + \frac{h(\bar{n})}{S_2} r_2^{n/2} \cos \frac{n}{2} \theta_2 \right\},
\end{aligned} \tag{3.3}$$

where:

$$r_m = \sqrt{x^2 + S_m^2 y^2}, \quad \theta_m = \tan^{-1}(S_m y / x), \quad m=1,2, \quad S_1 = \sqrt{1 - (c/c_L)^2}, \quad S_2 = \sqrt{1 - (c/c_S)^2},$$

$$h(n) = \begin{cases} 2S_1 S_2 / (1 + S_2^2): & n \text{ odd} \\ (1 + S_2^2) / 2: & n \text{ even} \end{cases} \quad \text{and} \quad h(\bar{n}) = h(n+1),$$

$$c_L = \sqrt{\frac{(1+\nu)\mu}{(1-\nu)\dots}}, \quad c_S = \sqrt{\frac{\mu}{\dots}}, \quad \lambda = \begin{cases} (3-2\nu)/(1+\nu): & \text{plane stress} \\ (3-4\nu): & \text{plane strain} \end{cases},$$

$$B_I(c) = \frac{(1+S_2^2)}{D}, \quad B_{II}(c) = \frac{2S_2}{D}, \quad D = 4S_1 S_2 - (1+S_2^2)^2.$$

(3.4)

In the above,  $c_L$  is the longitudinal wave speed,  $c_S$  is the shear wave speed,  $c$  is the velocity of the crack,  $\rho$  is the mass density, and  $x$  and  $y$  are the Cartesian coordinates with  $x$  aligned with the crack. The crack initiation SIF ( $K_{I-ini}^d$ ) was determined to be the SIF value for last image before crack growth was observed. In both quasi-static and dynamic cases, least squares analysis was performed incorporating the above equations with the first and second terms of the expansion. The SIFs were associated with the  $n=1$  term ( $(K_I)_1$  and  $(K_{II})_1$ ), and the  $n=2$  term accounted for rotation of the field ( $(K_I)_2$  and  $(K_{II})_2$ ).

### 3.2.3 Ultrasonic Determination of Elastic Constants: Isotropic Materials

In order to solve the displacement field equations for  $K_I$  and  $K_{II}$ , the elastic constants must be known. Because the focus of this work is on dynamic fracture measurements, all elastic constants have been determined ultrasonically using an OLYMPUS Epoch 600 flaw detector. Isotropic elastic constants were determined in pulse-echo mode. Material wave speeds were determined by dividing twice the sample thickness by the time-of-flight measured for the ultrasonic wave to pass through the material and return back to the transducer. The following equations were used to determine the elastic properties from the measured longitudinal and shear wave speeds:

$$c_L = \sqrt{\frac{E(1-\nu)}{2\rho(1+\nu)(1-2\nu)}}, \quad c_S = \sqrt{\frac{E}{2\rho(1+\nu)}} \quad (3.5)$$

The various material properties used in the FEA simulation and experimental analysis are given in Table 3.1.

Material Property	PMMA	Bone Cement	Al 7075 T6
$E$ (GPa)	6.16	5.99	71.7
$\nu$	0.32	0.31	0.30
$G$ (GPa)	2.33	2.29	27.6
$\rho$ (kg/m <sup>3</sup> )	1160	1180	2730
$c_L$ (m/s)	2430	2370	5370
$c_S$ (m/s)	1420	1390	3180

**Table 3.1:** Material properties used in the computational and experimental analyses.

### 3.2.4 Finite Element Analysis

The use of relatively small samples, the resulting complex stress wave reflections and the SIF estimation scheme based on a few terms of the asymptotic expansion field, all demanded an independent SIF evaluation scheme to enhance the confidence level of measurements in the pre- and post-initiation regime. Accordingly, complementary finite element analyses (FEA) were carried out to supplement experimental results prior to crack initiation. A 3D, transient, elasto-dynamic, finite element model using ABAQUS®/Explicit software was developed. The model included the specimen and the long-bar (Fig. 3.6) in order to ensure that the stress wave propagating into the specimen was captured as accurately as possible. The model consisted of 160,000 linear, fully integrated, tetrahedral elements with highly refined elements of size 0.1 mm in the impact and crack tip vicinities. The model had a total of 100,000 degrees of freedom. The particle velocity ( $V_{pl}$ ) in the long-bar was determined from the measured strain history on the long-bar using:

$$V_{pl} = c_l V_I \quad (3.6)$$

and was subsequently input at the far right flat surface of the long-bar (Fig. 3.7). (In the above subscript  $I$  denotes ‘incident,’  $c_I$  the bar wave speed and  $v_I$  the measured strain on the long-bar.) After propagating along the long-bar, the stress waves were transmitted into the specimen using a frictionless contact definition for the semi-circular region of the long-bar that is initially in contact with the flat edge of the specimen. The time increments automatically chosen during computations by the software were approximately 10 ns.

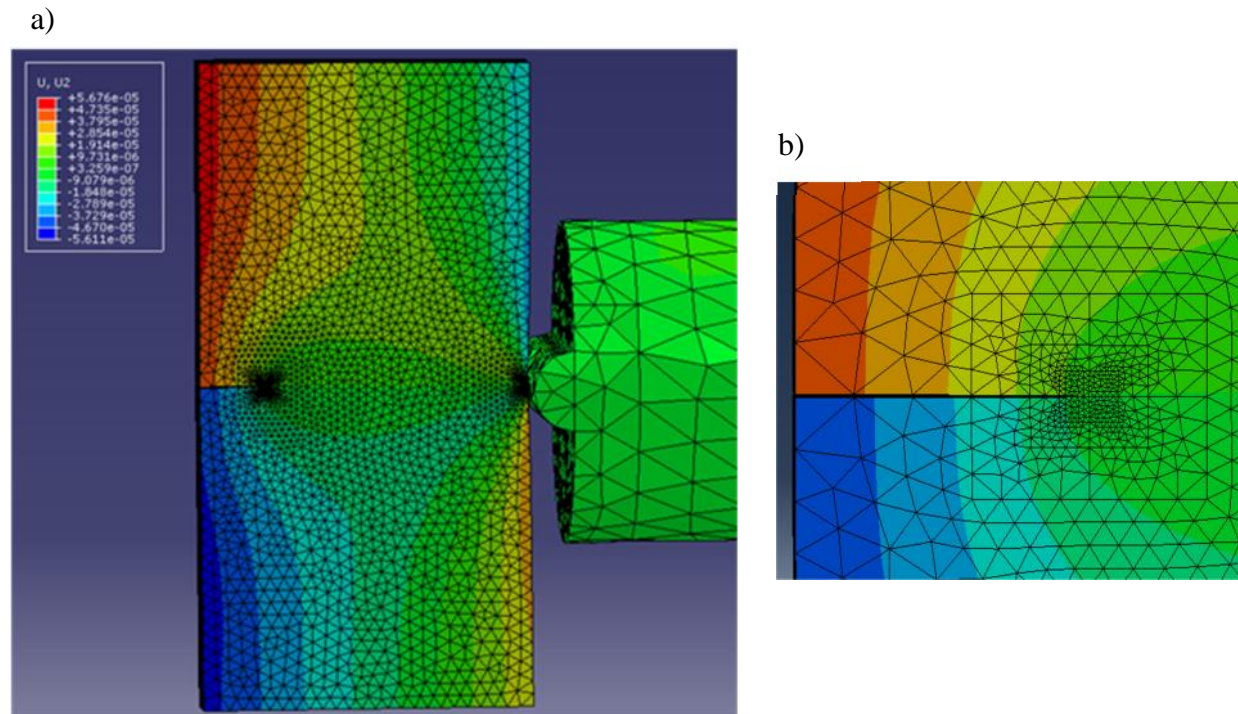


**Fig. 3.6:** a) Finite element model with corresponding crack opening displacement contours shown on the specimen, along with the far left end of the long-bar. b) A fine mesh is used near the impact site to ensure that contact and crack tip deformation responses are captured accurately. The field corresponds to a time instant 35  $\mu$ s after impact.

SIFs were computed from FEA results using a regression analysis of crack flank displacements. Apparent stress intensity factors ( $\bar{K}_I$ ) were calculated using crack opening displacements ( $\delta_y$ ) near the crack tip according to:

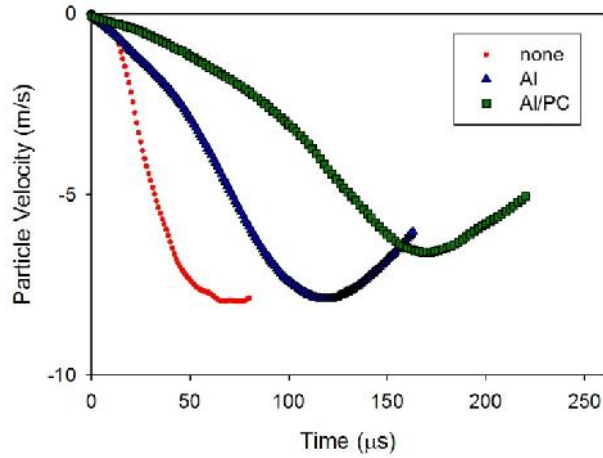


**Fig. 3.7:** Particle velocity input for FEA for each of three different loading rates at 15 psi. Particle velocity is independent of sample material properties.

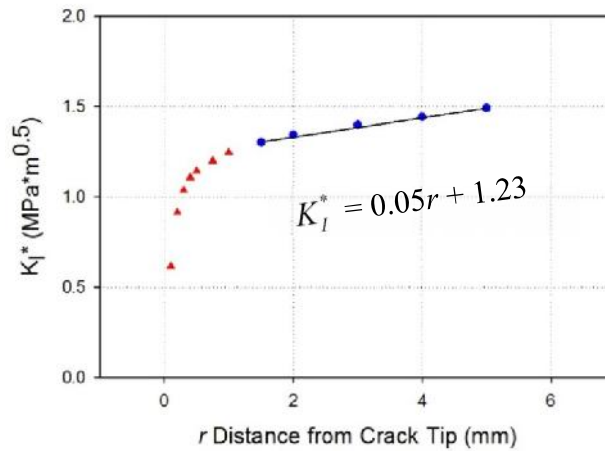


**Fig. 3.8:** Stress intensity factors are determined for each time increment of the FEA simulation by first finding the crack opening displacements for a series of nodes along the upper crack lip in Fig. 3.6.  $K_I^*$  values are calculated using Eq. 3.7, where  $r$  is the distance from the crack tip and  $u_y$  is the crack opening displacement associated with each node. The y-intercept of the best fit curve of the asymptote (away from the singularity caused by the crack tip) indicates the actual mode-I stress intensity factor ( $K_I$ ) for that time step.

$$u_y \Big|_{r=\pm f, r \rightarrow 0} = \frac{8K_I^*}{E} \sqrt{\frac{r}{2f}}. \quad (3.7)$$

The linear regions of  $K_I^*$  vs.  $r$  plots were then extrapolated to the crack tip to obtain instantaneous SIFs as  $K_I = \lim_{r \rightarrow 0} K_I^*$  [99] (see Fig. 3.8).

In order to ensure proper mesh size, the convergence of the FEA model shown in Fig. 3.6 was compared to two models with decreased mesh density (Fig. 3.9). The “Coarse Mesh” has specimen nodes every 4 mm in the unrefined region, the “Fine Mesh” has specimen nodes every 2 mm, and the “Finer Mesh” (given in Fig. 3.6) has specimen nodes every 1 mm. In Fig. 3.9a, the corresponding SIF histories are in good agreement when aligned according to the experimentally-determined dynamic crack initiation toughness for PMMA of  $2.44 \text{ MPa}\sqrt{\text{m}}$ . However, when the same SIF histories are aligned according to time of impact (Fig. 3.9b), convergence is demonstrated with increasing mesh density.

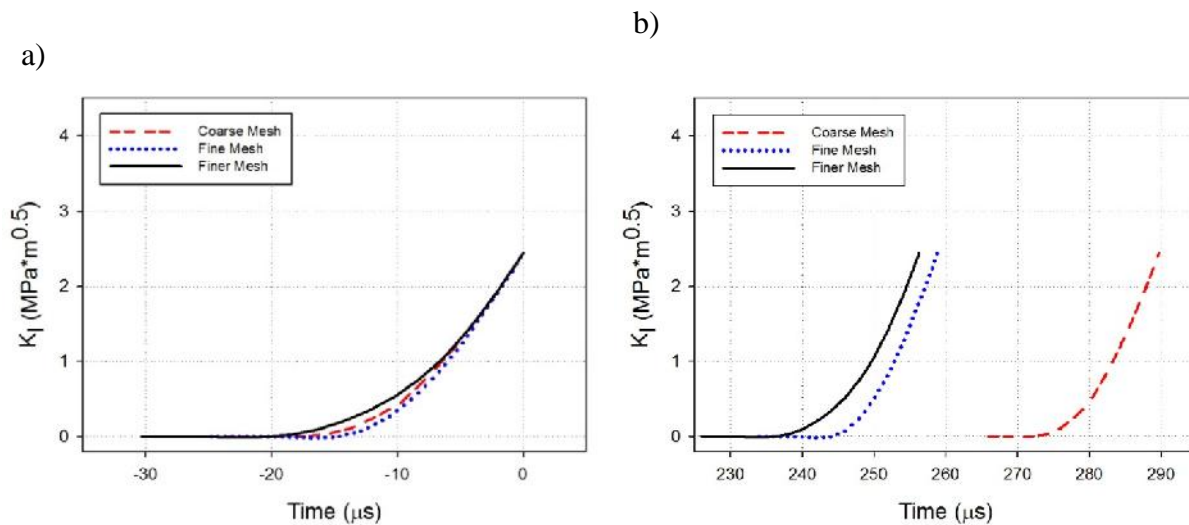


**Fig. 3.9:** SIF histories for three different FEA mesh densities: Coarse (4 mm node spacing), Fine (2 mm node spacing) and Finer (1 mm node spacing). FEA models are in good agreement a) when they are aligned according to crack initiation, whereas convergence is demonstrated when b) they are aligned according to time of impact.

### 3.3 Results

#### 3.3.1 Quasi-Static Results

A pair of load vs. load-point deflection responses for PMMA and bone cement specimens is shown in Fig. 3.10. As noted earlier, the peak load values were used in Eq. 3.1 for determining the quasi-static crack initiation SIF  $K_{IC}$ . The results did not show significant difference in quasi-static crack initiation SIF between PMMA and BC.  $K_{IC}$  was found to be  $1.32 \pm 0.17 \text{ MPa}\sqrt{\text{m}}$  for PMMA and  $1.34 \pm 0.06 \text{ MPa}\sqrt{\text{m}}$  for BC. In Fig. 3.10, PMMA response is linear prior to crack initiation before failing catastrophically. On the other hand, BC samples show modest nonlinearity prior to initiation, and the load drop during growth is slightly more gradual.

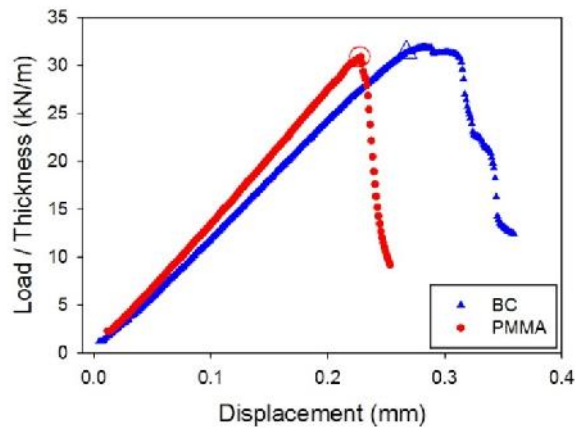


**Fig. 3.10:** Quasi-static load vs. displacement curves for PMMA and bone cement. Loads have been normalized by specimen thickness. Peak loads are similar, but BC fracture is relatively less catastrophic than PMMA.

#### 3.3.2 Dynamic Results

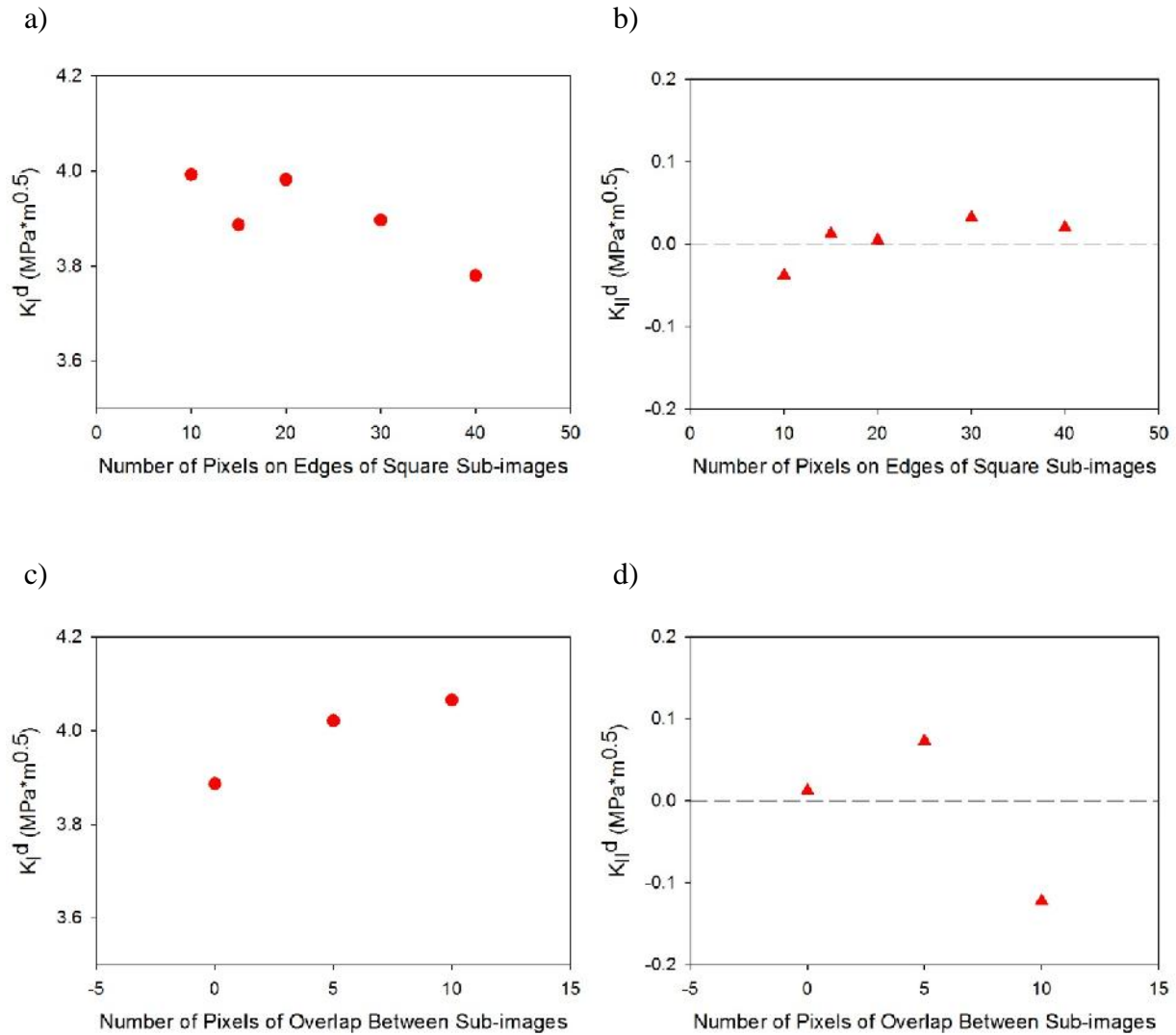
Fig. 3.11 gives the dynamic SIFs ( $K_I^d$ ,  $K_{II}^d$ ) corresponding to the sub-image size study presented in Section 3.2.2 (Figs. 3.3 – 3.5). Fig. 3.11a gives the variation in  $K_I^d$  using non-



overlapping sub-images of size 10 x 10, 15 x 15, 20 x 20, 30 x 30, and 40 x 40 pixels, whereas Fig. 3.11b gives the variation in  $K_{II}^d$  with the same variation in sub-image size. There is very little change in  $K_I^d$  or  $K_{II}^d$  with sub-image size; however, it should be noted that crack tip locations could not be accurately identified for the larger sub-images (30 x 30 and 40 x 40 pixels) using the  $v$  matrix and instead were approximated based on the contour plots of displacements. Note that the crack tip is typically identified as the location in the  $v$  matrix where the difference between top and bottom crack lip displacements decreases to less than four  $\mu\text{m}$ . Note also that SIFs determined from the displacement fields given in Figs. 3.3 – 3.5 are dependent on the crack tip location, which is a source of error in this sub-image size study.

Fig. 3.11c gives the variation in  $K_I^d$  using sub-images of size 15 x 15 pixels that overlap by 0, 5, and 10 pixels, whereas Fig. 3.11d gives the variation in  $K_{II}^d$  with the same variation in sub-image overlap. Again, there is no significant change in  $K_I^d$  values. Unlike Fig. 3.11b, Fig. 3.11d indicates increasing  $K_{II}^d$  values as the amount of sub-image overlap increases. This is likely due to the increase in noise as seen in Fig. 3.5 with increasing sub-image overlap. However,  $K_{II}^d$  values remain relatively small (less than  $0.1 \text{ MPa}\sqrt{m}$ ) compared to  $K_I^d$  values. This was typical of all dynamic mode-I fracture experiments, where  $K_{II}$  values rarely exceeded  $0.3 \text{ MPa}\sqrt{m}$ .

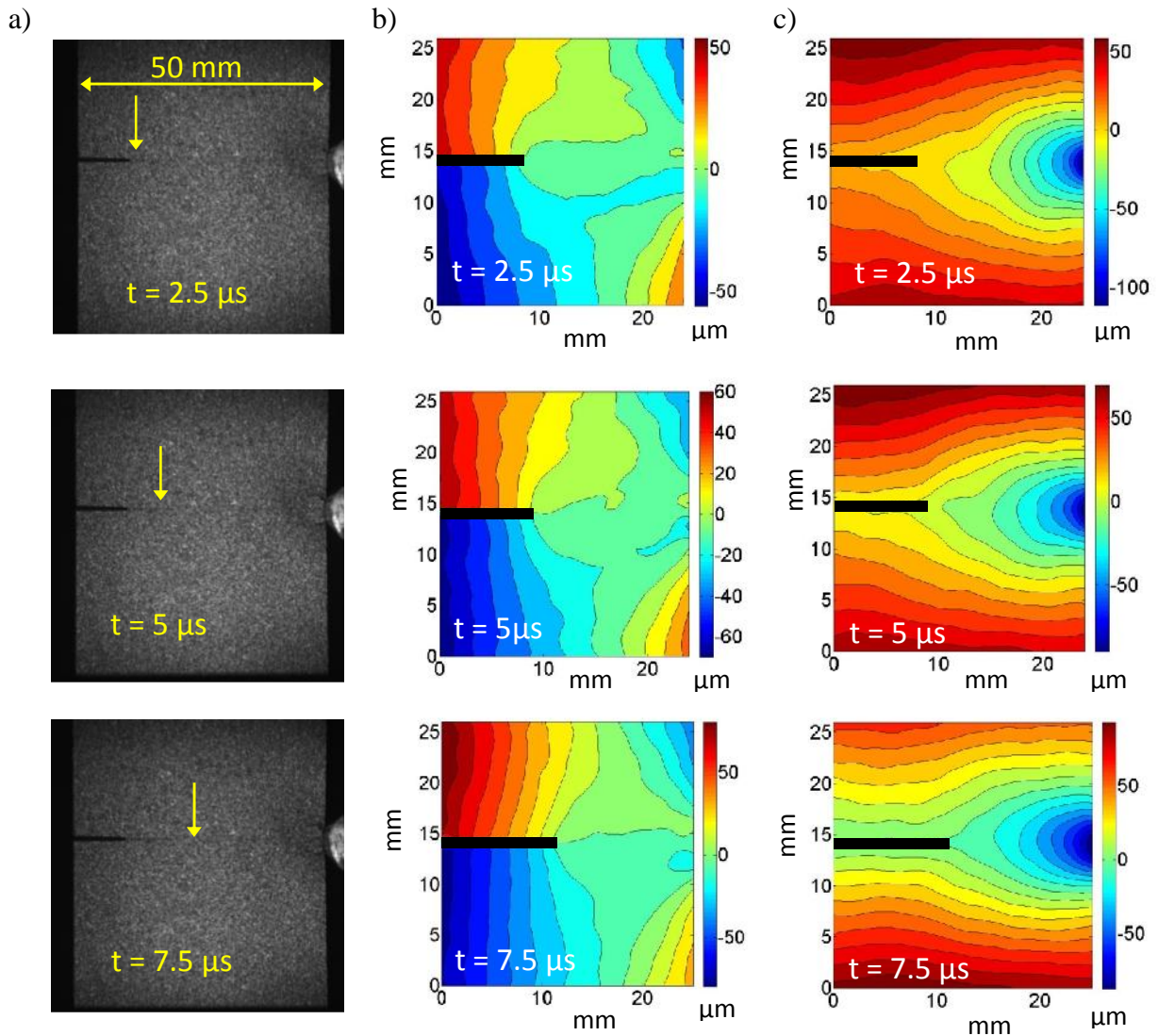
Sample contour plots based of the  $v$  and  $u$  displacement matrices from DIC are shown in Fig. 3.12b and 3.12c, respectively, corresponding to the deformed images in Fig. 3.12a. Time  $t$  in the images is time after crack initiation. The crack moves from left to right in all images, and the contour density continues to increase with time as well. (Contour interval is 10  $\mu\text{m}$ .)



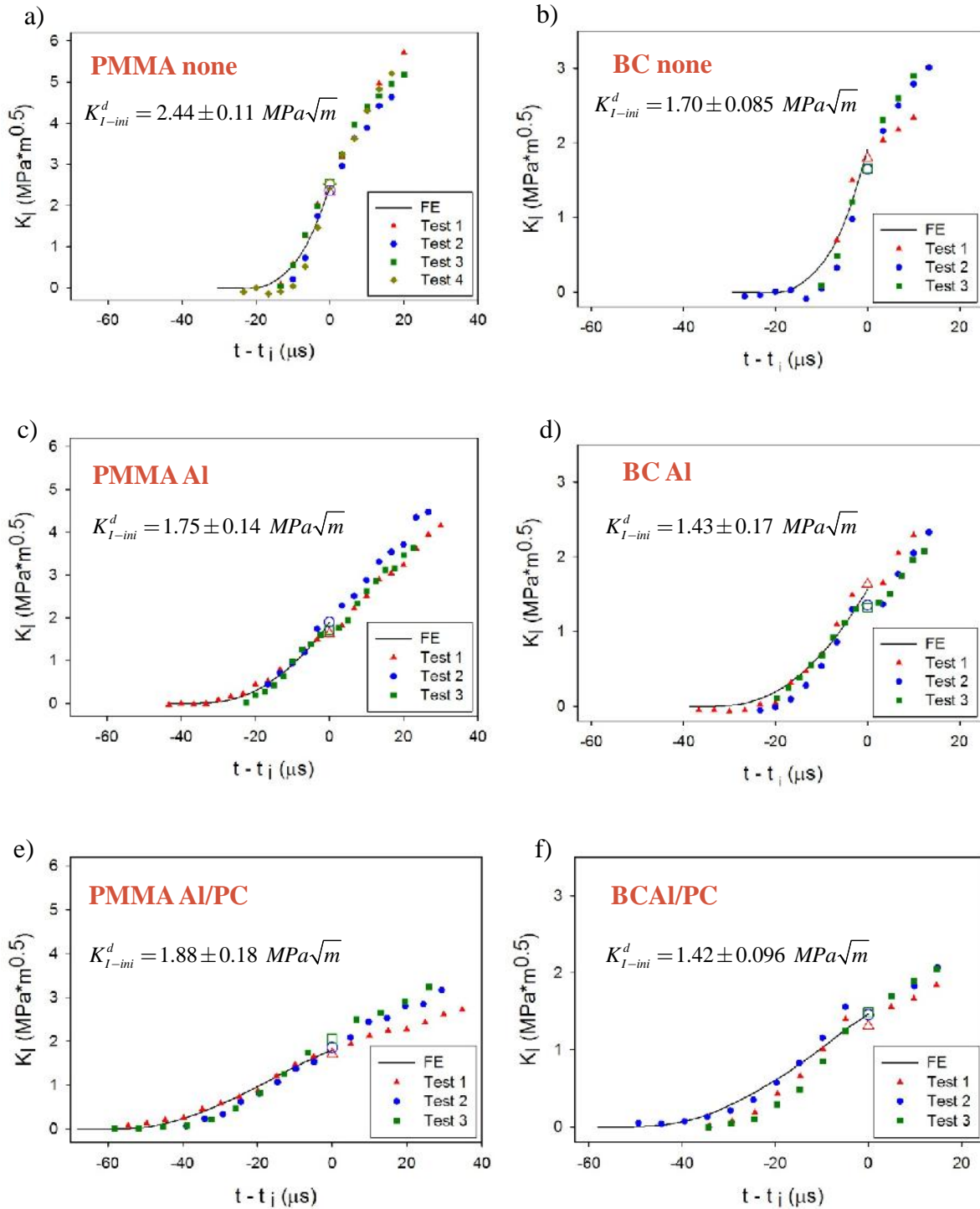
**Fig. 3.11:** SIFs corresponding to the displacement fields given in Fig. 3.3 – 3.5. a) and b) give the  $K_I^d$  and  $K_{II}^d$  values when sub-image size is varied. c) and d) give the  $K_I^d$  and  $K_{II}^d$  values when sub-images of size 15 x 15 pixels are overlapped by 0, 5, and 10 pixels.

Fig. 3.13 shows SIF histories for PMMA and bone cement (BC), along with those from FEA simulations prior to crack initiation. Data from at least three test specimens for each material type are presented in these plots. Given the highly transient nature of crack growth, remarkable consistency in dynamic SIF histories is evident. In each of these graphs, solid

symbols are used to denote pre- and post-initiation values, whereas the values corresponding to crack initiation are denoted by enlarged open symbols.



**Fig. 3.12:** Images recorded of a crack growing in bone cement using an Al pulse shaper at 2.5, 5, and 7.5  $\mu\text{s}$  after initiation. Corresponding crack opening b) and sliding c) displacement fields are shown. Contour interval is 10  $\mu\text{m}$ . Magnification is 30  $\mu\text{m}/\text{pixel}$ . Symmetry of sliding displacements indicates mode-I dominant fracture. Arrows indicate crack tip location.



**Fig. 3.13:** SIF histories for a) PMMA with no pulse shaper, b) PMMA with Al pulse shaper, c) PMMA with Al/PC sandwich pulse shaper, d) BC with no pulse shaper, e) BC with Al pulse shaper, f) BC with Al/PC sandwich pulse shaper. Curves have been aligned according to time of crack initiation ( $t_i$ ). (Note: The scale used is consistent for a material type but different for PMMA and BC.)

As to be expected, the pre-initiation slope of  $K_I$  vs.  $t$  plot increases with increasing loading rate, regardless of the material being tested. This portion of the SIF histories prior to initiation closely resembles the shape of the corresponding stress wave input from Fig. 2.7b. Immediately after initiation, a dip occurs for the Al pulse shaper (medium loading rate: 10.7 strains/second) and Al/PC pulse shaper (low loading rate: 3.7 strains/second) tests, while the SIFs for the highest loading rate tests (without any pulse shaper: 42.0 strains/second) continue to increase significantly. For the remaining portion of the SIF histories,  $K_I^d$  values increase monotonically for every test type. For this region, the slopes of dynamic stress intensity factors  $K_I^d$  vs.  $t$  increase significantly with increasing loading rate for both material types, even though there was little difference in crack initiation SIF ( $K_{I-ini}^d$ ) between the two lower loading rate groups. In all the cases presented in Fig. 3.13, the finite element simulations capture the overall behavior rather well up to crack initiation. Because crack growth criteria were not included in the computational model, the numerical data was plotted up to initiation only.

It is important to note that, although tests involving the same loading rate have very similar shapes, the scales for PMMA and BC are not the same. (All tests of the same material share the same scale.) For each loading rate used, higher dynamic crack initiation SIF is seen in PMMA than the corresponding tests on BC. For both PMMA and BC, the high loading rate groups (no pulse shaper case) had significantly higher  $K_{I-ini}^d$  than the other two groups for the same material, although there was little difference in  $K_{I-ini}^d$  between the Al and Al/PC pulse shaper cases. In order to more easily visualize these comparisons, a representative plot from each of 6 testing groups is given in Fig. 3.14. Unlike Fig. 3.13, these plots are aligned according to time of impact rather than time of crack initiation.

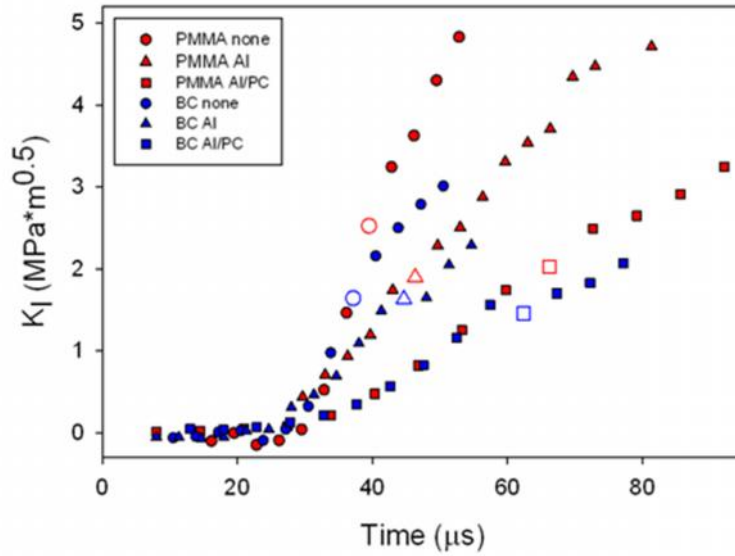


**Fig. 3.14:** Representative SIF histories from each of 6 testing groups from Fig. 3.13. Curves have been aligned according to time of impact rather than time of crack initiation as in Fig. 3.13.

All quasi-static and dynamic crack initiation SIFs are compiled in Table 3.2, along with the corresponding  $\dot{K}$  values representing the loading rate. The rate of change in SIF over time,  $\dot{K}$ , was determined experimentally for each type of pulse shaper using dynamic experimental results of PMMA just before crack initiation. All three dynamic  $\dot{K}$  values are more than 6 orders of magnitude greater than the quasi-static case. All dynamic crack initiation SIF values ( $K_{I-ini}^d$ ) are higher than the quasi-static crack initiation SIF values ( $K_{IC}$ ), but the difference is much more significant for PMMA than BC.

Fig. 3.15 shows velocity histories for the growing crack. A combination of high loading rates and relatively small samples produces fewer data points when compared to typical drop-tower tests [17]. The severity of transients also results in larger error bars since they are estimated via numerical differentiation of crack length data (back difference method). Within these limitations, the following observations can be made. For each loading rate, BC had significantly higher crack tip velocity than PMMA. Because BC crack tips were moving faster,

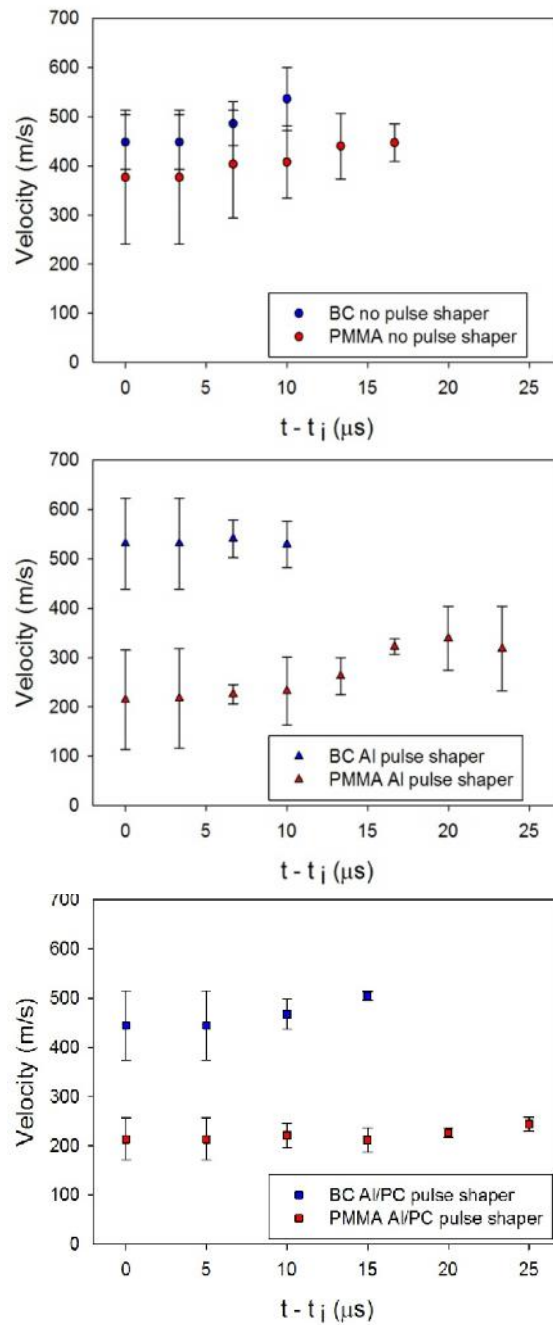


**Fig. 3.15:** The effect of material type on crack velocity is shown for a) no pulse shaper (high loading rate:  $42.0 \text{ second}^{-1}$ ), b) Al pulse shaper (medium loading rate:  $10.7 \text{ second}^{-1}$ ), and c) Al/PC pulse shaper (low loading rate:  $3.7 \text{ second}^{-1}$ ).  $t = 0$  corresponds to crack initiation. Error bars indicate one standard deviation relative to the average value.

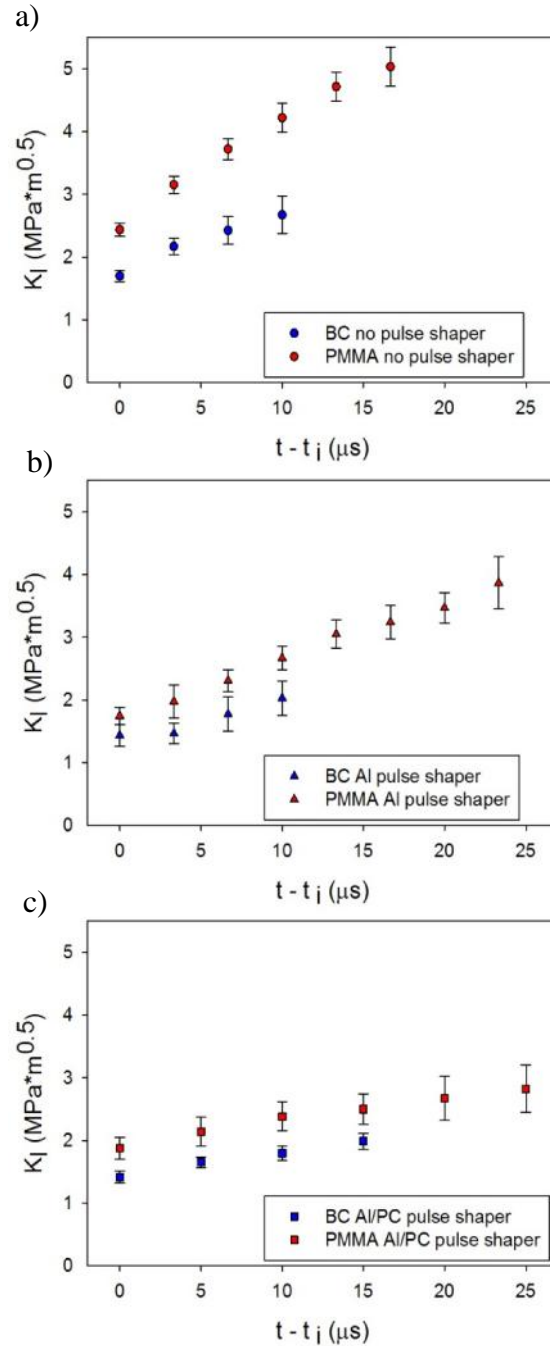


**Fig. 3.16:** The effect of material type on dynamic SIF is shown for a) no pulse shaper (high loading rate:  $42.0 \text{ second}^{-1}$ ), b) Al pulse shaper (medium loading rate:  $10.7 \text{ second}^{-1}$ ), and c) Al/PC pulse shaper (low loading rate:  $3.7 \text{ second}^{-1}$ ).  $t = 0$  corresponds to crack initiation. Error bars indicate one standard deviation relative to the average value.



the data was available for collection over a shorter duration. Further, there was little variation in crack speed for BC with loading rate; all crack tip velocities were around 500 m/s. In contrast, PMMA crack velocities generally increased with loading rate. Throughout the observation period, PMMA crack speeds were significantly higher for the highest loading rate compared to the other two rates. Both Al and Al/PC pulse shaper cases for PMMA initially have crack velocities around 200 m/s; however, velocity in the Al pulse shaper case increases steadily throughout the test to around 300m/s, while Al/PC pulse shaper case maintains fairly constant velocity, near 200 m/s.

Pulse Shaper	Average $\dot{K}$ ( $MPa\sqrt{m} s^{-1}$ )	Average PMMA $K_{IC} / K_{I-ini}^d$ ( $MPa\sqrt{m}$ )	Average BC $K_{IC} / K_{I-ini}^d$ ( $MPa\sqrt{m}$ )
None	$2.40 \times 10^5$	$2.44 \pm 0.11$	$1.70 \pm 0.09$
Al	$0.98 \times 10^5$	$1.75 \pm 0.14$	$1.43 \pm 0.17$
Al/PC	$0.65 \times 10^5$	$1.88 \pm 0.18$	$1.42 \pm 0.10$
Quasi-static	$3.00 \times 10^{-2}$	$1.32 \pm 0.17$	$1.34 \pm 0.06$

**Table 3.2:** Compilation of crack initiation SIFs for PMMA and BC for each of the four loading rates.

Fig. 3.16 shows combined dynamic SIF history comparison for the growing crack in PMMA and BC. For each loading rate, PMMA had significantly higher  $K_I^d$  values than BC. Again, fewer post-initiation data points are available for BC due to higher crack velocity for all loading rates. As mentioned earlier, the rate of change of  $K_I^d$  (post-initiation) increases with loading rate for both material types. For BC, the highest loading rate group had significantly higher  $K_I^d$  values than the two lower loading rate groups, and there was no significant distinction between the two lower loading rate groups. For PMMA, the same trend continued as with crack

tip velocity. The highest loading rate group had significantly higher  $K_I^d$  values than the other two groups throughout the entire test period, while the medium loading rate group had similar values to the lower loading rate group initially, but eventually increased to well over  $3 \text{ MPa}\sqrt{\text{m}}$ .

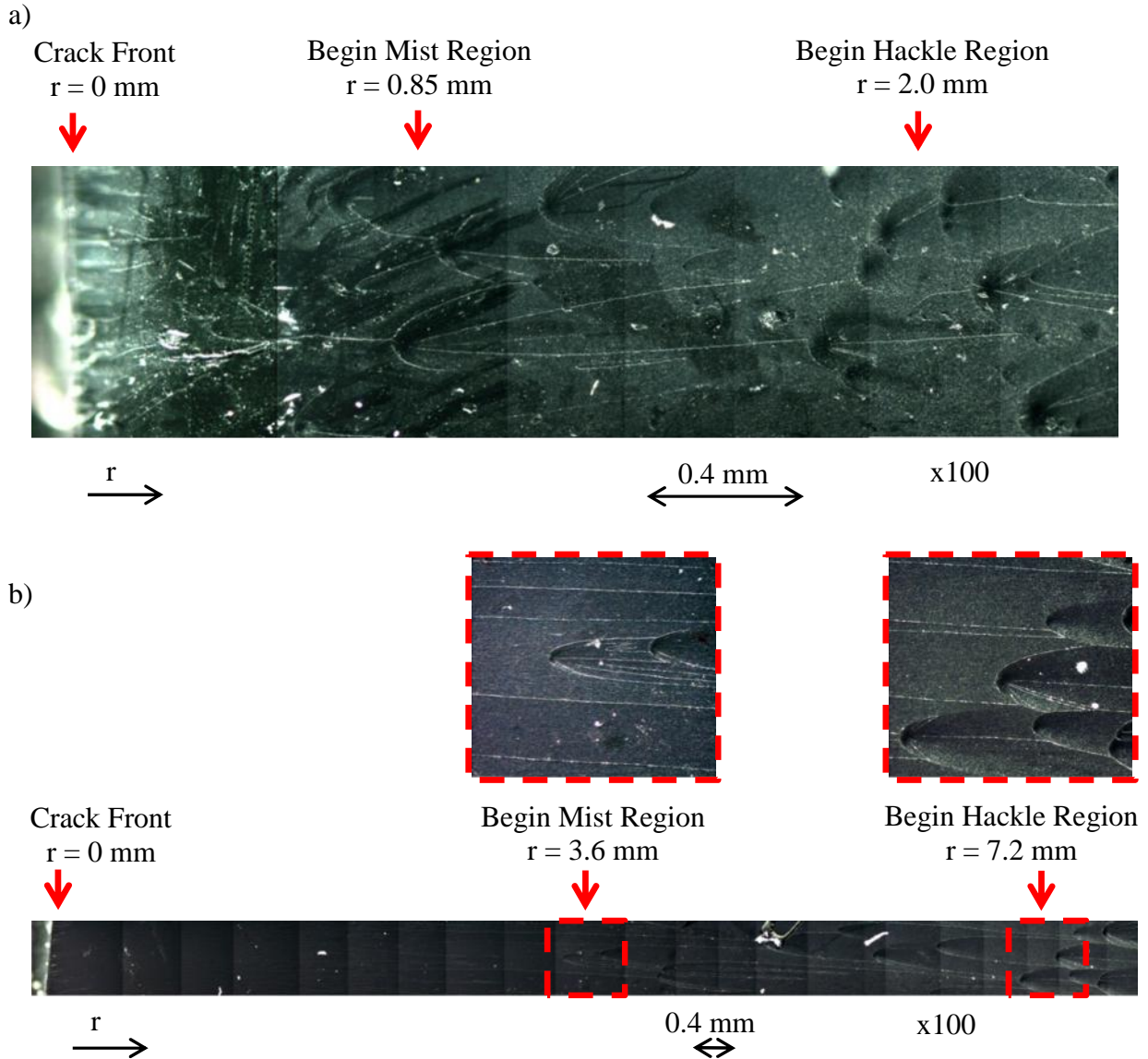


**Fig. 3.17:** Micrographs of PMMA fracture surfaces: a) no pulse shaper and b) Al/PC pulse shaper. Arrows indicate the beginning of common fracture surface regions. Increasing distance  $r$  is related to decreased resistance to crack growth.

To further examine the relative strain rate effects on PMMA and BC, fractographic examination of failed specimens was undertaken. Micrographs of the fracture surfaces are shown in Fig. 3.17 for PMMA and Fig. 3.18 for BC. (Several optical micrographs were imaged and stitched to produce Fig. 3.17 and hence the contrast jumps along the crack growth direction periodically.) Typical mirror, mist and hackle regions were observed on PMMA fracture surfaces. Parabolic features first appear in the mist region. The pattern becomes increasingly dense with increasing resistance to crack growth until the hackle region, where parabolas overlap indicating maximum surface roughness [100]. Because the specimen in Fig. 3.17a experiences a much higher loading rate than in Fig. 3.17b, these features occur much closer to the original crack front. This trend continues in Table 3.3 for all three loading rates. The distance  $r$  from the original crack front to these key surface features increases with decreasing loading rate.

Pulse Shaper	None	Al	Al/PC
Mist	0.58 mm	1.7 mm	2.2 mm
Hackle	1.2 mm	2.9 mm	5.5 mm

**Table 3.3:** Average distance ( $r$ ) from the original crack front to fracture regions for each loading rate.  $r$  increases with decreasing loading rate.

In contrast, scanning electron microscopy (SEM) of gold-coated bone cement (Fig. 3.18) does not show these parabolic features. Instead, these images indicate that the crack bypassed pre-polymerized beads. That is, fracture occurred either within the interbead matrix or along the interfaces of the two phases. Thus both images indicate higher roughness of the fracture surface than PMMA. Roughness is again higher for the higher loading rate image (Fig. 3.18a). Note that all SEM was performed on a JEOL JSM-7000F (Fig. 3.19).

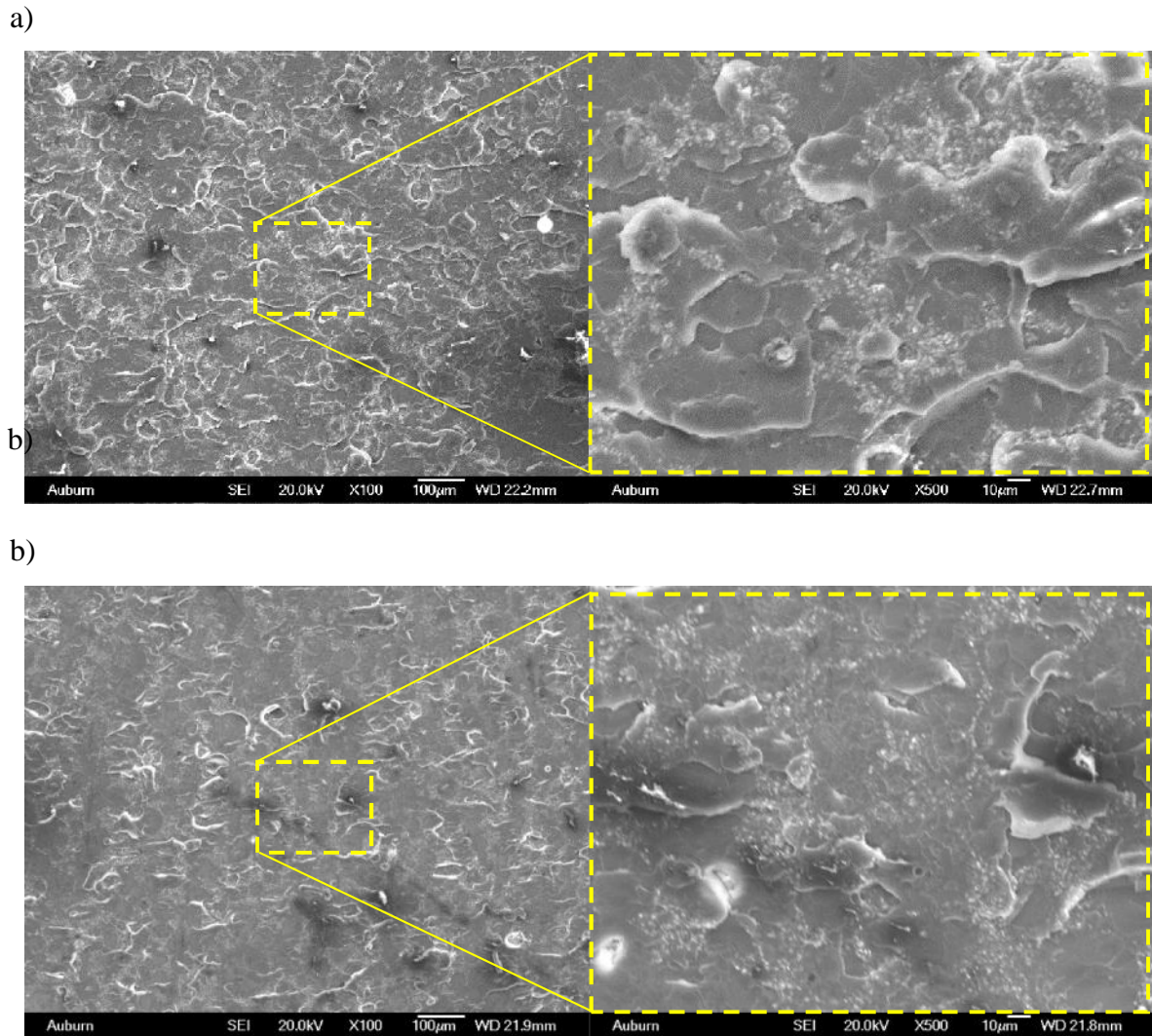


**Fig. 3.18:** SEM micrographs of fractured BC samples: a) no pulse shaper (100x and 500x) and b) Al/PC pulse shaper (100x and 500x). Higher roughness is shown for the higher loading rate in a), and both images exhibit more roughness than PMMA (Fig. 3.17). Images were captured at a distance of ~5mm from crack front.



**Fig. 3.19:** JEOL JSM-7000F used to generate SEM images.

### 3.4 Discussion

A methodology to perform high strain rate fracture tests on relatively small size specimens made of bone cement has been presented. It involves full-field measurement of displacements near a propagating crack using DIC and high-speed photography. The approach is capable of measuring pre- and post-crack initiation response of materials subjected to transient loading using a long-bar and gas-gun apparatus. Potential applications of the methodology include

understanding dynamic fracture mechanics of cortical bone (Chapter 4), bone cement/bone interfaces, bone cement/implant interfaces, and other materials that are difficult to obtain in traditional sizes/geometries (such as carbon composites in Chapters 5 and 6).

Quasi-static crack initiation SIF  $K_{IC}$  for PMMA and bone cement ( $1.32 \pm 0.17$  and  $1.34 \pm 0.06 \text{ MPa}\sqrt{m}$ , respectively) showed good agreement with the results reported in the literature (Tables 1.1 and 1.2). Dynamic crack initiation SIFs ( $K_{I-ini}^d$ ) for PMMA ( $1.75 - 2.44 \text{ MPa}\sqrt{m}$ ) measured at  $\dot{K} = 6.5 - 24 \times 10^3 \text{ MPa}\sqrt{m} / \text{sec}$  is also within the range of values reported from previous tests (Table 1.2).

Both PMMA and BC show modest loading rate dependency, but the effect is much greater for PMMA. This is evidenced by the crack initiation SIFs reported in Table 3.2, as well as the crack velocity and post-initiation dynamic SIF histories in Fig. 3.15 and Fig. 3.16. PMMA exhibits much greater disparity for all these fracture data at initiation and after initiation than bone cement. Additionally, the microscopy of PMMA shows a clear change in surface morphology with an increase in loading rate, while there is little change for bone cement with the same increase in loading rate at the same magnification. These findings are likely due to the microscopic inhomogeneity of BC, shrinkage stresses along the interfaces of the two phases, and the non-bonding BaSO<sub>4</sub> inclusions within the interbead matrix of BC. While these results are not particularly encouraging for the usage of cemented implants in active patients where dynamic impact events are likely, further investigation with pure PMMA (without cross-linking agent) and with various types of bone cements is warranted.

In their fatigue failure studies, Baleani and Viceconti [29] found a 66% reduction in crack growth rate with the addition of 10% by weight BaSO<sub>4</sub> to the powder phase. They reasoned that this decrease in crack growth rate was due to cracks bypassing pre-polymerized PMMA beads

and instead propagating through the interbead matrix, which contained non-bonding BaSO<sub>4</sub> inclusions [29]. These BaSO<sub>4</sub> inclusions attracted the crack, turning it away from its original path. This increased the effective stress intensity factor and slowed the crack growth [29]. Similar behavior could also explain the nonlinearity of the load-deflection curve observed prior to initiation in the quasi-static tests of BC in this work, as well as the increased resistance to crack growth immediately after initiation (Fig. 3.10). In contrast, quasi-static load-deflection graphs for PMMA were linear until abrupt failure. However, in all of the dynamic cases, PMMA was superior in resisting crack growth (higher SIFs and lower crack velocities) despite much lower roughness than BC. This suggests that either the two phases of the BC were weakly bonded and allowed pre-polymerized beads to pull out of the interbead matrix, or the BaSO<sub>4</sub> non-bonding inclusions greatly weakened the interbead matrix and caused the crack to follow the interbead matrix at relatively high speeds.

## Chapter 4. Dynamic Fracture of Orthotropic Cortical Bone

In order to further demonstrate applications of the experimental methodology for characterizing the dynamic fracture of small specimens introduced in Chapter 2 and calibrated in Chapter 3, orthotropic cortical bone is investigated in this chapter. Displacement field equations for orthotropic materials are provided for determining stress intensity factors (SIFs) using in-plane displacements determined by DIC (Chapter 2). These displacement field equations also require orthotropic elastic property inputs, whose determination is described in this chapter.

### 4.1 Specimen Preparation

Fresh bovine metacarpals were obtained from the Lambert-Powell Meats Laboratory of Auburn University and frozen for about four years. Samples were gradually thawed, and soft

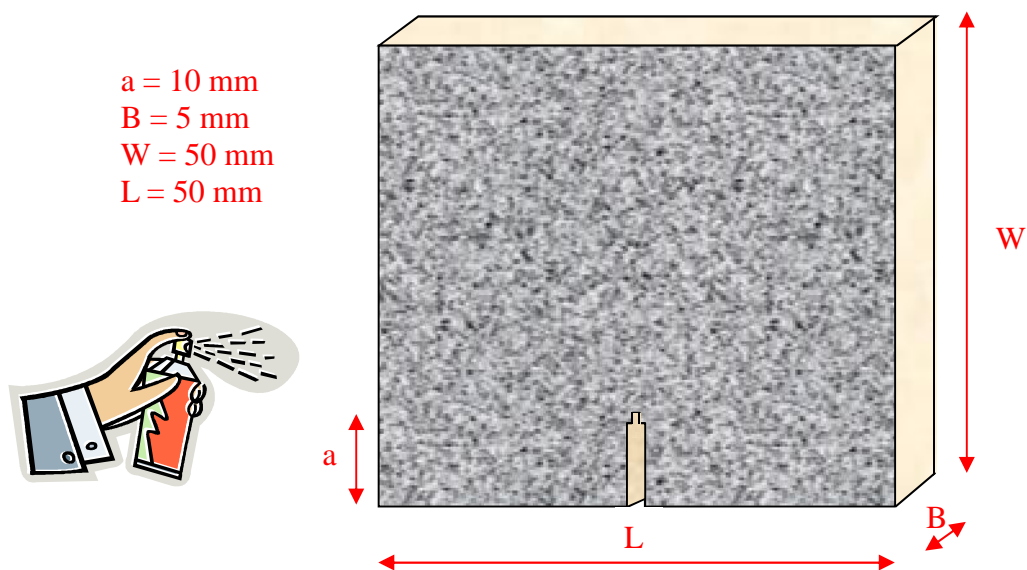


**Fig. 4.1:** Specimen geometry for dynamic fracture of bovine cortical bone.



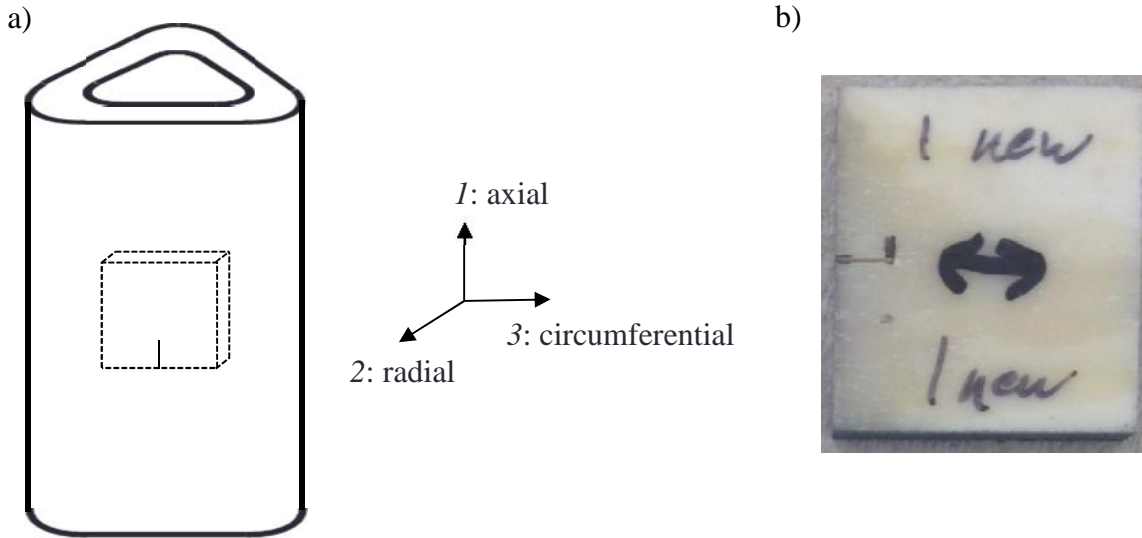


**Fig. 4.2:** a) Orientation of dynamic fracture specimens within bovine metacarpal for ultrasonic determination of orthotropic elastic constants. b) Photograph of a dried bovine cortical bone sample machined for axial dynamic fracture. Arrows indicate the axial direction, while “new” indicates that the sample was recently removed from the freezer for dynamic fracture testing.

tissue was removed at the Necropsy Laboratory of the Auburn University College of Veterinary Medicine. Specimens were machined to 30 mm x 30 mm x 5 mm dimensions (Fig. 4.1) from the posterior middle third of the metacarpals, as this was determined to be the largest plate-shaped geometry that could be achieved for the axial fracture of bovine cortical bone. Machined specimens were subsequently dried in order to be able to apply a speckle coating with spraypaint. Pre-notches were machined and sharpened with a razor blade, such that the cracks would propagate along the axial direction and open along the circumferential direction (Fig. 4.2). The samples needed to be thick enough (B) so that the sample would not suffer out-of-plane bending during loading. The sample needed to be wide enough (W) in the crack growth direction (axial direction) such that post-initiation images could be collected before the crack tip reached the compressive region near the point of impact and began to decelerate. Finally, the sample needed to be long enough (L) such that wave reflections from the free edges (left and right in Fig. 4.1)

would not interfere with crack initiation and propagation. Ideally, the sample would be longer in the L direction than in the W direction for this nearly isotropic material, but that would have severely limited all post-initiation SIF measurements. Thus the location and specimen size below were chosen. Fig. 4.3 shows three posterior halves of axially-sliced bovine metacarpals. Dynamic fracture specimens (Fig. 4.2b) were milled from the central portion.



**Fig. 4.3:** Posterior portion of bovine cortical bone after axial slicing. Dynamic fracture specimens (Fig. 4.4) were milled from the central region.

## 4.2 Experimental Details

### 4.2.1 Dynamic Fracture Tests

The methodology involving digital image correlation (DIC) and high-speed photography for determining the dynamic fracture properties of relatively small size specimens (detailed in

Chapter 2) was used to examine dynamic SIFs of bovine cortical bone using the highest dynamic loading rate (no pulse shaper- “none” Fig. 2.7). Due to the wide array of quasi-static  $K_{IC}$  values for cortical bone in the literature (Table 1.3) and very limited data on dynamic  $K_{I-III}^d$  (Table 1.4), this highest rate of loading was selected in order to ensure that pre-notched cortical bone specimens initiated and propagated during dynamic fracture testing.

The following orthotropic in-plane displacement field equations [101] were used to determine SIFs for all dynamically-loaded specimens prior to crack initiation:

$$\begin{aligned}
 u(r, \theta) &= K_I \sqrt{\frac{2r}{f}} \operatorname{Re} \left[ \frac{1}{\tilde{\nu}_2 - \tilde{\nu}_1} (p_1 \tilde{\nu}_2 z_1 - p_2 \tilde{\nu}_1 z_2) \right] + K_{II} \sqrt{\frac{2r}{f}} \operatorname{Re} \left[ \frac{1}{\tilde{\nu}_2 - \tilde{\nu}_1} (p_1 z_1 - p_2 z_2) \right] \\
 v(r, \theta) &= K_I \sqrt{\frac{2r}{f}} \operatorname{Re} \left[ \frac{1}{\tilde{\nu}_2 - \tilde{\nu}_1} (q_1 \tilde{\nu}_2 z_1 - q_2 \tilde{\nu}_1 z_2) \right] + K_{II} \sqrt{\frac{2r}{f}} \operatorname{Re} \left[ \frac{1}{\tilde{\nu}_2 - \tilde{\nu}_1} (q_1 z_1 - q_2 z_2) \right].
 \end{aligned} \tag{4.1}$$

For fracture of an orthotropic material with  $x$ - $z$  and  $y$ - $z$  planes as symmetry planes,  $\tilde{\nu}_j$  ( $j=1,2$ ) are the two roots of  $S_{11} \tilde{\nu}^4 + (2S_{13} + S_{55}) \tilde{\nu}^2 + S_{33} = 0$ ,

$$\begin{aligned}
 p_j &= \tilde{\nu}_j^2 S_{11} + S_{13}, \\
 q_j &= \tilde{\nu}_j S_{13} + \frac{S_{33}}{\tilde{\nu}_j}, \\
 z_j &= \sqrt{\cos \theta + \tilde{\nu}_j \sin \theta},
 \end{aligned} \tag{4.2}$$

In the above equations,  $K_I$  is the mode-I SIF,  $K_{II}$  is the mode-II SIF (which is expected to be near zero for this symmetric loading case), and  $u$  and  $v$  are the sliding and opening displacements.  $S_{11}$ ,  $S_{33}$ ,  $S_{13}$ , and  $S_{55}$  are coefficients of the compliance matrix; their ultrasonic determination will be described later in this chapter in Section 4.2.2. Knowing displacements in the crack tip vicinity from DIC measurements, an overdeterministic least-squares analysis was

used to determine a single  $K_I$  and  $K_{II}$  value for each pair of images recorded during the fracture event as described in Section 2.3. For consistency, the critical SIF ( $K_{IC}$  for quasi-static loading and  $K_{I-ini}^d$  for dynamic loading) was chosen to be the mode-I SIF value for the image immediately prior to visible crack initiation in the images. For the case of a dynamically but steadily growing crack, the orthotropic displacement field equations [102] are:

$$\begin{aligned}
u(r, \theta) &= \frac{2}{C_{55}R(c)} \operatorname{Re} \left[ \left( \frac{\tilde{z}_2 - \tilde{z}_1}{\tilde{y}_1 - \tilde{y}_2} \sqrt{\frac{z_1}{2f}} - \frac{\tilde{z}_1 - \tilde{z}_2}{\tilde{y}_1 - \tilde{y}_2} \sqrt{\frac{z_2}{2f}} \right) K_I^d - \left( \frac{x - \tilde{y}^2 \tilde{z}_2}{\tilde{y}_1 - \tilde{y}_2} \sqrt{\frac{z_1}{2f}} - \frac{x - \tilde{y}^2 \tilde{z}_1}{\tilde{y}_1 - \tilde{y}_2} \sqrt{\frac{z_2}{2f}} \right) K_{II}^d \right] \\
v(r, \theta) &= \frac{2}{C_{55}R(c)} \operatorname{Re} \left[ - \left( \frac{\tilde{z}_2 - \tilde{z}_1}{\tilde{y}_1 - \tilde{y}_2} \sqrt{\frac{z_1}{2f}} - \frac{\tilde{z}_1 - \tilde{z}_2}{\tilde{y}_1 - \tilde{y}_2} \sqrt{\frac{z_2}{2f}} \right) K_I^d + \left( \frac{x - \tilde{y}^2 \tilde{z}_2}{\tilde{y}_1 - \tilde{y}_2} \sqrt{\frac{z_1}{2f}} - \frac{x - \tilde{y}^2 \tilde{z}_1}{\tilde{y}_1 - \tilde{y}_2} \sqrt{\frac{z_2}{2f}} \right) K_{II}^d \right].
\end{aligned} \tag{4.3}$$

For fracture of an orthotropic material with  $x$ - $z$  and  $y$ - $z$  planes as symmetry planes,

$$\begin{aligned}
\tilde{z}_j (j=1,2) \text{ are the 2 roots of: } \tilde{z}^4 + \left( r_i^2(c)y^2 + \frac{r_s^2(c)}{y^2} - \frac{(1+x)^2}{y^2} \right) \tilde{z}^2 + \frac{r_i^2(c)r_s^2(c)}{\tilde{y}} &= 0, \\
\tilde{y} = \frac{S_{11}}{S_{33}}, \quad \tilde{y}' = \frac{2S_{13} + S_{55}}{2\sqrt{S_{11}S_{33}}}, \quad \tilde{y} = \frac{3\sqrt{S_{11}S_{33}} + S_{13}}{\sqrt{S_{11}S_{33}} - S_{13}}, \quad c_i = \sqrt{\frac{C_{11}}{\dots}}, \quad c_s = \sqrt{\frac{C_{55}}{\dots}}, \quad r_i^2(c) = 1 - \left( \frac{c}{c_i} \right)^2, \quad r_s^2(c) = 1 - \left( \frac{c}{c_s} \right)^2, \\
y^2 = \left( \frac{|+1|}{|-1|} \right) \left( \frac{3 - |+1| + ' (|+1|)}{4\sqrt{\tilde{y}}} \right), \quad x = \sqrt{\tilde{y}} y^2 \left( \frac{3 - |}{1 + |} \right), \quad \tilde{y}_j(c) = \frac{y^2 r_i^2(c) + \tilde{z}_j^2(c)}{(1+x)\tilde{z}_j(c)} \quad (j=1,2), \\
R(c) = \sqrt{\tilde{y}} y^2 r_i(c) r_s(c) - \frac{\sqrt{\tilde{y}} y^2 r_i(c) + x^2 r_s(c)}{\sqrt{\tilde{y}} y^2 r_i(c) + r_s(c)}, \quad z_j = r(\cos \theta + \tilde{z}_j(c) \sin \theta).
\end{aligned} \tag{4.4}$$

In the above equations,  $K_I^d$  and  $K_{II}^d$  are the mode-I and mode-II SIFs for a dynamically growing crack tip,  $c$  is the crack tip velocity, and  $\rho$  is the mass density.  $S_{11}$ ,  $S_{33}$ ,  $S_{13}$ , and  $S_{55}$  are coefficients of the  $S$ -matrix, whereas  $C_{11}$  and  $C_{55}$  are elements of the stiffness matrix; the ultrasonic determination of both matrices is described in Section 4.2.2.

### 4.2.2 Ultrasonic Determination of Orthotropic Elastic Constants

There are twelve elastic constants in the stiffness and compliance matrices for an orthotropic material, although only nine are independent due to matrix symmetry ( $S_{ij} = S_{ji}, C_{ij} = C_{ji}$ ). They are given below as a function of the compliance matrix ( $S$ -matrix):

$$\begin{pmatrix} v_{11} \\ v_{22} \\ v_{33} \\ 2v_{23} \\ 2v_{31} \\ 2v_{12} \end{pmatrix} = \begin{pmatrix} S_{11} & S_{12} & S_{13} & 0 & 0 & 0 \\ S_{21} & S_{22} & S_{23} & 0 & 0 & 0 \\ S_{31} & S_{32} & S_{33} & 0 & 0 & 0 \\ 0 & 0 & 0 & S_{44} & 0 & 0 \\ 0 & 0 & 0 & 0 & S_{55} & 0 \\ 0 & 0 & 0 & 0 & 0 & S_{66} \end{pmatrix} = \begin{pmatrix} \frac{1}{E_1} & -\hat{\nu}_{21} & -\hat{\nu}_{31} \\ \frac{-\hat{\nu}_{12}}{E_1} & \frac{1}{E_2} & -\hat{\nu}_{32} \\ \frac{-\hat{\nu}_{13}}{E_1} & -\hat{\nu}_{23} & \frac{1}{E_3} \\ 0 & 0 & 0 & \frac{1}{G_{23}} \\ 0 & 0 & 0 & 0 & \frac{1}{G_{31}} \\ 0 & 0 & 0 & 0 & 0 & \frac{1}{G_{12}} \end{pmatrix} \begin{pmatrix} \dagger_{11} \\ \dagger_{22} \\ \dagger_{33} \\ \dagger_{23} \\ \dagger_{31} \\ \dagger_{12} \end{pmatrix}. \quad (4.5)$$

These nine independent elastic constants can be determined ultrasonically in terms of the stiffness matrix ( $C$ -matrix), which is the inverse of the  $S$ -matrix:

$$\begin{pmatrix} \dagger_{11} \\ \dagger_{22} \\ \dagger_{33} \\ \dagger_{23} \\ \dagger_{31} \\ \dagger_{12} \end{pmatrix} = \begin{pmatrix} C_{11} & C_{12} & C_{13} & 0 & 0 & 0 \\ C_{21} & C_{22} & C_{23} & 0 & 0 & 0 \\ C_{31} & C_{32} & C_{33} & 0 & 0 & 0 \\ 0 & 0 & 0 & C_{44} & 0 & 0 \\ 0 & 0 & 0 & 0 & C_{55} & 0 \\ 0 & 0 & 0 & 0 & 0 & C_{66} \end{pmatrix} \begin{pmatrix} v_{11} \\ v_{22} \\ v_{33} \\ 2v_{23} \\ 2v_{31} \\ 2v_{12} \end{pmatrix}, \quad [C] = [S]^{-1}. \quad (4.6)$$

Once all nine  $C$ -matrix coefficients are determined ultrasonically, the  $S$ -matrix coefficients can be determined by a matrix inversion. These coefficients were determined using an Epoch 600 Ultrasonic Flaw Detector from OLYMPUS. Composite material cubes (approximately 6 mm

per side) were machined such that the faces aligned with the 1-, 2-, and 3-directions (Fig. 4.5), as defined originally in Fig. 4.2, where 1- is the axial and specimen crack growth direction, 2- is the radial and specimen thickness direction, and 3- is the circumferential and specimen crack opening direction.

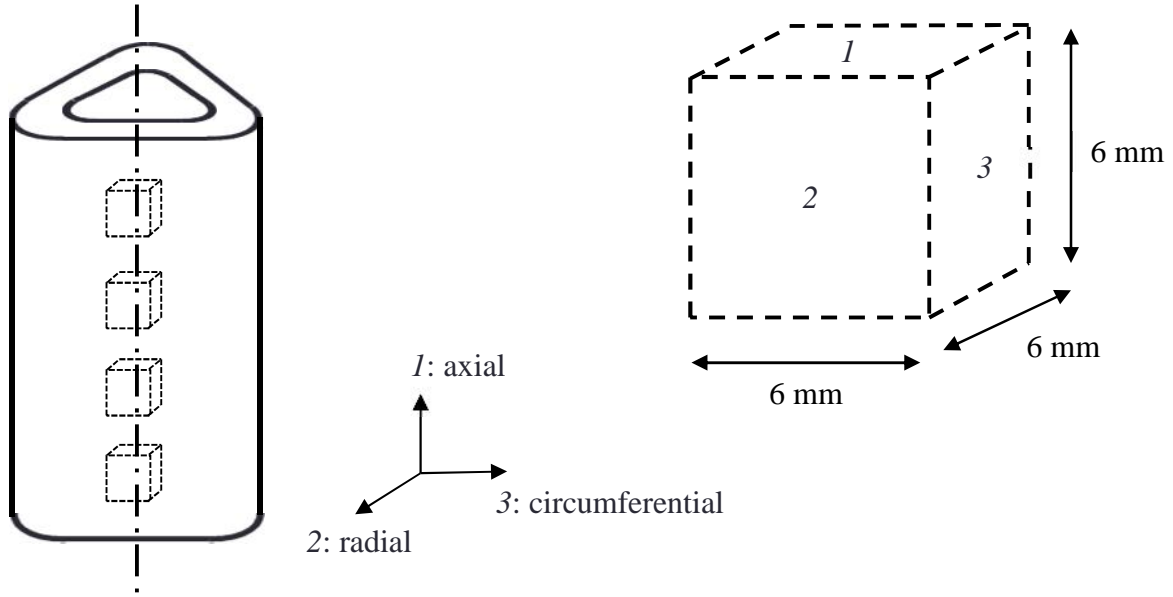


**Fig. 4.4:** Specimen geometry for the ultrasonic determination of orthotropic elastic constants of bovine cortical bone.

Following the notations used in Van Buskirk et al. [36], let  $V_{ij}$  denote the speed of a wave traveling in the  $i$ -direction with displacements in the  $j$ -direction.  $V_{11}$ ,  $V_{22}$ , and  $V_{33}$  are then longitudinal wave speeds, whereas  $V_{12}$ ,  $V_{13}$ , and  $V_{23}$  are shear wave speeds. (Note that  $V_{11}$ , and  $V_{13}$ , are equal to  $c_l$  and  $c_s$ , respectively, from Eq. 4.4.) These wave speeds are related to the diagonal terms of the  $C$ -matrix according to the following equations, where  $\rho$  is mass density:

$$\begin{aligned}
 C_{11} &= \rho V_{11}^2, & C_{44} &= \rho V_{23}^2 = \rho V_{32}^2, \\
 C_{22} &= \rho V_{22}^2, & C_{55} &= \rho V_{13}^2 = \rho V_{31}^2, \\
 C_{33} &= \rho V_{33}^2, & C_{66} &= \rho V_{12}^2 = \rho V_{21}^2.
 \end{aligned}
 \tag{4.7}$$

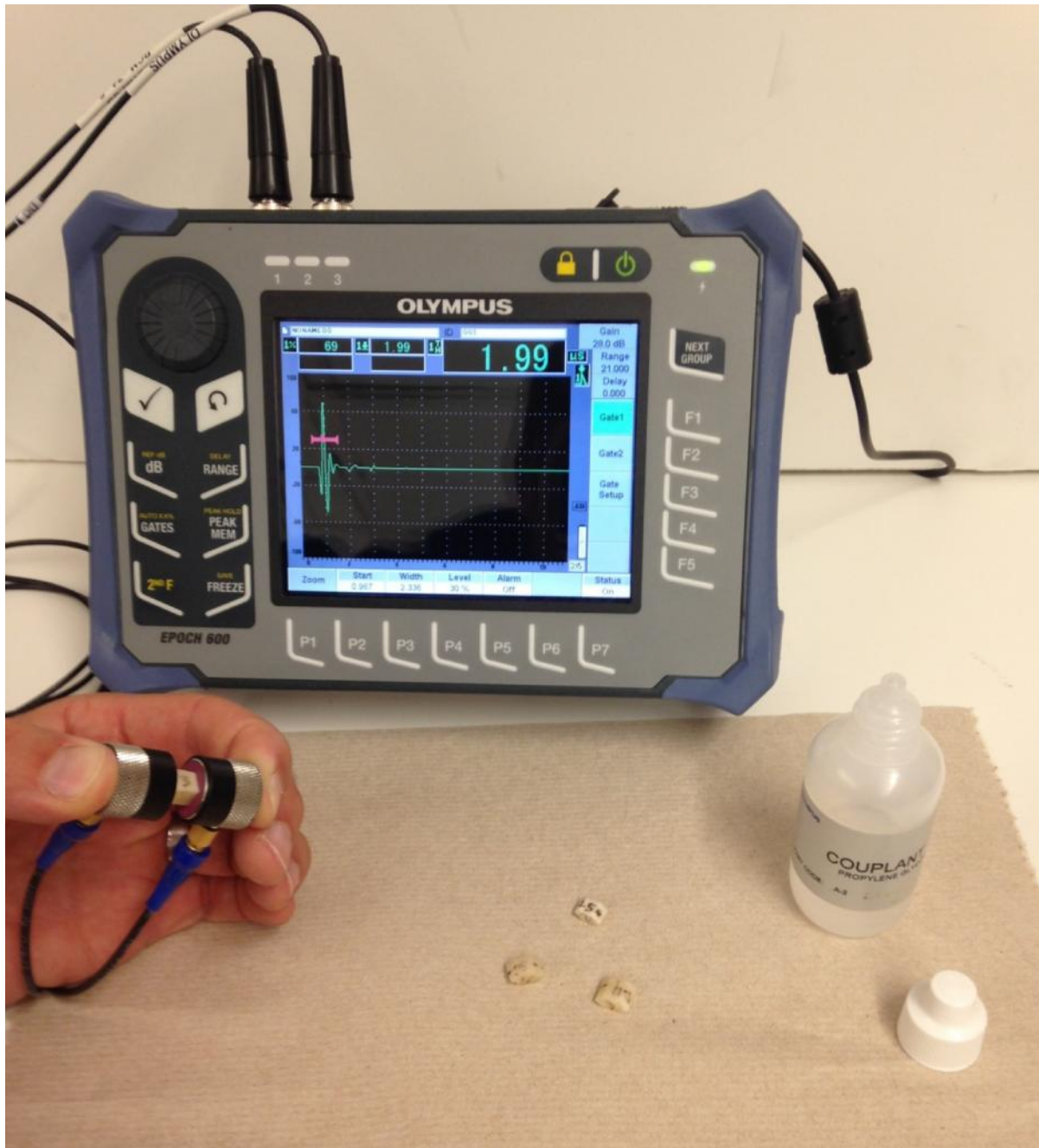


**Fig. 4.5:** Photographs of measuring  $V_{22}$  with the Epoch 600 Ultrasonic Flaw Detector. Specimen is held between longitudinal transducer and receiver with the 1- and 3-faces showing. Note that all orthotropic measurements were made in through-transmission mode (requiring 2 identical transducers, one of which acts like a receiver). Also pictured are the three additional specimens required to measure off-diagonal C-matrix coefficients.

Fig. 4.6 is a photograph of the Epoch 600 Ultrasonic Flaw Detector and two identical V106-RM longitudinal transducers. One is acting as a transducer, and the other as a receiver. A

drop of Couplant A (supplied by OLYMPUS) is used between each transducer and the specimen in longitudinal mode, while a drop of Shear Gel (not pictured, supplied by SONOTECH) is used on each shear wave transducer in shear mode. In order to measure  $V_{12}$ ,  $V_{13}$ , and  $V_{23}$ , a pair of identical V154-RM shear wave transducers must be used instead. All four samples necessary to measure the nine independent elastic constants of orthotropic bone are pictured here.

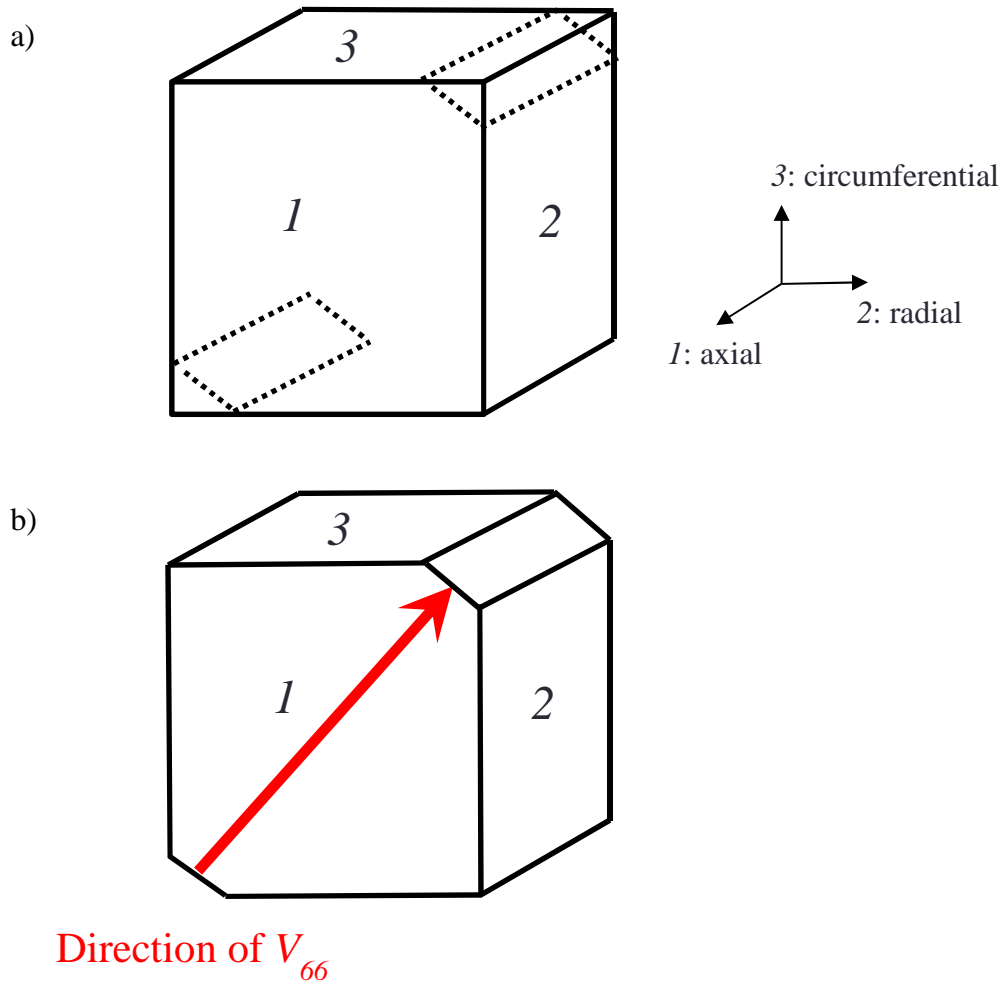


**Fig. 4.6:** In order to measure  $V_{66}$ , a) an original cube like the one in Fig. 4.5 is machined. b) Opposite corners are milled off between the 2- and 3-faces, such that ultrasonic transducer and receiver can be placed on the newly milled faces. Note that all ultrasonic measurements were made in through-transmission mode.



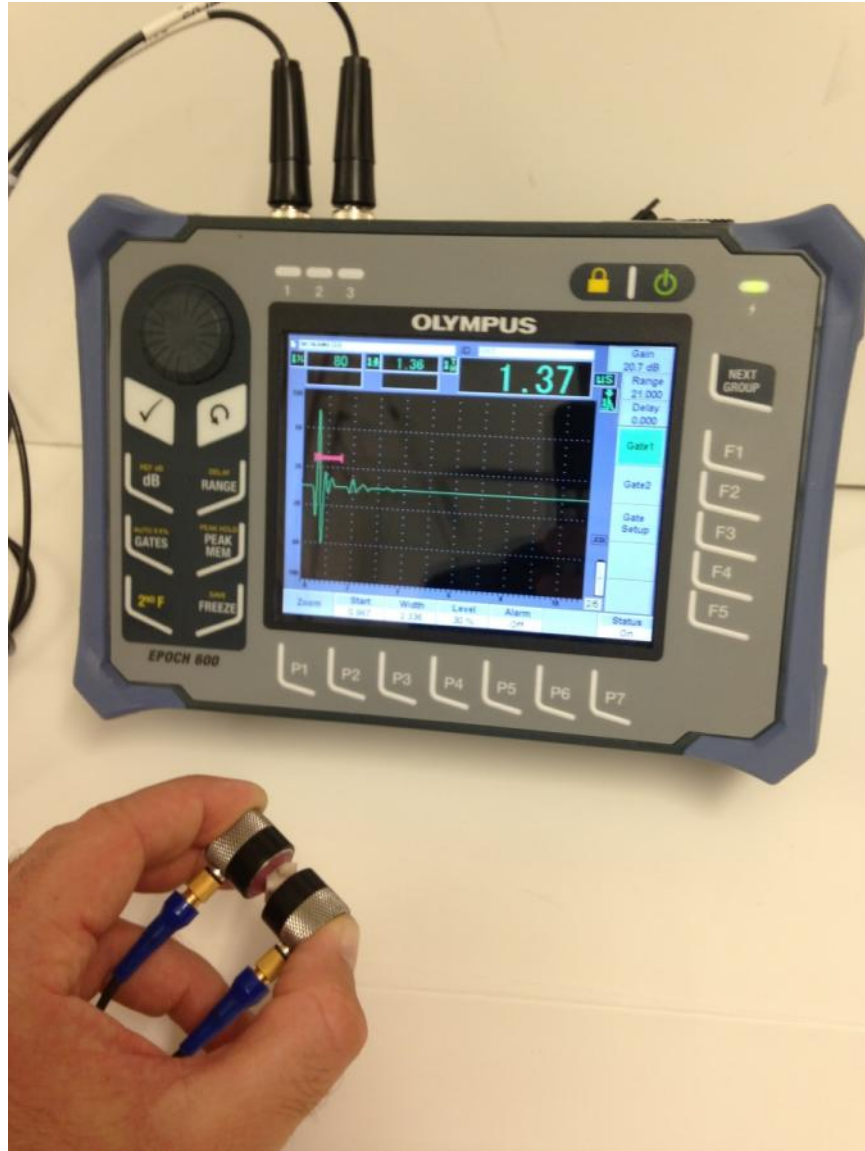


**Fig. 4.7:** Photograph of measuring  $V_{44}$  with the Epoch 600 Ultrasonic Flow Detector. Opposite corners that have been milled off between the  $I$ - and  $2$ -faces, such that longitudinal transducer and receiver can be placed on the newly milled faces.

In order to measure the off-diagonal terms of the  $C$ -matrix, three additional cubes were machined as before, and then parallel slices were made with a  $45^\circ$  rotation relative to the  $I$ -,  $2$ -, or  $3$ -directions. Fig. 4.7 shows a  $45^\circ$  rotation about the  $I$ -direction, with slices taken between the  $2$ - and  $3$ -faces. This new face is labeled the “ $6$ -face,” with corresponding longitudinal wave

speed denoted as  $V_{66}$ <sup>18</sup>. Similarly,  $V_{44}$  was measured using opposing faces between the 1- and 2-faces (Fig. 4.8), whereas  $V_{55}$  is measured using opposing faces between the 1- and 3-faces (not pictured). The off-diagonal  $C$ -matrix terms are then given by [36]:

$$\begin{aligned}
C_{12} = C_{21} &= \sqrt{(C_{11} + C_{66} - 2...V_{44}^2)(C_{22} + C_{66} - 2...V_{44}^2)} - C_{66}, \\
C_{13} = C_{31} &= \sqrt{(C_{11} + C_{55} - 2...V_{55}^2)(C_{33} + C_{55} - 2...V_{55}^2)} - C_{55}, \\
C_{23} = C_{32} &= \sqrt{(C_{22} + C_{44} - 2...V_{66}^2)(C_{33} + C_{44} - 2...V_{66}^2)} - C_{44}.
\end{aligned}
\tag{4.8}$$

The resulting elastic constants are compared to those reported in Van Buskirk et al. [36] from a dried human femur in Table 4.1.

Material Property	Present work	Literature [36]
$E_1$ (GPa) <sup>a</sup>	$25.9 \pm 1.0$	26.5
$E_2$ (GPa)	$21.0 \pm 0.4$	18.1
$E_3$ (GPa) <sup>a</sup>	$19.8 \pm 1.0$	19.4
$G_{23}$ (GPa)	$8.24 \pm 0.13$	7.22
$G_{13}$ (GPa) <sup>a</sup>	$9.22 \pm 0.18$	8.67
$G_{12}$ (GPa)	$9.63 \pm 0.16$	8.65
$\hat{\nu}_{12}$	$0.26 \pm 0.05$	0.207
$\hat{\nu}_{13}$ <sup>a</sup>	$0.30 \pm 0.02$	0.305
$\hat{\nu}_{23}$	$0.28 \pm 0.07$	0.325
$\hat{\nu}_{21}$	$0.21 \pm 0.05$	0.283
$\hat{\nu}_{31}$	$0.23 \pm 0.02$	0.285
$\hat{\nu}_{32}$	$0.26 \pm 0.06$	0.222
(kg/m <sup>3</sup> ) <sup>a</sup>	$1980 \pm 20$	-

**Table 4.1:** Ultrasonically-determined elastic constants of dried bovine cortical bone.

<sup>a</sup> Material properties used to calculate SIFs for bovine cortical bone.

<sup>18</sup> For simplicity, the notation for wave speeds  $V_{44}$ ,  $V_{55}$ , and  $V_{66}$ , differs from [36].

### 4.2.3 Finite Element Analysis

Finite element analysis was carried out to supplement dynamic experimental results prior to crack initiation. A 3D, transient, elasto-dynamic, finite element model using ABAQUS<sup>®</sup>/Explicit software was developed. The numerical model included the specimen and the long-bar (Fig. 4.9) in order to ensure that the stress wave propagating into the specimen was captured as accurately as possible. Material property input for the model included all of the elastic properties in Table 4.1, along with the density. The model consisted of 160,000 tetrahedral elements with highly refined elements of size 0.1 mm in the impact and crack tip vicinities. The model had a total of 98,000 degrees of freedom. The particle velocity ( $V_{pl}$ ) in the bar was determined from the measured strain history on the long-bar using:

$$V_{pl} = c_I v_I, \quad (4.9)$$

and input at the far right flat surface of the long-bar (Fig. 4.9). (In the above subscript  $I$  denotes ‘incident,’  $c$  the bar wave speed and  $v$  the measured strain on the long-bar.) After propagating along the long-bar, the stress waves were transmitted into the specimen using a contact definition for the semi-circular region that impacts the flat edge of the specimen. Time increments automatically chosen during computations by the software were approximately 3.5 ns.

Instantaneous values of SIFs were computed from finite element results using a regression analysis of crack flank displacements. Apparent stress intensity factors ( $K_I^*$ ) were calculated using crack opening displacements ( $\delta_y$ ) near the crack tip according to:

$$u_y \Big|_{x=\pm f, r \rightarrow 0} = 2K_I^* \sqrt{\frac{2r}{f}} \operatorname{Re} \left[ \frac{1}{z_2 - z_1} (q_1 z_2 z_1 - q_2 z_1 z_2) \right]. \quad (4.10)$$

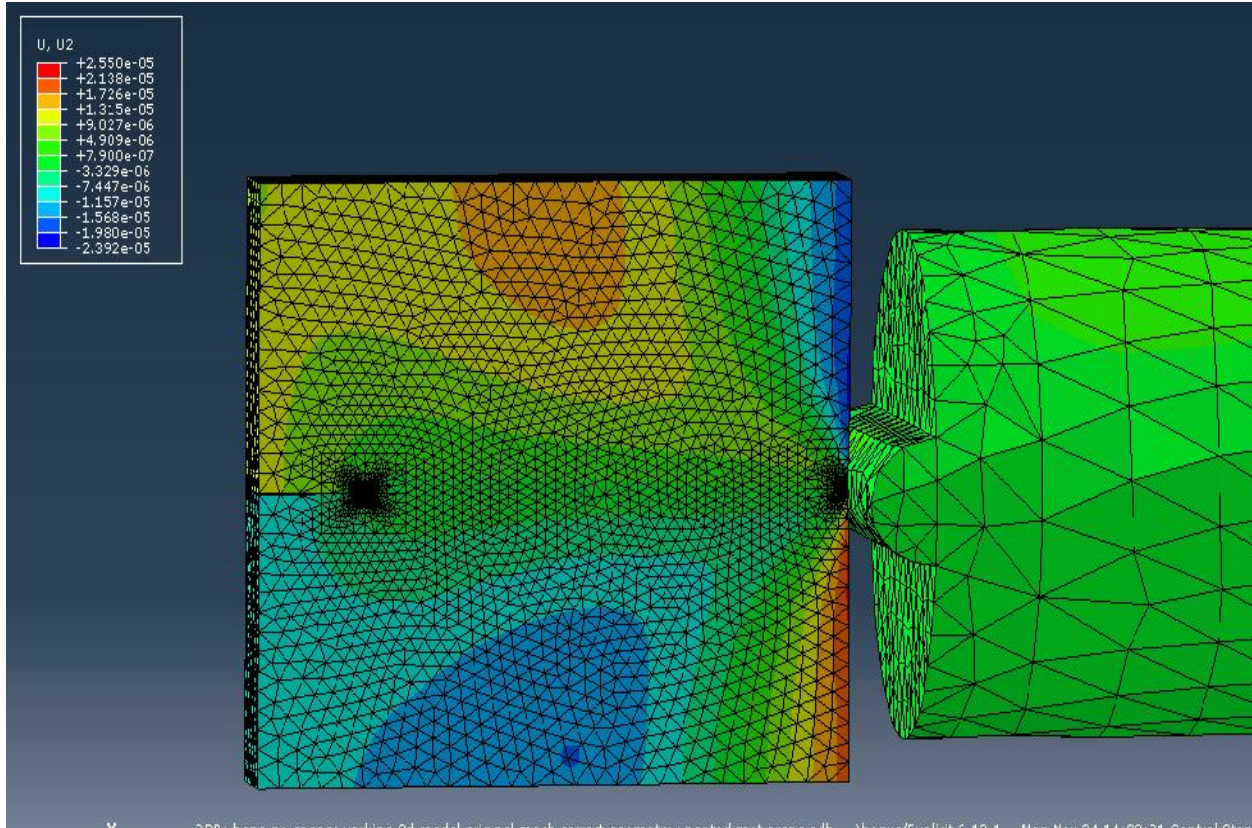


**Fig. 4.8:** Finite element model with corresponding crack opening displacement contours are shown on the bovine cortical bone specimen, along with the far left end of the long-bar. A fine mesh is used near the impact site to ensure that contact and crack tip deformation responses are captured accurately. The field corresponds to a time instant  $8 \mu\text{s}$  after impact and  $1 \mu\text{s}$  before crack initiation.

The linear regions of  $K_I^*$  vs.  $r$  plots were then extrapolated to the crack tip to obtain instantaneous SIFs as  $K_I = \lim_{r \rightarrow 0} K_I^*$  [99, 103].

### 4.3 Results

Sample contour plots based of the  $v$  and  $u$  displacement matrices from DIC are shown in Fig. 4.10b and 4.10c, respectively, corresponding to the deformed images in Fig. 4.10a. Time  $t$  in the images is time after crack initiation. The crack can be seen moving from left to right in all images, and the contour density continues to increase with time as well. (Contour interval is 2

$\mu\text{m}$ .) Due to the high stiffness and reduced specimen length compared to calibration samples in Chapter 3, small rollers of putty have been used only on the impact side of the specimen so as not to interfere with crack opening (as opposed to the wide putty bars in Fig. 2.4). Unlike previous images (Fig. 3.11), putty supports are clearly visible in Fig. 4.10a, and associated noisy regions are evident in Fig 4.10b and 4.10c. Because no smoothing is performed over the entire displacement fields, and displacement data input for determining SIFs is only retrieved from behind the crack tip (Fig. 2.10), the visible putty rollers do not affect measured SIFs.

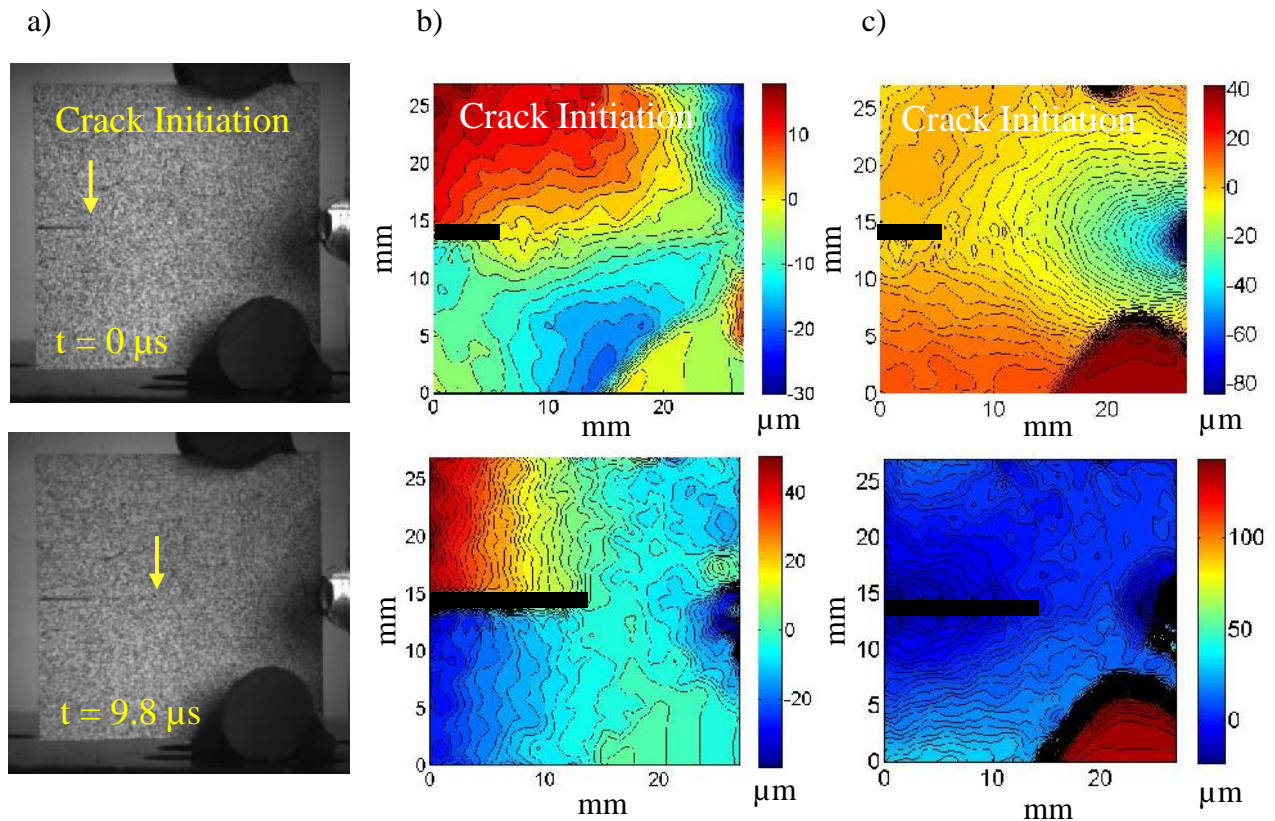


**Fig. 4.9:** Images recorded of a crack growing in bovine cortical bone using no Al pulse shaper at crack initiation and 10  $\mu\text{s}$  later. Corresponding b) crack opening and c) sliding displacement fields are shown. Contour interval is 2  $\mu\text{m}$ . Magnification is 33  $\mu\text{m}/\text{pixel}$ . Arrows indicate crack tip location.



Fig. 4.11 shows SIF histories for dried bovine cortical bone, along with the FEA simulation prior to crack initiation. Data from three test specimens are presented in these plots. Given the highly transient nature of crack growth, remarkable consistency in dynamic SIF histories is evident. In each of these graphs, solid symbols are used to denote pre- and post-initiation values, whereas the values corresponding to crack initiation are denoted by enlarged open symbols. The average crack tip speed was  $1067 \pm 151$  m/s.

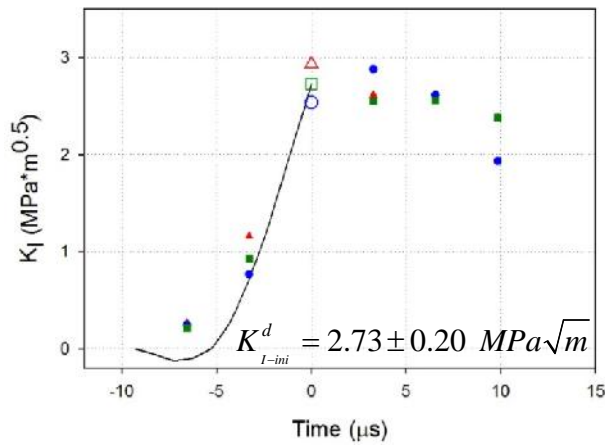


**Fig. 4.10:** Dynamic SIF histories for dried bovine cortical bone specimens with cracks growing in the axial direction. FEA is indicated by the solid line. Open symbols denote crack initiation at time  $t=0$ .

#### 4.4 Discussion

Ultrasonically-determined elastic constants are in good agreement with those in the literature for dried cortical bone (Table 4.1). The average  $K_{I-ini}^d$  ( $2.7 \text{ MPa}\sqrt{m}$ ) for dried bovine cortical bone was well within the  $1.2\text{--}6.5 \text{ MPa}\sqrt{m}$  range of quasi-static  $K_{IC}$  found in the literature for axial fracture of cortical bone [37-48]. (This is the first reported measurement of axial dynamic fracture crack initiation SIF ( $K_{I-ini}^d$ ) of cortical bone.) The only author to report axial quasi-static fracture of dried bone was Wang & Agrawal [47], who measured  $2.1 \text{ MPa}\sqrt{m}$

for bovine cortical bone; this is reasonably close to the current result of  $2.7 \text{ MPa}\sqrt{\text{m}}$ , considering the likelihood of loading rate effects for cortical bone.

Adharapurapu et al. [37] measured transverse dynamic fracture of bovine cortical bone with a modified Kolsky bar for 3-point bending and used strain gages instead of DIC to measure  $K_{I\text{-ini}}^d$ . They found  $K_{I\text{-ini}}^d$  of  $1.0 \text{ MPa}\sqrt{\text{m}}$  for dried bovine bone and  $2.5 \text{ MPa}\sqrt{\text{m}}$  for  $K_{I\text{-ini}}^d$  of wet bovine bone when using dynamic loading conditions. The current results are not consistent with these numbers; typically cortical bone exhibits higher  $K_{IC}$  when wet [37, 41, 47], and when fractured in the transverse direction rather than the axial direction [39, 40, 43, 48]. However, Kulin et al. [41] measured  $5.7 \text{ MPa}\sqrt{\text{m}}$  for  $K_{I\text{-ini}}^d$  of wet transversely-fractured, dried equine bone using a very similar methodology (4-point bending instead of 3-point bending) to Adharapurapu et al. [37]. The  $K_{I\text{-ini}}^d$  of Kulin et al. [41] is in closer agreement with the current work.

In order to ensure that enough energy was supplied to initiate and propagate these cracks in cortical bone, no pulse shaper was used. If a pulse shaper had been used, there likely would have been a few additional images of pre-initiation and possibly a few more images of post-initiation crack growth if the lower loading rate had led to slower crack tip speeds. Because of the high speeds of the crack tips and the small size of the specimens, there were not enough images to evaluate how crack tip speed was changing with respect to time or  $(K_I^d)$ . In order to generate more data, the high-speed camera could also be run faster than the 300,000 frames per second used here.

## **Chapter 5. Quasi-static and Dynamic Characterization of CNT/Epoxy Nanocomposites**

In this chapter, the quasi-static tensile, quasi-static fracture, and dynamic fracture properties of neat epoxy and epoxy modified with carbon nanotubes (CNTs) is described. Many different CNT dispersion techniques are considered, resulting in a wide array of dispersion patterns; however, no significant changes in terms of mechanical properties were found. Additional variables that were found to have little or no effect on the mechanical properties of epoxy were the type of CNT, the cure schedule, the notching technique, and the ratio of resin:hardener.

### **5.1 Experimental Details**

#### **5.1.1 Quasi-Static Fracture and Tensile Tests**

Quasi-static tension and fracture tests were performed for each type of nanocomposite produced and compared to neat epoxy resin. Specimen geometry is given in Fig. 5.1. Both tests were performed on an Instron 4465 testing machine in displacement control. Tension tests were performed at 1.27 mm/min according to ASTM Standard D638 using a 6.25 mm gauge length extensometer to collect strain values. Three-point bend fracture tests were performed on single-edge notched samples at a cross-head speed of 0.01 mm/s after notches were sharpened using a razor blade. The quasi-static crack initiation SIF values ( $K_{IC}$ ) were calculated based on the maximum recorded load using



$$K_{IC} = \frac{\left(\frac{P_{\max}}{B\sqrt{W}}\right)\left(3\frac{S}{W}\sqrt{\frac{a}{W}}\right)}{2\left(1+2\frac{a}{W}\right)\left(1-\frac{a}{W}\right)^{3/2}} \left[1.99 - \frac{a}{W}\left(1-\frac{a}{W}\right)\left\{2.15 - 3.93\left(\frac{a}{W}\right) + 2.7\left(\frac{a}{W}\right)^2\right\}\right], \quad (5.1)$$

where  $P_{\max}$  is the peak load prior to fracture,  $B$  is thickness,  $W$  is width,  $S$  is span (50.4 mm), and  $a$  is crack length. Material preparation information is provided in the Section 5.2 for each nanocomposite considered.

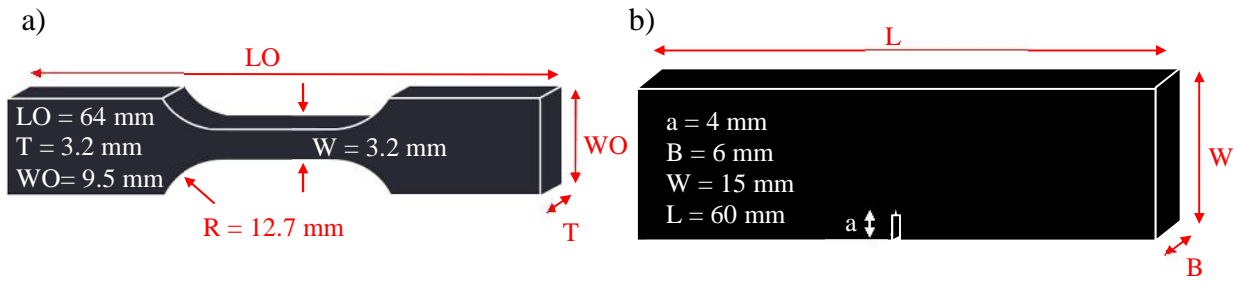


**Fig. 5.1:** Specimen geometries used for quasi-static a) tension and b) fracture.

Dynamic mechanical analysis (DMA) was performed using a 5°C/minute ramp from room temperature to around 240°C in dual cantilever beam mode with a frequency of 1 Hz and an amplitude of 15  $\mu\text{m}$ . Specimens were machined to 60 mm x 12 mm x 3 mm, and the span length was 35 mm.

### 5.1.2 Dynamic Fracture Tests

The methodology involving digital image correlation (DIC) and high-speed photography for determining the dynamic fracture properties of relatively small size specimens (detailed in Chapter 2) was used to examine dynamic SIFs of neat epoxy and epoxy reinforced with CNTs using 10 psi of compressed air and the medium dynamic loading rate (soft aluminum pulse

shaper- “Al”) (see Fig. 2.7). Plate-shaped specimens were machined to the same dimensions (Fig. 5.2) used previously for isotropic PMMA and bone cement in Chapter 3 (50 x 25 x 5 mm).

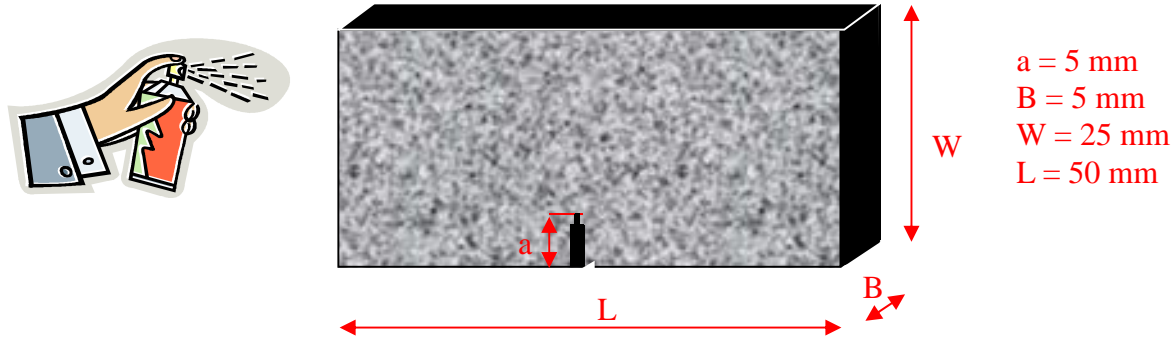


**Fig. 5.2:** Specimen geometry used for dynamic fracture studies.

The isotropic stress intensity factors (SIFs) were determined for each image prior to crack initiation using an overdeterministic least squares method and the asymptotic expressions for displacements in an isotropic material, given in Section 3.2.2. Because the testing and evaluation of dynamic fracture parameters by this methodology is much more tedious and time-consuming than quasi-static tests, the original goal was to first develop a nanocomposite with improved quasi-static mechanical properties, and then evaluate its dynamic fracture properties. When the difficulties of finding significant quasi-static properties were realized, some of the dynamic fracture tests were evaluated only at time instants in the neighborhood of crack initiation to minimize the effort.

### **5.1.3 Ultrasonic Determination of Isotropic Elastic Constants**

In order to solve the displacement field equations for  $K_I$  and  $K_{II}$ , the elastic constants must be known. Because the focus of this work is on dynamic fracture measurements, all elastic constants were determined ultrasonically using an OLYMPUS Epoch 600 flaw detector.

Isotropic elastic constants were determined in pulse-echo mode. Material wave speeds were calculated by dividing twice the sample thickness by the time measured for the ultrasonic wave to pass through the material and return back to the transducer. The following equations were used to determine the elastic properties from the measured longitudinal and shear wave speeds:

$$c_L = \sqrt{\frac{E(1-\nu)}{2\rho(1+\nu)(1-2\nu)}}, \quad c_S = \sqrt{\frac{E}{2\rho(1+\nu)}} \quad (5.2)$$

The various material properties used in the FEA simulation and experimental analysis are given in Table 5.1.

Material Property	Epoxy	Al 7075 T6
$E$ (GPa)	3.54	71.7
$\nu$	0.37	0.30
$G$ (GPa)	1.29	27.6
$\rho$ (kg/m <sup>3</sup> )	1150	2730
$c_L$ (m/s)	1890	5370
$c_S$ (m/s)	1060	3180

**Table 5.1:** Material properties used in the computational and experimental analyses.

#### 5.1.4 Finite Element Analysis

The use of relatively small samples, the resulting complex stress wave reflections and the SIF estimation scheme based on a few terms of the asymptotic expansion field, all demanded an independent SIF evaluation scheme to enhance the confidence level of measurements in the pre- and post-initiation regimes. Accordingly, complementary finite element analyses were carried out to supplement experimental results prior to crack initiation. A 3D, transient, elasto-dynamic, finite element model using ABAQUS®/Explicit software was developed. The model included

the specimen and the long-bar (Fig. 5.3) in order to ensure that the stress wave propagating into the specimen was captured as accurately as possible. The model consisted of 160,000 tetrahedral elements with highly refined elements of size 0.1 mm in the impact and crack tip vicinities. The model had a total of 100,000 degrees of freedom. The particle velocity ( $V_{pl}$ ) in the long-bar was determined from the measured strain history on the long-bar using:

$$V_{pl} = c_I v_I \quad (5.3)$$

and was subsequently input at the far right flat surface of the long-bar (Fig. 5.3). (In the above subscript  $I$  denotes ‘incident,’  $c$  the bar wave speed and  $v$  the measured strain on the long-bar.)

After propagating along the long-bar, the stress waves were transmitted into the specimen using a contact definition for the semi-circular region that impacts the flat edge of the specimen. Time increments automatically chosen during computations by the software were approximately 13 ns.

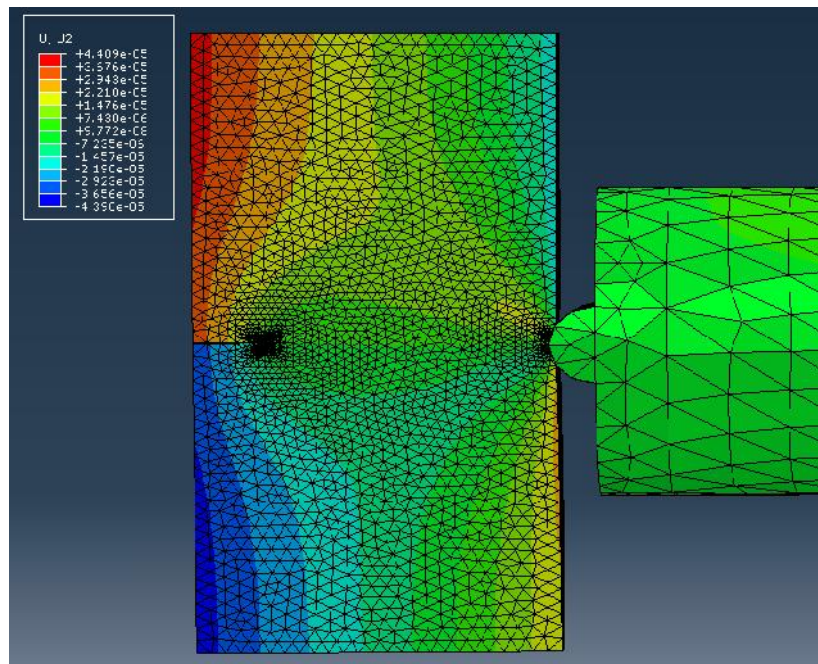


**Fig. 5.3:** Finite element model with corresponding crack opening displacement contours shown on the specimen, along with the far left end of the long-bar. A fine mesh is used near the impact site to ensure that contact and crack tip deformation responses are captured accurately. The field corresponds to a time instant 48  $\mu$ s after impact and 5  $\mu$ s before crack initiation.

SIFs were computed from FEA results using a regression analysis of crack flank displacements. Apparent stress intensity factors ( $K_I^*$ ) were calculated using crack opening displacements ( $\delta_y$ ) near the crack tip according to:

$$u_y \Big|_{r=\pm f, r \rightarrow 0} = \frac{8K_I^*}{E} \sqrt{\frac{r}{2f}}. \quad (5.4)$$

The linear regions of  $K_I^*$  vs.  $r$  plots were then extrapolated to the crack tip to obtain instantaneous SIFs as  $K_I = \lim_{r \rightarrow 0} K_I^*$  [99, 103].

## 5.2 Carbon Nanotube Dispersion Techniques

### 5.2.1 Bath Sonication with Mechanical Stirring

#### 5.2.1.1 Methods

Initial samples were prepared using Epon 862 resin and Epikure W hardener from Momentive Chemicals, USA. Because functionalization methods cannot yet be controlled, functionalization tends to occur at random defect sites, and functionalization has been shown to weaken the properties of CNTs [104], unfunctionalized MWCNTs (Baytubes C 150P) were initially dispersed into the epoxy matrix. Unfunctionalized CNTs are amphiphobic, so they do not interact well with epoxy resin; however, because of their amphoteric nature, they can accept electrons from the amine groups found in epoxy hardeners in order to achieve some level of compatibilization during dispersion [104]. In addition to the thermodynamic approach of dispersing the CNTs first in the hardener (donor-acceptor interaction), the kinetic approach of simultaneous mechanical stirring at 400 rpm (Eurostar 20 – Fig. 5.4) and 45 kHz bath sonication

(dispersion via cavitation) using an Elma Ultrasonics Transsonic Ti-H-6 bath sonicator (Fig. 5.5) at 80°C for 30 minutes was employed. After that the stoichiometric amount (100g resin:26.5g hardener) of resin was added (manufacturer recommendation was a molar ratio of 1:1 resin:hardener), followed by an additional 30 minutes of mechanical stirring at 1500 rpm and 45 kHz bath sonication at 80°C.

With the future goal of creating three-phase CNT/epoxy/carbon fiber nanocomposites in mind [105], the following cure schedule was used. Samples were poured into a steel mold and degassed for 30 minutes at 80°C. Samples were then heated to 80°C for 30 minutes, cured at 120°C for 2.5 hours, and post-cured at 180°C for 3 hours. This degassing technique and cure schedule was applied to all Epon 862 and Epikure W samples presented in this work (except when stoichiometry was intentionally varied as described in Section 5.2.5), although other cure schedules were also tried without successful mechanical enhancement of epoxy.



**Fig. 5.4:** Eurostar 20 overhead stirrer from IKA used for simultaneous bath sonication and mechanical stirring. (Also used independently of bath sonication for mechanical stirring of some samples.)<sup>19</sup>

---

<sup>19</sup> www.ika.com



**Fig. 5.5:** Transsonic Ti-H-6 ultrasonic cleaner from Elma Ultrasonics used for simultaneous bath sonication and mechanical stirring.<sup>20</sup>

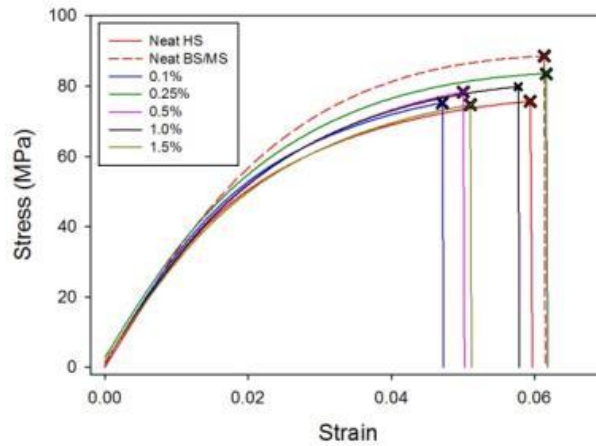
#### 5.2.1.2 Results

Two types of neat samples (without CNTs) were produced. The first batch of neat samples were made using only hand-stirring (HS) of the resin and hardener. The stress vs. strain response and load vs. load-point deflection response measured for these samples are shown as solid red curves in Fig. 5.6a and 5.7a (the cross represents the breaking point). A second set of neat samples were made with the exact same methodology involving bath sonication and mechanical stirring applied to the preparation of CNT-modified epoxy (BS/MS) (dashed red curve in Fig. 5.6a and 5.7a). The latter set of samples provides a strict one-to-one correspondence regarding the sample preparation protocol used for preparing CNT-modified material. The importance of applying the same methodology to the neat and CNT-modified sample preparation is demonstrated in Fig. 5.6b, 5.6c, and 5.7b. Evidently, the matched protocol leads to an increase in

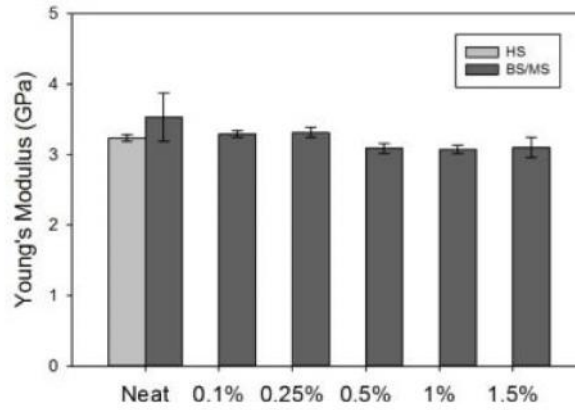
---

<sup>20</sup> [www.elmaultrasonic.com](http://www.elmaultrasonic.com)

a)



b)



c)

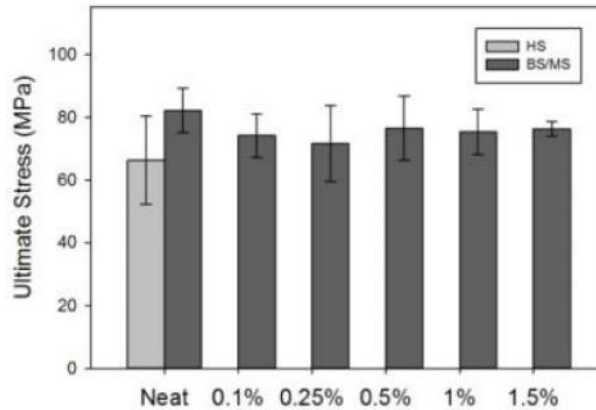


**Fig. 5.6:** Results from quasi-static tension tests using hand-stirring (HS) or bath sonication with mechanical stirring (BS/MS) for 0-1.5 wt% CNTs: a) representative stress-strain curves ('x' indicates failure point), b) average Young's modulus, and c) average ultimate stress. Error bars here and throughout indicate one standard deviation from the mean.



Young's modulus, ultimate stress, and crack initiation SIF, respectively, even without the addition of CNTs. (This is a subtle but often overlooked or unreported aspect in many reports.) Therefore, all subsequent neat samples presented in this work have been processed in the same way that the corresponding CNT-modified samples are prepared.

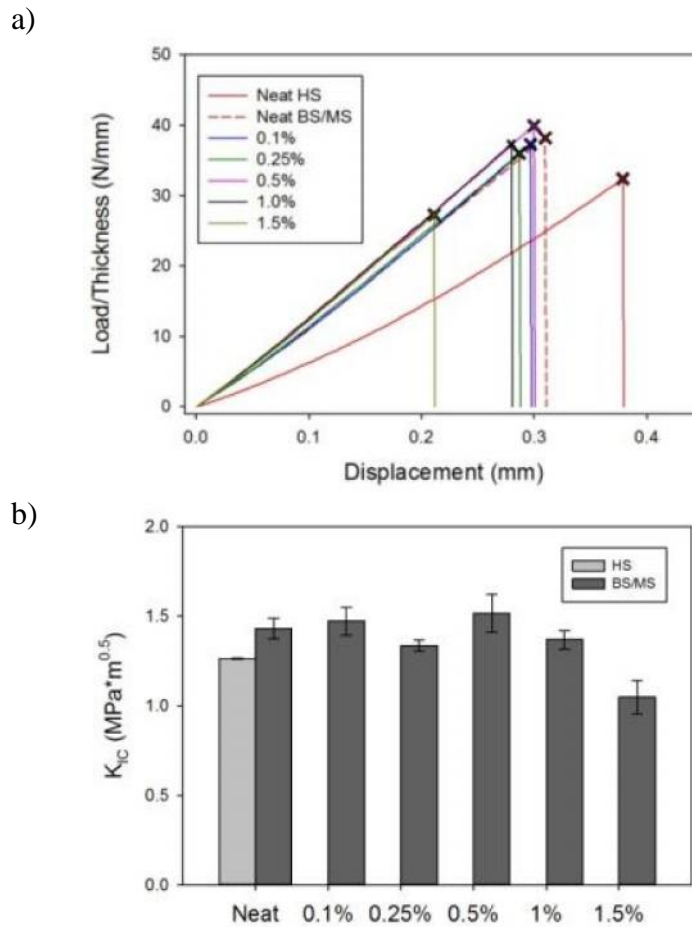


**Fig. 5.7:** Results from quasi-static fracture tests using hand-stirring (HS) or bath sonication with mechanical stirring (BS/MS) for 0-1.5 wt% CNTs: a) representative load-displacement curves normalized by specimen thickness, where ‘x’ indicates crack initiation, and b) average crack initiation SIF ( $K_{IC}$ ).  $K_{IC}$  of neat epoxy increases from  $1.26 \text{ MPa}\sqrt{m}$  to  $1.43 \text{ MPa}\sqrt{m}$  when the control sample is mechanically stirred and bath sonicated instead of only hand-stirred.

The addition of CNTs over a wide range of weight percentages (0.1-1.5 wt%) caused an insignificant decrease in Young's modulus and ultimate strength (Fig.5.6) and no significant

improvement in crack initiation SIF ( $K_{IC}$ ) (Fig.5.7). The largest improvement in  $K_{IC}$  was approximately +6% at 0.5 wt% CNTs.

### 5.2.1.3 Microscopy of Fracture Surfaces

Fig. 5.8 shows the full width ( $B = 6$  mm, Fig. 5.1b) of fracture surfaces from two different samples. The line discontinuity at the bottom of each image shows the sharpened crack front from where the crack initiated and propagated towards the top. Large agglomerates settled to the bottom (left side of images) during curing, particularly for the higher weight percentages of CNTs pictured here. Simultaneous bath sonication and homogenization does not appear to be a strong enough methodology to disperse unfunctionalized CNTs (Baytubes) into the hardener. These large agglomerates likely led to the decrease in  $K_{IC}$  for higher CNT loadings beyond 0.5 wt% in Fig. 5.7b.

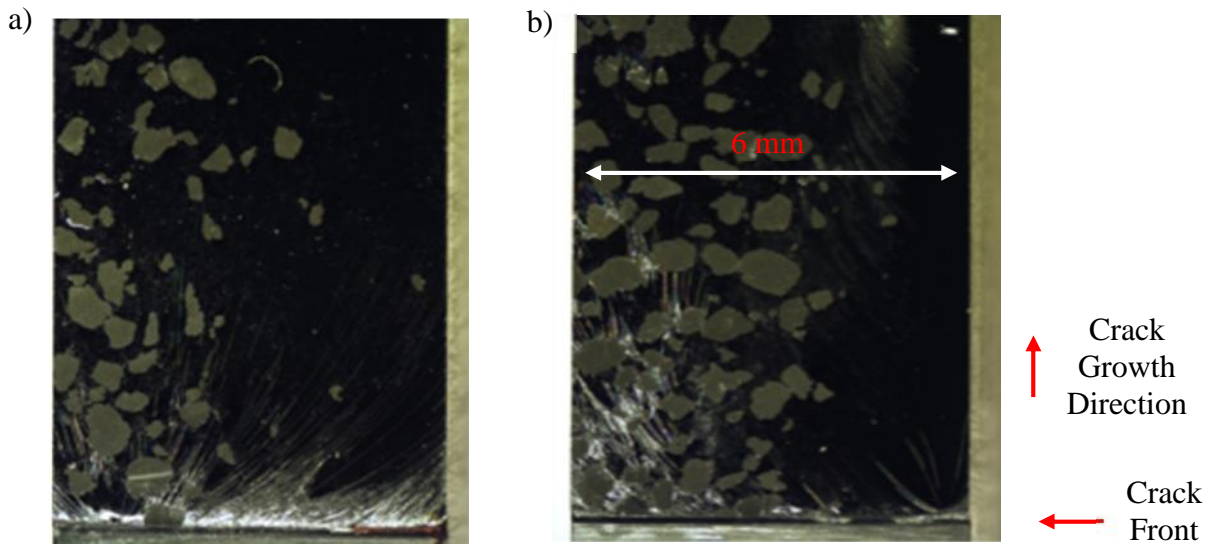


**Fig. 5.8:** Optical microscopy of fracture surfaces: a) 1 wt% CNTs and b) 1.5 wt% CNTs. Large agglomerates (nearly 1 mm in diameter) settled to the bottom (left side in the images) during curing. (The higher concentration of agglomerates to the left of the cross-section is due to settling during curing.)

## 5.2.2 Optimization of Dispersion

### 5.2.2.1 Methods

CNT dispersion was optimized according to optical microscopy using smaller batch sizes (~20g) with 0.1 wt% CNTs. (Note that, even when only CNTs and hardener are present, 0.1 wt% CNTs is calculated according to the final formulation including the resin; therefore, 0.1 wt% CNTs and Epikure W is actually ~0.5 wt% CNTs prior to the addition of resin.) As in Section 5.2.1, Baytubes were dispersed into Epikure W for achieving the thermodynamic effect before adding Epon 862 resin. A Cole-Parmer Labgen 7 homogenizer (Fig. 5.9) (250  $\mu\text{m}$  gap between rotating blade and stationary blade) was used to initially break up large agglomerates in the CNT-hardener mixture. Its speed was varied between 5,000 and 35,000 rpm. Mechanical stirring was again performed simultaneously with bath sonication (either with 25 or 45 kHz setting). Cup horn sonication (Misonix Sonicator 3000) with higher cavitation intensity than bath sonication, was varied between 25-160 W. Drops of CNT/hardener were collected from the batch onto glass slides periodically in order to monitor the effect of each of these dispersion techniques over time. The results are summarized in Fig. 5.10.

The interaction between Epikure W and Baytubes is not strong enough compared to that between nanotube and nanotube in order to break up the CNT agglomerates (>1 mm) effectively by hand-stirring (Fig. 5.10a). Subsequent homogenization (H) dispersed some of the CNTs well but continued to leave behind large agglomerates (>50  $\mu\text{m}$ ) (Fig. 5.10b). Subsequent cup horn sonication (CS) dispersed some CNTs even more thoroughly, although large agglomerates (<50  $\mu\text{m}$ ) remained (Fig. 5.10c). Instead of cup horn sonication, when the sample was hand-stirred, homogenized, and then bath sonicated at 45 kHz (Fig. 5.10d), the largest agglomerates were reduced to around 10  $\mu\text{m}$  in diameter, but the CNTs appeared to remain tightly packed. Instead,

if the sample was first bath sonicated at 25 kHz (Fig. 5.10e) and then the frequency was increased to 45 kHz, the final dispersion (Fig. 5.10f) produced the “fluffy-loosely-packed” description of good dispersion noted in Park et al. [104].

This final methodology (Fig. 5.10f) was chosen as the optimized methodology, with the following details: 15 minutes of homogenization (first 10 minutes at 35,000 rpm, then 5 minutes at 25,000 rpm), 45 minutes of simultaneous mechanical stirring at 400 rpm and 25 kHz bath sonication at 80°C, and 60 minutes of simultaneous mechanical stirring at 400 rpm and 45 kHz bath sonication at 80°C. Then the resin was hand-stirred in, and the entire mixture was simultaneously stirred mechanically at 1,500 rpm and bath sonicated at 45 kHz for another 30 minutes at 80°C.

The succession of dispersion in the optimized methods is explained as follows: Homogenization caused large CNT aggregates to be broken down into smaller pieces using extremely high shear stress within the narrow homogenizer gap. Next, 25 kHz bath sonication was used to break these CNT aggregates into smaller and looser aggregates with simultaneous mechanical stirring. Note that 25 kHz sonication offers greater size cavitation than 45 kHz with a higher force among greater size interfaces. (The cavity size and force are inversely proportional to the sonication frequency.) The 25 kHz sonication frequency provides higher cavitation forces but cannot break up small-scale aggregates because the cavity size is too big to form within small scale interfaces. Therefore, 45 kHz sonication with smaller size cavitation was used next to break the loosened small aggregates further, creating the loose, fluffy CNT dispersion in Fig. 5.10f. The final dispersion after scaling up to full batch sizes and doubling the final CNT wt% is shown in Fig. 5.11. This figure closely resembles Figs. 1.10c and 1.10d, which led to the greatest improvement in  $K_{ic}$  (Fig. 1.11a) found by Mirjalili et al. [63].



**Fig. 5.9:** Labgen 7 homogenizer from Cole-Parmer used to break up large agglomerates.<sup>21</sup>

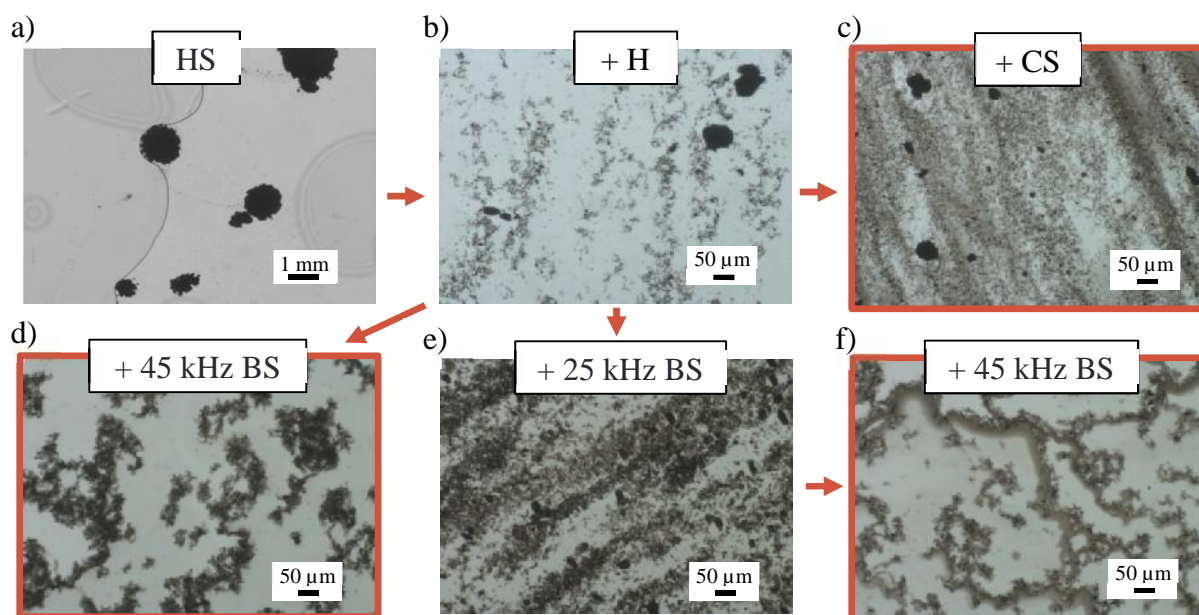


**Fig. 5.10:** Optical microscopy of optimization process of 0.1 wt% Baytubes dispersed into Epikure W: a) hand-stirring (HS); b) hand-stirring and homogenization (HS+H); c) hand-stirring, homogenization, and cup horn sonication (HS+H+CS); d) hand-stirring, homogenization, and 45 kHz bath sonication (HS+H+BS); e) hand-stirring, homogenization, and 25 kHz bath sonication; and f) hand-stirring, homogenization, 25 kHz bath sonication, and 45 kHz bath sonication.  indicates a final step in the optimization process.

<sup>21</sup> www.coleparmer.com

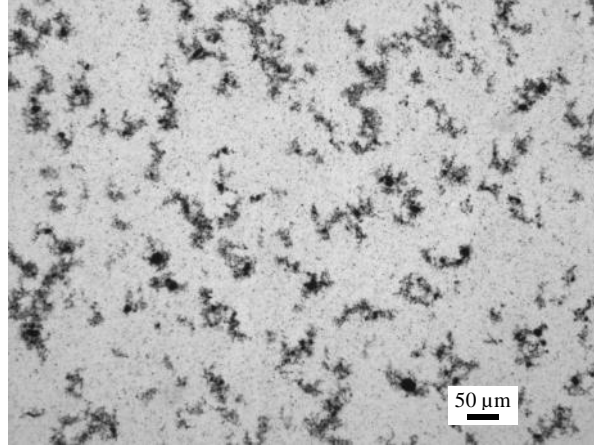


**Fig. 5.11:** Optical microscope image from the optimized methodology of uncured Epon 862, Epikure W, and 0.2 wt% Baytubes.

#### 5.2.2.2 Results

The crack initiation SIF results from the sample preparation methods described above are presented in Fig. 5.12. Despite apparent improvements in CNT dispersion, no improvements were found in fracture toughness for nanocomposites with 0.05-0.25 wt% CNTs. Also the optimized methodology applied to the neat sample improved  $K_{IC}$  to  $1.51 \text{ MPa}\sqrt{m}$ , compared to  $1.43 \text{ MPa}\sqrt{m}$  for the original methods (Section 5.2.1). Perhaps the dispersion level achieved here (Fig. 5.11) is not good enough to effectively improve the toughness, or the nanotubes may be damaged during processing, thereby degrading their properties. This image (Fig. 5.11) shows separated (localized), loosened, fluffy CNTs, instead of evenly dispersed CNTs throughout the entire matrix. This dispersion level was later improved upon by introducing calendaring (Section 5.2.4).

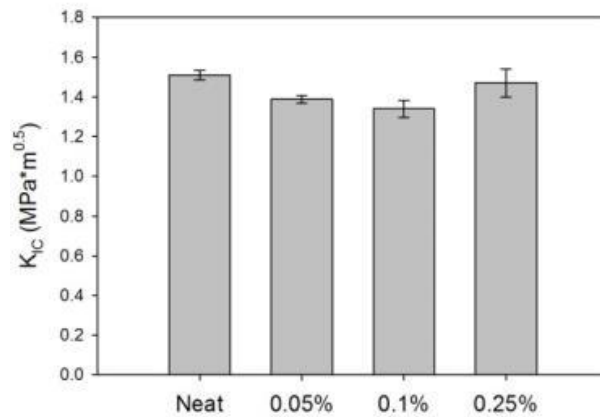


**Fig. 5.12:** Crack initiation SIF for samples from the optimized methodology samples. No improvements in  $K_{IC}$  for 0.05-0.25 wt% CNTs are evident.

### 5.2.3 Other Methods of Dispersing CNTs into the Hardener First

#### 5.2.3.1 Methods

When the technique optimized by microscopy did not result in any increase in the crack initiation SIF beyond that of neat epoxy with the same processing steps, several other methodologies were attempted based on the optimization study (Fig. 5.10).

Samples similar to the optimized methods but with less bath sonication time were produced (Fig. 5.10d), both with 0.2 wt% Baytubes and with 0.2 wt% of a second type of unfunctionalized CNTs from Nanostructured and Amorphous Materials (NAMs). This method included 15 minutes of homogenization (first 10 minutes at 35,000 rpm, then 5 minutes at 25,000 rpm) and 30 minutes of simultaneous mechanical stirring at 400 rpm and 45 kHz bath sonication at 80°C. Then the resin was hand-stirred into the mixture, and the entire batch was simultaneously mechanically stirred at 1,500 rpm and bath sonicated at 45 kHz for another 30 minutes at 80°C. Note that this is the same methodology as presented in Section 5.2.1 but with the addition of homogenization.



**Fig. 5.13:** Vibracell VCX 750 probe tip sonicator provides high cavitation intensity for the dispersion of CNT agglomerates.<sup>22</sup>

Two additional methodologies were attempted with higher cavitation intensity using 0.2 wt% Baytubes. The cup horn sonicator (CS) (Fig. 5.10c) uses a water medium between the horn and the sample, while probe tip sonication (PS) involves placing the probe tip directly into the sample for even higher, but very localized, cavitation intensity. In both cases, CNTs were dispersed with 15 minutes of homogenization (first 10 minutes at 35,000 rpm, then 5 minutes at 25,000 rpm), 2 hours of high cavitation intensity sonication (CS or PS) at 5 seconds “on”/5 seconds “off” cycling for 1 hour of “on time,” and then 30 minutes of simultaneous mechanical stirring at 400 rpm and 45 kHz bath sonication at 80°C. Then the resin was hand-stirred in, and the entire mixture was simultaneously mechanically stirred at 1,500 rpm and bath sonicated at 45 kHz for another 30 minutes at 80°C. The cup horn sonicator was set to an amplitude of 3.5, which delivered ~80 W of power. The probe tip sonicator (Vibracell VCX 750 – Fig. 5.13) was set to an amplitude of 35%, which delivered ~260 W of power.

---

<sup>22</sup> www.sonics.com



### 5.2.3.2 Results

Fig. 5.14 gives the results of the mechanical tests (stress vs. strain and load vs. load-point deflection graphs are not shown for brevity) of samples with homogenization and less bath sonication time than the optimized methods described in Section 5.2.2. These samples were homogenized and then processed in the same way as in Section 5.2.1. In the tension tests, there is no change in Young's modulus, and the decreases in ultimate strength and ultimate strain are insignificant. While both Baytubes and NAMs gave improvements in  $K_{IC}$  (+27% and +14%, respectively), neither improvement is considered significant with respect to the associated error bars due to large scatter in the data.

Fig. 5.15 shows the mechanical test results for the cases of higher cavitation intensity. The only significant improvements in mechanical properties are the ultimate stress (+1%) and crack initiation SIF (+19%) of cup horn sonication samples (CS). It should be noted that this significant improvement in  $K_{IC}$  is actually due to a decrease in the crack initiation SIF of the neat epoxy due to processing ( $1.29 \text{ MPa}\sqrt{m}$ ), rather than any real improvement of the material properties caused by the CNTs. Probe tip sonication on the other hand causes a slight decrease (-2%) in crack initiation SIF relative to neat epoxy, indicating possible CNT damage by the localized sonication energy.

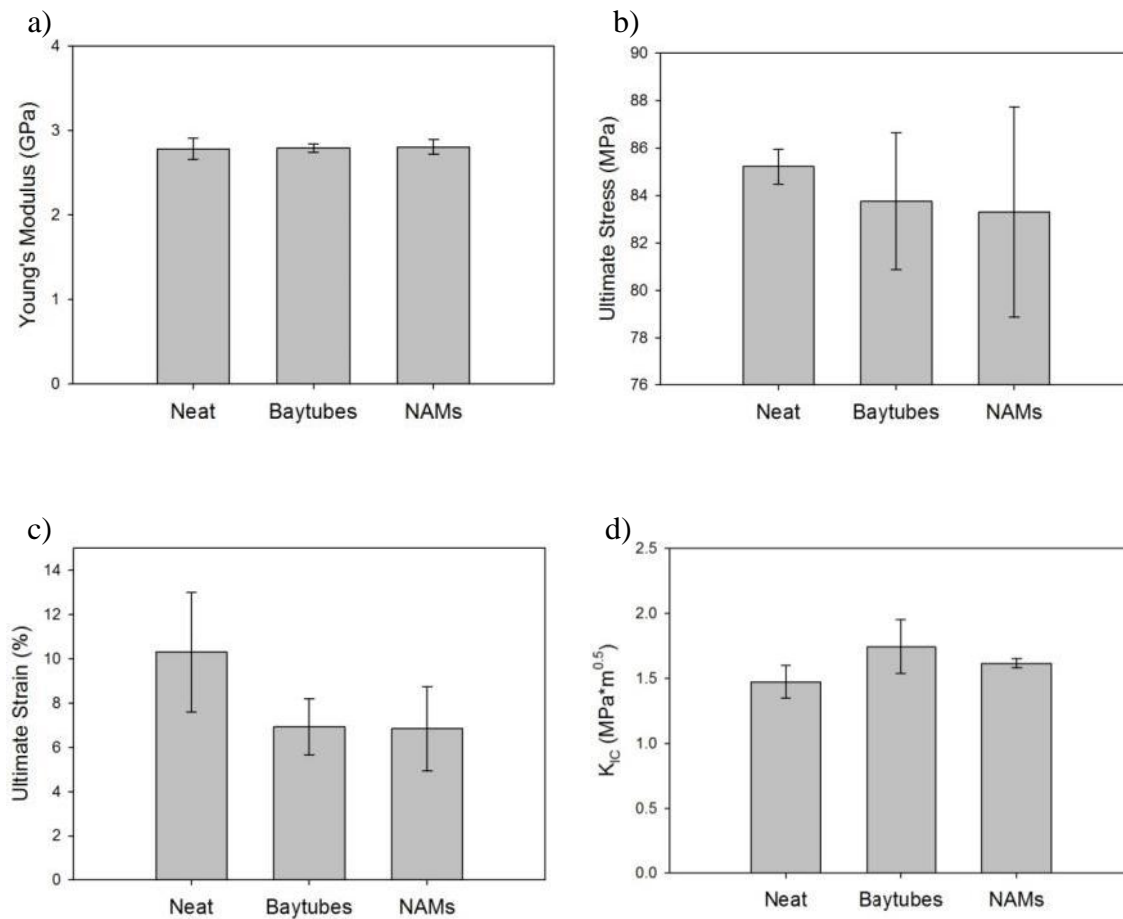


**Fig. 5.14:** Results of quasi-static tension and fracture tests of methods involving homogenization and less bath sonication time than the optimized methods with two different types of unfunctionalized 0.2 wt% CNTs (Baytubes and NAMs). No change is observed in a) Young's modulus, and decreases in b) ultimate stress and c) ultimate strain are not significant. Improvements in d) crack initiation SIF are not significant with respect to the error bars.

Table 5.2 gives a summary of the important  $K_{IC}$  values from Sections 5.2.1-5.2.3 while dispersing CNTs into the hardener first. The largest improvement was from homogenization and bath sonication (HBS), although these improvements were not beyond the error bars due to high scatter in this data. The only significant improvement in  $K_{IC}$  relative to the error bars is with cup horn sonication (CS); however, this sample also has the lowest neat  $K_{IC}$  value. Practically

speaking, this improvement is not significant relative to the same neat epoxy without significant processing.

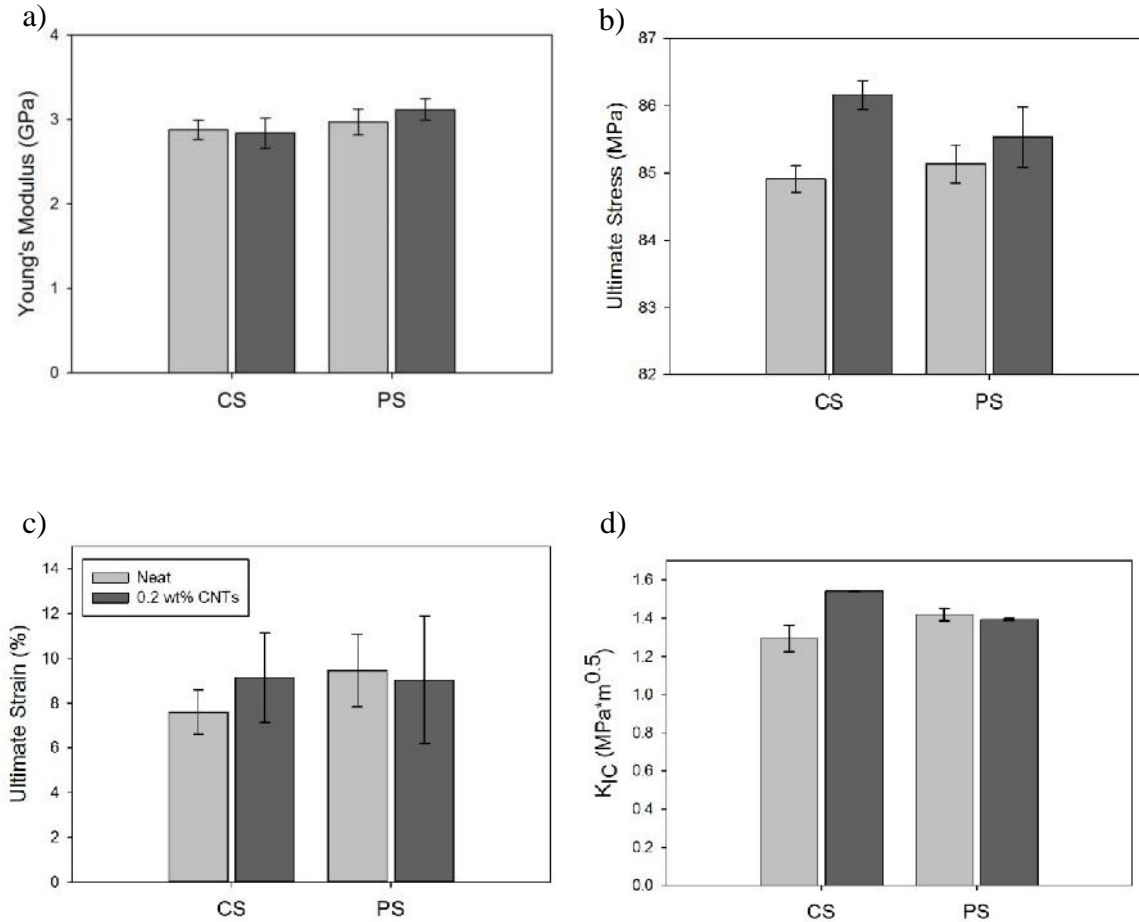


**Fig. 5.15:** Results of quasi-static tension and fracture tests of methods involving higher cavitation intensity (CS = cup horn sonication, PS = probe tip sonication) using 0.2 wt% Baytubes. No significant changes are observed in a) Young's modulus or c) ultimate strain. Improvements in b) ultimate stress and d) crack initiation SIF are significant with respect to the error bars using the CS methodology.

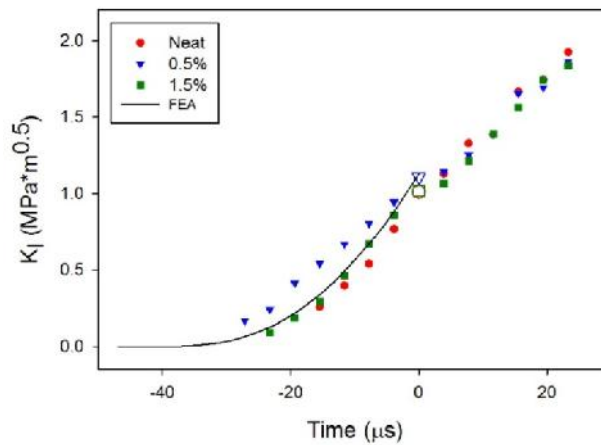
Because significant improvements had not yet been found in quasi-static mechanical properties, several dynamic fracture tests were run. Fig. 5.16 shows complete SIF histories for neat epoxy (HBS = homogenization and bath sonication), 0.5 wt% CNTs (HBS), and 1.5 wt% CNTs (BS = bath sonication). FEA, indicated by the solid line, agrees well with pre-initiation

SIFs. No significant changes were observed in  $K_{I-ini}^d$  or in post-initiation  $K_I^d$  values by the addition of CNTs.

Dispersion Technique	CNT Type	Neat $K_{IC}$ ( $MPa\sqrt{m}$ )	CNT $K_{IC}$ ( $MPa\sqrt{m}$ )	+% $K_{IC}$
BS/MS	0.5 wt% Baytubes	$1.43 \pm 0.06$	$1.52 \pm 0.10$	6
Optimized	0.25 wt% Baytubes	$1.51 \pm 0.02$	$1.47 \pm 0.07$	-3
HBS	0.2 wt% Baytubes	$1.47 \pm 0.13$	$1.74 \pm 0.21$	27
HBS	0.2 wt% NAMs	$1.47 \pm 0.13$	$1.62 \pm 0.04$	14
CS	0.2 wt% Baytubes	$1.29 \pm 0.07$	$1.54 \pm 0.002$	19
PS	0.2 wt% Baytubes	$1.42 \pm 0.03$	$1.39 \pm 0.005$	-2

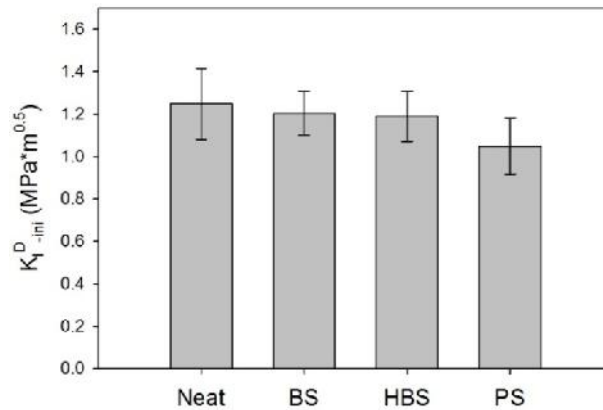
**Table 5.2:** Summary of important  $K_{IC}$  results when dispersing CNTs into the hardener first

<sup>a</sup> Note that all CNT-modified samples show significant improvement in  $K_{IC}$  compared to the original hand-stirred neat sample from Section 3.1 ( $K_{IC} = 1.26 \pm 0.01 MPa\sqrt{m}$ ).



**Fig. 5.16:** SIF history for 0.5 wt% CNTs, added by HBS (homogenization and bath sonication), and 1.5 wt% CNTs, added by BS (bath sonication), compared to neat epoxy, prepared by HBS.

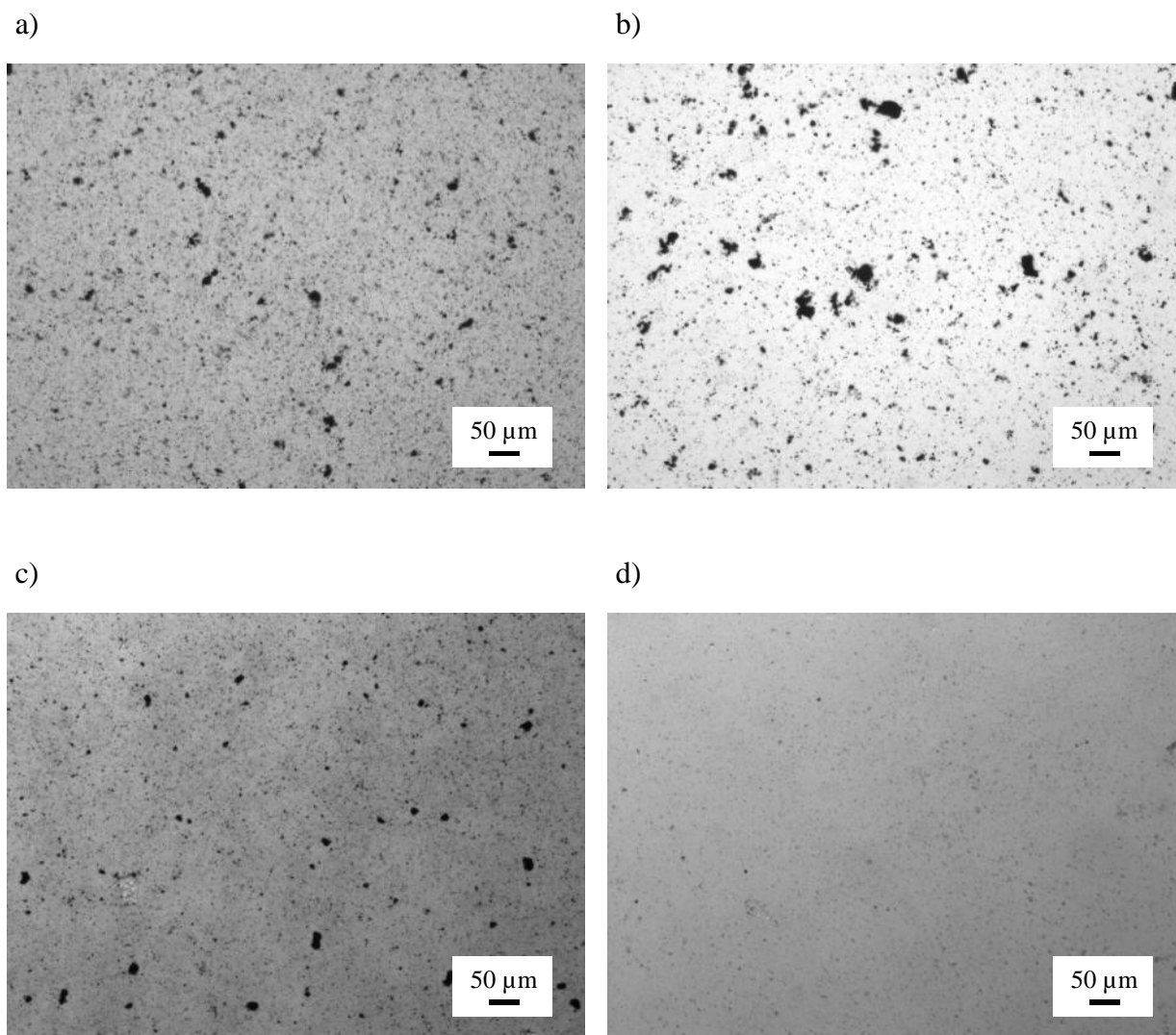
Fig. 5.17 gives average crack initiation SIF ( $K_{I-ini}^d$ ) for two or three dynamic fracture tests of several different methodologies, all at 0.2 wt% CNTs (PS = probe tip sonication, Neat = HBS). CNTs did not improve the average  $K_{I-ini}^d$  for any methodology. Because of the high scatter and tedious nature of this work, dynamic fracture testing was abandoned until quasi-static improvements could be demonstrated for CNT-infused epoxy.



**Fig. 5.17:** Dynamic crack initiation SIF for 0.2 wt% samples from several different methodologies. HBS = homogenization and bath sonication, BS = bath sonication, and PS = probe tip sonication. No improvements in  $K_{I-ini}^d$  are evident due to CNTs.

### 5.2.3.3 Microscopy

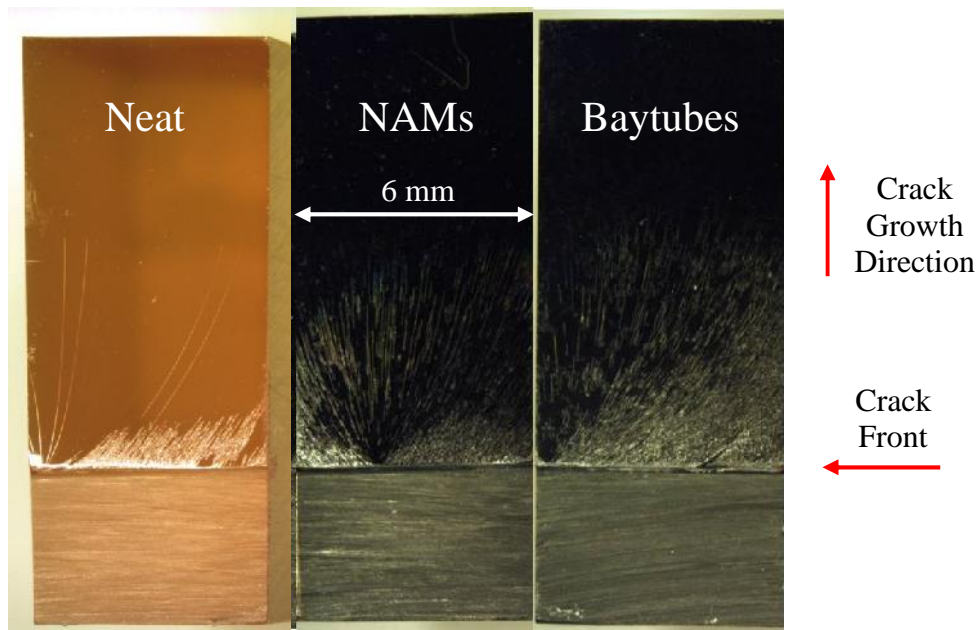
Fig. 5.18 shows the dispersion state of the four different samples presented in this section. All samples contain Baytubes except for Fig. 5.18b, which has CNTs from NAMs. Uncured samples contain 0.2 wt% CNTs, Epikure W, and Epon 862. Agglomerates are largest in Fig. 5.18b with CNTs from NAMs and smallest in Fig. 5.18d with probe tip sonication (PS). All employed processing methods were not sufficient to optically disperse CNT agglomerates according to these images. The smallest agglomerates shown in Fig. 5.18d (which exhibited decreased toughness) may suggest that more aggressive probe tip sonication could damage the CNTs.



**Fig. 5.18:** Optical microscopy of uncured 0.2 wt% unfunctionalized CNTs dispersed into both hardener and resin: a) Baytubes with homogenization and less bath sonication than the optimized methods, b) CNTs from NAMs with homogenization and less bath sonication than the optimized methods, c) cup horn sonication (CS), and d) probe tip sonication (PS). All images contain Baytubes except in b).

Fig. 5.19 shows the optical microscope images of the full fracture surfaces of the samples containing CNTs dispersed using homogenization and less bath sonication time than the samples optimized by optical microscopy. In comparison to Fig. 5.8, the size of the agglomerates has clearly decreased significantly, as no agglomerates are visible at this scale. (Note that the only difference in material processing method is the use of homogenization). Despite the apparent

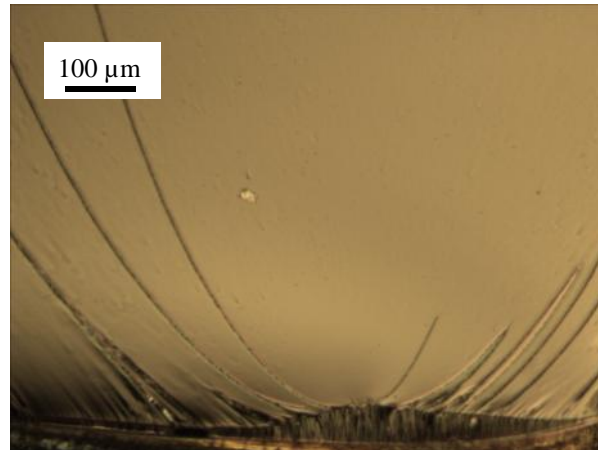
differences in surface roughness, there was no significant increase in crack initiation SIF ( $K_{Ic}$ ) by adding either type of unfunctionalized CNTs. Baytubes show the highest surface roughness, while the neat epoxy has the lowest. All three fracture surfaces are initially very rough close to the initial notch, but surface roughness is visibly different in the post-initiation region and could be an indication of higher post-initiation SIFs due to the presence of CNTs.



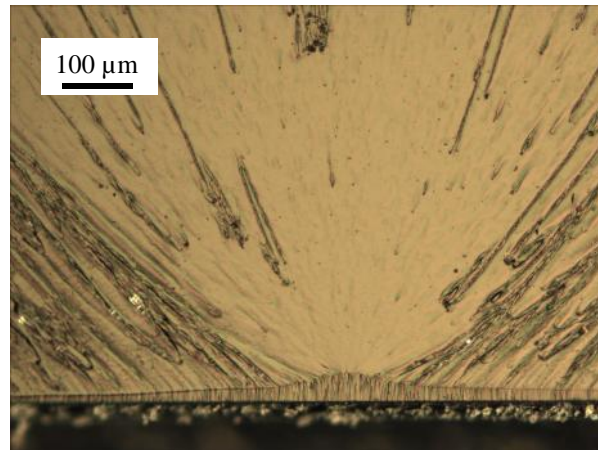
**Fig. 5.19:** Optical micrographs of fracture surfaces of 0.2 wt% unfunctionalized CNTs. Baytubes show the highest surface roughness, while the neat epoxy has the lowest.

Fig. 5.20 shows the optical microscopy of the initiation region of fracture surfaces of the samples containing CNTs dispersed using homogenization and less bath sonication time than the samples optimized by optical microscopy. Despite the apparent differences in fracture surface roughness, there was no significant increase in crack initiation toughness ( $K_{Ic}$ ) by adding either type of unfunctionalized CNTs.

a)



b)



c)

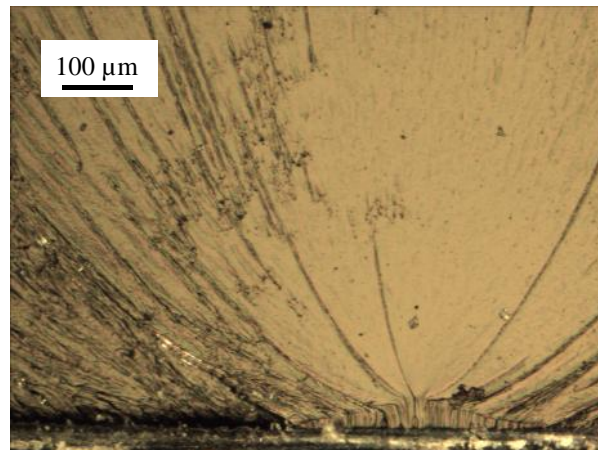


**Fig. 5.20:** Optical micrographs of fracture surfaces of (a) neat epoxy, (b) 0.2 wt% NAMs, and (c) 0.2 wt% Baytubes. Baytubes show the highest surface roughness, while the neat epoxy has the lowest.



## 5.2.4 *Dispersing CNTs into the Resin First*

### 5.2.4.1 *Methods*

After having limited or no improvement in mechanical properties by dispersing unfunctionalized CNTs into the hardener first, NH<sub>2</sub>-functionalized MWCNTs (Nanocyl 3152) were next dispersed into the resin first. The functional groups on the CNTs interact thermodynamically with the resin, leading to much better initial dispersion by hand-stirring than when unfunctionalized CNTs were dispersed into the hardener first. Also by dispersing CNTs into the resin first, the original dispersion was diluted far less when adding the second part of the epoxy, since the stoichiometric ratio of resin:hardener was 100:26.5 by weight.

Many samples were processed using calendering (Exakt Model 80E – Fig. 5.21), the popular industrial technique for dispersing CNTs in polymer systems. Resin and NH<sub>2</sub>-CNTs are fed between three opposing rollers rotating at angular velocity ratio of 1:3:9, with the fastest roller rotating at 200 rpm. The two gap sizes of the calender can be set independently from 5-100 μm, and various combinations of these gap sizes were investigated. Because calendering is a high shear technique, it works better with higher viscosity material. The masterbatch technique is frequently used [69, 70, 106] in order to raise the viscosity during dispersion by first adding a small amount of resin to the CNTs, and then later diluting the CNT/resin mixture to the desired final wt% by adding additional resin.

Samples processed using “calendering with a masterbatch” (CM) approach were first hand-stirred using 1.0 wt% NH<sub>2</sub>-CNTs in the resin (where 1.0 wt% is calculated to include the hardener—that is ~1.3 wt% NH<sub>2</sub>-CNTs in the resin.) The first pass of the masterbatch through the calender was with 90 and 30 μm gap settings. The second and third passes had 30 and 10 μm gap settings. Then resin was added to dilute the mixture to the final loading of 0.1, 0.2, or 0.3

wt% NH<sub>2</sub>-CNTs (note that these weight percentages account for the hardener, which has not yet been added), and a fourth pass was made at 30 and 10 μm gap settings. Finally the hardener was hand-stirred and then mechanically stirred for 10 minutes at 2,000 rpm.



**Fig. 5.21:** Exakt 80E calender used to disperse relatively large quantities of nanomaterials.<sup>23</sup>

The “calendering methodology” (C) involves hand-stirring the full amount of resin and NH<sub>2</sub>-CNTs (0.3 wt% including hardener) together and then passing the mixture through the calender three times (no masterbatch). Note that 0.3 wt% was chosen for this and many of the following methodologies based on the CM results, as well as the high viscosity observed in nanocomposites with more than 0.3 wt% NH<sub>2</sub>-CNTs using this method. On the first pass, both gaps are set to 30 μm; on the second pass, both gaps are set to 20 μm; and on the third pass, both gaps are set to 10 μm. Hardener was hand-stirred and then mechanically stirred at 2,000 rpm for 10 minutes.

A third calendering methodology also included probe tip sonication (PTC) with a Vibracell VCX 750 – Fig. 5.13. 0.3 wt% NH<sub>2</sub>-CNTs were hand-stirred into the resin and then probe tip

---

<sup>23</sup> www.exakt.com

sonicated using 25% amplitude at 20 seconds “on”/20 seconds “off” cycling for 30 minutes of “on time.” Then the sample was passed through the calender three times, with both gaps set to 20  $\mu\text{m}$  on the first pass, 10  $\mu\text{m}$  on the second pass, and 5  $\mu\text{m}$  on the third pass. Finally the hardener was hand-stirred and then mechanically stirred for 10 minutes at 2,000 rpm.



**Fig. 5.22:** FlakTek DAC 150 FVZ-K SpeedMixer.<sup>24</sup>

A fourth calendaring methodology included speedmixing (CMS) in an effort to better distribute the well-dispersed masterbatch material into the additional resin. Both unfunctionalized Baytubes (initially 2.7 wt% in resin) and  $\text{NH}_2$ -CNTs (initially 1.3 wt% in resin) were initially processed much like the CM method. The first pass of the masterbatch through the calender was with 90 and 30  $\mu\text{m}$  gap settings. The second pass had 30 and 10  $\mu\text{m}$  gap settings. The third and fourth passes had 30 and 5  $\mu\text{m}$  gap settings. Then resin was hand-stirred to dilute the mixture to 1.3 wt% Baytubes and 0.4 wt%  $\text{NH}_2$ -CNTs. Unlike the CM methodology, a FlakTek DAC 150 FVZ-K SpeedMixer (Fig. 5.22) was used to further disperse the masterbatch into the additional resin with 3 cycles of 5 minutes each at 3,000 rpm. The hardener was then hand-stirred and speedmixed for 3 additional cycles, such that the final specimens were 1 wt%

---

<sup>24</sup> [www.speedmixer.com](http://www.speedmixer.com)

Baytubes and 0.3 wt% NH<sub>2</sub>-CNTs. Note that the viscosity was actually higher for 0.3 wt% NH<sub>2</sub>-CNTs than 1 wt% Baytubes.



**Fig. 5.23:** Elmasonic E60H ultrasonic cleaner from Elma Ultrasonics used for simultaneous bath sonication and mechanical stirring.<sup>25</sup>

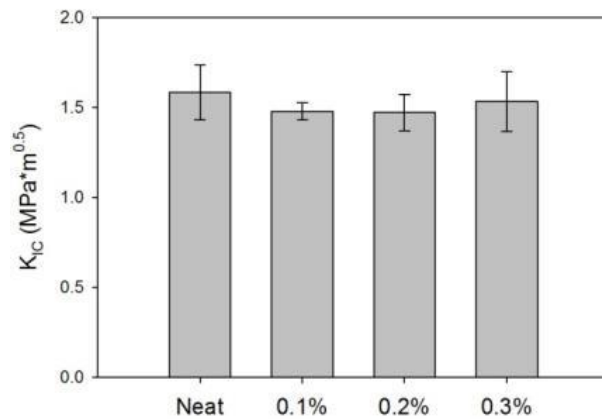
Additional samples were processed similarly to those that gave the highest improvement (+27%) in  $K_{IC}$  when unfunctionalized CNTs were dispersed into the hardener first. NH<sub>2</sub>-CNTs were first homogenized with Epon 862 for 5 minutes at 25,000 rpm. Then the sample was simultaneously mechanically stirred at 1,000 rpm and bath sonicated at 37 kHz using an Elmasonic E60H bath sonicator (Fig. 5.23) for 30 minutes at 80°C. Hardener was added such that the final weight percent of CNTs was 0.3 wt%, and then the mixture was mechanically stirred at room temperature for 10 minutes at 2,000 rpm.

#### 5.2.4.2 Results

Fig. 5.24 shows the crack initiation SIF results when calendaring with a masterbatch (CM) for 0.1-0.3 wt% NH<sub>2</sub>-CNTs. In all of these cases, samples were homogenized for 5 minutes prior to calendaring. Evidently, no improvements in measured  $K_{IC}$  values were observed.

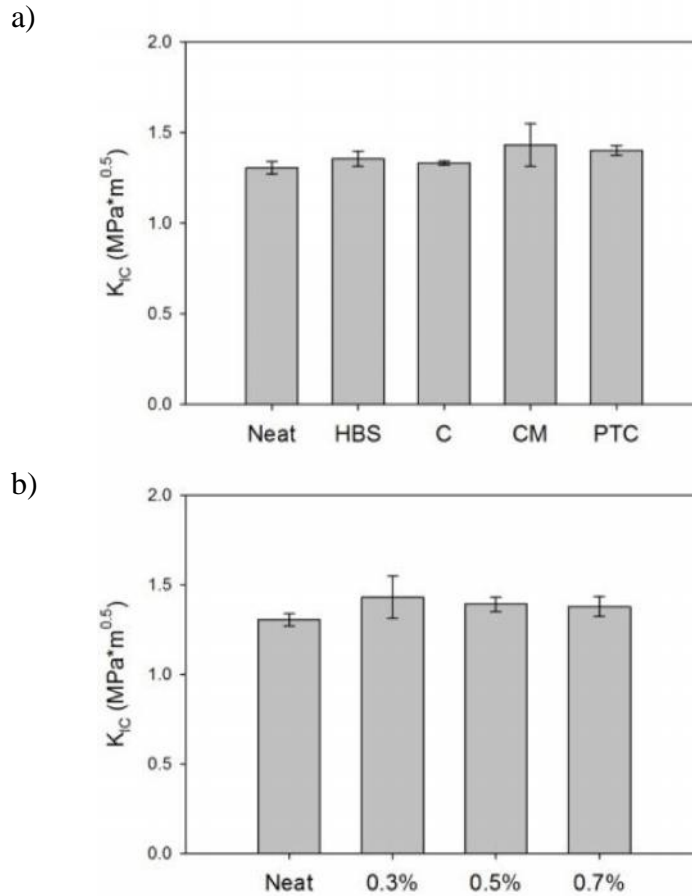
---

<sup>25</sup> www.elmaultrasonic.com



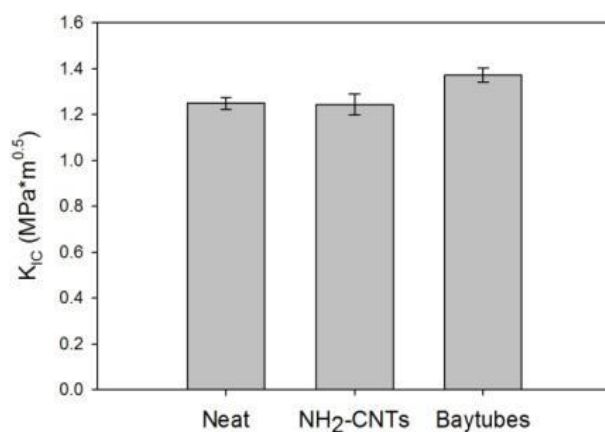
**Fig. 5.24:** Crack initiation SIF of different wt.% NH<sub>2</sub>-CNTs dispersed first into resin using homogenization and calendaring with a masterbatch (CM).

Fig. 5.25a shows crack initiation SIF results for several different methodologies using 0.3 wt% NH<sub>2</sub>-CNTs. Fig. 5.25b gives the crack initiation SIF results when calendaring with a masterbatch (CM) without homogenization using 0.3-0.7 wt% NH<sub>2</sub>-CNTs. Note that 0.3 wt% CM appears in both Figs. 5.25a and 5.25b. As shown in Fig. 5.25a, homogenization and bath sonication (HBS) gave a +4% (insignificant) improvement, calendaring (C) without homogenization gave a +2% (insignificant) improvement, calendaring with masterbatch (CM) without homogenization resulted in a +10% (insignificant) improvement, and probe tip sonication and calendaring (PTC) without homogenization gave a +7% (insignificant) improvement in crack initiation SIF. On the other hand, as shown in Fig. 5.25b, 0.5 wt% CNTs gave a +7% (significant) improvement and 0.7 wt% gave a +6% (insignificant) improvement in  $K_{IC}$ ; however, these two mixtures were far too viscous to be useful to process any three-phase fiber reinforced composite such as carbon fiber/CNT/epoxy composite.



**Fig. 5.25:** Crack initiation SIF of NH<sub>2</sub>-CNTs dispersed first into resin using a) several different methodologies all at 0.3 wt% (HBS = homogenization and bath sonication, C = calendering, CM = calendering with a materbatch, and PTC = probe tip sonication and calendering), and b) using calendering with a masterbatch (no homogenization) at three different weight percentages. All methodologies gave small improvements in  $K_{IC}$ .

Fig. 5.26 shows crack initiation SIF for specimens dispersed by calendering and speedmixing (CMS). 0.3 wt% NH<sub>2</sub>-CNTs had no effect on  $K_{IC}$ , while 1 wt% Baytubes caused a small but significant (+10%) improvement in  $K_{IC}$ .



**Fig. 5.26:** Crack initiation SIF of 0.3 wt% NH<sub>2</sub>-CNTs and 1 wt% Baytubes dispersed by calendering and speedmixing (CMS). Baytubes gave a small but significant improvement in  $K_{IC}$ .

Dispersion Technique	CNT Type	Neat $K_{IC}$ (MPa $\sqrt{m}$ )	CNT $K_{IC}$ (MPa $\sqrt{m}$ )	+% $K_{IC}$
HBS	0.3 wt% NH <sub>2</sub> -CNTs	1.31 ± 0.03	1.36 ± 0.04	4
C	0.3 wt% NH <sub>2</sub> -CNTs	1.31 ± 0.03	1.33 ± 0.01	2
CM	0.3 wt% NH <sub>2</sub> -CNTs	1.31 ± 0.03	1.43 ± 0.12	10
PTC	0.3 wt% NH <sub>2</sub> -CNTs	1.31 ± 0.03	1.40 ± 0.03	7
CMS <sup>a</sup>	0.3 wt% NH <sub>2</sub> -CNTs	1.25 ± 0.03	1.24 ± 0.05	-1
CMS <sup>a</sup>	1.0 wt% Baytubes	1.25 ± 0.03	1.37 ± 0.03	10

**Table 5.3:** Summary of important  $K_{IC}$  results when dispersing CNTs into the hardener first

<sup>a</sup> CMS batches were prepared with older hardener that had oxidized, likely leading to the reduced Neat  $K_{IC}$  value

Table 5.3 gives a summary of the important  $K_{IC}$  values from this section while dispersing CNTs into the resin first. Despite improvements in dispersion beyond those achieved when dispersing CNTs into the hardener first (see Section 5.2.3.3), improvements in  $K_{IC}$  are less than

those presented in Table 5.2. Note also that the notch sharpening technique here differs from Table 5.2, likely causing the discrepancy in Neat  $K_{Ic}$  values between the two tables.

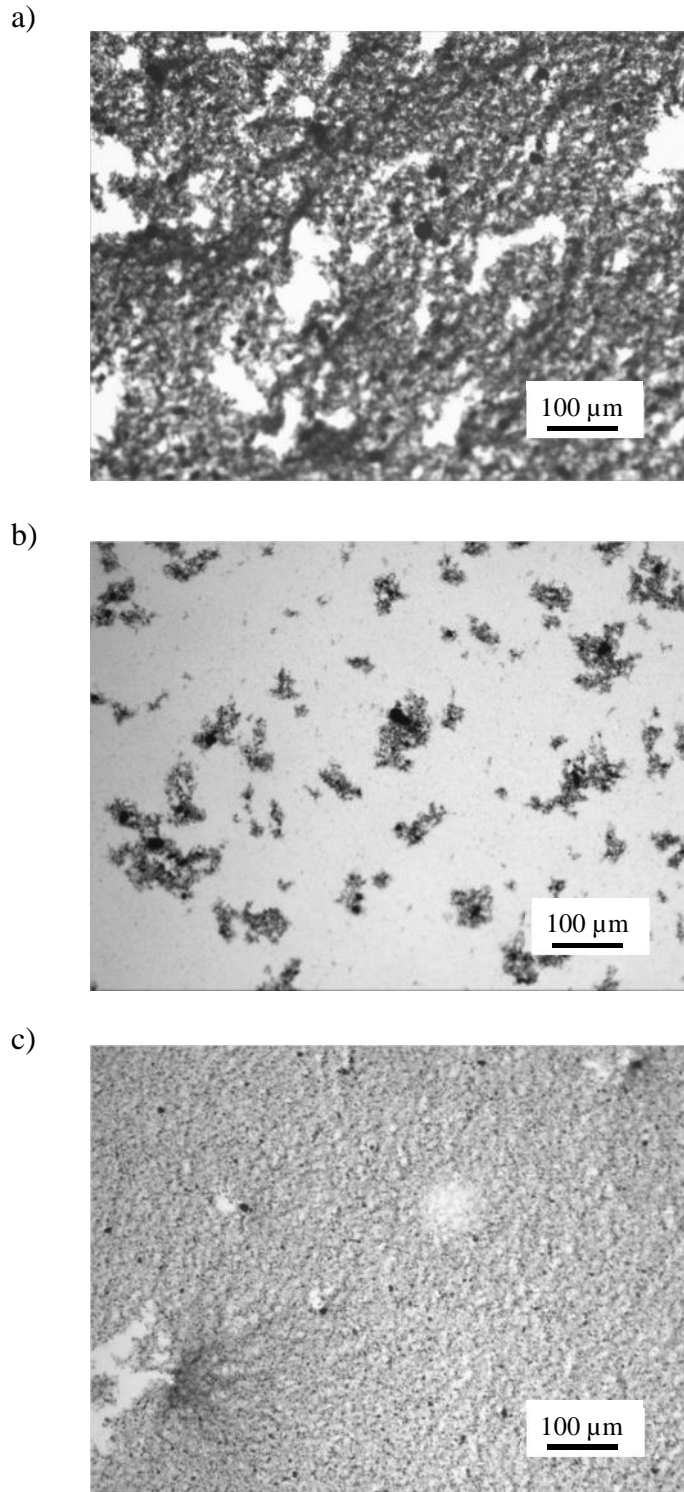
#### 5.2.4.3 Microscopy

Fig. 5.27 illustrates the difference between dilution effects of dispersing into the hardener first compared to dispersing into the resin first. Initial dispersion in Fig. 5.27a (hardener and unfunctionalized CNTs) is seemingly good; however, once the resin is added to the mixture as in Fig. 5.27b, the well-dispersed network of CNTs and hardener appear to be broken into many small, isolated patches. On the contrary, excellent dispersion was obtained by dispersing the  $\text{NH}_2$ -CNTs into the resin first and then adding hardener into the mixture (Fig. 5.27c).

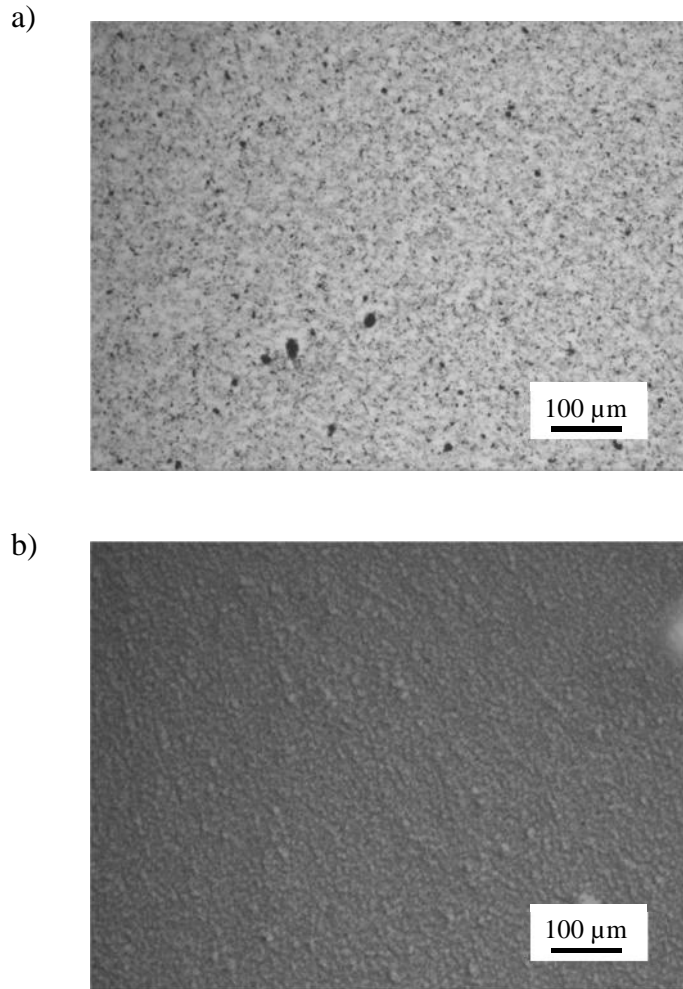
Fig. 5.28 shows optical microscopy of specimens produced by calendering and speedmixing (CMS) two different types of CNTs into the resin first. Fig. 5.28a closely resembles Fig. 5.27c, both of which involve calendering  $\text{NH}_2$ -CNTs with a masterbatch technique. Fig. 5.28b shows improved dispersion by using unfunctionalized Baytubes. These CNTs can be processed at a much higher wt% while remaining relatively inviscous due to the lack of interactions between functional groups and epoxy resin.

Fig. 5.29 shows the scanning electron microscopy (SEM) images of three different resin-first methodologies. Calendering without a masterbatch (C) (Fig. 5.29a) has several agglomerates in the micron scale and several large patches of neat resin. Calendering with a masterbatch (CM) (Fig. 5.29b) shows fairly homogeneous dispersion without agglomeration; however, this image has the least fracture surface features which are typically indicative of resistance to crack growth. Probe tip sonication and calendering (PTC) (Fig. 5.29c) has a large 10  $\mu\text{m}$  agglomerate which appears to cause a significant disruption in the crack growth pattern.





**Fig. 5.27:** Optical micrographs of uncured CNT dispersions: a) 0.25 wt% Baytubes dispersed in hardener using homogenization and bath sonication, b) resin added to a), and c) 0.5 wt% NH<sub>2</sub>-CNTs dispersed into resin first using calendaring with a masterbatch (CM) after the addition of hardener. The final dispersion state in c) is far superior to the final dispersion state in b).



**Fig. 5.28:** Optical micrographs of uncured CNTs, resin and hardener: a) 0.3 wt% NH<sub>2</sub>-CNTs and b) 1 wt% Baytubes. Both samples were dispersed using calendaring and speedmixing (CMS). The dispersion state in b) is superior to the dispersion state in a).

Fig. 5.30 shows optical microscopy of the initiation region of fracture surfaces of samples containing CNTs dispersed using calendaring. Baytubes dispersed by calendaring and speedmixing show the most surface roughness features; however, neat epoxy has the deepest features. It appears that the toughening mechanisms of the epoxy and the CNTs are competing with each other, possibly explaining the modest (+10%) improvements in  $K_{IC}$  with well dispersed Baytubes in Fig. 5.30d.

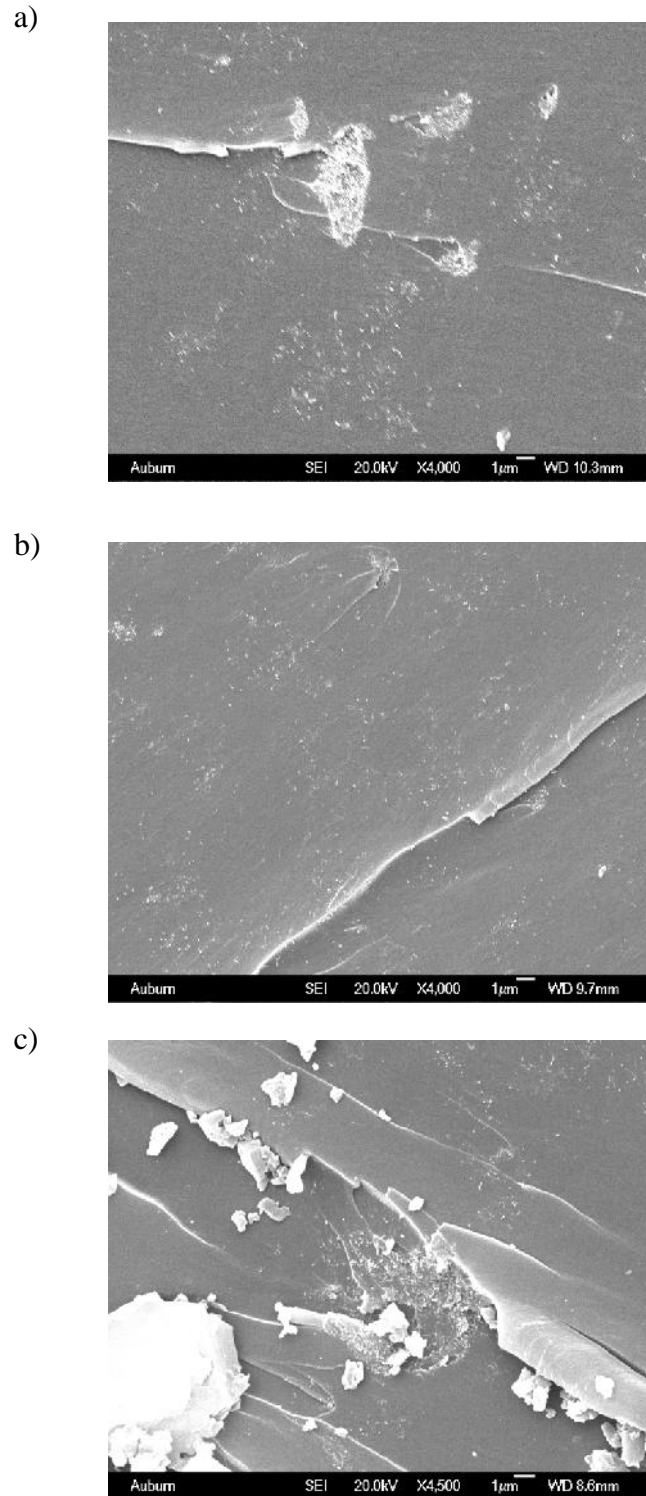


**Fig. 5.29:** SEM of 0.3 wt% NH<sub>2</sub>-CNTs dispersed first into the resin using different calendaring methodologies: a) calendaring without a masterbatch (C), b) calendaring with a masterbatch (CM), and c) probe tip sonication and calendaring (PTC).

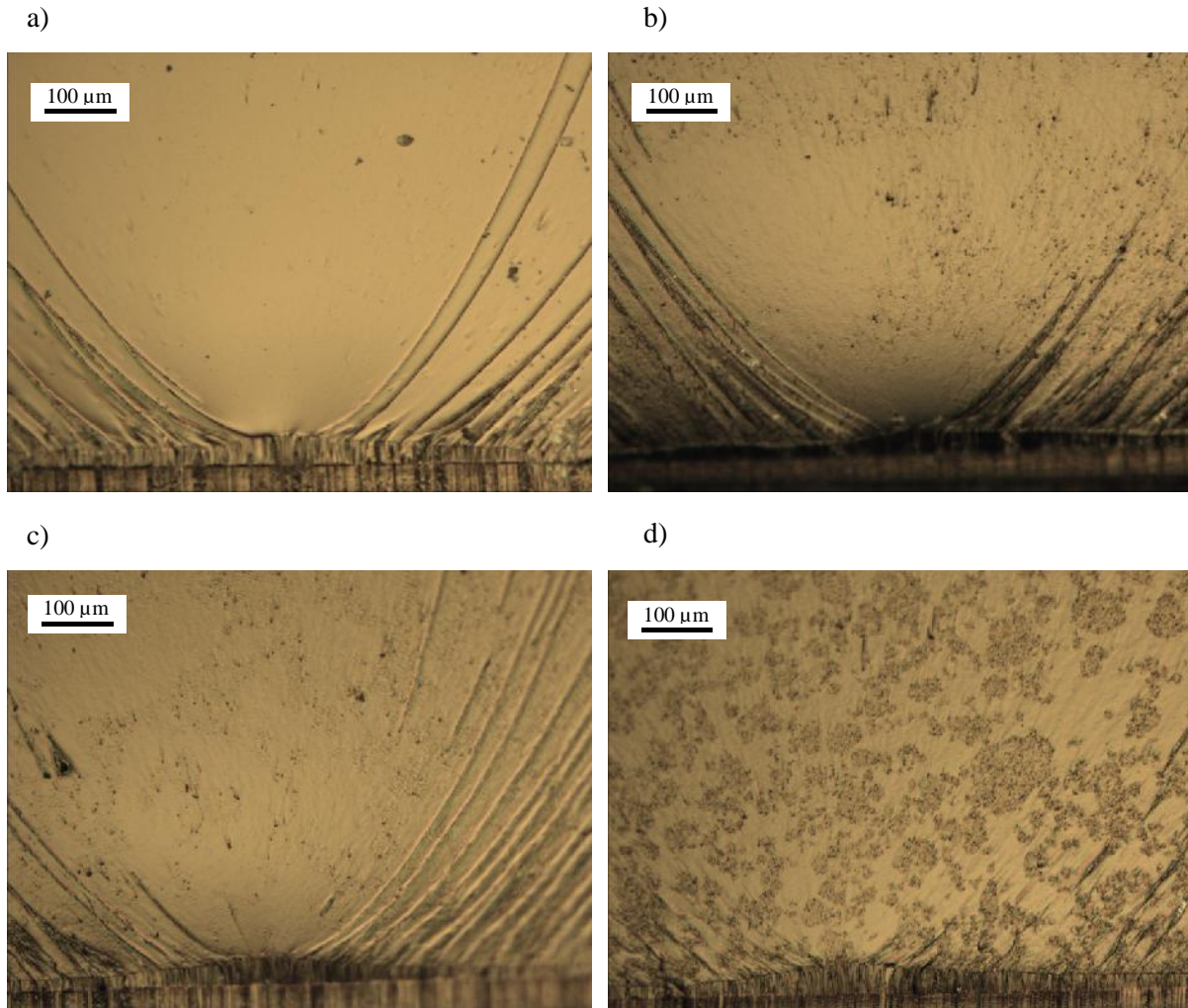


**Fig. 5.30:** Optical micrographs of fracture surfaces of (a) neat epoxy, (b) 0.3 wt%  $\text{NH}_2$ -CNTs calendaring with a masterbatch, (c) 0.3 wt%  $\text{NH}_2$ -CNTs calendaring with a masterbatch and speedmixing, and (d) 1 wt% Baytubes calendaring with a masterbatch and speedmixing.

## 5.2.5 Altering Resin Stoichiometry

### 5.2.5.1 Methods

After dispersing CNTs into the resin first, achieving excellent dispersion, and yet failing to achieve improvements in crack initiation SIF significant enough to justify the expense, potential health hazard, and tediousness of adding CNTs, a new variable was considered. Ashrafi et al. [50] initially achieved insignificant (+20%) improvement in  $K_{Ic}$  at the manufacturer-

recommended stoichiometry (1:0.8 molar ratio) with 0.2 wt% functionalized CNTs (and a -28% decrease in  $K_{IC}$  with 0.2 wt% unfunctionalized CNTs); however, by adding 25% more hardener than the manufacturer-recommended stoichiometry (1:1 molar ratio), along with functionalized CNTs, they found significant improvements in  $K_{IC}$  (+38%), ultimate stress (34%), and ultimate strain (56%) (see Tables 1.6 and 1.7).

In order to study the effects of varying the stoichiometry, samples were made with and without 0.2 wt%  $\text{NH}_2$ -CNTs with an additional +5%, +10%, and +25% hardener (Epikure W) beyond the manufacturer-recommended 1:1 molar ratio of resin:hardener. In all these trials, CNTs were dispersed using calendaring, with the first pass at 90 and 30  $\mu\text{m}$  gap settings, the second pass at 30 and 10  $\mu\text{m}$  gap settings, and then three more passes at 30 and 5  $\mu\text{m}$  gap settings. The altered amounts of Epikure W were hand-stirred and then mechanically stirred for 10 minutes. Unlike previous samples of Epon 862 and Epikure W, these were cured for 3.5 hours at 140°C after degassing for 30 minutes at 80°C. Note that this new curing schedule was chosen based on optimizing the cure kinetics of  $\text{NH}_2$ -CNTs in Epon 862 and Epikure W at the manufacturer-recommended ratio of resin:hardener.

#### 5.2.5.2 Results

Figs. 5.31 and 5.32 give the results of dynamic mechanical analysis (DMA) using three-point bending samples with the normal amount of hardener, as well as an additional +5%, +10%, and +25%. Figs. 31a and 32a correspond to neat epoxy samples, while Figs. 31b and 32b correspond to CNT-modified samples with 0.2 wt%  $\text{NH}_2$ -CNTs dispersed by calendaring. CNTs reduce the initial storage modulus of samples with the normal amount and +5% additional hardener, whereas little initial change was observed for the samples with +10% and +25%

additional hardener. The glass transition occurred at a much higher temperature ( $\sim 20^\circ\text{C}$ ) for normal (1:1 molar ratio) epoxy with CNTs than the corresponding neat sample. Similar increases in the glass transition temperature occurred with additional +5% and +10% hardener *with or without adding CNTs*. No change was attributed to the addition of CNTs to any of the samples

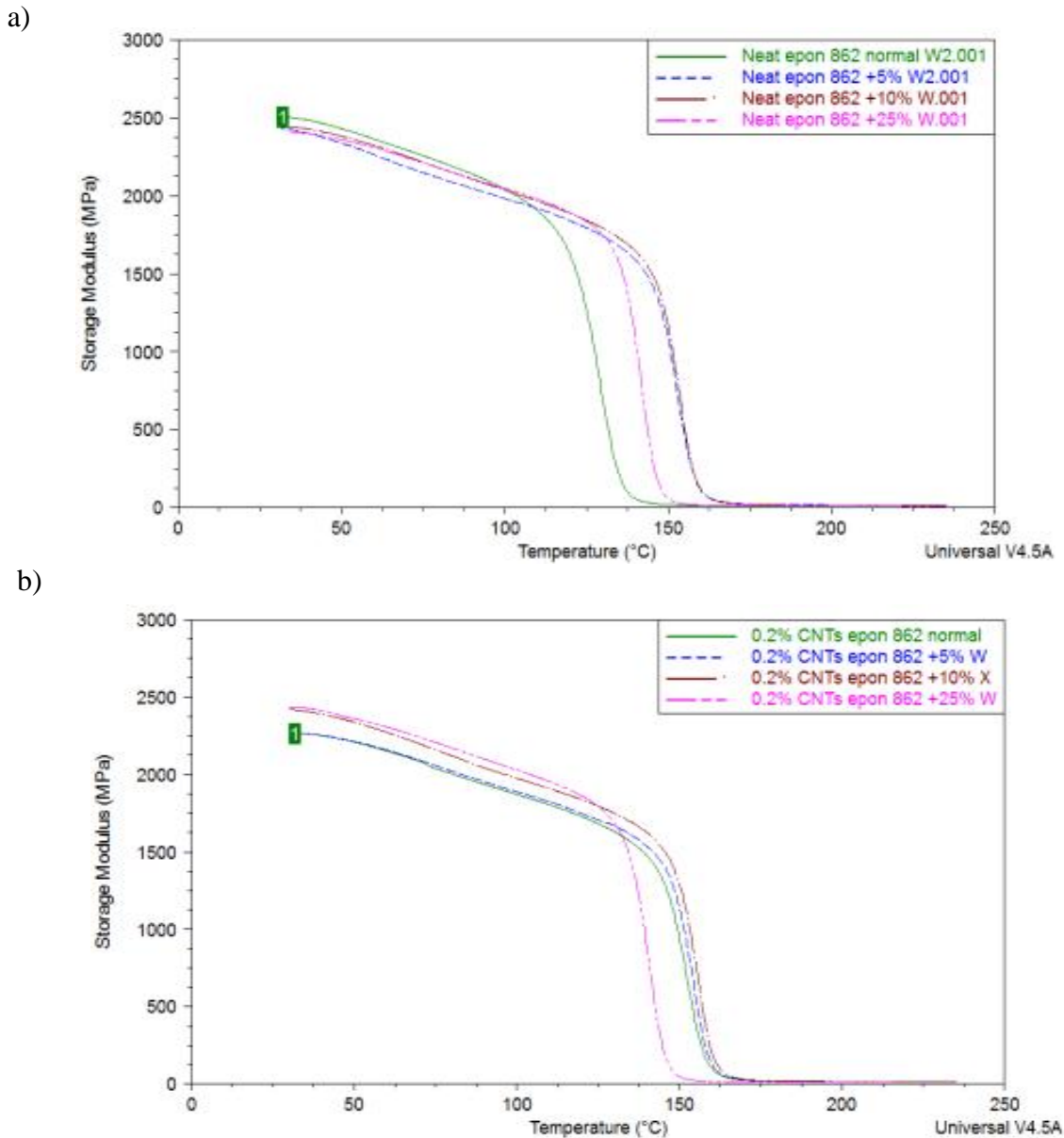


**Fig. 5.31:** Effect of additional hardener (+5%, +10%, +25%) beyond the manufacturer-recommended (1:1 molar) ratio, with and without 0.2 wt%  $\text{NH}_2\text{-CNTs}$  on storage modulus of a) neat epoxy samples and b) CNT-modified epoxy samples.

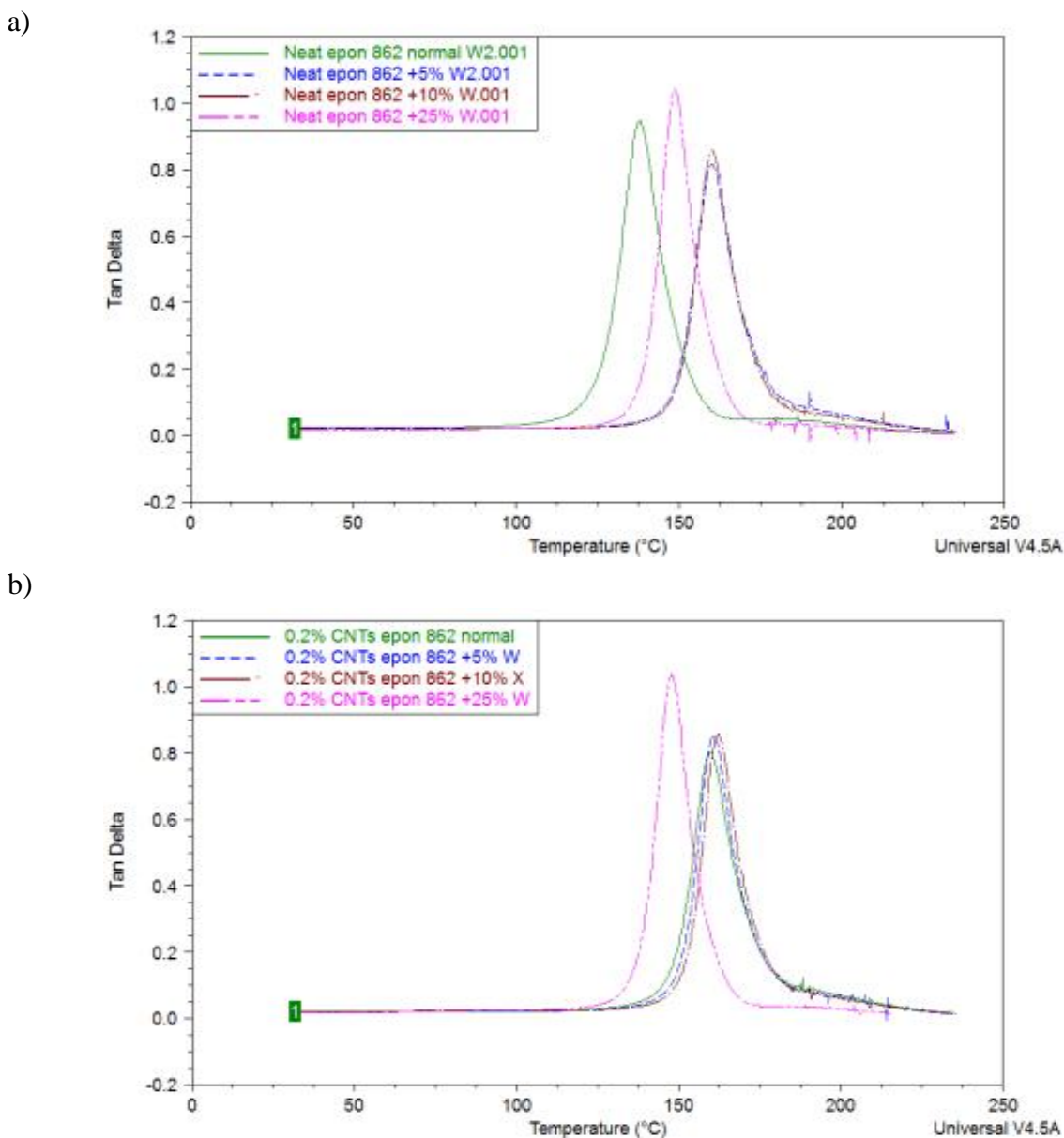


**Fig. 5.32:** Effect of additional hardener (+5%, +10%, +25%) beyond the manufacturer-recommended (1:1 molar) ratio, with and without 0.2 wt%  $\text{NH}_2$ -CNTs on tan delta of a) neat epoxy samples and b) CNT-modified epoxy samples.

with additional (+5%, +10%, +25%) hardener. It appears that the amine groups on the CNTs participate in the epoxy reaction, especially for the manufacturer recommended stoichiometry.

Fig. 5.33 gives the results of thermal and mechanical tests of epoxy when the amount of hardener was varied, with and without 0.2 wt%  $\text{NH}_2$ -CNTs. The glass transition temperature ( $T_g$ )



(Fig. 5.33a) was determined to be the peak of the tan delta curve (Fig. 5.32). The crosslink density Fig. 5.33b was determined using,

$$\eta = \frac{E'}{3RT}, \quad T = T_g + 40^\circ C, \quad (5.5)$$

where  $\eta$  is the crosslink density,  $E'$  is the storage modulus evaluated at  $T$ , and  $R$  is the gas constant [107]. Because the primary reaction between the diamine hardener and the resin prepolymer is more reactive than the secondary amine reaction (Fig. 5.34), additional hardener lowers the crosslink density. This decreased crosslink density has little effect on Young's modulus (Fig. 5.33c), ultimate stress (Fig. 5.33d), or ultimate strain (Fig. 5.33e), but it has an inverse relationship with the crack initiation SIF (Fig. 5.33f), with or without the presence of CNTs. Decreased crosslink density causes a decrease in brittleness and hence an increase in crack initiation SIF. While the mechanical improvements of adding additional hardener and CNTs simultaneously to neat epoxy of Ashrafi et al. [50] were not realized, there is a decrease in the ultimate stress (Fig. 5.33d) and ultimate strain (Fig. 5.33e) when CNTs are added without additional hardener. These properties are regained with a small amount (+5%) of extra hardener.

In addition to the processing conditions, different stoichiometry and the presence of amine groups on functionalized CNTs can change the nature of the epoxy matrix significantly. When  $\text{NH}_2$ -CNTs are well-dispersed, they can have a similar effect on the entire matrix as adding extra amine-based hardener. When enough additional hardener (+25%) was added, a 19% improvement in  $K_{Ic}$  was found *without CNTs*, most likely due to the decrease in crosslink density. It is therefore very important to compare CNT-modified samples with neat epoxy using the same processing conditions and the same chemical environments (when functionalized CNTs are used).



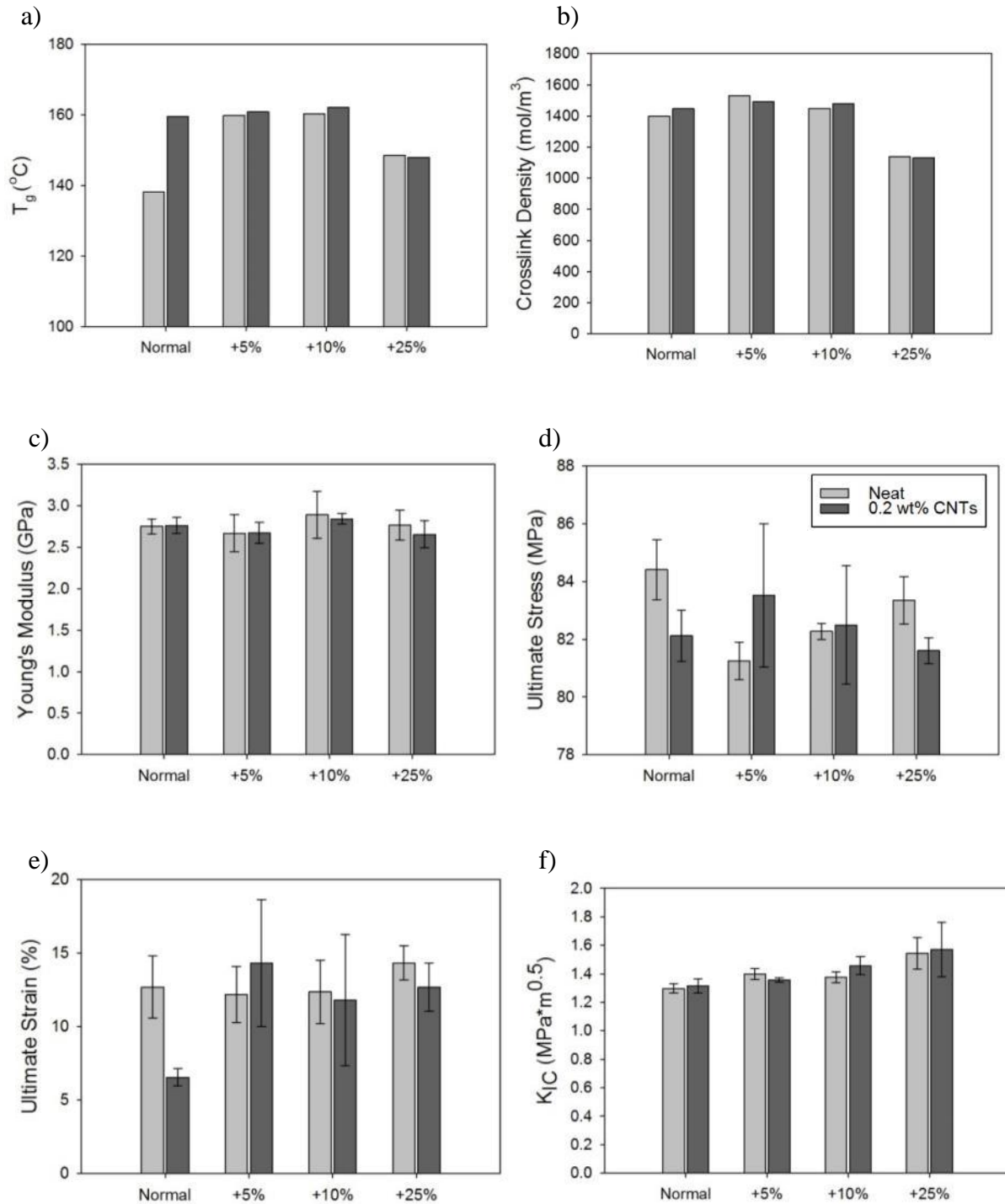


**Fig. 5.33:** Effect of altering the stoichiometry with additional hardener (+5%, +10%, +25%) (beyond the manufacturer-recommended resin:hardener 1:1 molar ratio), with and without 0.2 wt% NH<sub>2</sub>-CNTs, on a) glass transition temperature ( $T_g$ ), b) crosslink density, c) Young's modulus, d) ultimate stress, e) ultimate strain, and f) crack initiation SIF ( $K_{IC}$ ).

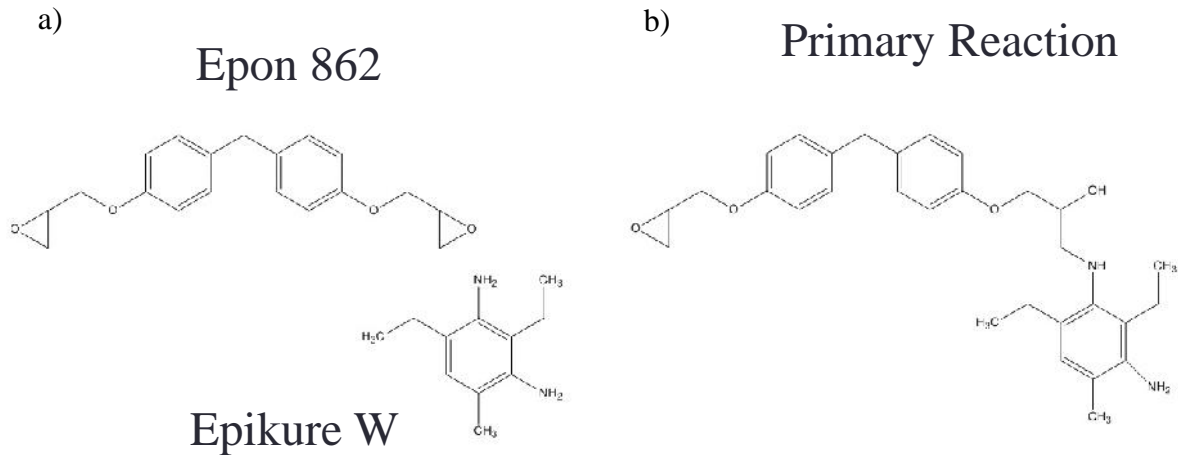


**Fig. 5.34:** a) Molecular structure of Epon 862 and Epikure W and b) primary reaction between Epon 862 and Epikure W. Note that up to four epoxide groups can react with a single molecule of Epikure W, but the primary reaction is the most reactive. Thus additional hardener beyond the stoichiometric ratio results in reduced crosslink density.

### 5.3 Discussion and Conclusions

Despite various attempts<sup>26</sup> to improve the crack initiation SIF of epoxy using CNTs through many different dispersion techniques detailed above, no significant improvements were observed large/significant enough to justify the elaborate processing needed and the cost of carbon nanotubes. Four different types of carbon nanotubes were used; their descriptions and the largest improvements in  $K_{IC}$  found with each are listed in Table 5.4. (Note that all works detailed above using functionalized CNTs involved Nanocyl 3152.)

Depending on the dispersion technique, age of the resin and hardener, cure cycle, and notch sharpening technique, a wide variety of  $K_{IC}$  values ( $1.29\text{-}1.59 \text{ MPa}\sqrt{m}$ ) have been reported in this work for *neat* Epon 862 and Epikure W at the manufacturer-recommended resin:hardener ratio of 100:26.5 by weight. When holding all of these variables constant and

<sup>26</sup> Many other iterations of material preparation were also attempted but are not detailed here in favor of brevity.

increasing the amount of hardener (+5%, +10%, +25%) more than the manufacturer-recommended ratio by weight),  $K_{IC}$  increased from 1.30-1.54  $MPa\sqrt{m}$  with insignificant changes in the tensile properties (Fig. 5.33). In other words, without sacrificing tensile properties,  $K_{IC}$  of Epon 862 and Epikure W can be improved significantly (+19%) by adding relatively inexpensive hardener *instead of CNTs*. This is consistent with the observations of Ashrafi et al. [50], as well as Fernandez et al. [108] and Gupta et al. (1985) [109], who all measured increases in  $K_{IC}$  after adding additional hardener beyond the 1:1 molar ratio of resin:hardener. Most researchers attribute improvements in CNT-modified epoxy to the superior material properties of the nanofiller material, but it is quite possible that many of these improvements are instead due to changes in the curing chemistry caused by the presence of carbon nanotubes and by the processing of these CNTs.

MWCNT	Functionalized?	OD (nm)	Length ( $\mu m$ )	+% $K_{IC}$
Baytubes C150P	No	15	1 - >10	27
NAMs <sup>b</sup>	No	< 8	20	14
Nanocyl 3152 (short thin)	NH <sub>2</sub>	9	> 1	10
Nanocyl 7000 (plasma)	NH <sub>2</sub>	9.5	1.5	2

**Table 5.4:** Details of multi-walled CNTs used and largest improvement in  $K_{IC}$ .

<sup>b</sup>NAMs = Nanostructured and Amorphous Materials

Similarly, the addition of homogenization to the methodology consistently increased  $K_{IC}$  of the neat epoxy. During homogenization of the hardener without CNTs, Epikure W was observed to oxidize, which also typically occurs as it ages. It is quite possible that this oxidation

affected the polymerization chemistry in much the same way that additional hardener did in Fig. 5.33f.

Four different epoxy systems were used unsuccessfully to *significantly* improve the crack initiation SIF of neat epoxy with carbon nanotubes; they are listed in Table 5.5 along with the percent improvement in  $K_{IC}$  found *without CNTs* between the lowest and highest  $K_{IC}$  measured for each epoxy system. The differences in  $K_{IC}$  for the other three epoxy systems are attributed largely to differences in cure schedule (typically room temperature vs. high temperature cure). It should be emphasized here that the combination of Epon 862 and Epikure W does not cure at room temperature.

Resin	Hardener	Lowest $K_{IC}$ measured ( $MPa\sqrt{m}$ )	Highest $K_{IC}$ measured ( $MPa\sqrt{m}$ )	+% $K_{IC}$
Epon 862	Epikure W	1.3	1.6	23
Epon 862	Epikure 3230	2.0	3.8	90
SC15 Part A	SC15 Part B	1.8	2.7	50
US Composites 635	Medium (speed)	1.8	2.7	50

**Table 5.5:** Different epoxy systems used and largest improvement in  $K_{IC}$  of neat epoxy.

Evidence in this work, as well as the works of Mirjalili et al. [63] and Thostenson and Chou [71], suggests that it is possible for dispersion to be too complete for improvement in crack initiation SIF. Instead it may be that a certain agglomeration size and distribution is ideal for resisting crack initiation. Mirjalili et al. [63] quantified dispersion using optical microscopy and saw the highest improvement in  $K_{IC}$  for a CNT area fraction ( $A_f$ ) value around 0.5 using optical microscopy. Specimens with  $A_f$  values of 0.2 (poor dispersion) had decreased  $K_{IC}$  compared to

neat epoxy, while specimens with  $A_f$  values greater than 0.9 (better dispersion) had negligible improvements in  $K_{IC}$ . Similarly, Thostenson and Chou [71] reported higher  $K_{IC}$  for more highly agglomerated samples and lower  $K_{IC}$  for samples with optimized dispersion. In the present work, optimized dispersion techniques (Section 5.2.2) led to decreases in  $K_{IC}$  when dispersing into the hardener first. When dispersing into the resin first, calendaring with a masterbatch with (CMS) and without (CM) speedmixing led to excellent dispersion but only 10% improvements in  $K_{IC}$ , provided that samples were not homogenized first. (Homogenization may actually improve the crack initiation SIF of neat samples more than the addition of well-dispersed CNTs.) Calendaring without a masterbatch and the combination of probe tip sonication and calendaring both gave inferior dispersion to calendaring with a masterbatch, and yet both demonstrated higher surface roughness under SEM (Fig. 5.30). Furthermore, the best overall improvements presented here (+27% in Fig. 5.14d) have relatively inferior dispersion (Fig. 5.18a) of CNTs.

Calendaring without a masterbatch and the combination of probe tip sonication and calendaring both gave inferior dispersion to calendaring with a masterbatch, and yet both demonstrated higher surface roughness near micron-scale agglomerates under SEM (Fig. 5.30). Fracture surface roughness is an indicator of increased toughness once the crack reaches that location; however, it does not necessarily correlate with toughness at crack initiation. CNTs appear to be good at absorbing energy from a growing crack, but (in the results presented in this work) they do not cause much difference in terms of crack initiation toughness. One possible explanation is that the crack initiates in a location with relatively few CNTs. Another explanation is that the CNT agglomerates act like material defects and aid in crack initiation. It is also possible that the interface between resin and CNTs is weak (possibly due to damage to the CNTs

that occurred during processing), such that the superior properties of CNTs are not transferred to the matrix. Finally, CNTs are much smaller than the cracks that have been introduced into fracture samples, (particularly the functionalized CNTs in this study as detailed in Table 5.4). A mathematically sharp crack tip is assumed, but in reality, the crack has a finite size, which may be significantly larger than individual (well-dispersed) CNTs.

Excluding the methodologies recreated by the current authors without finding significant improvements in  $K_{Ic}$ , only four previous reports in Table 1.5 (Alishahi et al. [52], Ayatollahi et al. [53], Gkikas et al. [55], and Shtein et al. [66]) have improved the crack initiation SIF of their CNT-modified epoxy nanocomposites beyond the values measured here for neat Epon 862 and Epikure W. This suggests that it is easier to improve the fracture toughness of an epoxy system with nanotubes if the initial neat  $K_{Ic}$  is relatively low. Fig. 5.29 may indicate that the toughening mechanism provided by well-dispersed CNTs (as demonstrated in many previous works with relatively brittle epoxy) actually competes with the toughening mechanism of the relatively tough epoxy system investigated in this work (Epon 862 and Epikure W). Ultimately, the practical application of modifying epoxy with CNTs appears to reside with a few researchers [52, 53, 55, 66] who have produced relatively tough epoxy nanocomposites, in all cases using probe tip sonication of unfunctionalized MWCNTs.

## **Chapter 6. Quasi-static and Dynamic Fracture of CFRPs**

In this chapter, details on the quasi-static and dynamic fracture of interlaminar and intralaminar cracks in unidirectional carbon fiber reinforced polymers (CFRPs) are presented. Orthotropic displacement field equations for determining stress intensity factors (SIFs) for both intralaminar and interlaminar cracks using in-plane displacements determined by DIC (Chapter 2) are discussed. These displacement field equations also require orthotropic elastic property inputs, whose determination for both interlaminar and intralaminar configurations are described. Because CFRPs experience failure in the interlaminar region, carbon nanotubes (CNTs) and MCFs (milled carbon fibers) have been incorporated into the epoxy matrix in order to test their ability to resist interlaminar crack growth.

### **6.1 Specimen Preparation**

This chapter involves the incorporation of CNTs and MCFs dispersed first into the resin and then painted on between layers of carbon fiber using a hand layup procedure similar to Karapappas et al. [92] and Romhany & Szebenyi [94] with the goal of enhancing interlaminar and intralaminar fracture properties under quasi-static and dynamic loading conditions. Table 6.1 gives the dimensions for CNTs and MCFs, which are nanoscale and microscale rod-shaped fillers, respectively.

Filler	Length	Diameter
NH <sub>2</sub> -CNTs (NC 3152)	1 μm	9 nm
MCFs	100 μm	8 μm

**Table 6.1:** Dimensions of Fillers: NH<sub>2</sub>-CNTs vs. MCFs

### 6.1.1 Dispersion of Fillers

Unidirectional carbon fiber fabric was provided by V2 Composites, Inc. The resin system was Epon 862 and curing agent Epikure W from Momentive Specialty Chemicals, Inc. Three thick CFRPs were prepared in order to compare the effects of carbon nanotubes on the interlaminar and intralaminar fracture properties: carbon fiber/epoxy (“Neat”), CNT/carbon fiber/epoxy (with multi-walled NH<sub>2</sub>-functionalized NC 3152 CNTs from Nanocyl), and MCF/carbon fiber/epoxy (with MCFs from Toho Tenax).

CNTs were dispersed by calendaring with a masterbatch technique using an Exakt 80E Calender (see Section 5.2.4.1). CNTs were first dispersed in the resin at 1.3 wt% using the calender until a thick paste was formed using three passes. The first pass through the calender was with 90 and 30 μm gap settings. The second and third passes had 30 and 10 μm gap settings. This masterbatch was then diluted with additional resin to 0.4 wt% CNTs by hand-stirring, followed by two additional passes through the calender at 30 and 5 μm gap settings. Lastly, Epikure W was hand-stirred and mechanically stirred in, such that the final weight percentage of CNTs in epoxy was 0.3 wt%.

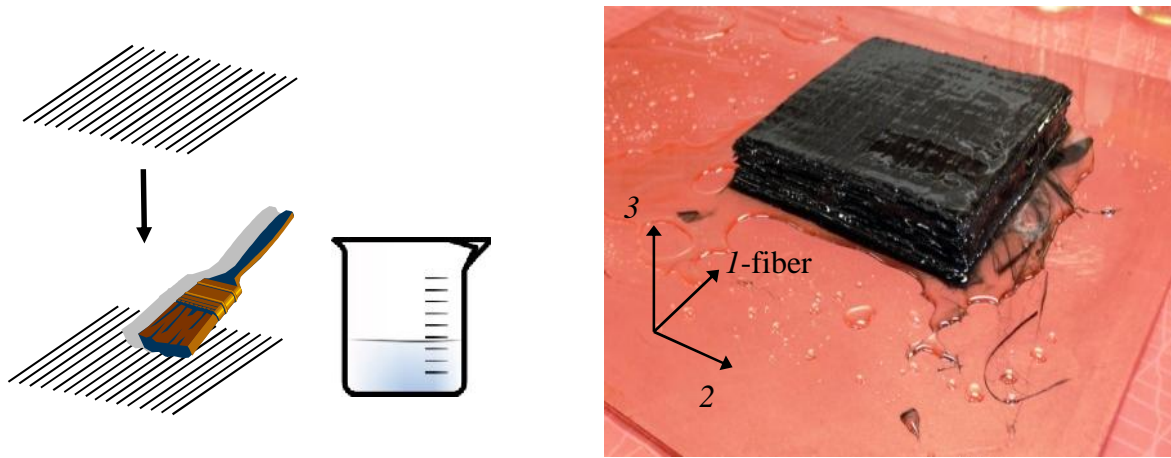
MCFs were dispersed using mechanical stirring (Fig. 5.4), such that the final weight percentage of MCFs was 5 wt%. Due to their size and the low viscosity of the resin system, MCFs were not dispersed as well as CNT. Note also that MCFs were 100x longer and had 1000x greater diameter than CNTs, which translates to 10x greater aspect ratio for CNTs (Table 6.1).



### **6.1.2 Fabrication of Carbon Fiber Reinforced Polymers (CFRPs)**

Thick CFRP plates were fabricated using a hand layup and vacuum-bagging procedure. Resin (with or without pre-dispersed fillers) was painted on between each of 60 layers of unidirectional carbon fiber fabric, all oriented in the same direction ( $[0^\circ]_{60}$ ) as shown in Fig. 6.1a. Each sample was originally cured for 2.5 hours at  $120^\circ\text{C}$  inside a vacuum bag. Samples were then machined with a tile saw to create interlaminar and intralaminar specimens from the same original composite plate; interlaminar and intralaminar orientations are given schematically in Fig. 6.1b. Dimensions of interlaminar slices are given in Fig. 6.2a. Three such interlaminar slices were stacked and glued together (Fig. 6.2b) in a vise using the same epoxy system as before in order to achieve ~50 mm thick interlaminar samples, such that the methodology involving digital image correlation (DIC) and high-speed photography could be implemented in order to measure fracture parameters during both pre- and post-initiation phases of the dynamic fracture event. Both interlaminar and intralaminar specimens were heated back to  $120^\circ\text{C}$  for 2.5 hours (in order to cure the epoxy glue used in interlaminar specimens) before post-curing for 3 hours at  $180^\circ\text{C}$ , such that the final geometry of all dynamic fracture specimens was 50 mm x 50 mm x 6 mm (Fig. 6.3b), and all samples were subjected to identical curing schedules. Quasi-static interlaminar and intralaminar fracture samples were prepared similarly, with dimensions given in Fig. 6.3a. Specimens were given a speckle coating for performing measurements using DIC. Pre-notches were then made with a diamond-tipped saw and sharpened by pressing a razor blade into the notch tip. This notching technique was chosen as an alternative to the difficulties of Teflon tape insertion for intralaminar samples detailed in Czabaj & Ratcliffe [75], who also measured interlaminar and intralaminar fracture of specimens machined from the same original composite sheet.

a)



b)

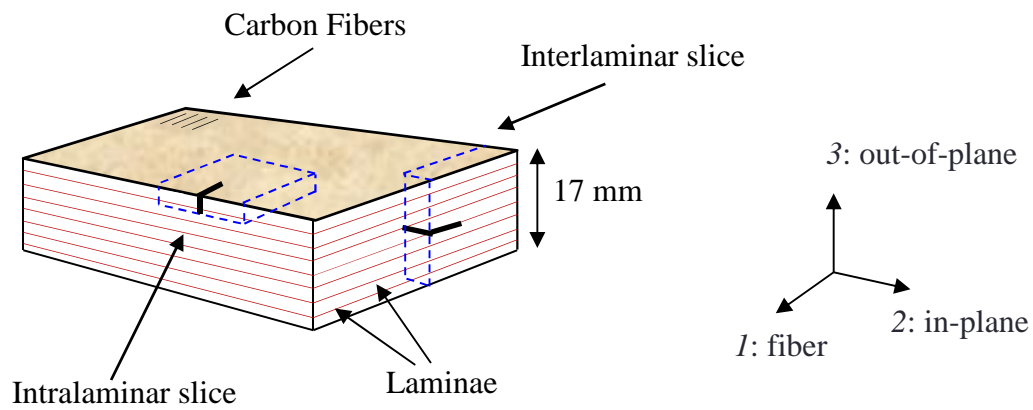
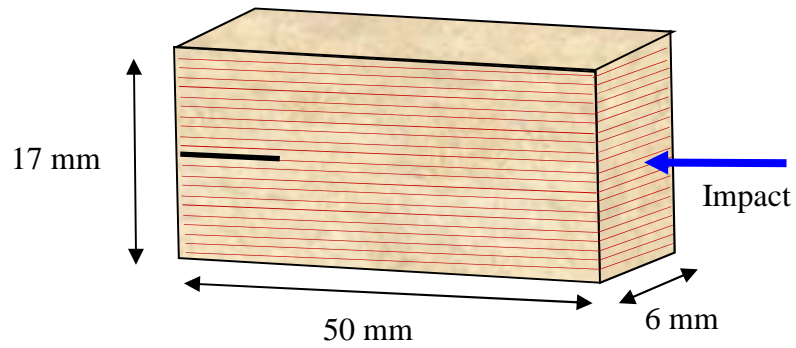


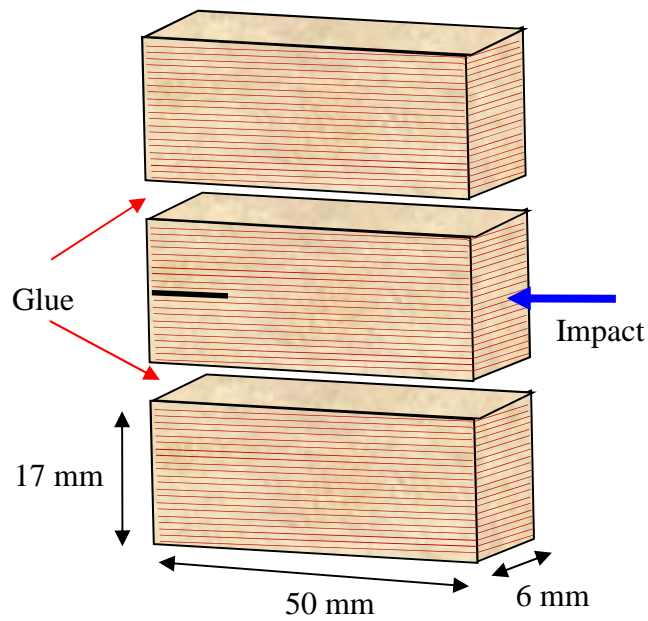
**Fig. 6.1:** CFRP plate preparation details: a) Wet layup procedure for 60-layer CFRPs. b) Orientation of interlaminar and intralaminar slices machined from the same thick composite plate.

a)



Interlaminar Slice

b)



Final Interlaminar Specimen

**Fig. 6.2:** Interlaminar specimen preparation details: a) Dimensions of a single interlaminar slice machined from the CFRP manufactured in Fig. 6.1 for dynamic fracture experiments. b) Preparation of dynamic interlaminar fracture specimens by stacking and gluing three blocks with the dimensions shown in a).

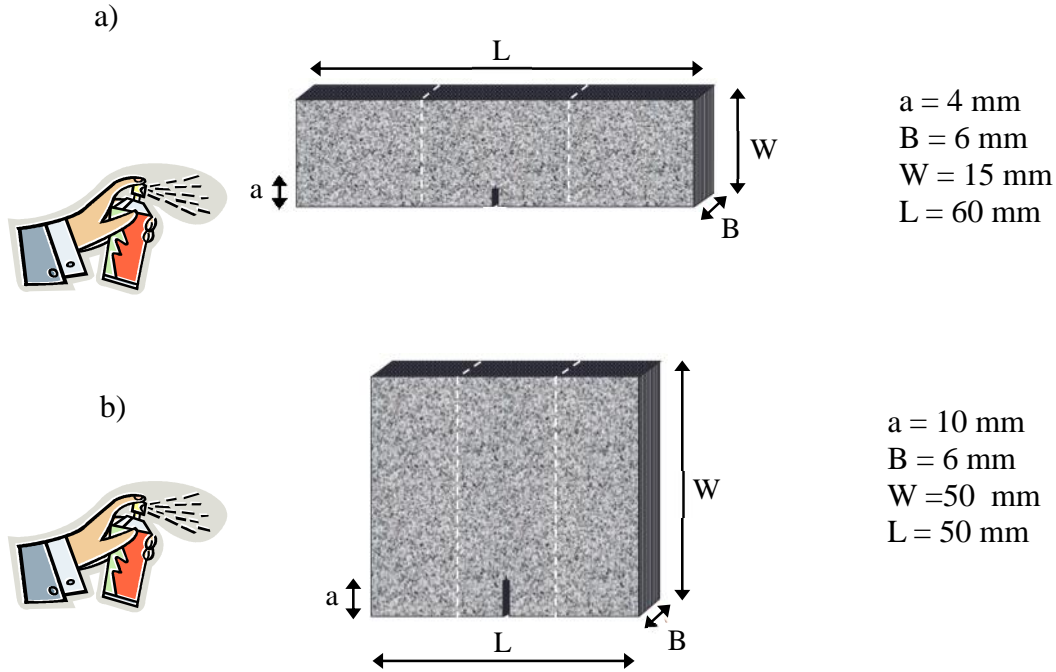


**Fig. 6.3:** Dimensions of fracture specimens subjected to a) quasi-static loading and b) dynamic impact loading. White dash lines indicate epoxy glue lines for interlaminar specimens. Both specimens were given a speckle coating for performing DIC.

## 6.2 Experimental Details

### 6.2.1 Quasi-Static Fracture Tests

Three-point bend quasi-static fracture tests (Fig. 6.4a) were performed on an Instron 4465 test stand at a crosshead speed of 0.01 mm/s using a 5 kN load cell. Load-point displacement was assumed to be the crosshead displacement. Load and displacement data were collected at a sample rate of  $10 \text{ s}^{-1}$ . Digital images were recorded every 3 seconds for determining SIFs from surface displacement fields. The critical SIF ( $K_{IC}$ ) was chosen to be the SIF associated with the image immediately prior to visible crack tip movement. Crack growth was continued at least until the load decreased below half of the peak load, at which time cracks had all grown well beyond an  $a/W$  value of 0.5.

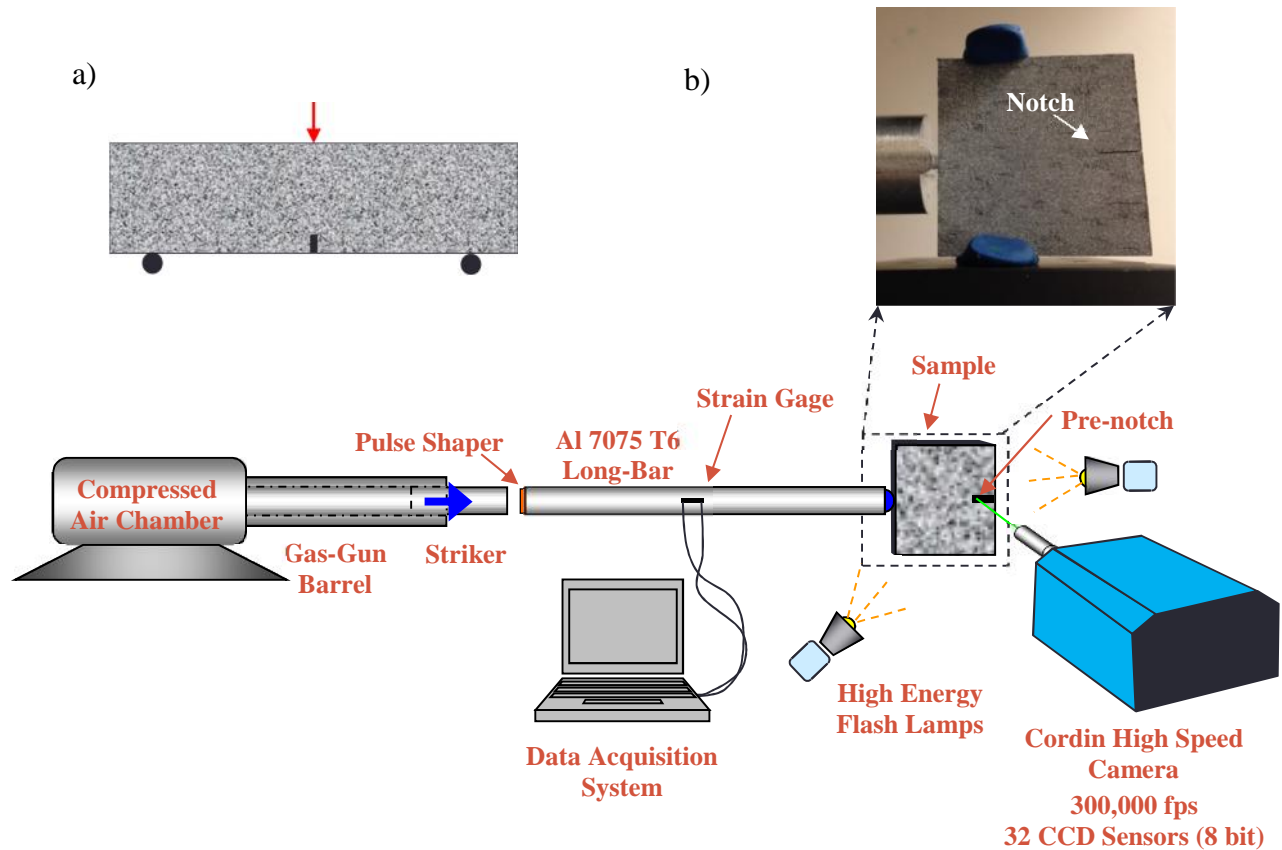


**Fig. 6.4:** Specimen and experimental setup details: a) Quasi-static 3-point bending of edge-cracked specimen and b) Dynamic 1-point impact of edge-cracked specimen.

### 6.2.2 Dynamic Fracture Tests

Dynamic 1-point impact tests (10 psi) were performed using the Kolsky bar (long-bar), detailed in Section 2.1 and depicted in Fig. 6.4b. A soft aluminum pulse shaper was used between the striker and the long-bar in order to temper the loading rate such that more images could be captured in the pre- and post-initiation phases of the dynamic fracture event. Due to the increased sensitivity of the orthotropic displacement field equations for these highly anisotropic materials, small rollers of putty have been used only on the impact side of the specimen so as not to interfere with crack opening. The high-speed camera collected images at ~300,000 frames per second during the dynamic fracture event. These images were paired with undeformed images

taken at the same framing rate prior to testing. Pairs of images were compared using DIC (Section 2.3) in order to determine full-field in-plane displacements on the specimen surface.

The following orthotropic displacement field equations [101] were then used to determine SIFs *for each deformed image for all quasi-static specimens, as well as for all dynamic specimens prior to crack initiation*:

$$\begin{aligned}
 u(r, \theta) &= K_I \sqrt{\frac{2r}{f}} \operatorname{Re} \left[ \frac{1}{\tilde{\nu}_2 - \tilde{\nu}_1} (p_1 \tilde{\nu}_2 z_1 - p_2 \tilde{\nu}_1 z_2) \right] + K_{II} \sqrt{\frac{2r}{f}} \operatorname{Re} \left[ \frac{1}{\tilde{\nu}_2 - \tilde{\nu}_1} (p_1 z_1 - p_2 z_2) \right] \\
 v(r, \theta) &= K_I \sqrt{\frac{2r}{f}} \operatorname{Re} \left[ \frac{1}{\tilde{\nu}_2 - \tilde{\nu}_1} (q_1 \tilde{\nu}_2 z_1 - q_2 \tilde{\nu}_1 z_2) \right] + K_{II} \sqrt{\frac{2r}{f}} \operatorname{Re} \left[ \frac{1}{\tilde{\nu}_2 - \tilde{\nu}_1} (q_1 z_1 - q_2 z_2) \right].
 \end{aligned} \tag{6.1}$$

For intralaminar fracture of an orthotropic material with  $x$ - $z$  and  $y$ - $z$  planes as symmetry planes,  $\tilde{\nu}_j$  ( $j = 1, 2$ ) are the two roots of:  $S_{11} \tilde{\nu}^4 + (2S_{12} + S_{66}) \tilde{\nu}^2 + S_{22} = 0$ ,

$$\begin{aligned}
 p_j &= \tilde{\nu}_j^2 S_{11} + S_{12}, \\
 q_j &= \tilde{\nu}_j S_{12} + \frac{S_{22}}{\tilde{\nu}_j}, \\
 z_j &= \sqrt{\cos \theta + \tilde{\nu}_j \sin \theta},
 \end{aligned} \tag{6.2}$$

For interlaminar fracture of an orthotropic material with  $x$ - $z$  and  $y$ - $z$  planes as symmetry planes,  $\tilde{\nu}_j$  ( $j = 1, 2$ ) are the two roots of:  $S_{11} \tilde{\nu}^4 + (2S_{13} + S_{55}) \tilde{\nu}^2 + S_{33} = 0$ ,

$$p_j = \tilde{\nu}_j^2 S_{11} + S_{13}, \quad q_j = \tilde{\nu}_j S_{13} + \frac{S_{33}}{\tilde{\nu}_j}, \quad z_j = \sqrt{\cos \theta + \tilde{\nu}_j \sin \theta}. \tag{6.3}$$

In the above equations,  $K_I$  is the mode-I SIF,  $K_{II}$  is the mode-II SIF (which is expected to be near zero for this symmetric loading case),  $u$  and  $v$  are the sliding and opening displacements, and  $S_{11}$ ,  $S_{22}$ ,  $S_{33}$ ,  $S_{12}$ ,  $S_{13}$ ,  $S_{55}$ , and  $S_{66}$  are coefficients of the  $S$ -matrix; their ultrasonic

determination has been described in Section 4.2.2. A least-squares analysis was used to determine a single  $K_I$  and  $K_{II}$  value for each pair of images. For consistency, the critical SIF ( $K_{IC}$  for quasi-static loading and  $K_{I-ini}^d$  for dynamic loading) was chosen to be the mode-I SIF value for the image immediately prior to visible crack initiation in the images. For the case of a dynamically growing crack, the orthotropic displacement field equations [102] are:

$$\begin{aligned}
u(r, \theta) &= \frac{2}{C_{66}R(c)} \operatorname{Re} \left[ \left( \frac{\tilde{z}_2 - \beta_2}{\beta_1 - \beta_2} \sqrt{\frac{z_1}{2f}} - \frac{\tilde{z}_1 - \beta_1}{\beta_1 - \beta_2} \sqrt{\frac{z_2}{2f}} \right) K_I^d - \left( \frac{x - \beta y^2 - \tilde{z}_2}{\beta_1 - \beta_2} \sqrt{\frac{z_1}{2f}} - \frac{x - \beta y^2 - \tilde{z}_1}{\beta_1 - \beta_2} \sqrt{\frac{z_2}{2f}} \right) K_{II}^d \right] \\
v(r, \theta) &= \frac{2}{C_{66}R(c)} \operatorname{Re} \left[ - \left( \beta_1 \frac{\tilde{z}_2 - \beta_2}{\beta_1 - \beta_2} \sqrt{\frac{z_1}{2f}} - \beta_2 \frac{\tilde{z}_1 - \beta_1}{\beta_1 - \beta_2} \sqrt{\frac{z_2}{2f}} \right) K_I^d + \left( \beta_1 \frac{x - \beta y^2 - \tilde{z}_2}{\beta_1 - \beta_2} \sqrt{\frac{z_1}{2f}} - \beta_2 \frac{x - \beta y^2 - \tilde{z}_1}{\beta_1 - \beta_2} \sqrt{\frac{z_2}{2f}} \right) K_{II}^d \right].
\end{aligned} \tag{6.4}$$

For intralaminar fracture of an orthotropic material with  $x$ - $z$  and  $y$ - $z$  planes as symmetry planes,

$$\begin{aligned}
\tilde{z}_j (j=1,2) \text{ are the 2 roots of: } \tilde{z}^4 + \left( r_l^2(c)y^2 + \frac{r_s^2(c)}{y^2} - \frac{(1+x)^2}{y^2} \right) \tilde{z}^2 + \frac{r_l^2(c)r_s^2(c)}{\beta} &= 0, \\
\beta = \frac{S_{11}}{S_{22}}, \quad \beta' = \frac{2S_{12} + S_{66}}{2\sqrt{S_{11}S_{22}}}, \quad |\beta| = \frac{3\sqrt{S_{11}S_{22}} + S_{12}}{\sqrt{S_{11}S_{22}} - S_{12}}, \quad c_l = \sqrt{\frac{C_{11}}{\dots}}, \quad c_s = \sqrt{\frac{C_{66}}{\dots}}, \quad r_l^2(c) = 1 - \left( \frac{c}{c_l} \right)^2, \quad r_s^2(c) = 1 - \left( \frac{c}{c_s} \right)^2, \\
y^2 = \left( \frac{|+1|}{|-1|} \right) \left( \frac{3 - |+'(|+1|)}{4\sqrt{\beta}} \right), \quad x = \sqrt{\beta} y^2 \left( \frac{3 - |}{1 + |} \right), \quad \beta_j(c) = \frac{y^2 r_l^2(c) + \tilde{z}_j^2(c)}{(1+x)\tilde{z}_j(c)} \quad (j=1,2), \\
R(c) = \sqrt{\beta} y^2 r_l(c) r_s(c) - \frac{\sqrt{\beta} y^2 r_l(c) + x^2 r_s(c)}{\sqrt{\beta} y^2 r_l(c) + r_s(c)}, \quad z_j = r(\cos \theta + \tilde{z}_j(c) \sin \theta).
\end{aligned} \tag{6.5}$$

For interlaminar fracture of an orthotropic material with  $x$ - $z$  and  $y$ - $z$  planes as symmetry planes,

$$\tilde{z}_j (j=1,2) \text{ are the 2 roots of: } \tilde{z}^4 + \left( r_l^2(c)y^2 + \frac{r_s^2(c)}{y^2} - \frac{(1+x)^2}{y^2} \right) \tilde{z}^2 + \frac{r_l^2(c)r_s^2(c)}{\beta} = 0,$$

$$\begin{aligned}
\beta &= \frac{S_{11}}{S_{33}}, \quad \beta' = \frac{2S_{13} + S_{55}}{2\sqrt{S_{11}S_{33}}}, \quad \beta'' = \frac{3\sqrt{S_{11}S_{33}} + S_{13}}{\sqrt{S_{11}S_{33}} - S_{13}}, \quad c_l = \sqrt{\frac{C_{11}}{\rho}}, \quad c_s = \sqrt{\frac{C_{55}}{\rho}}, \quad r_l^2(c) = 1 - \left(\frac{c}{c_l}\right)^2, \quad r_s^2(c) = 1 - \left(\frac{c}{c_s}\right)^2, \\
y^2 &= \left(\frac{\beta + 1}{\beta - 1}\right) \left(\frac{3 - \beta + \beta'(\beta + 1)}{4\sqrt{\beta}}\right), \quad x = \sqrt{\beta} y^2 \left(\frac{3 - \beta}{1 + \beta}\right), \quad \beta_j(c) = \frac{y^2 r_l^2(c) + \beta_j^2(c)}{(1+x)\beta_j(c)} \quad (j=1,2), \\
R(c) &= \sqrt{\beta} y^2 r_l(c) r_s(c) - \frac{\sqrt{\beta} y^2 r_l(c) + x^2 r_s(c)}{\sqrt{\beta} y^2 r_l(c) + r_s(c)}, \quad z_j = r(\cos \theta_j + \beta_j(c) \sin \theta_j).
\end{aligned} \tag{6.6}$$

In the above equations,  $K_I^d$  and  $K_{II}^d$  are the mode-I and mode-II SIFs for a dynamically growing crack tip,  $c$  is the crack tip velocity, and  $\rho$  is the mass density.  $S_{11}$ ,  $S_{22}$ ,  $S_{33}$ ,  $S_{12}$ ,  $S_{13}$ ,  $S_{55}$ , and  $S_{66}$  are coefficients of the  $S$ -matrix, whereas  $C_{11}$ ,  $C_{55}$ , and  $C_{66}$  are elements of the stiffness  $C$ -matrix; the ultrasonic determination of both matrices has been described in Section 4.2.2.

### 6.2.3 Ultrasonic Determination of Orthotropic Elastic Constants

Because the primary emphasis of this work is dynamic fracture, ultrasonic determination of material properties is more appropriate than the quasi-static measurements typically reported in the literature. Several authors [86, 87] have measured the elastic constants of composite materials; however, this is the first work to measure the constants ultrasonically in both in-plane and out-of-plane directions for fracture parameter assessment.

The coefficients of the  $C$ -matrix were determined using an Epoch 600 Ultrasonic Flaw Detector from OLYMPUS, as detailed in Section 4.2.2. Composite material cubes were machined such that the faces aligned with the 1-, 2-, and 3-directions (Fig. 6.5), as defined originally in Fig. 6.1, where 1- is the fiber and crack growth direction, 2- is the crack opening direction for intralaminar specimens, and 3- is the crack opening direction for interlaminar specimens. Fig. 6.6 is a photograph of all four CNT (CNT/epoxy/carbon fiber) ultrasonic



specimens used to determine the nine independent elastic constants of the  $C$ -matrix for this material.

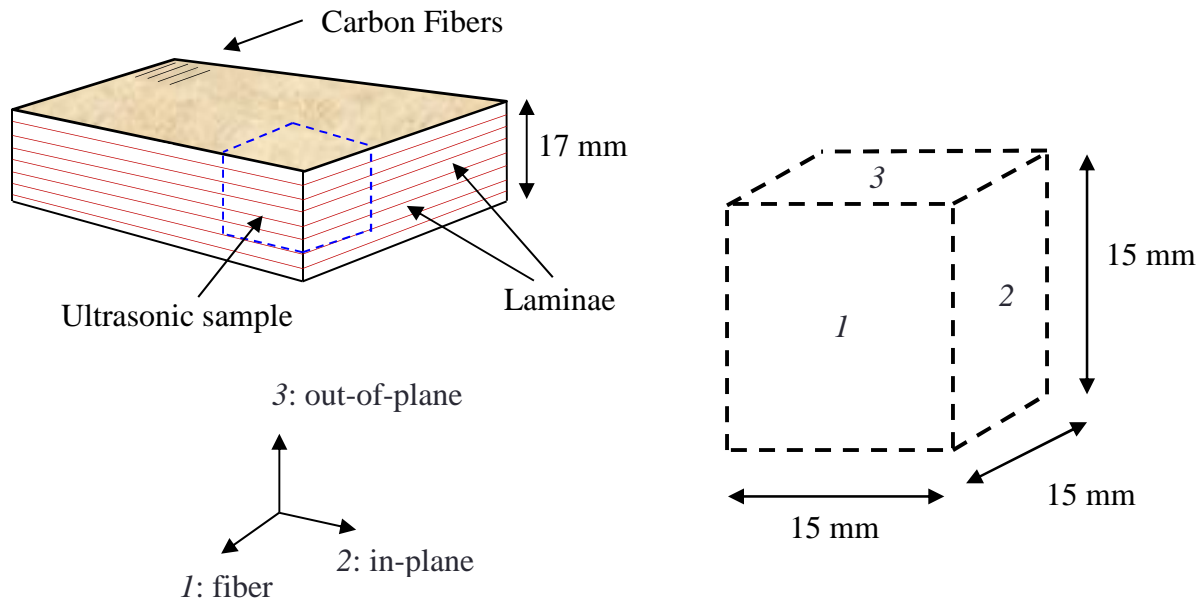


**Fig. 6.5:** Orientation of cube specimens for ultrasonic determination of orthotropic elastic constants.

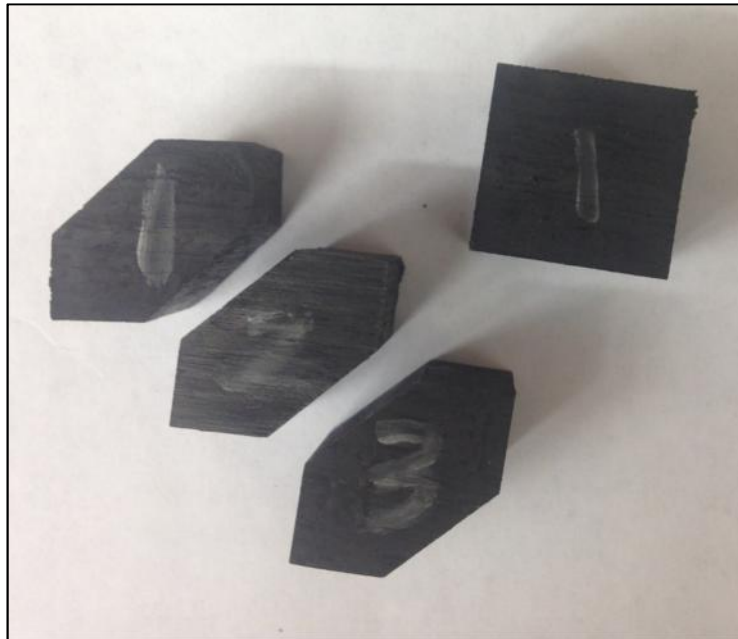


**Fig. 6.6:** CNT/epoxy/carbon fiber ultrasonic specimens used to evaluate the orthotropic elastic constants listed in Table 6.2.

The resulting material properties are listed in Table 6.2, where “Neat” refers to epoxy/carbon fiber composites, “CNT” refers to CNT/epoxy/carbon fiber nanocomposites, and “MCF” refers to MCF/epoxy/carbon fiber composites. The  $C$ -matrix coefficients are also compared to those given by Solodov et al. [87], who measured all 9 independent elastic constants ultrasonically for a nearly unidirectional carbon fiber composite (18 aligned  $0^\circ$  plies with  $2 \pm 45^\circ$  plies in the center). Neat CFRP values follow the same trends as those found in the literature [87] at a slightly lower magnitude. This decrease in magnitudes may be due to a lower density of the material processed for this work.

From Table 6.2, a slight drop in the material density with the inclusion of CNTs or MCFs into the matrix is evident; this is attributed to the fillers. Well-dispersed CNTs caused the viscosity of CNT-modified resin to increase, which caused less resin to be vacuumed out during curing. This contributed to modestly higher resin content, causing a decrease in  $\nu$ ,  $E_2$ ,  $E_3$ ,  $G_{12}$ ,  $G_{13}$ , and fiber volume fraction  $V_f$ . Meanwhile, much larger MCFs acted as spacers, significantly increasing the interlaminar spacing without much change in viscosity. The increased interlaminar spacing caused similar material property decreases to those caused by CNTs. By intentionally manipulating the elastic constant input while solving Eqs. 6.1-6.6, it was found that the shear moduli ( $G_{12}$ ,  $G_{13}$ ) have the greatest effect on measured SIFs, whereas crack-opening direction elastic moduli ( $E_2$ ,  $E_3$ ) corresponding to intra- and inter-laminar crack opening directions, respectively, also make a significant contribution to the calculated SIF. Measured SIFs increase as shear moduli and elastic moduli in the respective crack opening directions increase. Meanwhile, the resulting fluctuations in *Poisson’s ratios* ( $\hat{\nu}_{12}$ ,  $\hat{\nu}_{13}$ ) *have almost no effect on extracted SIFs.*

Material Property	Neat	CNT	MCF	C-matrix Coefficient	Neat	Literature [87]
$E_1$ (GPa)	94.54	100.72	101.93	$C_{11}$ (GPa)	102	127
$E_2$ (GPa)	8.29	7.60	9.00	$C_{22}$ (GPa)	11.6	13.8
$E_3$ (GPa)	7.10	4.34	4.29	$C_{33}$ (GPa)	10.0	12.8
$G_{23}$ (GPa)	2.47	2.00	1.86	$C_{44}$ (GPa)	2.5	3.6
$G_{13}$ (GPa)	4.32	3.67	3.32	$C_{55}$ (GPa)	4.3	5.0
$G_{12}$ (GPa)	5.31	5.11	5.17	$C_{66}$ (GPa)	5.3	6.7
$\hat{\nu}_{12}$	0.42	0.41	0.45	$C_{12}$ (GPa)	8	7
$\hat{\nu}_{13}$	0.52	0.54	0.39	$C_{13}$ (GPa)	8	6
$\hat{\nu}_{23}$	0.54	0.58	0.37	$C_{23}$ (GPa)	6	7
$\hat{\nu}_{21}$	0.04	0.03	0.04	(kg/m <sup>3</sup> )	1482	1600
$\hat{\nu}_{31}$	0.04	0.02	0.02			
$\hat{\nu}_{32}$	0.46	0.33	0.17			
Fiber $V_f$	50%	44%	39%			
(kg/m <sup>3</sup> )	1482	1442	1411			

**Table 6.2:** Material properties of thick CFRPs (‘Neat’ refers to epoxy/carbon fiber composites. ‘CNT’ refers to CNT/epoxy/carbon fiber nanocomposites. ‘MCF’ refers to MCF/epoxy/carbon fiber composites.)

The reported Poisson’s ratios are less accurate than the elastic and shear moduli calculated by this ultrasonic method (Section 4.2.2). That is, a 1% change in ultrasonic wave speed  $V_{66}$  (easily within the uncertainty of this method) results in a 32% change in  $\hat{\nu}_{12}$ , a 15% change in  $\hat{\nu}_{13}$ , and a 1% change in  $E_1$ . A similar 1% change in  $V_{11}$  results in a 2% change in  $E_1$ , a 0.03% change in  $E_2$  and  $E_3$ , and a 2% change in  $\hat{\nu}_{12}$ . Thus for applications of this method to materials of high degree of anisotropy (such as CFRPs) where the accuracy of the Poisson terms is essential, the authors recommend independent verification of the Poisson’s ratios.

### 6.2.4 Finite Element Analysis

Finite element analyses were carried out to supplement dynamic experimental results prior to crack initiation. A 3D, transient, elasto-dynamic, finite element model using ABAQUS<sup>®</sup>/Explicit software was developed. The numerical model included the specimen and the long-bar (Fig. 6.7) in order to ensure that the stress wave propagating into the specimen was captured as accurately as possible. Material property input for the model included all of the elastic properties in Table 6.2, along with the density. The model consisted of 218,000 tetrahedral elements with highly refined elements of size 0.1 mm in the impact and crack tip vicinities. The model had a total of 133,000 degrees of freedom. The particle velocity ( $V_{pl}$ ) in the bar was determined from the measured strain history on the long-bar using

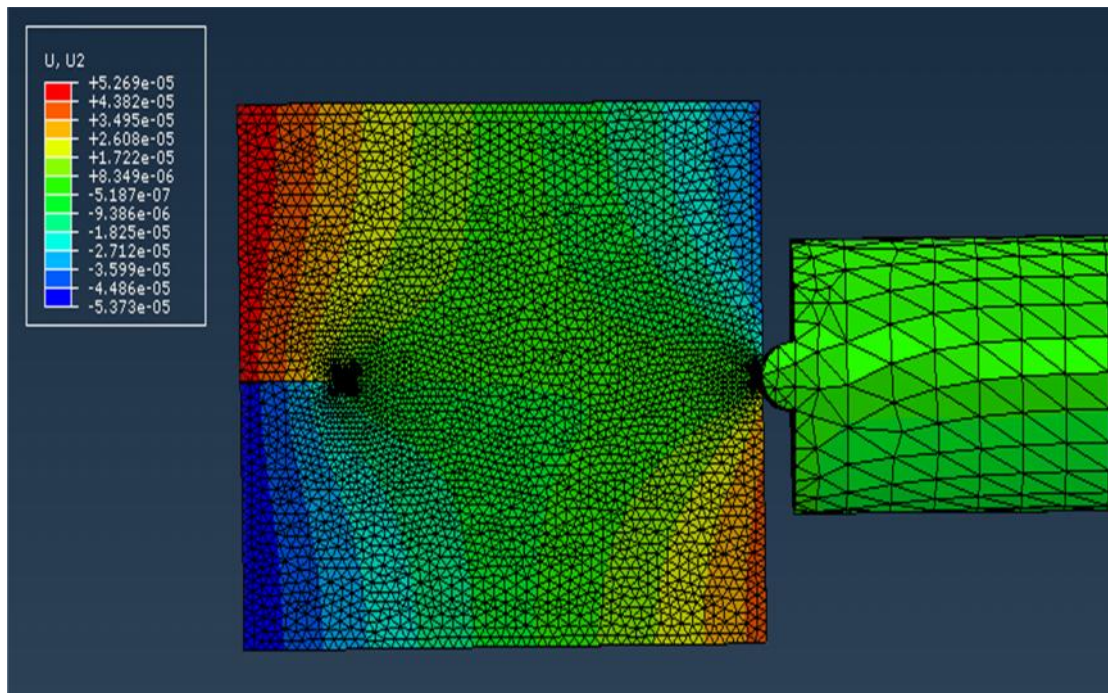


**Fig. 6.7:** Finite element model with corresponding crack opening displacement contours are shown on the neat intralaminar specimen, along with the far left end of the long-bar. A fine mesh is used near the impact site to ensure that contact and crack tip deformation responses are captured accurately. The field corresponds to a time instant 23  $\mu\text{s}$  after impact and 1  $\mu\text{s}$  before crack initiation.

$$V_{pl} = c_I v_I \quad (6.7)$$

and input at the far right flat surface of the long-bar (Fig. 6.7). (In the above subscript  $I$  denotes ‘incident,’  $c$  the bar wave speed and  $v$  the measured strain on the long-bar.) After propagating along the long-bar, the stress waves were transmitted into the specimen using a contact definition for the semi-circular region that impacts the flat edge of the specimen. Time increments automatically chosen during computations by the software were approximately 5 ns.

Instantaneous values of SIFs were computed from finite element results using a regression analysis of crack flank displacements. Apparent stress intensity factors ( $K_I^*$ ) were calculated using crack opening displacements ( $\delta_y$ ) near the crack tip according to:

$$u_y \Big|_{r=\pm f, r \rightarrow 0} = 2K_I^* \sqrt{\frac{2r}{f}} \operatorname{Re} \left[ \frac{1}{\tilde{\nu}_2 - \tilde{\nu}_1} (q_1 \tilde{\nu}_2 z_1 - q_2 \tilde{\nu}_1 z_2) \right]. \quad (6.8)$$

The linear regions of  $K_I^*$  vs.  $r$  plots were then extrapolated to the crack tip to obtain instantaneous SIFs as  $K_I = \lim_{r \rightarrow 0} K_I^*$  [99, 103].

## 6.3 Results

### 6.3.1 Quasi-Static Results

To estimate baseline inter- and intra-laminar fracture parameters at crack initiation, quasi-static experiments were carried out on the 3-point bend configuration described in Fig. 6.3a. Representative load-displacement curves are given for Neat (carbon fiber/epoxy without CNTs) samples in Fig. 6.8. Intralaminar specimens consistently showed more area under the curve than interlaminar specimens. Apart from the intrinsic inter- and intra-laminar elastic characteristics

(Table 6.2), this increase is likely amplified by the presence of a thermoplastic-coated fiberglass scrim on the front and back of the carbon fiber fabric used to hold the unidirectional fibers in line for ease of handling (Fig. 6.9). Thus, intralaminar cracks were aligned to propagate through the scrim fibers (Fig. 6.10a), whereas interlaminar cracks propagated between layers of carbon fiber held by scrim without being affected by the fiberglass scrim (Fig. 6.10b).

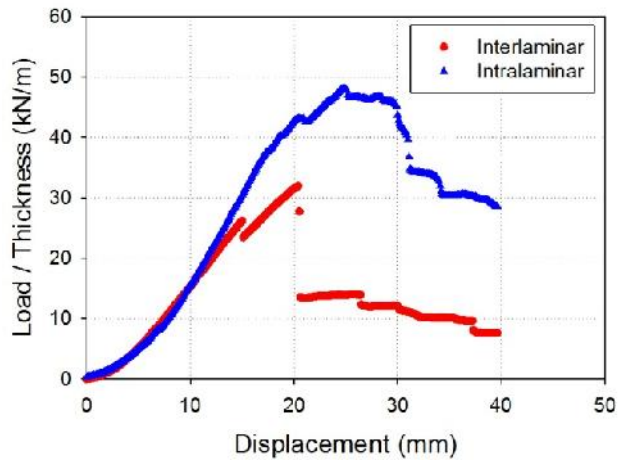


**Fig. 6.8:** Representative intralaminar and interlaminar load-displacement curves for Neat fracture specimens tested under quasi-static loading conditions.

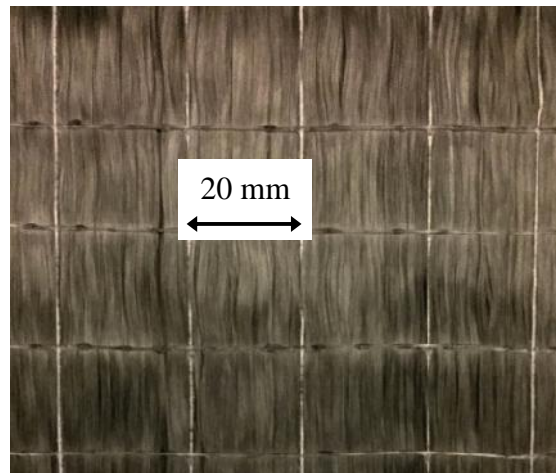


**Fig. 6.9:** Thermo-plastic coated fiberglass scrim material (white) on the front and back surfaces of unidirectional carbon fiber fabric. Carbon fibers are running vertically. Intralaminar cracks propagated through this material, whereas interlaminar cracks propagated between layers of carbon fiber and scrim.

Fig. 6.11a and 6.11b show the measured SIF histories from quasi-static fracture experiments on Neat samples (three experiments in each case) with cracks growing in the interlaminar and intralaminar directions, respectively. Intralaminar specimens had significantly higher critical SIFs than interlaminar specimens, likely attributed to the presence of the scrim on each of the 60 layers of the original composite plates. Specimens exhibited controlled crack growth for several seconds after crack initiation (even longer for intralaminar specimens), and measured SIFs continued to increase due to fiber bridging [75]. However, the addition of CNTs (Fig. 6.11c and 6.11d) and MCFs (Fig. 6.11e and 6.11f) had no significant effect on quasi-static SIFs. The average quasi-static  $K_{IC}$  values at crack initiation are summarized in Fig. 6.12, where CNTs led to no improvements in  $K_{IC}$ , whereas the intralaminar specimens had significantly higher  $K_{IC}$  values than the corresponding interlaminar specimens.

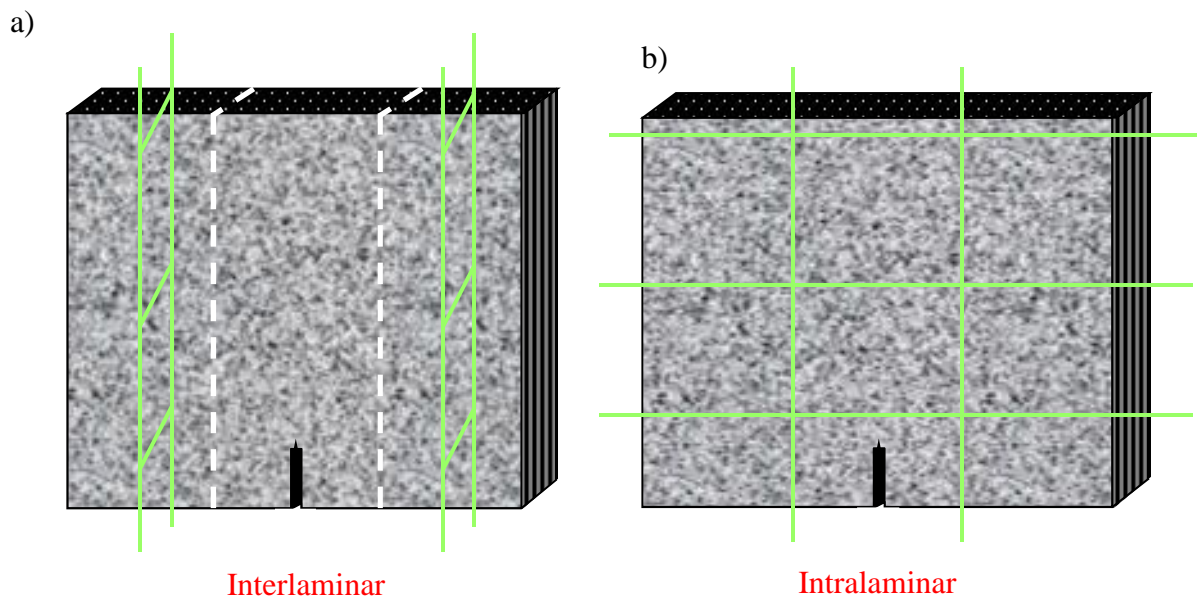


**Fig. 6.10:** Dynamic fracture specimens from Fig. 6.3b with the thermoplastic-coated fiberglass scrim drawn in green. Note that there are actually about 300 layers of scrim across the sample from left to right in the interlaminar specimen a), and about 40 layers of scrim through the thickness in the intralaminar specimen b). Note also that the scrim orientation will be similar for quasi-static specimens.

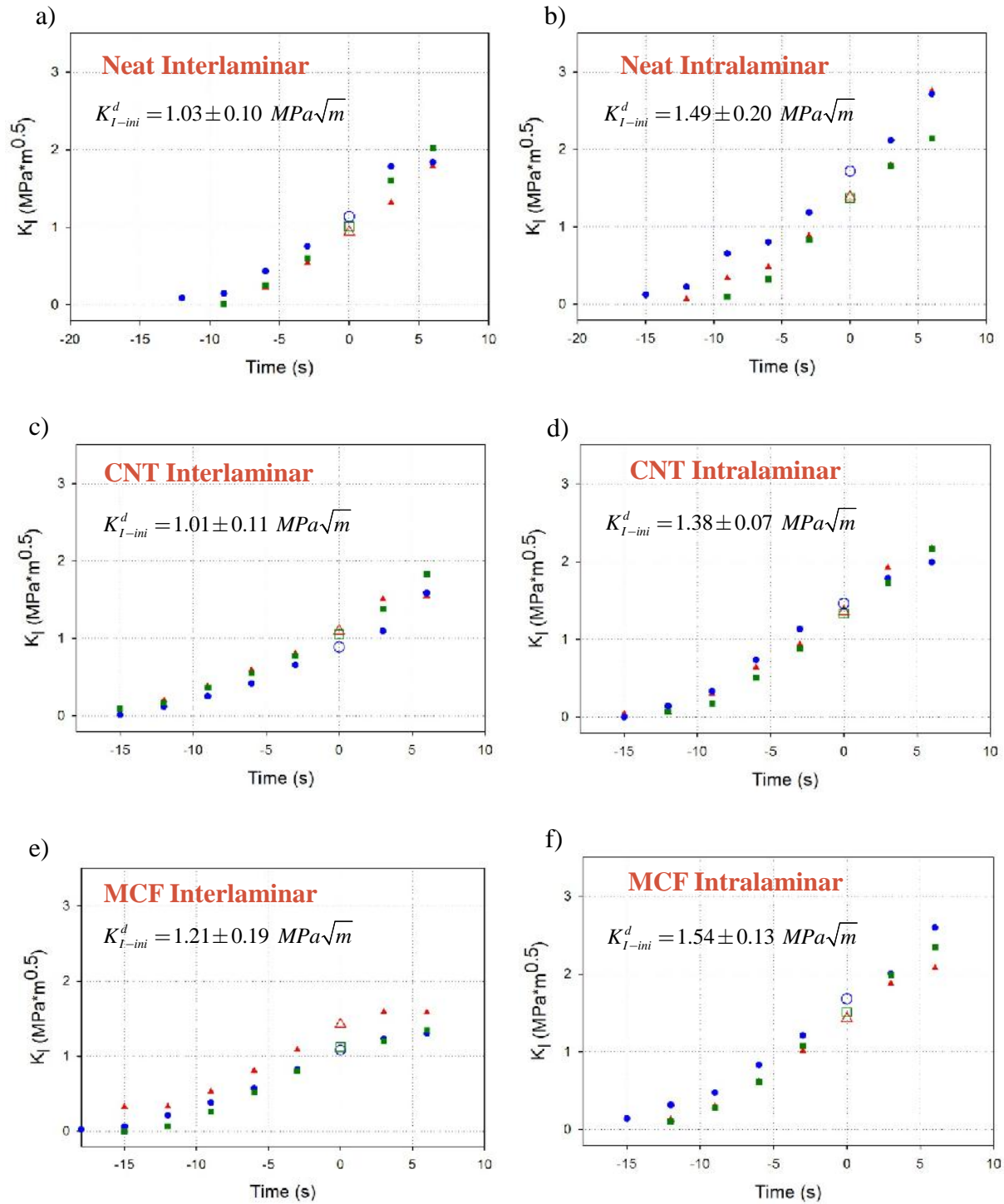


**Fig. 6.11:** Quasi-static SIF histories (cross-head speed = 0.01 mm/sec) for edge-cracked CFRP 3-point bend specimens with cracks growing in the interlaminar or intralaminar directions. The presence of a fiberglass scrim caused an increase in  $K_{IC}$  and post-initiation SIFs of intralaminar specimens, whereas the presence of CNTs and MCFs did not significantly improve critical SIFs. Three experimental results for each case are presented to show repeatability, and the open symbols denote crack initiation (designated by time  $t = 0$ ).



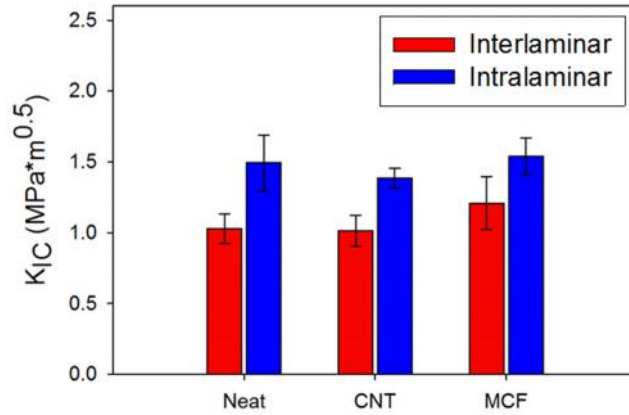


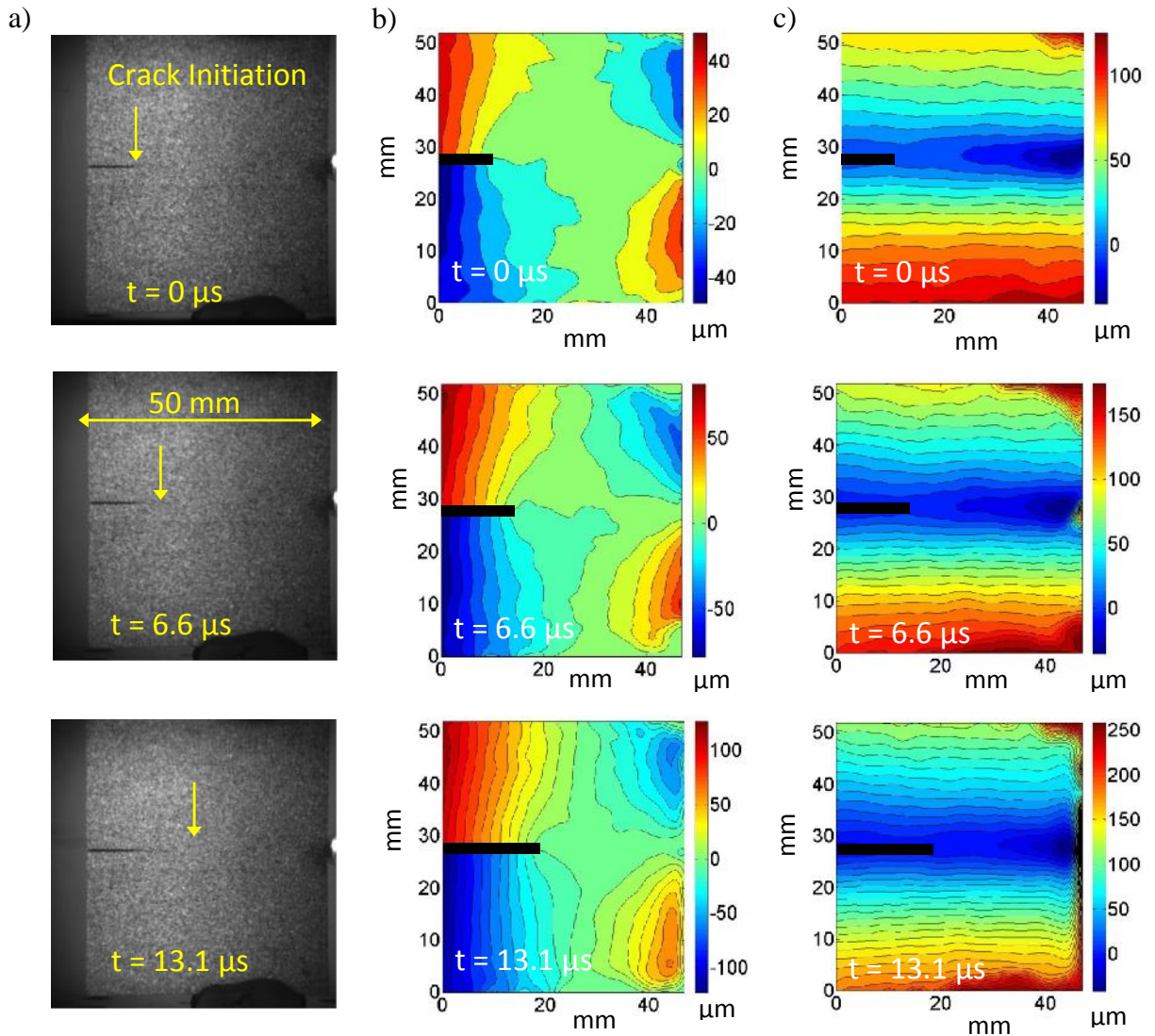
**Fig. 6.12:** Average of measured quasi-static  $K_{IC}$  values. Intralaminar specimens had significantly higher  $K_{IC}$  than interlaminar specimens, whereas the addition of CNTs and MCFs did not have a significant effect on  $K_{IC}$ .

### 6.3.2 Dynamic Results

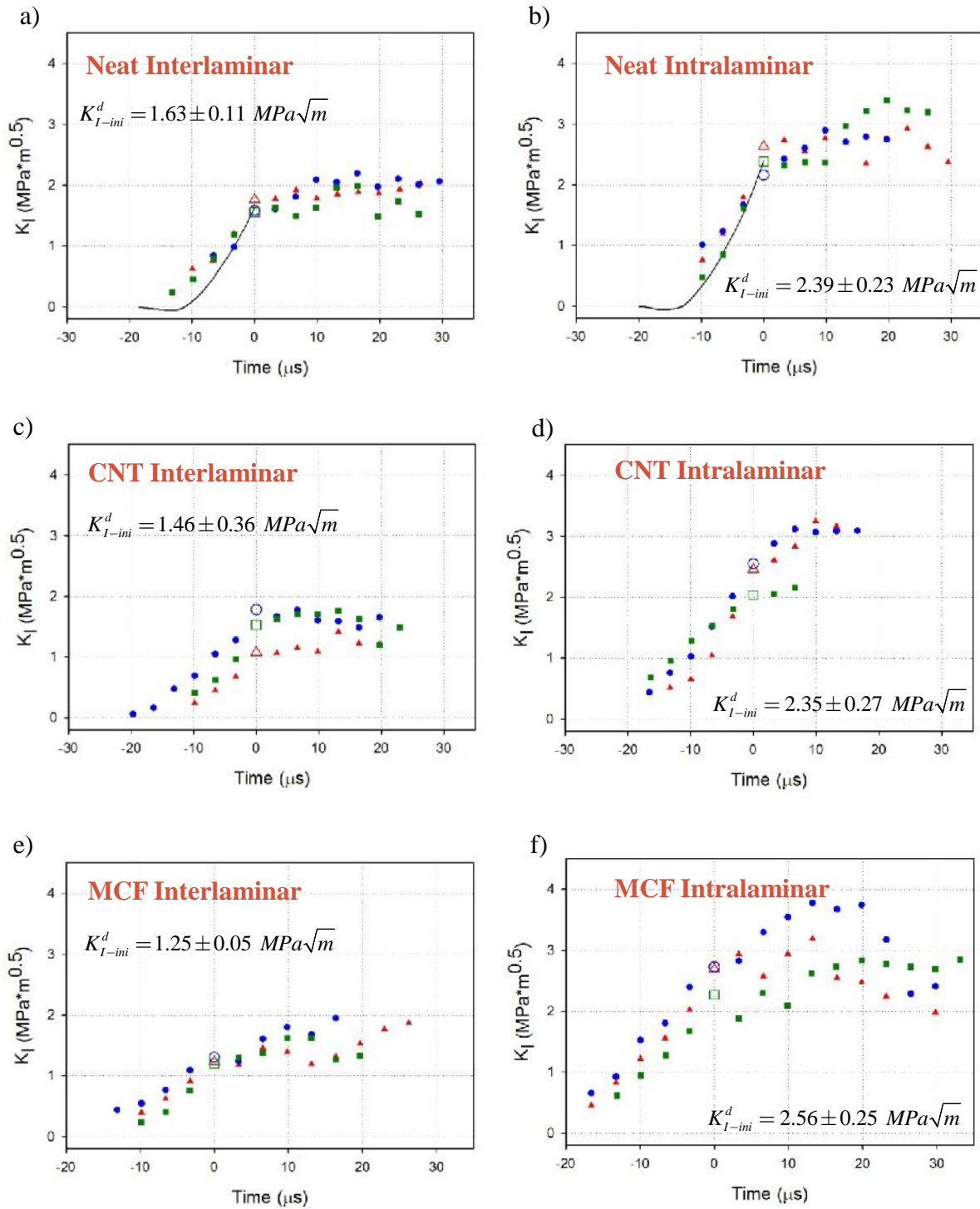
Sample contour plots based of the  $v$  and  $u$  displacement matrices from DIC are shown in Fig. 6.13b and 6.14c, respectively, corresponding to the deformed images in Fig. 6.13a. Time  $t$  in the images is time after crack initiation. The crack can be seen moving from left to right in all images, and the contour density continues to increase with time as well. (Contour interval is 10  $\mu\text{m}$ .) Due to the high stiffness and reduced aspect ratio compared to calibration samples in Chapter 3, small rollers of putty have been used only on the impact side of the specimen so as not to interfere with crack opening (as opposed to the wide putty bars in Fig. 2.4).

Fig. 6.14a and 6.14b show the measured SIF histories from dynamic fracture experiments on Neat samples (three experiments in each case) with cracks growing in the interlaminar and intralaminar directions, respectively. As in the quasi-static case, intralaminar specimens had significantly higher critical SIF ( $K_{I-ini}^d$ ) and post-initiation SIFs ( $K_I^d$ ) than interlaminar specimens, likely attributed to the presence of the thermoplastic-coated fiberglass scrim. The

solid lines indicate FEA models (aligned with the average crack initiation SIF) generated using strain gage data on the long-bar which closely match the pre-initiation SIF values obtained from DIC and high-speed photography. FEA models are somewhat stiffer than optically-measured



**Fig. 6.13:** Full-field measurement of deformations using DIC: a) Three of 32 images collected during an interlaminar dynamic fracture test of neat epoxy/carbon fiber, with arrows indicating the approximate location of the crack tip, b)  $v$ -opening contours of displacement, and c)  $u$ -sliding contours of displacement. The crack initiates at time  $t=0$ . Contour interval is  $10\ \mu\text{m}$ . Magnification is  $54\ \mu\text{m}/\text{pixel}$ .



**Fig. 6.14:** Dynamic SIF histories for CFRP specimens with cracks growing in the interlaminar and intralaminar directions. The presence of scrim caused an increase in ( $K_{I-ini}^d$ ) and post-initiation SIFs of intralaminar specimens, whereas the presence of CNTs and MCFs did not significantly improve SIFs at or after crack initiation. Results from FEA are indicated by the solid line in a) and b). Open symbols denote values at crack initiation, at time  $t = 0$ .

SIFs, likely due to the usage of fully integrated tetrahedral elements in these models. The addition of CNTs (Fig. 6.14c and 6.14d) and MCFs (Fig. 6.14e and 6.14f) gave similar  $K_{I-ini}^d$  and  $K_I^d$  values compared to corresponding Neat specimens but with a higher degree of scatter. This increase in scatter was likely due to inconsistencies in dispersion of fillers near the crack tip.

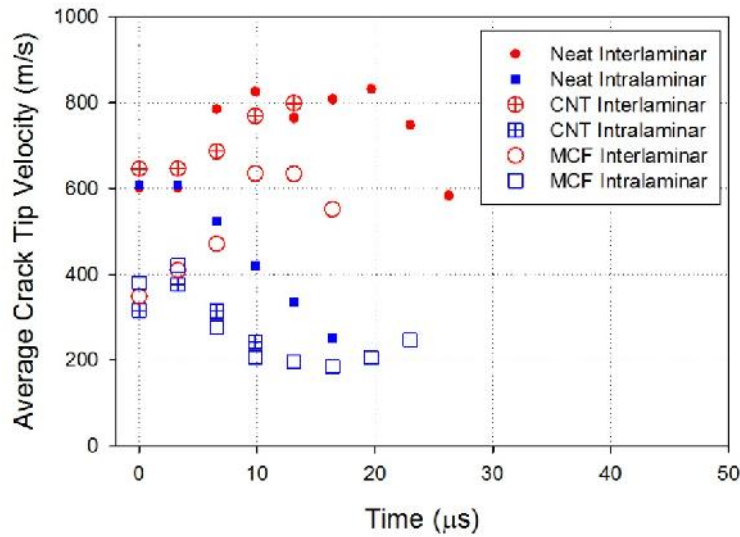


**Fig. 6.15:** Crack tip velocities of CFRPs. Following crack initiation, intralaminar cracks (blue) decelerated quickly and arrested, whereas interlaminar cracks (red) accelerated to ~800 m/s.

The measured crack tip velocity histories are given in Fig. 6.15. Following crack initiation, the intralaminar cracks quickly decelerated and eventually arrested, whereas the interlaminar cracks accelerated to 600-800 m/s. Fig. 6.16 is a photograph of two CNT samples after dynamic fracture. Fig. 6.16a is an interlaminar sample where the crack propagated completely through the sample; Fig. 6.16b is an intralaminar sample where the crack propagated only a few millimeters before arresting. The intralaminar samples with CNTs, as well as both specimen types with MCFs, had lower crack tip velocities than corresponding Neat specimens, indicating higher resistance to crack growth; however, these specimens also had reduced average  $K_{I-ini}^d$ .

The average dynamic  $K_{I-ini}^d$  values are summarized in Fig. 6.17, where fillers caused reductions in  $K_{I-ini}^d$ , whereas the intralaminar specimens had significantly higher  $K_{I-ini}^d$  values than the corresponding interlaminar specimens. All quasi-static (QS) and dynamic (D) critical SIF values are listed in Table 6.3 along with the corresponding loading rate ( $\dot{K}$ ), quantified by the rate of change of SIF immediately before crack initiation.

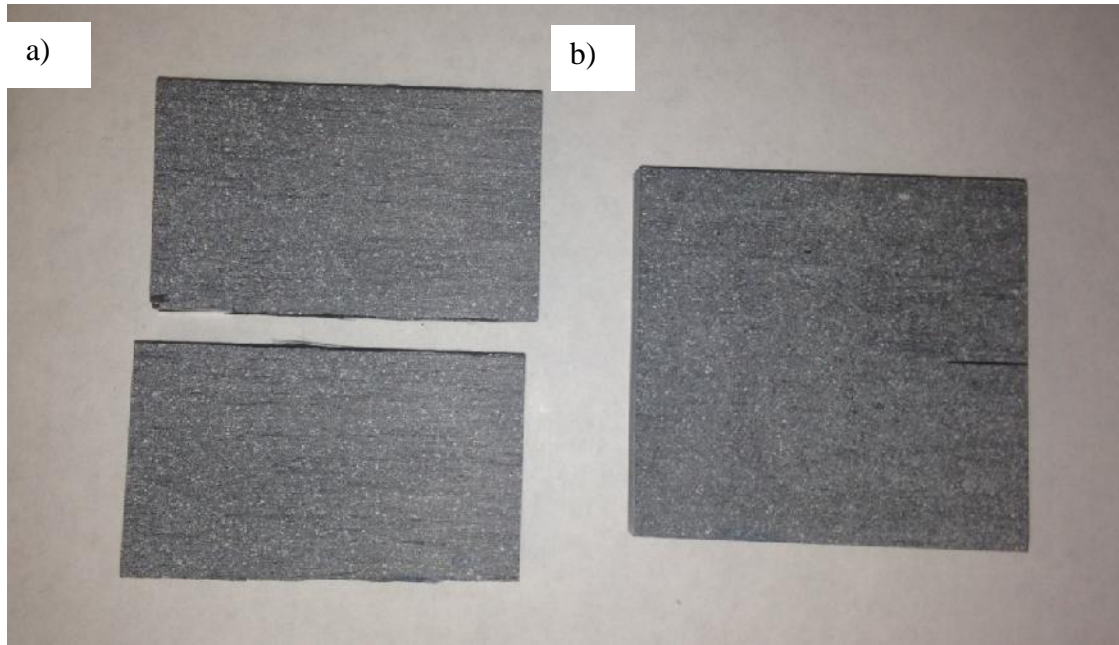


**Fig. 6.16:** CNT dynamic fracture specimens. a) Interlaminar cracks propagated through the sample every time. b) Intralaminar samples always initiated, propagated a few millimeters, and then arrested.

Because fracture toughness is typically reported in terms of  $G_{IC}$  (critical energy release rate) instead of critical SIF in the composites community,  $K_{IC} / K_{I-ini}^d$  values have been converted to  $G_{IC} / G_{I-ini}^d$  in Table 6.4 using the following equation for intralaminar fracture [110]:

$$G_I = -\frac{K_I^2}{2} S_{22} \operatorname{Im} \left[ \frac{\tilde{\nu}_1 + \tilde{\nu}_2}{\tilde{\nu}_1 \tilde{\nu}_2} \right], \quad (6.9)$$

where  $\tilde{\gamma}_j (j = 1, 2)$  are the two roots of:  $S_{11}\tilde{\gamma}^4 + (2S_{12} + S_{66})\tilde{\gamma}^2 + S_{22} = 0$ , and the following equation for interlaminar fracture:

$$G_I = -\frac{K_I^2}{2} S_{33} \operatorname{Im} \left[ \frac{\tilde{\gamma}_1 + \tilde{\gamma}_3}{\tilde{\gamma}_1 \tilde{\gamma}_3} \right], \quad (6.10)$$

where  $\tilde{\gamma}_j (j = 1, 2)$  are the two roots of:  $S_{11}\tilde{\gamma}^4 + (2S_{13} + S_{55})\tilde{\gamma}^2 + S_{33} = 0$ .

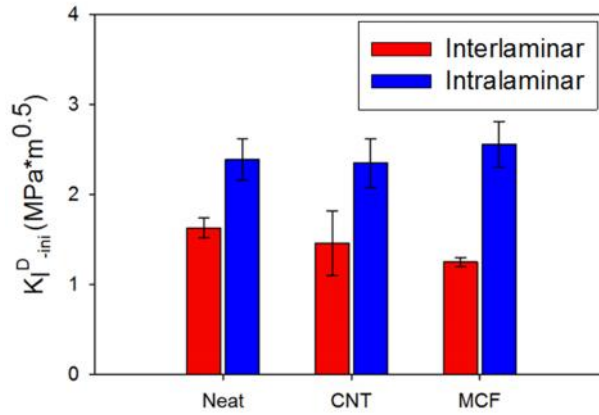


**Fig. 6.17:** Average of measured dynamic  $K_{I-ini}^d$  values. Intralaminar specimens had significantly higher  $K_{I-ini}^d$  than interlaminar specimens, whereas the addition of CNTs and MCFs caused reductions in  $K_{I-ini}^d$ .

Fig. 6.18 gives the average critical energy release rate values for quasi-static ( $G_{IC}$ ) and dynamic ( $G_{I-ini}^d$ ) fracture, converted from critical SIFs according to Eqs. 6.9 and 6.10. While CNTs did not lead to improvements in critical stress intensity factors, they produced a 34% insignificant improvement in quasi-static interlaminar  $G_{IC}$  and a 16% insignificant improvement in dynamic interlaminar  $G_{I-ini}^d$  over Neat interlaminar samples. Meanwhile, MCFs led to a 106% significant improvement in interlaminar  $G_{IC}$  and a -15% reduction in interlaminar  $G_{I-ini}^d$ . Both CNT-infused and MCF-infused composites had similar intralaminar critical energy release rate



compared to corresponding neat samples, where fracture was dominated by the fiberglass scrim. This trend is consistent with critical intralaminar SIFs.

<i>Test Type</i>	Average Rate	Average Neat	Average CNT	Average MCF
	$\dot{K}$ (MPa $\sqrt{m}$ s $^{-1}$ )	$K_{IC} / K_{I-ini}^d$ (MPa $\sqrt{m}$ )	$K_{IC} / K_{I-ini}^d$ (MPa $\sqrt{m}$ )	$K_{IC} / K_{I-ini}^d$ (MPa $\sqrt{m}$ )
QS Inter	1.31 x 10 $^{-1}$	1.03 $\pm$ 0.10	1.01 $\pm$ 0.11	1.21 $\pm$ 0.19
QS Intra	1.76 x 10 $^{-1}$	1.49 $\pm$ 0.20	1.38 $\pm$ 0.07	1.54 $\pm$ 0.13
D Inter	1.55 x 10 $^5$	1.63 $\pm$ 0.11	1.46 $\pm$ 0.36	1.25 $\pm$ 0.05
D Intra	2.14 x 10 $^5$	2.39 $\pm$ 0.23	2.35 $\pm$ 0.27	2.56 $\pm$ 0.25

**Table 6.3:** Average quasi-static (QS) and dynamic (D) critical SIF values for interlaminar and intralaminar specimens.

<i>Test Type</i>	Average Neat	Average CNT	Average MCF
	$G_{IC} / G_{I-ini}^d$ (J / m $^2$ )	$G_{IC} / G_{I-ini}^d$ (J / m $^2$ )	$G_{IC} / G_{I-ini}^d$ (J / m $^2$ )
QS Inter	109 $\pm$ 22	149 $\pm$ 31	224 $\pm$ 73
QS Intra	197 $\pm$ 52	177 $\pm$ 17	199 $\pm$ 33
D Inter	274 $\pm$ 38	318 $\pm$ 146	234 $\pm$ 20
D Intra	500 $\pm$ 98	514 $\pm$ 115	551 $\pm$ 105

**Table 6.4:** Average critical energy release rate  $G_{IC} / G_{I-ini}^d$  calculated from  $K_{IC} / K_{I-ini}^d$  values (QS = Quasi-Static and D = Dynamic).

Using the current methodology, critical SIF refers to the SIF value calculated from the last image before the crack was observed to move in the sequence of photographs. Alternatively, if the initiation SIF is chosen to be the first image when the crack is observed to move, the assigned quasi-static initiation SIF values increase significantly, whereas the assigned dynamic initiation SIF values increase only slightly. This is because quasi-static SIFs continue to increase at approximately the same rate before and after crack initiation (Fig. 6.11), whereas dynamic

SIFs level off dramatically after initiation (Fig. 6.14), particularly in the interlaminar case where the scrim fibers do not participate in crack growth. Accordingly, Table 6.5 compares Neat  $K_{IC} / K_{I-ini}^d$  and  $G_{IC} / G_{I-ini}^d$  values calculated from the image before and after crack initiation.

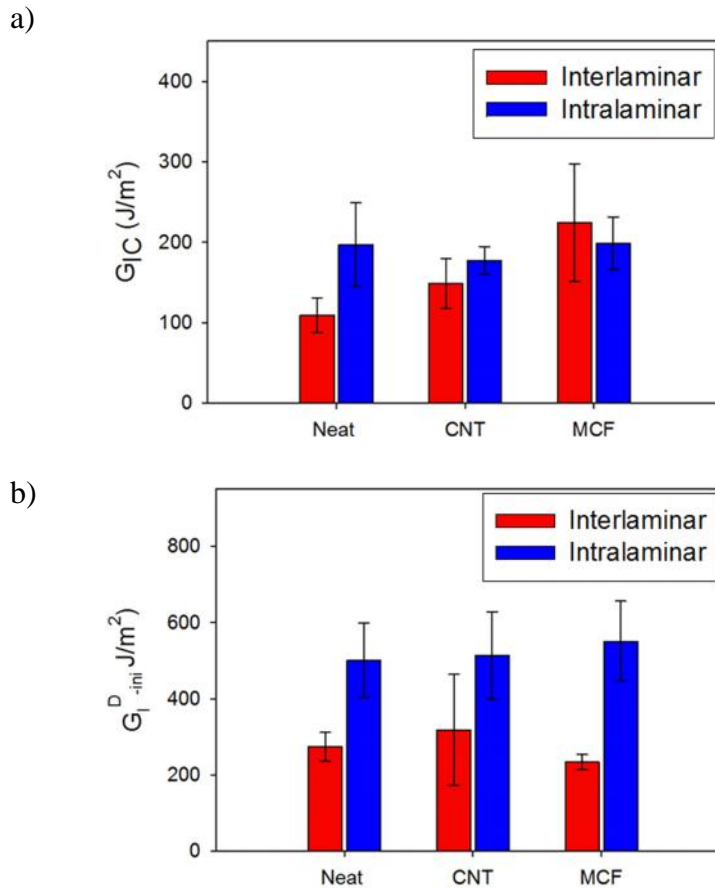


**Fig. 6.18:** Average critical energy release rate values from critical SIFs using Eqs. 6.9 and 6.10 a) quasi-static  $G_{IC}$  and b) dynamic  $G_{I-ini}^d$  values. CNTs led to statistically insignificant improvements in both quasi-static (+34%) and dynamic (+16%) critical energy release rate for interlaminar specimens, whereas interlaminar MCFs led to a large improvement (+106%) in the quasi-static case and a reduction (-15%) in the dynamic case. In all cases, intralaminar fracture, affected by fiberglass scrim, had similar critical energy release rate compared to Neat samples.

Scanning electron microscopy of fracture surfaces of CNT/epoxy nanocomposites (Section 5.2.4) indicates good dispersion of CNTs by this method (Fig. 6.19a). Optical microscopy of fracture surfaces of 3-phase MCF/CF/epoxy composites demonstrate poor



Test Type	Neat Before	Neat After	Neat Before	Neat After
	$K_{IC} / K_{I-ini}^d (MPa\sqrt{m})$	$K_{IC} / K_{I-ini}^d (MPa\sqrt{m})$	$G_{IC} / G_{I-ini}^d (J / m^2)$	$G_{IC} / G_{I-ini}^d (J / m^2)$
QS Inter	$1.03 \pm 0.10$	$1.57 \pm 0.24$	$109 \pm 22$	$256 \pm 75$
QS Intra	$1.49 \pm 0.20$	$1.90 \pm 0.19$	$197 \pm 52$	$316 \pm 65$
D Inter	$1.63 \pm 0.11$	$1.67 \pm 0.09$	$274 \pm 38$	$285 \pm 32$
D Intra	$2.39 \pm 0.23$	$2.49 \pm 0.22$	$500 \pm 98$	$544 \pm 95$

**Table 6.5:** Neat critical SIF assigned to the image before vs. after crack initiation, reported in terms of  $K_{IC} / K_{I-ini}^d$  and  $G_{IC} / G_{I-ini}^d$  (QS = Quasi-Static and D = Dynamic).

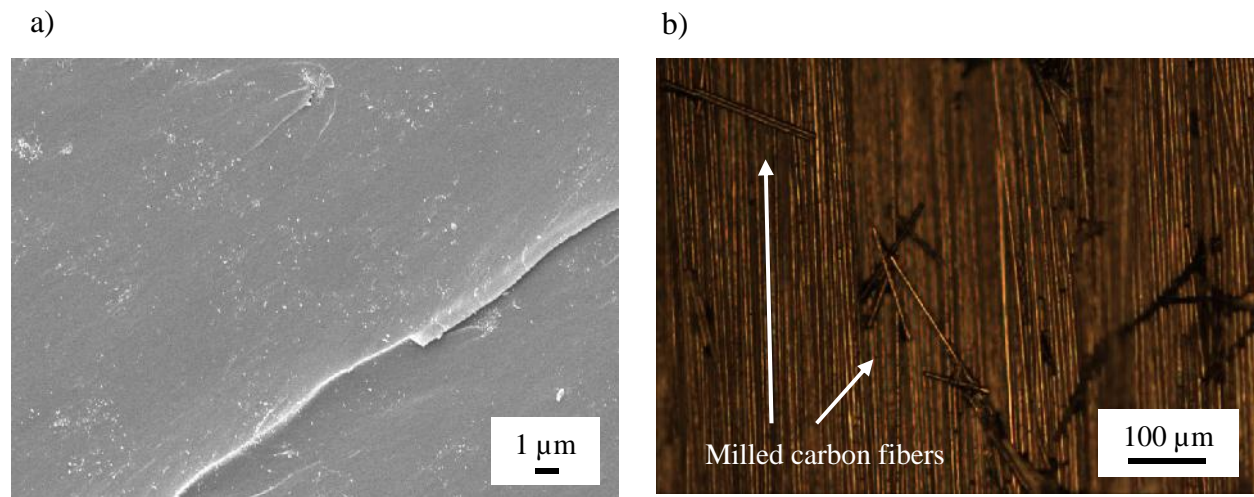


**Fig. 6.19:** a) Scanning electron micrograph of a fracture surface of an NH<sub>2</sub>-CNT/epoxy nanocomposite. CNTs are well-dispersed. b) Optical microscope image of a fracture surface of an MCF/epoxy/composite.

distribution of MCFs, which likely led to the high variability in MCF fracture results (Fig. 19b). Scanning electron micrographs of Neat CF/epoxy and CNT/CF/epoxy samples are shown in Fig. 6.20. Crack growth occurred along the fiber direction, vertically in each image. Addition of well-dispersed CNTs as evident in Fig. 6.20b and 6.20c does not appear to affect fracture surface features in the resin layer compared to the Neat fracture surface in Fig. 6.20a. This observation is consistent with the lack of critical SIF enhancements in the reported measurements. Optical

microscopy of larger MCFs on a fracture surface (Fig. 6.19b) does not indicate uniform dispersion, which likely prevents consistent significant improvement in critical SIF.

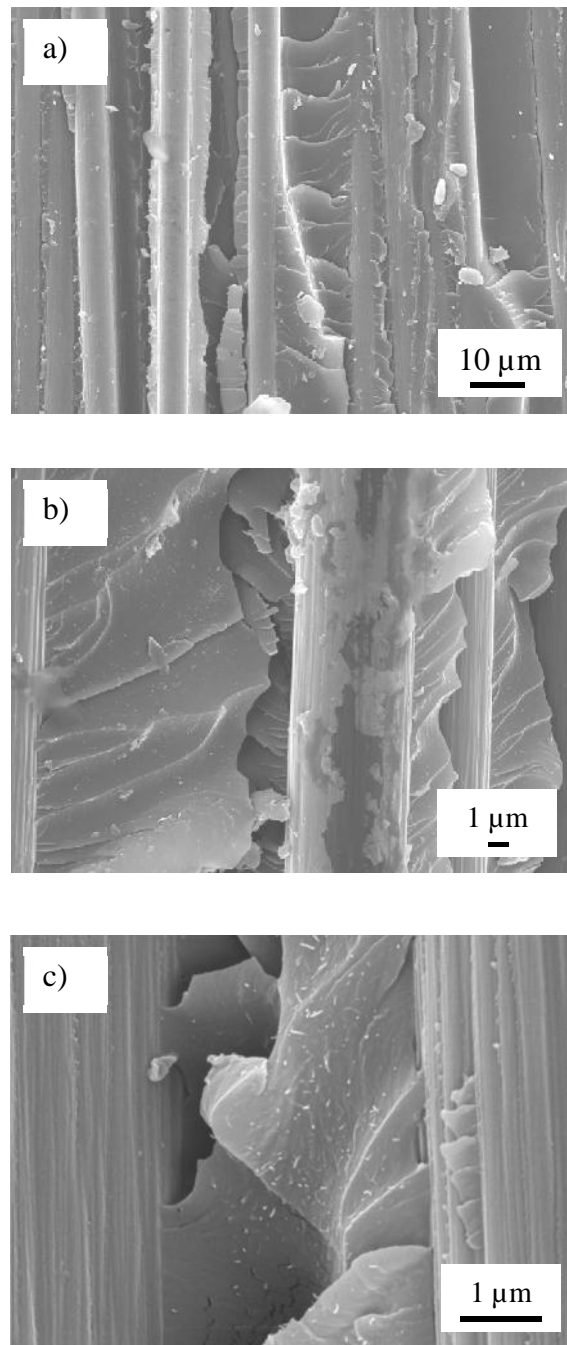


**Fig. 6.20:** Scanning electron microscopy of a) Neat CFRP at 1,000x, b) CNT CFRP at 4,000x, and c) CNT CFRP at 15,000x. Crack growth is in the vertical direction. CNTs appear to be reasonably well-dispersed throughout the resin layers but have little effect on resin layer fracture features or measured critical SIF.

## 6.4 Discussion and Conclusions

In this study, all interlaminar fracture specimens have higher initiation SIF under dynamic conditions than under quasi-static conditions, although this perceived loading rate effect could be due to the framing rate used as detailed in Table 6.5. Future works could use a slower loading rate or a faster framing rate, particularly under quasi-static conditions, in order to improve estimation of  $K_{IC}$  and  $G_{IC}$  values by this methodology. The interlaminar quasi-static  $G_{IC}$  values immediately after crack initiation in Table 6.5 are in good agreement with the literature [58, 75, 91, 95].

Despite the high quality of dispersion demonstrated in Fig. 6.20, the addition of CNTs did not improve the critical stress intensity factor ( $K_{IC} / K_{I-ini}^d$ ), although it did lead to some insignificant improvement comparable to those in the literature [58, 88-95] in quasi-static interlaminar critical energy release rate ( $G_{IC}$ ) (+34%). CNTs also led to an insignificant improvement in interlaminar  $G_{I-ini}^d$  (+16%). Meanwhile, poorly dispersed MCFs (Fig. 6.19b) led to a statistically insignificant improvement in interlaminar  $K_{IC}$  (+17%) and a statistically significant improvement in interlaminar  $G_{IC}$  (+106%), along with a significant decrease in interlaminar  $K_{I-ini}^d$  (-23%) and an insignificant decrease in  $G_{I-ini}^d$  (-15%). The errors are magnified in energy release rate ( $G$ ) calculations due to the squaring of critical SIFs in Eqs. 6.9 and 6.10, making improvements in critical energy release rate of CNT-infused nanocomposites statistically not significant. The scatter is particularly high for dynamic interlaminar critical energy release rate of CNT-infused samples, due to high scatter of  $K_{I-ini}^d$  values for this material. Questions remain as to which fracture parameter ( $K$  vs.  $G$ ) is more industrially-relevant.

The volume fraction of fibers in the Neat CFRP processed for this work is on the lower end of the values reported in Tables 1.8 and 1.9 by other investigators. The addition of fillers led to further reductions in  $V_f$ . In the ideal case, three-phase nanocomposites should be compared with Neat epoxy/carbon fiber composites of the same  $V_f$ , although this variable is difficult to control due to the change in viscosity caused by well-dispersed CNTs and the ‘spacer’ effect of the MCFs between individual lamina. While CNTs appear to be uniformly dispersed (Fig. 6.20), MCFs did not remain suspended in the low viscosity resin system used here (Fig. 6.19b); therefore, more work with MCF-reinforced composites is necessary to determine their usefulness in this application, likely using a higher viscosity resin system in order to sustain dispersion levels. Questions regarding scalability and cost-effectiveness of both CNT-infused and MCF-infused composites are not well documented at this time.

The current work is unique in several respects:

- 1). The fabrication of relatively thick CFRPs allows for the comparison of interlaminar and intralaminar fracture data using the same testing procedures with samples machined to the same dimensions from the same original block of material. Under quasi-static loading conditions, where all material points sense the imposed loads simultaneously, measured SIFs are dependent on specimen geometry [78-80]; however, under stress wave loading conditions, measured SIFs are also dependent on elastic wave speeds, which differ significantly between interlaminar and intralaminar directions (Table 6.2). The presence of scrim on the front and back surfaces of the unidirectional carbon fiber fabric pinned intralaminar cracks whereas interlaminar cracks propagated through unsupported epoxy resin at the interlayer. Note that all intralaminar samples showed highly consistent initiation SIF and critical energy release rate regardless of filler type, likely due to the dominance of the fiberglass scrim. Future work to achieve this idealized

comparison of interlaminar and intralaminar fracture could involve similar preparation of thick carbon fiber composites using either unidirectional prepreg or dry unidirectional fabric held together by a thermoplastic scrim.

2). There is no current ASTM standard to study dynamic interlaminar fracture of composite materials. The current ASTM standard for quasi-static interlaminar fracture of composite materials (D5528) cannot be extended to study dynamic interlaminar fracture because thin specimens generally experience flexural stress waves. As the aerospace industry continues to replace aluminum with CFRP exposed to high speed events and cold temperatures, the behavior of these materials under dynamic loading conditions must be understood. Advantages of the current methodology involving DIC and high-speed photography include non-contact full-field deformations for the measurement of SIFs, as well as the precise location of the crack tip during the fracture event, which is necessary for estimating crack tip velocities for an accurate evaluation of dynamic SIF histories and hence crack growth resistance.

3). While several researchers [82-84] have previously investigated dynamic interlaminar fracture of CFRPs, they have assumed transverse isotropy and relied on statically-measured elastic properties in order to estimate dynamic fracture properties. In addition, they appear to have each used elastic properties reported by others who used similar materials. In other instances, out-of-plane elastic characteristics are estimated based on in-plane measurements of the same. The current research, on the other hand, includes the ultrasonic estimation of all dynamic elastic properties for orthotropic CFRP materials machined from the same composite plate, producing a high degree of consistency and reliability when in-plane and out-of-plane fracture characteristics are compared.

## **Chapter 7. Conclusions**

In this research, a methodology that employs digital image correlation (DIC) and high-speed photography to monitor in-plane deformations on plate-shaped edge-cracked specimens subjected to 1-point impact loading event has been developed (see Chapter 2). The methodology has been calibrated using commercial grade acrylic, and demonstrated on a wide variety of isotropic and orthotropic materials, including acrylic bone cement, cortical bone, neat epoxy, epoxy nanocomposites modified with carbon nanotubes (CNTs), traditional carbon fiber reinforced polymers (CFRPs), and CFRPs reinforced with CNTs and milled carbon fibers (MCFs). Several of these materials, including bone cement, CNT-infused epoxy nanocomposites, and CFRPs reinforced with CNTs and MCFs, have all been evaluated under dynamic conditions and reported for the first time. Other materials, such as cortical bone and unmodified CFRPs, have been previously investigated in the literature under dynamic fracture conditions; however, these materials have been evaluated for the first time in this dissertation using high-speed photography and DIC, such that full-field displacements on the specimen surface can be utilized to measure stress intensity factors (SIFs) accurately, and such that the crack tip can be located in order to determine crack tip velocities, which are necessary for accurate estimation of post-initiation SIFs.

The comparison of industrial grade acrylic to medical grade acrylic bone cement (Chapter 3) indicates that, while both materials perform similarly under quasi-static fracture conditions, industrial grade acrylic is superior under dynamic fracture conditions. For younger patients whose prosthetics are more likely to experience impact loading during activities (running,

tackling, and jumping) uncemented implants, where bone grows directly into the roughened surfaces of the implant, are likely a better choice for longevity of the artificial joint.

The evaluation of bovine cortical bone under dynamic fracture conditions (Chapter 4) is considered the first to study its axial fracture under impact loading conditions. Measured critical SIFs are higher than those reported for dynamic fracture of similar dried bovine cortical bone under transverse fracture conditions [37].

While the evaluation of the dynamic fracture properties of CNT-infused epoxy in Chapter 5 was the first such report in the literature, no significant changes were observed relative to neat epoxy counterparts. This result was consistent with the quasi-static work presented in this chapter, where only very small changes in quasi-static tensile and fracture properties were obtained, despite many different dispersion techniques and qualities of nanofiller dispersion.

The work presented in Chapter 6 is unique in its inclusion of both the ultrasonic determination of all nine independent elastic constants of an orthotropic material, as well as the application of these experimentally-determined values for fracture parameter calculations. While no significant improvements were found in the critical SIFs of samples modified with CNTs, some critical energy release rate improvements, comparable to those reported in the literature with CNTs [58, 88-95], were obtained. This difference in trends between critical SIF and critical energy release rate is attributed to the role elastic material properties play after the introduction of nanofillers. This also suggests the importance of evaluating not just the critical SIF ( $K_{IC} / K_{I-ini}^d$ ) but the critical energy release rate ( $G_{IC} / G_{I-ini}^d$ ) (often identified as fracture toughness in the composites community) as well.

## 7.1 Future Directions

Further research is necessary in order to improve the dynamic fracture characteristics of bone cement, as indicated in Chapter 3. Possible solutions include improving the bonding between radiopacifier and interbead matrix, and reducing shrinkage stresses between interbead matrix and pre-polymerized beads.

Due to the relatively limited research that has been previously conducted in the area of dynamic cortical bone fracture and the high disparity between published reports [37, 41], more work in this area is needed beyond that presented in Chapter 4. In addition to the dynamic axial fracture reported, loading rate studies, including quasi-static fracture and dynamic fracture using several different pulse shapers, could greatly improve our understanding of clinical bone fracture. Additional variables to be considered include age, species, and location of bone specimens. Perhaps most importantly, this work could be extended to include transverse fracture, as this is the direction of crack initiation in the clinical sense.

As the fracture behavior of bone and bone cement have already been examined in this work (Chapters 3 and 4), future research could then consider the clinically-relevant bimaterial case of an interfacial crack growing between bone cement and bone, which often leads to implant failure. Additionally, the bimaterial problem of an interfacial crack growing between bone cement and common prosthetic material such as titanium or cobalt chromium could be considered.

Despite presenting many different dispersion techniques to achieve various dispersion states using many different types of CNTs, epoxy systems, and curing cycles, no *mechanical* improvements significant enough to warrant the high cost, tedious processing, and unknown health risks of CNTs, have been reported in Chapter 5. It is quite possible that, relative to the crack tip in a traditional fracture mechanics experiment, CNTs are not large enough to



significantly influence crack growth or its path. Hence, future work could consider the effects of randomly dispersed graphene nanoplatelets within an epoxy matrix. In addition to the potential effects of graphene, there may be a significant interaction between graphene and CNTs if both are dispersed together into an epoxy matrix. If significant mechanical improvements can be found consistently using graphene, then the interlaminar properties of three-phase nanocomposites comprised of graphene, epoxy, and carbon fiber should be examined, as demonstrated in Chapter 6.

## References

- [1] R. J. Sanford, *Principles of Fracture Mechanics*. (Prentice Hall, Upper Saddle River, NJ, 2003).
- [2] C. E. Inglis, Stresses in a plate due to the presence of cracks and sharp corners. *Transactions Institution of Naval Architects*, 55, 219-241 (1913).
- [3] A. A. Griffith, Phenomena of rupture and flow in solids. *Philosophical Transactions of the Royal Society of London- A* 221, 163-197 (1921).
- [4] H. M. Westergaard, Bearing pressures and cracks. *Applied Mechanics* 61, A49-A53 (1939).
- [5] G. R. Irwin, in *Handbuch der Physik*, S. Flugge, Ed. (Springer, 1958), vol. VI, pp. 558-590.
- [6] J. W. Dally, W. F. Riley, *Experimental Stress Analysis*. (College House Enterprises, Knoxville, TN, ed. 4, 2005).
- [7] B. Hopkinson, A method of measuring the pressure produced in the detonation of high explosives or by the impact of bullets. *Philosophical Transactions of the Royal Society of London- A* 213 437-456 (1914).
- [8] H. Kolsky, An investigation of the mechanical properties of materials at very high rates of loading. *Proceedings of the Physical Society- Section B* 62, 676-700 (1949).
- [9] H. W. Nam, G. A. Aggag, K. Takahashi, K. S. Han, The dynamic behavior of metal-matrix composites under low-velocity impact. *Composites Science and Technology* 60, 817-823 (2000).
- [10] C. E. Martins, M. A. Irfan, V. Prakash, Dynamic fracture of linear medium density polyethylene under impact loading conditions. *Materials Science and Engineering a-Structural Materials Properties Microstructure and Processing* 465, 211-222 (2007).
- [11] G. Weisbrod, D. Rittel, A method for dynamic fracture toughness determination using short beams. *International Journal of Fracture* 104, 89-103 (2000).
- [12] F. Dai, R. Chen, M. J. Iqbal, K. Xia, Dynamic cracked chevron notched Brazilian disc method for measuring rock fracture parameters. *International Journal of Rock Mechanics and Mining Sciences* 47, 606-613 (2010).
- [13] F. Dai, R. Chen, K. Xia, A Semi-Circular Bend Technique for Determining Dynamic Fracture Toughness. *Experimental Mechanics* 50, 783-791 (2010).
- [14] S. M. Dong, Y. Wang, Y. M. Xia, A finite element analysis for using Brazilian disk in split Hopkinson pressure bar to investigate dynamic fracture behavior of brittle polymer materials. *Polymer Testing* 25, 943-952 (2006).
- [15] Q. Z. Wang, F. Feng, M. Ni, X. P. Gou, Measurement of mode I and mode II rock dynamic fracture toughness with cracked straight through flattened Brazilian disc

- impacted by split Hopkinson pressure bar. *Engineering Fracture Mechanics* 78, 2455-2469 (2011).
- [16] A. Shukla, V. Parameswaran, Y. Du, V. Evora, Dynamic crack initiation and propagation in nanocomposite materials. *Reviews on Advanced Materials Science* 13, 47-58 (2006).
- [17] D. Lee, H. Tippur, M. Kirugulige, P. Bogert, Experimental Study of Dynamic Crack Growth in Unidirectional Graphite/Epoxy Composites using Digital Image Correlation Method and High-speed Photography. *Journal of Composite Materials* 43, 2081-2108 (2009).
- [18] J. Charnley, Anchorage of the femoral head prosthesis to the shaft of the femur. *Journal of Bone and Joint Surgery-British Volume* 42, 28-30 (1960).
- [19] M. Stanczyk, Study on modelling of PMMA bone cement polymerisation. *Journal of Biomechanics* 38, 1397-1403 (2005).
- [20] G. Lewis, Effect of mixing method and storage temperature of cement constituents on the fatigue and porosity of acrylic bone cement. *Journal of Biomedical Materials Research* 48, 143-149 (1999).
- [21] S. Ramakrishna, J. Mayer, E. Wintermantel, K. W. Leong, Biomedical applications of polymer-composite materials: a review. *Composites Science and Technology* 61, 1189-1224 (2001).
- [22] K. T. Chu et al., Hydroxyapatite/PMMA composites as bone cements. *Bio-Medical Materials and Engineering* 14, 87-105 (2004).
- [23] M. Jasty et al., The initiation of failure in cemented femoral components of hip arthroplasties. *Journal of Bone and Joint Surgery-British Volume* 73, 551-558 (1991).
- [24] L. D. T. Topoleski, P. Ducheyne, J. M. Cuckler, A fractographic analysis of *in vivo* poly(methyl methacrylate) bone cement failure mechanisms. *Journal of Biomedical Materials Research* 24, 135-154 (1990).
- [25] M. Jasty et al., Porosity of various preparations of acrylic bone cements. *Clinical Orthopaedics and Related Research*, 122-129 (1990).
- [26] P. J. Buckley, J. F. Orr, I. C. Revie, S. J. Breusch, N. J. Dunne, Fracture characteristics of acrylic bone cement-bone composites. *Proceedings of the Institution of Mechanical Engineers Part H-Journal of Engineering in Medicine* 217, 419-427 (2003).
- [27] S. Ishihara, T. Goshima, K. Kanekasu, A. J. McEvily, The static and cyclic strength of a bone-cement bond. *Journal of Materials Science-Materials in Medicine* 13, 449-455 (2002).
- [28] C. I. Vallo, T. R. Cuadrado, P. M. Frontini, Mechanical and fracture behaviour evaluation of commercial acrylic bone cements. *Polymer International* 43, 260-268 (1997).
- [29] M. Baleani, M. Viceconti, The effect of adding 10% of barium sulphate radiopacifier on the mechanical behaviour of acrylic bone cement. *Fatigue & Fracture of Engineering Materials & Structures* 34, 374-382 (2011).

- [30] J. A. Johnson, D. W. Jones, The mechanical properties of PMMA and its copolymers with ethyl methacrylate and butyl methacrylate. *Journal of Materials Science* 29, 870-876 (1994).
- [31] D. Rittel, H. Maigre, An investigation of dynamic crack initiation in PMMA. *Mechanics of Materials* 23, 229-239 (1996).
- [32] T. Weerasooriya, P. Moy, and D. Casem, Fracture Toughness for PMMA as a Function of Loading Rate. *Proceedings of the 2006 SEM Annual Conference & Exposition on Experimental and Applied Mechanics* (2006).
- [33] H. Wada, Determination of dynamic fracture toughness for PMMA. *Engineering Fracture Mechanics* 41, 821-831 (1992).
- [34] H. Wada, M. Seika, C. A. Calder, T. C. Kennedy, Measurement of impact fracture toughness for pmma with single-point bending test using an air gun. *Engineering Fracture Mechanics* 46, 715-719 (1993).
- [35] P. Fratzl, H. S. Gupta, E. P. Paschalis, P. Roschger, Structure and mechanical quality of the collagen-mineral nano-composite in bone. *Journal of Materials Chemistry* 14, 2115-2123 (2004).
- [36] W. C. Van Buskirk, S. C. Cowin, R. N. Ward, Ultrasonic measurement of orthotropic elastic constants of bovine femoral bone. *Journal of Biomechanical Engineering-Transactions of the ASME* 103, 67-72 (1981).
- [37] R. R. Adharapurapu, F. Jiang, K. S. Vecchio, Dynamic fracture of bovine bone. *Materials Science & Engineering C-Biomimetic and Supramolecular Systems* 26, 1325-1332 (2006).
- [38] J. W. Ager, III, G. Balooch, R. O. Ritchie, Fracture, aging, and disease in bone. *Journal of Materials Research* 21, 1878-1892 (2006).
- [39] J. C. Behiri, W. Bonfield, Orientation dependence of the fracture mechanics of cortical bone. *Journal of Biomechanics* 22, 863-& (1989).
- [40] Z. D. Feng, J. Rho, S. Han, I. Ziv, Orientation and loading condition dependence of fracture toughness in cortical bone. *Materials Science & Engineering C-Biomimetic and Supramolecular Systems* 11, 41-46 (2000).
- [41] R. M. Kulin, F. Jiang, K. S. Vecchio, Effects of age and loading rate on equine cortical bone failure. *Journal of the Mechanical Behavior of Biomedical Materials* 4, 57-75 (2011).
- [42] M. Kuninori, H. Kikugawa, T. Asaka, H. Kasuya, Effect of Different Preservative Methods on Fracture Behavior of Bovine Cortical Bone. *Materials Transactions* 50, 305-312 (2009).
- [43] P. Lucksanasombool, W. A. J. Higgs, R. Higgs, M. V. Swain, Fracture toughness of bovine bone: influence of orientation and storage media. *Biomaterials* 22, 3127-3132 (2001).
- [44] C. L. Malik, S. M. Stover, R. B. Martin, J. C. Gibeling, Equine cortical bone exhibits rising R-curve fracture mechanics. *Journal of Biomechanics* 36, 191-198 (2003).
- [45] J. McCormack, X. S. Wang, S. M. Stover, J. C. Gibeling, D. P. Fyhrie, Analysis of miniature single- and double-notch bending specimens for estimating the fracture

- toughness of cortical bone. *Journal of Biomedical Materials Research Part A* 100A, 1080-1088 (2012).
- [46] T. L. Norman, D. Vashishth, D. B. Burr, Fracture toughness of human bone under tension. *Journal of Biomechanics* 28, 309-320 (1995).
- [47] X. D. Wang, C. M. Agrawal, Fracture toughness of bone using a compact sandwich specimen: Effects of sampling sites and crack orientations. *Journal of Biomedical Materials Research* 33, 13-21 (1996).
- [48] J. Yan, J. J. Mecholsky, Jr., K. B. Clifton, How tough is bone? Application of elastic-plastic fracture mechanics to bone. *Bone* 40, 479-484 (2007).
- [49] E. T. Thostenson, Z. F. Ren, T. W. Chou, Advances in the science and technology of carbon nanotubes and their composites: a review. *Composites Science and Technology* 61, 1899-1912 (2001).
- [50] B. Ashrafi et al., Influence of the reaction stoichiometry on the mechanical and thermal properties of SWCNT-modified epoxy composites. *Nanotechnology* 24, (2013).
- [51] M. L. Gupta et al., The effect of mixing methods on the dispersion of carbon nanotubes during the solvent-free processing of multiwalled carbon nanotube/epoxy composites. *Journal of Polymer Science Part B-Polymer Physics* 51, 410-420 (2013).
- [52] E. Alishahi, S. Shadlou, S. Doagou, M. R. Ayatollahi, Effects of Carbon Nanoreinforcements of Different Shapes on the Mechanical Properties of Epoxy-Based Nanocomposites. *Macromolecular Materials and Engineering* 298, 670-678 (2013).
- [53] M. R. Ayatollahi, S. Shadlou, M. M. Shokrieh, Fracture toughness of epoxy/multi-walled carbon nanotube nano-composites under bending and shear loading conditions. *Materials & Design* 32, 2115-2124 (2011).
- [54] S. Chatterjee et al., Size and synergy effects of nanofiller hybrids including graphene nanoplatelets and carbon nanotubes in mechanical properties of epoxy composites. *Carbon* 50, 5380-5386 (2012).
- [55] G. Gkikas, N. M. Barkoula, A. S. Paipetis, Effect of dispersion conditions on the thermo-mechanical and toughness properties of multi walled carbon nanotubes-reinforced epoxy. *Composites Part B-Engineering* 43, 2697-2705 (2012).
- [56] F. H. Gojny, M. H. G. Wichmann, B. Fiedler, K. Schulte, Influence of different carbon nanotubes on the mechanical properties of epoxy matrix composites - A comparative study. *Composites Science and Technology* 65, 2300-2313 (2005).
- [57] T. H. Hsieh, A. J. Kinloch, A. C. Taylor, I. A. Kinloch, The effect of carbon nanotubes on the fracture toughness and fatigue performance of a thermosetting epoxy polymer. *Journal of Materials Science* 46, 7525-7535 (2011).
- [58] N. Hu et al., Reinforcement effects of MWCNT and VGCF in bulk composites and interlayer of CFRP laminates. *Composites Part B-Engineering* 43, 3-9 (2012).
- [59] P. Jyotishkumar et al., Preparation and Properties of Multiwalled Carbon Nanotube/Epoxy-Amine Composites. *Journal of Applied Polymer Science* 127, 3063-3073 (2013).

- [60] S. U. Khan, J. R. Pothnis, J. K. Kim, Effects of carbon nanotube alignment on electrical and mechanical properties of epoxy nanocomposites. *Composites Part A-Applied Science and Manufacturing* 49, 26-34 (2013).
- [61] N. Lachman, H. D. Wagner, Correlation between interfacial molecular structure and mechanics in CNT/epoxy nano-composites. *Composites Part A-Applied Science and Manufacturing* 41, 1093-1098 (2010).
- [62] P. C. Ma, J. K. Kim, B. Z. Tang, Effects of silane functionalization on the properties of carbon nanotube/epoxy nanocomposites. *Composites Science and Technology* 67, 2965-2972 (2007).
- [63] V. Mirjalili, M. Yourdkhani, P. Hubert, Dispersion stability in carbon nanotube modified polymers and its effect on the fracture toughness. *Nanotechnology* 23, (2012).
- [64] H. Miyagawa, A. K. Mohanty, L. T. Drzal, M. Misra, Nanocomposites from biobased epoxy and single-wall carbon nanotubes: synthesis, and mechanical and thermophysical properties evaluation. *Nanotechnology* 16, 118-124 (2005).
- [65] M. M. Rahman et al., Mechanical characterization of epoxy composites modified with reactive polyol diluent and randomly-oriented amino-functionalized MWCNTs. *Polymer Testing* 31, 1083-1093 (2012).
- [66] M. Shtein, R. Nadiv, N. Lachman, H. D. Wagner, O. Regev, Fracture behavior of nanotube-polymer composites: Insights on surface roughness and failure mechanism. *Composites Science and Technology* 87, 157-163 (2013).
- [67] V. I. Solodilov, R. A. Korokhin, Y. A. Gorbatkina, A. M. Kuperman, Organic fiber reinforced plastics based on complex hybrid matrices including polysulfone and carbon nanotubes as modifiers of epoxy resins. *Russian Journal of Physical Chemistry B* 6, 425-432 (2012).
- [68] Srikanth, S. Kumar, A. Kumar, P. Ghosal, C. Subrahmanyam, Effect of amino functionalized MWCNT on the crosslink density, fracture toughness of epoxy and mechanical properties of carbon-epoxy composites. *Composites Part a-Applied Science and Manufacturing* 43, 2083-2086 (2012).
- [69] J. Sumfleth, K. Prehn, M. H. G. Wichmann, S. Wedekind, K. Schulte, A comparative study of the electrical and mechanical properties of epoxy nanocomposites reinforced by CVD- and arc-grown multi-wall carbon nanotubes. *Composites Science and Technology* 70, 173-180 (2010).
- [70] L. C. Tang et al., Fracture toughness and electrical conductivity of epoxy composites filled with carbon nanotubes and spherical particles. *Composites Part a-Applied Science and Manufacturing* 45, 95-101 (2013).
- [71] E. T. Thostenson, T.-W. Chou, Processing-structure-multi-functional property relationship in carbon nanotube/epoxy composites. *Carbon* 44, 3022-3029 (2006).
- [72] N. Yu, Z. H. Zhang, S. Y. He, Fracture toughness and fatigue life of MWCNT/epoxy composites. *Materials Science and Engineering a-Structural Materials Properties Microstructure and Processing* 494, 380-384 (2008).
- [73] Y. Zhou, F. Pervin, L. Lewis, S. Jeelani, Fabrication and characterization of carbon/epoxy composites mixed with multi-walled carbon nanotubes. *Materials*

- Science and Engineering a-Structural Materials Properties Microstructure and Processing 475, 157-165 (2008).
- [74] K. D. Cowley, P. W. R. Beaumont, The interlaminar and intralaminar fracture toughness of carbon-fibre/polymer composites: The effect of temperature. *Composites Science and Technology* 57, 1433-1444 (1997).
- [75] M. W. Czabaj, J. G. Ratcliffe, Comparison of intralaminar and interlaminar mode I fracture toughnesses of a unidirectional IM7/8552 carbon/epoxy composite. *Composites Science and Technology* 89, 15-23 (2013).
- [76] M. F. S. F. de Moura, R. D. S. G. Campilho, A. M. Amaro, P. N. B. Reis, Interlaminar and intralaminar fracture characterization of composites under mode I loading. *Composite Structures* 92, 144-149 (2010).
- [77] R. W. Truss, P. J. Hine, R. A. Duckett, Interlaminar and intralaminar fracture toughness of uniaxial continuous and discontinuous carbon fibre epoxy composites. *Composites Part a-Applied Science and Manufacturing* 28, 627-636 (1997).
- [78] M. Sakai, H. Kurita, Size-effect on the fracture toughness and the R-curve of carbon materials. *Journal of the American Ceramic Society* 79, 3177-3184 (1996).
- [79] J. A. Smith, S. T. Rolfe, The effect of crack depth (a) and crack depth to width ratio (A/W) on the fracture toughness of A533-B steel. *Journal of Pressure Vessel Technology-Transactions of the ASME* 116, 115-121 (1994).
- [80] Z.-X. Wang, F. Xue, J. Lu, H.-J. Shi, G.-G. Shu, Experimental and Theoretical Investigation of Size Effects on the Ductile/Brittle Fracture Toughness of a Pressure Steel. *International Journal of Damage Mechanics* 19, 611-629 (2010).
- [81] P. Kumar, N. N. Kishore, Initiation and propagation toughness of delamination crack under an impact load. *Journal of the Mechanics and Physics of Solids* 46, 1773-1787 (1998).
- [82] C. T. Sun, C. Han, A method for testing interlaminar dynamic fracture toughness of polymeric composites. *Composites Part B-Engineering* 35, 647-655 (2004).
- [83] S. N. Wosu, D. Hui, P. K. Dutta, Dynamic mixed-mode I/II delamination fracture and energy release rate of unidirectional graphite/epoxy composites. *Engineering Fracture Mechanics* 72, 1531-1558 (2005).
- [84] X. F. Wu, Y. A. Dzenis, Determination of dynamic delamination toughness of a graphite-fiber/epoxy composite using Hopkinson pressure bar. *Polymer Composites* 26, 165-180 (2005).
- [85] D. Lee, H. V. Tippur, B. J. Jensen, P. B. Bogert, Tensile and Fracture Characterization of PETI-5 and IM7/PETI-5 Graphite/Epoxy Composites Under Quasi-Static and Dynamic Loading Conditions. *Journal of Engineering Materials and Technology-Transactions of the ASME* 133, (2011).
- [86] B. Castagnede, K. Y. Kim, W. Sachse, M. O. Thompson, Determination of the elastic constants of anisotropic materials using laser generated ultrasonic signals. *Journal of Applied Physics* 70, 150-157 (1991).
- [87] I. Solodov, D. Doering, G. Busse, Ultrasonic Characterization of Elastic Anisotropy in Composites: Case Study of CFRP. *Materials Testing-Materials and Components Technology and Application* 50, 602-608 (2008).

- [88] K. Almuhammadi, M. Alfano, Y. Yang, G. Lubineau, Analysis of interlaminar fracture toughness and damage mechanisms in composite laminates reinforced with sprayed multi-walled carbon nanotubes. *Materials & Design* 53, 921-927 (2014).
- [89] B. Ashrafi et al., Enhancement of mechanical performance of epoxy/carbon fiber laminate composites using single-walled carbon nanotubes. *Composites Science and Technology* 71, 1569-1578 (2011).
- [90] A. Godara et al., Influence of carbon nanotube reinforcement on the processing and the mechanical behaviour of carbon fiber/epoxy composites. *Carbon* 47, 2914-2923 (2009).
- [91] S. C. Joshi, V. Dikshit, Enhancing interlaminar fracture characteristics of woven CFRP prepreg composites through CNT dispersion. *Journal of Composite Materials* 46, 665-675 (2012).
- [92] P. Karapappas, A. Vavouliotis, P. Tsotra, V. Kostopoulos, A. Paipetis, Enhanced Fracture Properties of Carbon Reinforced Composites by the Addition of Multi-Wall Carbon Nanotubes. *Journal of Composite Materials* 43, 977-985 (2009).
- [93] H. S. Kim, H. T. Hahn, Graphite fiber composites interlayered with single-walled carbon nanotubes. *Journal of Composite Materials* 45, 1109-1120 (2011).
- [94] G. Romhany, G. Szebenyi, Interlaminar crack propagation in MWCNT/fiber reinforced hybrid composites. *Express Polymer Letters* 3, 145-151 (2009).
- [95] R. J. Sager et al., Interlaminar Fracture Toughness of Woven Fabric Composite Laminates with Carbon Nanotube/Epoxy Interleaf Films. *Journal of Applied Polymer Science* 121, 2394-2405 (2011).
- [96] M. S. Kirugilige, H. V. Tippur, T. S. Denney, Measurement of transient deformations using digital image correlation method and high-speed photography: application to dynamic fracture. *Applied Optics* 46, 5083-5096 (2007).
- [97] M. Baleani, L. Cristofolini, C. Minari, A. Toni, Fatigue strength of PMMA bone cement mixed with gentamicin and barium sulphate vs pure PMMA. *Proceedings of the Institution of Mechanical Engineers Part H-Journal of Engineering in Medicine* 217, 9-12 (2003).
- [98] T. Nishioka, S. N. Atluri, Path-independent integrals, energy release rates, and general solutions of near-tip fields in mixed-mode dynamic fracture mechanics. *Engineering Fracture Mechanics* 18, 1-22 (1983).
- [99] C. E. Rousseau, H. V. Tippur, Influence of elastic gradient profiles on dynamically loaded functionally graded materials: cracks along the gradient. *International Journal of Solids and Structures* 38, 7839-7856 (2001).
- [100] L. Plangsangmas, J. J. Mecholsky, A. B. Brennan, Determination of fracture toughness of epoxy using fractography. *Journal of Applied Polymer Science* 72, 257-268 (1999).
- [101] G. C. Sih, P. C. Paris, G. R. Irwin, On cracks in rectilinearly anisotropic bodies. *International Journal of Fracture Mechanics* 1, 189-203 (1965).
- [102] C. Liu, A. J. Rosakis, M. G. Stout, Dynamic fracture toughness of a unidirectional graphite/epoxy composite. Paper Presented at the ASME International Mechanical



- Engineering Congress and Exposition. Proceedings of the Symposium on “Dynamic Effects in Composites Structures,” 2001 Nov 11-16, New York, NY.
- [103] R. Bedsole, H. V. Tippur, Dynamic Fracture Characterization of Small Specimens: A Study of Loading Rate Effects on Acrylic and Acrylic Bone Cement. *Journal of Engineering Materials and Technology-Transactions of the ASME* 135, (2013).
- [104] C. Park et al., Multifunctional nanotube polymer nanocomposites for aerospace applications: adhesion between SWCNT and polymer matrix. Proceedings of the 31<sup>st</sup> Adhesion Society Meeting, 2008 Feb 17-20, Austin, TX.
- [105] M. M. Rahman, M. Hosur, K. T. Hsiao, L. Wallace, S. Jeelani, Low velocity impact properties of carbon nanofibers integrated carbon fiber/epoxy hybrid composites manufactured by OOA-VBO process. *Composite Structures* 120, 32-40 (2015).
- [106] M. H. G. Wichmann, J. Sumfleth, B. Fiedler, F. H. Gojny, K. Schulte, Multiwall carbon nanotube/epoxy composites produced by a masterbatch process. *Mechanics of Composite Materials* 42, 395-406 (2006).
- [107] F. Bignotti, S. Pandini, F. Baldi, R. De Santis, Effect of the Resin/Hardener Ratio on Curing, Structure and Glass Transition Temperature of Nanofilled Epoxies. *Polymer Composites* 32, 1034-1048 (2011).
- [108] F. Fernandez-Nograro, A. Valea, R. LlanoPonte, I. Mondragon, Dynamic and mechanical properties of DGEBA/poly(propylene oxide) amine based epoxy resins as a function of stoichiometry. *European Polymer Journal* 32, 257-266 (1996).
- [109] V. B. Gupta, L. T. Drzal, C. Y. C. Lee, M. J. Rich, The temperature-dependence of some mechanical-properties of a cured epoxy-resin system. *Polymer Engineering and Science* 25, 812-823 (1985).
- [110] C. Sun, Z. Jin, *Fracture Mechanics*. (Academic Press, Waltham, MA, 2012).

## Appendix A. Comparison of Critical K vs. Critical G

In Chapter 6, reductions were found in terms of critical SIFs but improvements were found in terms of critical energy release rate when CNTs were added to the epoxy matrix of 3-phase CFRPs. In light of these unexpected results for, critical SIFs are converted to critical energy release rate in this appendix.

First, the isotropic materials presented in Chapter 3 are considered. Critical SIFs ( $K_{IC} / K_{I-ini}^d$ ) are related to critical energy release rates ( $G_{IC} / G_{I-ini}^d$ ) for a mode-I problem by:

$$G = \frac{K_I^2}{E}.$$

Table 3.2 has been modified to include critical energy release rates (Table A.1). No major changes occur in the trends when  $K_{IC} / K_{I-ini}^d$  values are converted to  $G_{IC} / G_{I-ini}^d$ . Note that the addition of CNTs to the epoxy matrix did not have a significant effect on the elastic modulus, so CNT-modified epoxies were not considered here.

Pulse Shaper	Average PMMA	Average BC	Average PMMA	Average BC
	$K_{IC} / K_{I-ini}^d$ (MPa $\sqrt{m}$ )	$K_{IC} / K_{I-ini}^d$ (MPa $\sqrt{m}$ )	$G_{IC} / G_{I-ini}^d$ (J / m <sup>2</sup> )	$G_{IC} / G_{I-ini}^d$ (J / m <sup>2</sup> )
None	2.44 ± 0.11	1.70 ± 0.09	942 ± 87	481 ± 49
AI	1.75 ± 0.14	1.43 ± 0.17	496 ± 80	347 ± 85
AI/PC	1.88 ± 0.18	1.42 ± 0.10	575 ± 108	336 ± 45
Quasi-static	1.32 ± 0.17	1.34 ± 0.06	285 ± 75	300 ± 26

**Table A.1:** Compilation of critical SIFs and energy release rates for PMMA and BC for each of the four loading rates.

The only orthotropic critical SIF values presented in this dissertation that have not already been converted to critical energy release rate are those for cortical bone from Chapter 4. The critical dynamic SIF ( $K_{I-ini}^d$ ) values of  $2.73 \pm 0.20 \text{ MPa}\sqrt{\text{m}}$  correspond to  $G_{I-ini}^d$  of  $360 \pm 51 \text{ J/m}^2$ .